Charles University

Faculty of Science

Study Program:

Molecular and Cellular Biology, Genetics and Virology



Mgr. Nikol Dibus

Functional Characterization of SCF^{FBXO38} Ubiquitin Ligase-dependent Protein Degradation

Funkční charakterizace proteinové degradace závislé na ubikvitin ligáze SCF^{FBXO38}

Doctoral Thesis

Supervisor: Mgr. Lukáš Čermák, Ph. D.

Prague, 2022

Prohlášení

Prohlašuji, že jsem závěrečnou práci zpracovala samostatně a že jsem uvedla všechny použité informační zdroje a literaturu. Tato práce ani její podstatná část nebyla předložena k získání jiného nebo stejného akademického titulu.

V Praze, 25. 6. 2022

Mgr. Nikol Dibus

Acknowledgments

I would like to thank all the people who made this project possible. Special thanks go to my supervisor Lukáš Čermák for giving me the opportunity to work in his laboratory, for all the effort and time he devoted to me, for his friendly attitude, and for showing me how to think big and not lose scientific enthusiasm. I also thank our lab members who created an easy-going environment and worked on this project, especially Eliška Zobalová and Mario Monleón. I also want to acknowledge all the people from the Institute of Molecular Genetics and BIOCEV who have ever participated in this project, either experimentally or intellectually. My special thank goes to my husband Michal for his endless love, patience, and encouragement. Lastly, I would like to thank my family, who have supported me since the beginning of my studies and made my education possible.

Abstract

Ubiquitin ligases are responsible for the specific recognition of proteins targeted for proteasome-dependent degradation. This project focused on the molecular and functional characterization of the SCF^{FBXO38} ubiquitin ligase. As with many others, its biological function has not yet been elucidated in detail, although it is the only ubiquitin ligase whose mutations lead to the onset of a distal form of muscle atrophy. In the first part of our project, we identified new substrates for this ubiquitin ligase, the nuclear proteins ZXDA and ZXDB, with insufficiently characterized functions. Using genetic and biochemical methods, we have shown that ZXDA/B proteins act as positive regulators of centromeric chromatin integrity and that experimental inactivation of the SCF^{FBXO38} ubiquitin ligase resulted in a ZXDA/B-dependent stabilization of CENP-A and CENP-B proteins in the centromeric regions.

In the second part of the project, we focused on analyzing the mouse model deficient in the *Fbxo38* gene. We demonstrated that loss of *Fbxo38* leads to growth retardation affecting various organs, including the male reproductive system. A detailed histological examination revealed pathological alterations in the seminiferous tubules, accompanied by a lower number of spermatozoa and decreased fertility. We have shown that FBXO38 is functionally expressed in Sertoli cells, the key orchestrators of spermatogenesis. Consistent with our observations from human cancer cell lines, loss of FBXO38 resulted in stabilization of ZXDB protein and an increase in centromeric chromatin density in Sertoli cells. Finally, we discovered that FBXO38 is involved in the terminal differentiation process of Sertoli cells, and its loss resulted in their delayed maturation.

This work described a novel biochemical pathway involved in the regulation of centromeric chromatin and mouse spermatogenesis.

Keywords: ubiquitin ligases, protein degradation, FBXO38, centromeres, spermatogenesis

Abstrakt

Ubikvitin ligázy jsou zodpovědné za specifické rozpoznání proteinů určených k odstranění pomocí proteazomu. Cílem našeho projektu byla molekulární a funkční charakterizace ubikvitin ligázy SCF^{FBXO38}. Podobně jako u mnoha jiných není její biologická funkce dosud podrobně objasněna, přestože se jedná o jedinou ubikvitin ligázu, jejíž mutace vedou k rozvoji distální formy svalové atrofie. V první části našeho projektu jsme identifikovali nové substráty této ubikvitin ligázy, a to jaderné proteiny ZXDA a ZXDB, jejichž funkce není dosud popsána. Pomocí genetických a biochemických metod jsme prokázali, že proteiny ZXDA/B jsou pozitivními regulátory integrity centromerického chromatinu, a že experimentální inaktivace ubikvitin ligázy SCF^{FBXO38} vede ke stabilizaci proteinů CENP-A a CENP-B v oblasti centromer, a to v závislosti na ZXDA/B.

Ve druhé části projektu jsme se zaměřili na analýzu myšího modelu s delecí genu *Fbxo38*. Prokázali jsme, že ztráta *Fbxo38* vede k poruchám růstu, které postihují různé orgány včetně samčí reprodukční soustavy. Podrobnou histologickou analýzou jsme odhalili patologické změny v semenotvorných kanálcích doprovázené nižší produkcí spermií a sníženou fertilitou. Dále jsme ukázali, že FBXO38 je funkčně exprimována v Sertoliho buňkách, které jsou nezbytným regulátorem spermatogeneze. V souladu s našimi pozorováními z lidských nádorových linií jsme potvrdili, že ztráta FBXO38 vede ke stabilizaci proteinu ZXDB a centromerického chromatinu také v Sertoliho buňkách. Nakonec jsme odhalili, že FBXO38 se účastní procesu terminální diferenciace Sertoliho buněk a že ztráta FBXO38 vede ke zpoždění jejich maturace.

Tato práce popisuje novou biochemickou dráhu účastnící se regulace centromerického chromatinu a myší spermatogeneze.

Klíčová slova: ubikvitin ligázy, proteinová degradace, FBXO38, centromery, spermatogeneze

List of Abbreviations

AAA^+	ATPases associated with various cellular activities
ACA	anti-centromeric antibodies
ALDH1A	aldehyde dehydrogenase 1a
AMH	anti-Müllerian hormone
APC/C	anaphase-promoting complex/cyclosome
APF1	ATP-dependent proteolysis factor 1
ATP	adenosine triphosphate
ATRA	all-trans retinoic acid
BCL6	B-cell CLL/lymphoma 6
bp	basepair
BTB	blood-testis barrier
cAMP	cyclic adenosine monophosphate
CAND1	cullin-associated NEDD8-dissociated protein 1
CBF3	centromere-binding factor 3
CCAN	constitutive centromere-associated network
CCL2	chemokine ligand 2
CDC20	cell division cycle homolog 20
CDE	centromeric DNA element
CDK	cyclin-dependent kinase
CENP	centromere protein
CIITA	class II trans-activator
CK2	casein kinase 2
CRL	cullin-RING ligase
CUL	cullin
CYP26	cytochrome P450 family 26
DCAF	DDB1 (DNA damage-binding protein 1)- and CUL4-associated factor
DEDD	death effector domain-containing protein
dHMN	distal hereditary motor neuronopathy
DUB	deubiquitinating enzyme
FBXL	F-box and leucine-rich repeat protein
FBXO38	F-box only protein 38
FBXW	F-box and WD repeat-containing protein
FGF9	Fibroblast growth factor 9
FSH	follicle-stimulating hormone
FSHR	FSH receptor
GDNF	glial cell-line-derived neurotrophic factor
GnRH	gonadotropin-releasing hormone
H3K4me2	dimethylation of histone H3 lysine 4
H3K9me3	trimethylation of histone H3 lysine 9
HAC	human artificial chromosomes
HECT	homologous to E6AP C-terminus
HJURP	Holliday junction recognition protein

HOR	higher-order repeat
HP1	heterochromatin protein 1
ChIP-seq	chromatin immunoprecipitation sequencing
KIF20B	kinesin family member 20B
KLF7	Krüppel-like transcription factor 7
KMN	KNL-1–Mis12 complex–Ndc80 complex
KNL-1	kinetochore scaffold 1
LH	luteinizing hormone
LHR	LH receptor
Mb	megabase
MCC	mitotic checkpoint complex
MHC	major histocompatibility complex
NAE	NEDD8-activating enzyme
ncRNA	noncoding RNA
NLS	nuclear localization signal
NPM	nucleophosmin
PD-1	programmed cell death 1
PD-L1	PD-1 ligand
PLK1	Polo-like kinase 1
RA	retinoic acid
RALDH	retinaldehyde dehydrogenase
RARE	retinoic acid response elements
RBP4	retinol-binding protein 4
RBR	RING-in between-RING
RBX	RING-box protein
RCR	RING-Cys-relay
RDH10	retinol dehydrogenase 10
RING	really interesting new gene
rRNA	ribosomal RNA
SAC	spindle assembly checkpoint
SALL4	Spalt-like transcription factor 4
SCF	SKP1–CUL1–F-box protein
SCP3	synaptonemal complex protein 3
SKP	S phase kinase-associated protein
SOX9	SRY-related high-mobility group (HMG) box 9
SRY	sex-determining region Y
SSC	spermatogonial stem cell
STRA	stimulated by retinoic acid
UPS	ubiquitin-proteasome system
USP7	ubiquitin-specific protease 7
YY1	Ying Yang 1
ZFAT	zinc-finger protein with AT-hook
ZXD	Zinc finger X-linked duplicated
β-TrCP1	β-transducin repeat-containing protein 1

Table of Contents

1. Introduction 15
   1.1 The Ubiquitin-Proteasome System 16
      1.1.1 Proteasome 18
      1.1.2 Ubiquitin Ligases 19
      1.1.3 RING Ligases 19
      1.1.4 FBXO38 22
   1.2 ZXDA and ZXDB 24
   1.3 Centromeres 25
      1.3.1 Centromeric DNA 26
      1.3.2 Centromeric Chromatin 27
      1.3.3 Centromeric Protein B (CENP-B) 29
      1.3.4 Kinetochore 31
   1.4 Spermatogenesis 32
      1.4.1 Hormonal Regulation of Spermatogenesis 33
      1.4.2 Retinoic Acid Pathway 35
      1.4.3 Sertoli Cells 35
      1.4.4 Sertoli Cells in Testis Development 36
2. Objectives 38
3. Publications 39
4. Results and Discussion 107
   4.1 Substrates of the SCF^{FBXO38} Ubiquitin Ligase 107
   4.2 The Biological Function of the SCF^{FBXO38}-dependent Protein Degradation 110
   4.3 The Phenotype of the Mouse Model Deficient in FBXO38 113
   4.4 Confirmation of *in vitro* Results in the Mouse Model 117
5. Conclusions 118
6. List of Publications 120
7. References 121
8. Appendix 133

1. Introduction

Dynamic cellular processes require strict control over protein spatiotemporal availability resulting from the precise balance between protein production and protein degradation. In contrast to non-selective protein degradation, which occurs in the lumen of a lysosome, dynamic processes are usually controlled via specific degradation mediated by the ubiquitin-proteasome system (UPS). To be degraded by the UPS, proteins are first marked by covalent attachment of ubiquitin chains and subsequently recognized and proteolytically cleaved by the proteasome complex. The selectivity of the UPS is ensured by ubiquitin ligases specifically recognizing and marking proteins targeted for degradation. The most prominent family represents cullin ligases that are implicated in the regulation of various cellular events. However, the function and target substrates of many of them remain unknown. In the past, studies of ubiquitin ligases were essential in understanding critical cellular processes, including stress response.

In this work, we aimed to characterize one of the insufficiently studied cullin-dependent ubiquitin ligases, FBXO38. This ubiquitin ligase was implicated in controlling cell division and the onset of muscular atrophy. Although these specific processes were not within the scope of this project, our results could lead to a better understanding of FBXO38 involvement in homeostasis maintenance and pathological conditions resulting from FBXO38 mutations.

The main objectives of this project were to identify and describe FBXO38 substrates, characterize their biological functions, and verify these discoveries in the mouse model deficient in the *Fbxo38* gene. We identified zinc-finger proteins ZXDA and ZXDB as FBXO38 substrates and showed their implication in centromere maintenance. In addition, we characterized the impact of FBXO38 loss on mouse spermatogenesis. These results provide the first comprehensive substrate description of this ligase and link its function to pathways involved in controlling the integrity of centromeres.

1.1 The Ubiquitin-Proteasome System

Protein degradation by the UPS consists of two essential steps: the covalent attachment of ubiquitin molecules (ubiquitination) to the target protein (substrate), and the recognition, unfolding, and proteolysis of such modified protein by the 26S proteasome.

Ubiquitin is a 76-amino acid peptide first identified by Ciechanover, Hod, and Hershko as a component of the ATP-dependent proteolytic system of rabbit reticulocytes and was therefore termed ATP-dependent proteolysis factor 1 (APF1) (Ciehanover et al., 1978). This discovery was later linked to the ubiquitously expressed highly conserved polypeptide previously identified by Goldstein et al. (Goldstein et al., 1975; Wilkinson et al., 1980). Ubiquitination of the substrate is accomplished by the cooperation of three enzymes – E1, E2, and E3. There are only two genes for E1 and approximately forty genes for the E2 enzyme in the human genome, but between 600 and 1000 genes encode E3 ubiquitin ligases (Baloghova et al., 2019). First, ubiquitin is activated by attachment to the ubiquitin-activating enzyme (E1 enzyme). During this ATP-dependent step, ubiquitin C-terminal glycine residue is adenylated, and consequently, a thioester bond is formed linking the C-terminus of ubiquitin and cysteine residue in E1. In the second step, ubiquitin is transferred by a trans-esterification reaction to the active cysteine residue in the ubiquitin-conjugating enzyme (E2). Finally, ubiquitin ligase (E3) mediates the linking of a glycine residue in ubiquitin with the ε-amino group of a lysine residue in the substrate through the formation of an isopeptide bond. Subsequently, another ubiquitin is attached to the lysine residue of the ubiquitin covalently linked to the substrate protein, usually to form a polyubiquitin chain (Figure 1) (Hershko and Ciechanover, 1998). Ubiquitin itself contains seven lysine residues (Lys6, Lys11, Lys27, Lys29, Lys33, Lys48, and Lys63) that can serve as acceptors for another ubiquitin. Ubiquitin can also be attached to the N-terminus of previous ubiquitin by a peptide bond to form a Met1-linked chain. All these residues allow the formation of eight homotypic and several mixed (heterotypic) conjugates that can also be assembled into branched structures (Komander and Rape, 2012). The formation of the polyubiquitin chain on different lysine residues results in the different fate of the substrates. Most commonly, the homotypic Lys48-linked polyubiquitination promotes proteasome-dependent degradation and represents the most abundant ubiquitin chain type (Chau et al., 1989). The second most abundant ubiquitination represents Lys63-linked which is involved in many non-proteolytic cellular functions (Swatek and Komander, 2016).

Ubiquitination is a reversible process mediated by a group of proteases called deubiquitinating enzymes (DUBs) that catalytically cleave ubiquitin from the substrates. In the human genome, around one hundred genes encoding for DUBs contribute to the control of ubiquitination. They can

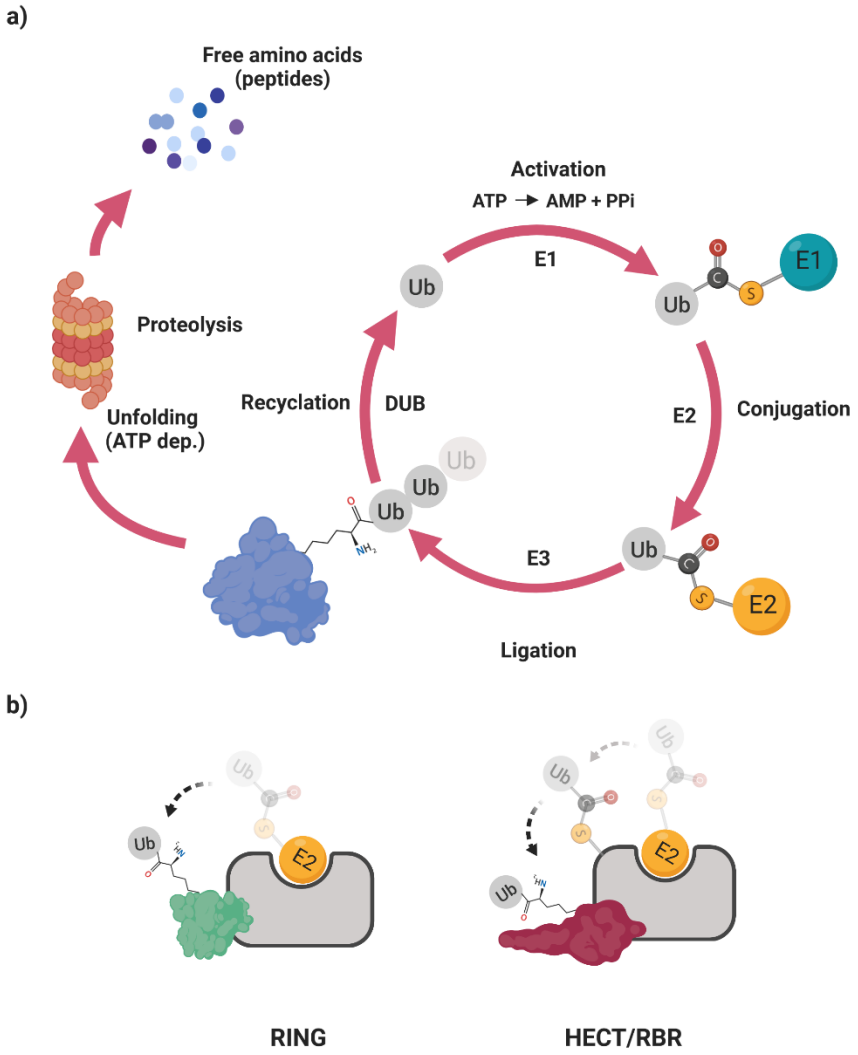


Figure 1. The Ubiquitin Proteasome System. (a) Ubiquitination is an ATP-dependent process achieved by the action of three enzymes that catalyze ubiquitin activation (E1-activating enzyme), conjugation (E2-conjugating enzyme) and finally ubiquitin transfer to the substrate (E3 ubiquitin ligase). Polyubiquitinated substrates are recognized by proteasome where they are unfolded and cleaved into peptides. **(b)** E3 ubiquitin ligases determine the specific selectivity of the substrates. They are classified into two main subgroups according to the mechanism of ubiquitin transfer. While RING ligases catalyze the direct transfer from E2 to the substrate, HECT and RBR form a thioester intermediate before ubiquitin transfer to the substrate lysine residue. Adapted from (Baloghova et al., 2019).

both prevent the degradation of ubiquitinated protein and remove the non-degradative ubiquitin signal (Komander et al., 2009).

1.1.1 Proteasome

As already mentioned, the multisubunit complex called proteasome recognizes ubiquitinated proteins targeted for degradation. Proteasome was first discovered in 1977 by Etlinger and Goldberg as an ATP-dependent protein degradation system in reticulocytes lacking lysosomes (Etlinger and Goldberg, 1977). It represents a large complex comprising the 20S core particle and one or two 19S regulatory particles. The 19S regulatory particle can be divided into the lid and base. The base consists of non-ATPase subunits that serve as receptors for the targeted substrate and the AAA^+ (ATPases associated with various cellular activities) subunits that drive its unfolding and translocation. Since one of the lid subcomplexes (Rpn11) belongs to the DUB family, it is involved in the removal of the ubiquitin chains attached to the substrate and the release of ubiquitin for further ubiquitination (Bard et al., 2018). The 20S core particle resembles a barrel with a central pore and consists of four heptameric rings (two outer α-rings and two inner β-rings) stacked on top of each other. While the α-rings act as a gate, the central parts execute the proteolytic activity. Three of their subunits (β1, β2, and β5) contain proteolytic active sites that cleave a broad range of peptide sequences (Finley, 2009).

Interestingly, two specialized subtypes of proteasome have evolved in the immune system, the immunoproteasome and thymoproteasome. Immunoproteasome has specialized β-subunits (β1i, β2i, and β5i) of the core particle that have distinct cleavage properties resulting in the generation of peptides that are presented on major histocompatibility complex (MHC) class I (Murata et al., 2018). Thymoproteasomes are characterized by the presence of a specialized β5t subunit exclusively expressed in the epithelial cells of the thymic cortex. They are involved in the positive selection of developing thymocytes (Murata et al., 2007).

Cancer cells often exhibit elevated proteasome activity, which can be reversed by specific pharmacologic proteasome inhibition. Bortezomib interacting with the β5 subunit is the first approved drug used for the treatment of multiple myeloma and mantle cell lymphoma. The other two inhibitors (carfilzomib and ixazomib) are currently used for the treatment of the mentioned B-cell neoplasms. Moreover, selective immunoproteasome inhibitor is tested for the treatment of autoimmune diseases (Wang et al., 2021).

1.1.2 Ubiquitin Ligases

E3 ubiquitin ligases represent the most heterogeneous and most critical component of the UPS, as they are responsible for specific substrate recognition. They are classified into two major groups. The first group is represented by RING (really interesting new gene)-type ubiquitin ligases, and the second group comprises HECT (homologous to E6AP C-terminus) and RBR (RING-in between-RING) ubiquitin ligases (Figure 1) (Zheng and Shabek, 2017). The main difference between these groups represents the mechanism by which they mediate the ubiquitin transfer to the target protein. While RING ubiquitin ligases catalyze the direct transfer of ubiquitin to the target protein, HECT and RBR ubiquitin ligases contain catalytic cysteine that forms an intermediate with ubiquitin before its transfer to the substrate (Deshaies and Joazeiro, 2009; Hatakeyama and Nakayama, 2003; Rotin and Kumar, 2009; Spratt et al., 2014). Recently, other classes of ubiquitin ligases were discovered: U-box ligases that are related to the RING family of ubiquitin ligases but lack the zinc-coordinating sites. And RCR (RING-Cys-relay) class that contains the RING domain and two catalytic cysteine residues out of which the upstream cysteine acts as a ubiquitin acceptor that further transfers it to the downstream cysteine by intramolecular transthiolation (Pao et al., 2018).

1.1.3 RING Ligases

RING-type represents the largest family of E3 ubiquitin ligases encompassing around 600 members. RING-finger typically bears zinc-coordinating cysteine and histidine residues, and it directly binds and orientates the E2 enzyme towards the substrate. RING-type ubiquitin ligases can act as monomers, homo- or heterodimers, or as multisubunit complexes. The latter includes the pivotal members of the E3 enzymes – cullin-RING ligase (CRL) family and the anaphase-promoting complex/cyclosome (APC/C) (Deshaies and Joazeiro, 2009; Metzger et al., 2014).

CRLs are characterized by the presence of scaffold protein cullin and RING-box protein (RBX1 or RBX2) recruited to the cullin C-terminus. The N-terminus typically binds an interchangeable adaptor that recruits the substrate receptor responsible for the complex selectivity. The important step in CRL activity regulation represents neddylation, an attachment of small ubiquitin-like

protein NEDD8. During this posttranslational modification, NEDD8 is activated by the NEDD8-activating enzyme (NAE; E1 enzyme), then transferred to the NEDD8-conjugating E2 enzyme, and finally, it is attached to the conserved lysine residue in the C-terminal part of cullin. This process leads to conformational changes bringing the E2 enzyme with covalently bound ubiquitin to the substrate proximity and thus catalyzing the ubiquitination (Figure 2). Moreover, these rearrangements prevent the binding of cullin-associated NEDD8-dissociated protein 1 (CAND1), which mediates the rapid exchange of substrate receptors in the CRL complex. Neddylation is reversed by the COP9 signalosome complex that proteolytically cleaves NEDD8 from cullin, allowing CAND1 binding and thus leading to the exchange of substrate receptors. Altogether, these dynamic cycles of (de)neddylation constitute crucial events in the control of CRL activity (Baek et al., 2021; Duda et al., 2008; Lyapina et al., 2001; Olma and Dikic, 2013). Importantly, neddylation can be experimentally blocked by MLN4924/Pevonedistat, a selective

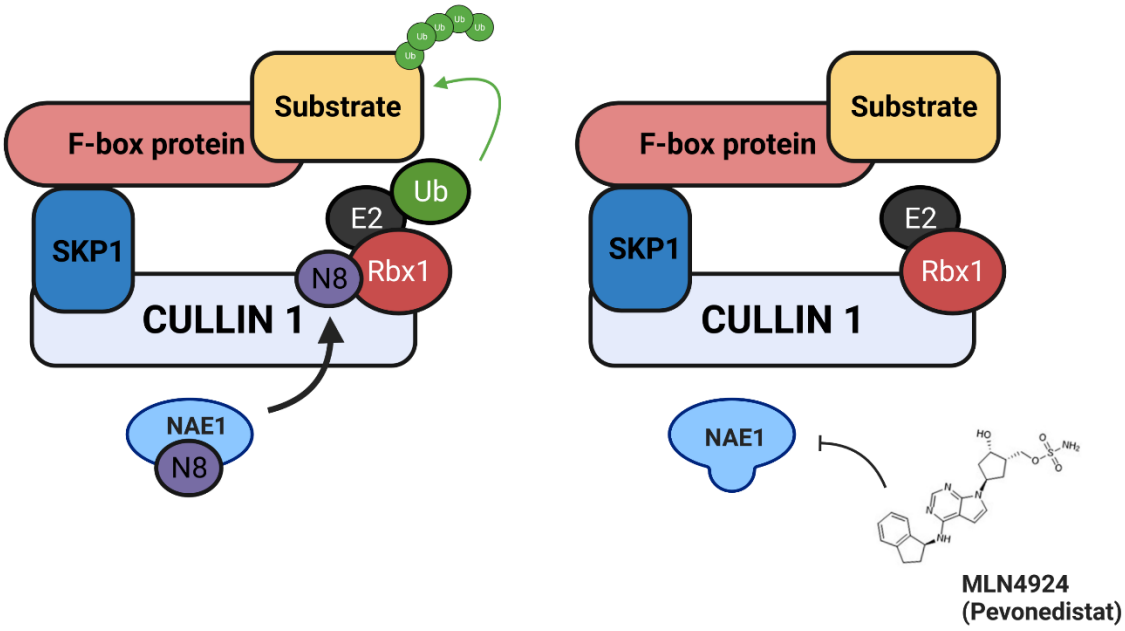


Figure 2. Structure and Function of Cullin-RING Ubiquitin Ligases (CRL). CRLs are characterized by the scaffold protein from the cullin family that recruits RING-box protein (RBX1) associating with E2 to its C-terminus. Cullin N-terminus binds adaptor protein recruiting substrate receptor. Cullin 1-dependent ubiquitin ligases represent the most typical CRLs. The adaptor protein is represented by SKP1 that binds to the substrate receptor from the F-box protein family. CRL-dependent ubiquitin transfer is regulated by the attachment of NEDD8 (N8) to the cullin C-terminus resulting in its conformational changes that bring ubiquitin to the close proximity of the substrate. N8 has to be activated by the NEDD8-activating enzyme (NAE1) the activity of which can be pharmacologically inhibited by MLN4924. If not stated otherwise, all figures were created with BioRender.com.

inhibitor of NAE, leading to the inactivation of CRLs. This represents a great tool in the research of CRL-dependent substrates, and it is also a promising drug in the treatment of several cancer types (Soucy et al., 2009; Zhou et al., 2019a).

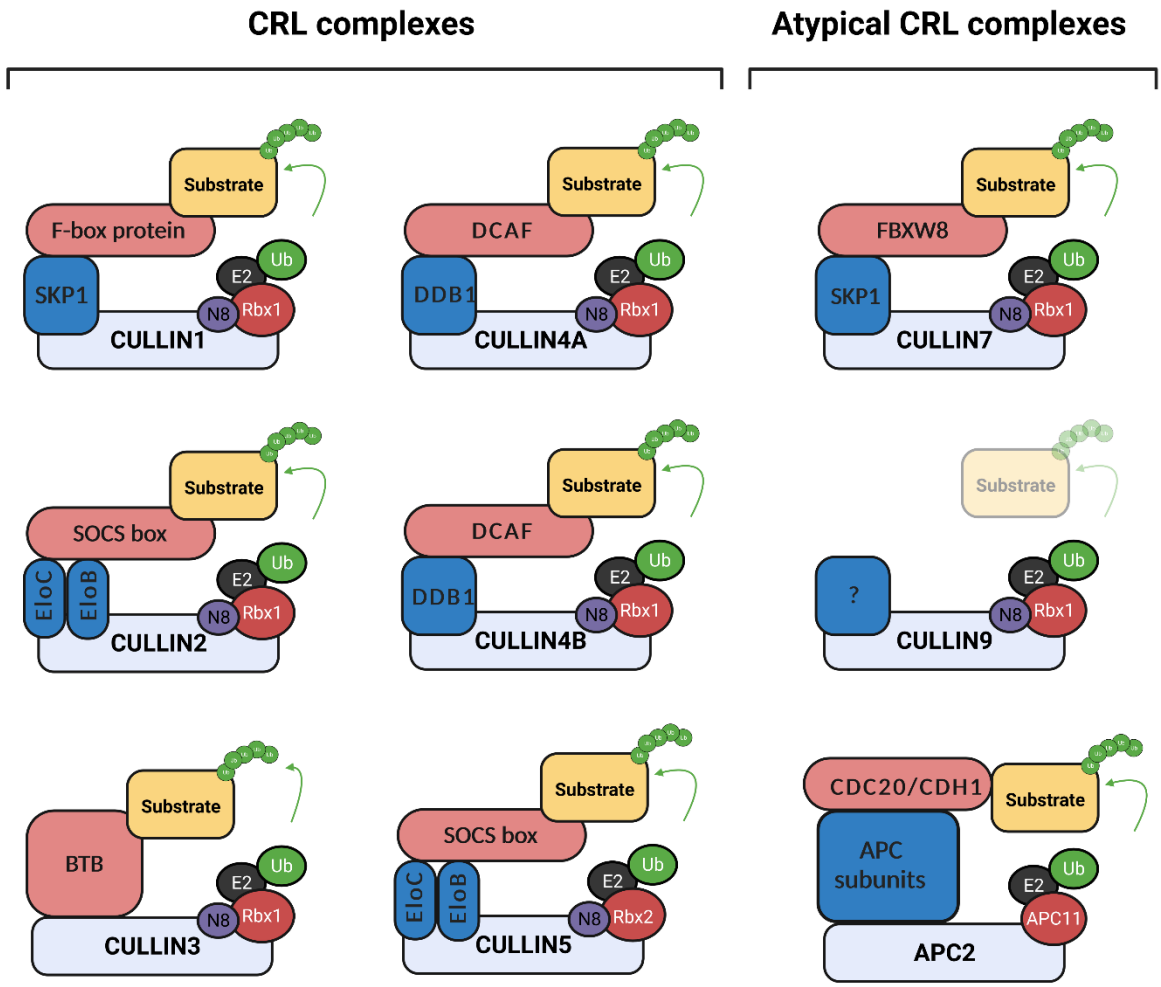


Figure 3. The Family of Cullin-RING Ligases. In humans, eight types of cullin (CUL1, CUL2, CUL3, CUL4A, CUL4B, CUL5, CUL7, and CUL9) exist that bind different adapters employing various substrate receptors. CUL7 and CUL9 represent atypical large cullins. The substrate receptor for CUL9 is unknown. Anaphase-promoting complex/cyclosome (APC/C) bears APC2 that is distantly related to cullins. Created according to (Skaar et al., 2013).

There are eight members of the cullin (CUL) family in humans (Figure 3) (Skaar et al., 2013). The first and best-characterized CRLs are CUL1-dependent (CRL1), known as S phase kinase-associated protein 1 (SKP1)–CUL1–F-box protein (SCF) ubiquitin ligases. In these

complexes, SKP1 acts as an adaptor connecting the CUL1 and the interchangeable substrate receptor F-box protein (Cardozo and Pagano, 2004). The F-box was first described within the cyclin F sequence as a conserved motif responsible for SKP1 interaction (Bai et al., 1996). In humans, there are 69 F-box-containing proteins classified into three subfamilies according to the presence of either WD40 repeats (FBXW), leucine-rich repeats (FBXL), or other domains (FBXO) (Jin et al., 2004). Some of these ubiquitin ligases have established substrates and well-defined functions, including cell cycle regulation, differentiation, or signaling. Dysregulation in SCF-mediated degradation is therefore implicated in many disorders. Indeed, many of the SCF ubiquitin ligases were identified as oncogenes or tumor-suppressors, and their alterations are often correlated with poor prognosis in cancer. A great example represents SKP2 (FBXL1) which is known to mediate the degradation of many important cell-cycle regulators, including cyclin-dependent kinase inhibitors p21 or p27 (Bornstein et al., 2003; Carrano et al., 1999). Importantly, a number of F-box proteins bind multiple substrates. For example, one of the best-characterized SCF ligase β-transducin repeat-containing protein 1 (β-TrCP1; FBXW1) targets various substrates for degradation, including pivotal proteins involved in the regulation of the cell cycle or signaling (Low et al., 2014). On the other hand, the functions and substrates of many ubiquitin ligases have not yet been described, and therefore, they are nicknamed orphan ubiquitin ligases.

An essential step in SCF-mediated degradation is substrate recognition and the stimuli that lead to substrate interaction and subsequent degradation. F-box proteins usually recognize substrates via a stretch of specific amino acids, a motif referred to as a degron. The degron to be recognized by SCF ubiquitin ligase may exist in its unmodified form, but more often, it undergoes specific posttranslational modification positively or negatively affecting the interaction. The substrate recognition may also be mediated by conformational changes or small molecule binding (Skaar et al., 2013). For instance, the already mentioned β-TrCP1 recognizes the consensus degron DSGxxS, where the phosphorylation of serine residues is critical for the interaction (Wu et al., 2003; Yaron et al., 1998).

1.1.4 FBXO38

F-box protein FBXO38 is a poorly characterized substrate receptor for SCF ubiquitin ligase. To date, only Programmed cell death 1 (PD-1), a transmembrane receptor serving as one of the immune checkpoints, was identified as its substrate. PD-1, upon interaction with its ligand

(PD-L1), negatively regulates T cells to prevent autoimmunity, which is often misused by cancer cells that over-express PD-L1 to evade anti-tumor immunity (Chamoto et al., 2017; Meng et al., 2018). SCF^{FBXO38} was shown to mediate ubiquitination and subsequent proteasomal degradation of internalized PD-1 in activated T cells. Mouse T cells deficient in FBXO38 showed upregulation of PD-1 on the cell surface resulting in faster tumor progression in the melanoma and colorectal carcinoma mouse model. The authors of the study were able to identify PD-1 cytoplasmic lysine residue (Lys233) as the target of polyubiquitination; however, the mechanism of its recognition by FBXO38 remains unknown (Meng et al., 2018). Contradictory to this observation, FBXO38 contains one functional nuclear localization signal (NLS), and it was shown to be predominantly a nuclear protein (Smaldone and Ramirez, 2006). Indeed, FBXO38 was initially identified as a co-activator of Krüppel-like transcription factor 7 (KLF7), a regulator of neuronal differentiation. They were shown to be co-expressed in the developing nervous system and in the adult spinal cord and testes. Moreover, FBXO38 was confirmed to interact with and enhance the transcription activity of KLF7; however, no ubiquitination activity towards it was observed (Smaldone et al., 2004). Similarly, acting independently of the SCF complex formation, FBXO38 was suggested to interact with and stabilize kinesin KIF20B, involved in proper cytokinesis. In this study, it was reported that FBXO38 itself is a target of ubiquitination and subsequent proteasomal degradation. However, it is stabilized by USP7 deubiquitinase, and inhibition of either FBXO38 or USP7 results in depletion of KIF20B at the midbodies and subsequently leads to defects in cytokinesis (Georges et al., 2019).

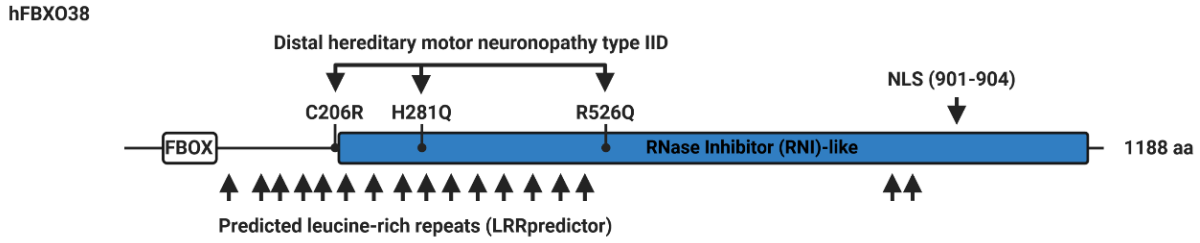


Figure 4. Schematic representation of FBXO38 structure and location of its atrophy-associated mutations. Human FBXO38 is a large protein of 1188 amino acids. The F-Box motif is located in the N-terminus followed by a region of predicted leucine-rich repeats. The nuclear localization sequence is located in the C-terminus. Three mutations (C206R, H281Q, and R526Q) found in patients with distal motor neuronopathy type IID are depicted.

Importantly, FBXO38 is implicated in the homeostasis of the nervous system. To date, three different missense point mutations within the *FBXO38* gene were found in patients suffering from one form of spinal muscular atrophy – distal hereditary motor neuronopathy (dHMN) (Figure 4). This syndrome is characterized by degeneration of neurons leading to muscle weakness and atrophy preferentially in the legs. The first and best-characterized FBXO38 mutation involved in dHMN development is Cys206Arg substitution, which was found to be dominantly inherited in two families. People affected by this mutation showed different severity and age of onset of the disease, but most often, they developed calf weakness, which progressed into walking difficulties, and arm weakness (Sumner et al., 2013). The later identified hereditary homozygous mutation Arg526Gln manifested itself in early-onset muscle weakness accompanied by hearing loss and organ anomalies (Akcimen et al., 2019). Recently, *de novo* mutation leading to His281Gln substitution was identified by an individual with upper limb weakness (Grunseich et al., 2021). The molecular consequences of such alterations remain elusive; however, the first study proposed that the identified mutation causes disrupted KLF7 activation, which could result in the failure of neurite outgrowth (Sumner et al., 2013). Interestingly, another substitution, Met30Arg, located in the F-box region, was identified as the cause of neurodevelopmental disorder – gender dysphoria in a study of monozygotic twins (Morimoto et al., 2017).

1.2 ZXDA and ZXDB

Zinc finger X-linked duplicated A (*ZXDA*) and *ZXDB* are genes located on the short arm of the X chromosome. As a single-exon gene, *ZXDA* emerged in placentals by retrotransposition from the later identified *ZXDC* gene. Later in *Boreoeutheria*, *ZXDB* originated from *ZXDA* by duplication; thus, both genes share 98.7 % identity. Their protein products contain ten tandem C2H2 zinc fingers with the potential transcription factor activity (Figure 5) (Greig et al., 1993). However, their function is not fully described. ZXDC is encoded by the gene located on chromosome 3 and was



Figure 5. Schematic representation of ZXDA and ZXDB structure. Human ZXDA and ZXDB represent almost identical proteins with tandem arrays of ten C2H2 zinc finger motifs

named thanks to its 73 % identity with ZXDA/B proteins. It was identified as an interacting partner of class II trans-activator (CIITA), the regulator of MHC gene transcription, and it was shown to potentiate MHC class II gene expression. Although ZXDA shares a 50 % amino acid identity of its transcriptional activation domain sequence with ZXDC, it lacks the C-terminal domain that was described to be necessary for ZXDC to interact with CIITA. However, ZXDA was shown to interact with ZXDC through their zinc-finger region, and by creating this complex, they were shown to promote MHC class II gene expression (Al-Kandari et al., 2007a; Al-Kandari et al., 2007b). ZXDC was also shown to activate chemokine ligand 2 (CCL2) expression probably by inhibition of transcriptional repressor B-cell CLL/lymphoma 6 (BCL6), and thus it can promote monocyte differentiation (Ramsey and Fontes, 2013). Moreover, ZXDC variant Phe418Leu was detected as a possible predisposition to hematological neoplasm polycythemia vera (Hirvonen et al., 2017). Nonetheless, the molecular function of ZXDA and ZXDB proteins remains elusive.

1.3 Centromeres

Centromeres were first observed in the late 19th century as primary constrictions of condensed chromosomes during mitosis and later as sites for spindle fiber attachment (Yanagida, 2014). Although centromeres are more complex, they can still be defined as specialized chromosomal regions that serve as platforms for kinetochore assembly. Microtubule attachment represents one of the crucial events during mitosis, ensuring proper chromatid segregation and thus the equal

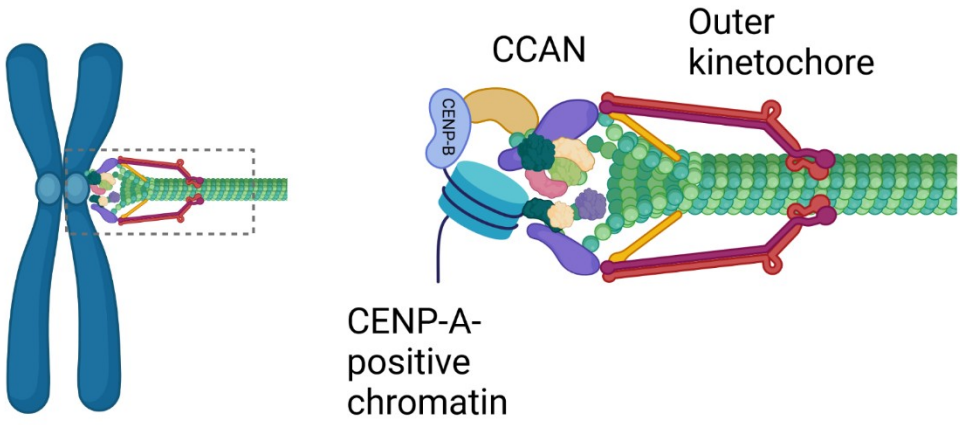


Figure 6. Centromeres. Eukaryotic chromosomes have a single centromere that serves as a platform for kinetochore assembly and connects sister chromatids during mitosis. Centromere-specific histone H3 variant CENP-A together with DNA-binding protein CENP-B form chromatin recruiting proteins of constitutive centromere-associated network (CCAN, or inner kinetochore) that leads to assembly of outer kinetochore proteins.

distribution of newly replicated chromosomes into daughter cells. Therefore, centromeres represent essential chromosomal sites that form multi-protein complexes with kinetochores before and during mitosis (Westhorpe and Straight, 2014). Their characteristic hallmarks are tandem DNA repetitions and the substitution of histone H3 with its variant centromere protein A (CENP-A) in some of their nucleosomes (Earnshaw and Rothfield, 1985; Palmer et al., 1987; Vafa and Sullivan, 1997). First centromeric proteins (CENP-A, CENP-B, and CENP-B) were detected by autoantibodies from sera of patients with systemic scleroderma (Earnshaw and Rothfield, 1985). CENP-A, together with DNA-binding protein CENP-B, constitute centromeric chromatin, serving as a platform for inner kinetochore, collectively referred to as constitutive centromere-associated network (CCAN), recruiting outer kinetochore involved in direct microtubule attachment (Figure 6) (Cheeseman and Desai, 2008).

1.3.1 Centromeric DNA

Mammalian centromeric DNA is composed of tandem repetitions that are not conserved across species. The existence of highly repetitive sequences in DNA was discovered by gradient centrifugation of DNA from various tissues and species using cesium chloride. The resulting gradient revealed the presence of separated "satellite" bands originating from different sedimentation compared to the rest of the genome (Kit, 1961). Human centromeres are represented by tandem repeats of AT-rich monomers of approximately 171 base pair (bp) length, termed α-satellites. The monomers are further organized into arrays of higher-order repeat (HOR) units that can span up to five megabases (Mb). However, only one HOR array per chromosome is functional, associated with the kinetochore proteins. Monomeric α-satellites not ordered to HORs are also found in the pericentromeric regions and exhibit no repeating structures (Altemose et al., 2022; Fukagawa and Earnshaw, 2014; Wu and Manuelidis, 1980). Centromeric α-satellites contain

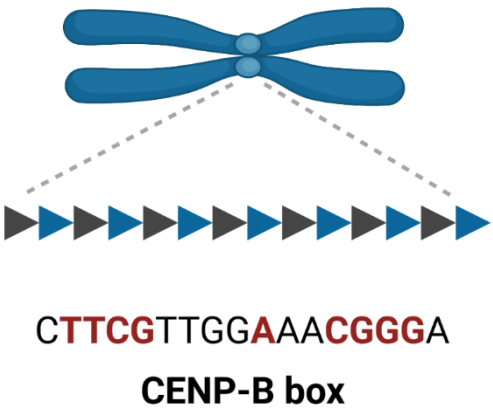


Figure 7. Centromeric DNA. Scheme illustrating centromeric higher-order repeat unit. Arrowheads show 171-bp α-satellite monomers. Blue arrowheads indicate monomers with functional CENP-B boxes. CENP-B box sequence is depicted below with nucleotides required for CENP-B binding in red.

17 bp sequence motifs (5‘-CTTCGTTGGAAACGGGA-3’) termed CENP-B boxes that occupy every other monomer and are recognized by CENP-B protein (Figure 7).

Interestingly, CENP-B boxes are found in all but the Y chromosome. Moreover, they are absent from neocentromeres that were ectopically formed in non-repetitive sequences after disruption of the original centromere, which indicates that CENP-B boxes are not essential for centromere assembly (du Sart et al., 1997; Masumoto et al., 1989). However, studies on the human artificial chromosomes (HAC) showed that the presence of CENP-B boxes is required for the establishment of centromere *de novo*. The first HACs were constructed by introducing a HOR array into the human fibrosarcoma cell line resulting in the formation of the functional centromere. Further studies showed that only α-satellite DNA containing CENP-B boxes leads to the formation of functional HAC. Accordingly, alphoid DNA bearing mutations within CENP-B boxes or lacking them, such as chromosome Y alphoid, did not form functional HAC (Harrington et al., 1997; Ohzeki et al., 2002 77).

1.3.2 Centromeric Chromatin

As already mentioned, centromeric chromatin is predominantly defined by the presence of nucleosomes containing CENP-A, a variant of histone H3. CENP-A plays a crucial role in centromere identity, as it marks active centromeres and is essential for centromeric maintenance and kinetochore assembly (Cheeseman and Desai, 2008). Accordingly, loss of CENP-A has detrimental consequences, and *Cenp-A* deficiency in mice leads to early embryonal lethality accompanied by chromosomal mis-segregation and micronuclei and macronuclei formation (Howman et al., 2000). However, it was estimated that CENP-A-containing nucleosomes account only for approximately 4 % of all nucleosomes in the centromeres of healthy cells (Bodor et al., 2014). Nucleosomes with CENP-A were shown to be dispersed with nucleosomes containing conventional histones H3 enriched for Lys4 dimethylation (H3K4me2), a modification characteristic for open but not active chromatin. This distinct chromatin composition was termed centrochromatin (Sullivan and Karpen, 2004). The flanking regions of satellite DNA called pericentromeres are occupied by heterochromatin enriched for H3K9 trimethylation (H3K9me3) that is mediated by Suv39h histone methyltransferase (Figure 8) (Peters et al., 2003). Interestingly, the H3K9me3 modification serves as a binding site for the family of heterochromatin proteins 1

(HP1) that was shown to maintain the cohesion of sister chromatids before chromosome segregation (Lachner et al., 2001; Yi et al., 2018).

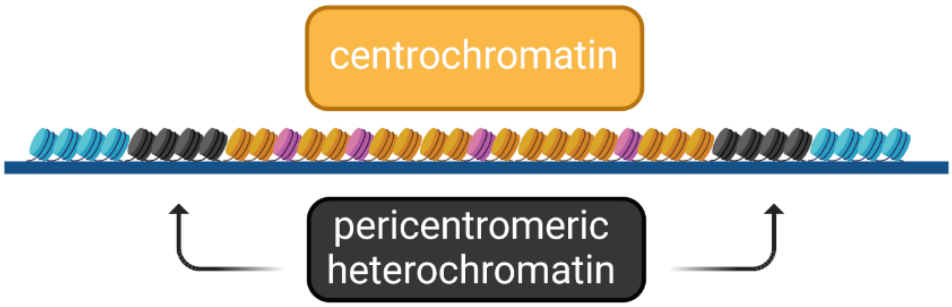


Figure 8. Centromeric chromatin exhibit distinct histone modifications. The centromeric core is characterized by substitution of histone H3 by its variant CENP-A (magenta) that are interspersed with H3K4me2-containing nucleosomes (yellow). The centrochromatin is flanked by pericentric heterochromatin characterized by nucleosomes containing H3K9me3 (black).

The CENP-A deposition is critical for kinetochore assembly and centromeric function, as the presence of more than one active centromere in each chromosome has a detrimental effect on chromatid segregation (McKinley and Cheeseman, 2016). In contrast with conventional histones that are deposited during DNA replication, CENP-A is replenished in mitotic exit and during the G1 phase (Jansen et al., 2007). Its incorporation is facilitated by specialized chaperone Holliday junction recognition protein (HJURP) that is targeted to centromeric regions during anaphase and telophase transition. Moreover, recruitment of HJURP requires centromeric deposition of Mis18 complex, consisting of Mis18α, Mis18β, and M18BP1 (Dunleavy et al., 2009; Foltz et al., 2009; Fujita et al., 2007; Moree et al., 2011; Pan et al., 2019). This process is tightly controlled by phosphorylation. Polo-like kinase 1 (PLK1) modulates Mis18 complex localization by phosphorylating M18BP1. On the other hand, cyclin-dependent kinase 1 (CDK1) and CDK2-mediated phosphorylation of M18BP1 and HJURP prevent their premature targeting to centromeres and ensure temporal control of CENP-A assembly (McKinley and Cheeseman, 2014; Stankovic et al., 2017). Interestingly, depletion of H3K4me2 modification leads to mistargeting of HJURP and subsequently to defective incorporation of CENP-A. The elevated heterochromatin occupancy in the centromeres has also a negative effect on genomic stability, as H3K9me3 was shown to inhibit *de novo* CENP-A assembly. On the other hand, long-term removal of H3K9me3 results in a decreased level of CENP-A, and subsequently in mis-segregation. The balance of

centromeric chromatin and pericentromeric heterochromatin is thus essential for centromere integrity and chromosome segregation (Bergmann et al., 2011; Martins et al., 2020; Ohzeki et al., 2012).

1.3.3 Centromeric Protein B (CENP-B)

CENP-B is the only sequence-specific DNA binding protein in human centromeres. With its N-terminal domain, CENP-B recognizes CENP-B boxes within satellite DNA (Masumoto et al., 1989; Muro et al., 1992). Interestingly, CENP-B originated from a member of the pogo-like transposase family, and its domestication occurred in several independent events. Orthologs of CENP-B are highly conserved in mammals, but they are absent from other vertebrates. However, three CENP-B homologs in fission yeast (Abp1, Cbh1 and Cbh2) emerged from the domestication of different pogo-like transposase. Moreover, CENP-B-like proteins are also found in insects (Casola et al., 2008; Kipling and Warburton, 1997; Mateo and Gonzalez, 2014).

The function of CENP-B is enigmatic and controversial. It seems not to be essential in centromere maintenance, as mice deficient in *Cenp-B* are viable with no apparent health issues except decreased body weight, lower sperm count, and age-dependent disruption in the uterine epithelium (Fowler et al., 2000; Fowler et al., 2004; Hudson et al., 1998; Kapoor et al., 1998; Perez-Castro et al., 1998). Accordingly, the Y chromosome, which lacks CENP-B due to the absence of CENP-B boxes, is still functional, indicating that CENP-B is not essential for the maintenance of established centromere (Masumoto et al., 1989). However, the Y chromosome exhibits an increased frequency of mis-segregation compared to other CENP-B-containing chromosomes, which was measured by micronuclei formation in the male cell line (Fachinetti et al., 2015). The same applies to the neocentromeres, which are usually formed after chromosomal rearrangements on ectopic sites lacking satellite DNA. Although neocentromeres do not contain CENP-B boxes and hence are unable to bind CENP-B protein, they still interact with other centromeric proteins and preserve functions similar to natural centromeres. However, as with the Y chromosomes, neocentromeres tend to form micronuclei with increased frequency (Fachinetti et al., 2015; Marshall et al., 2008; Voullaire et al., 1993).

One of the functions of CENP-B is to stabilize the interaction between centromeric chromatin and kinetochore and thus promote proper chromosome segregation (Figure 9). It was shown that CENP-B interacts directly with CENP-C and CENP-A and stabilizes CENP-A-containing

nucleosomes. Although CENP-A is necessary for kinetochore protein recruitment and assembly, it requires the presence of CENP-B. Once kinetochore is assembled, CENP-A presence in the centromere is not required since CENP-B interacting with CENP-C stabilizes kinetochore assembly and promotes chromosome segregation. It was proposed that mutual interplay between all the major centromeric proteins and DNA sequence is essential for the modulation of centromeric functions (Fachinetti et al., 2013; Fachinetti et al., 2015; Fujita et al., 2015; Hoffmann et al., 2016). Moreover, as already mentioned, the *de novo* formation of a functional centromere in HAC requires the presence of CENP-B boxes and is dependent on the expression of CENP-B protein (Figure 9). However, the N-terminal truncated form of CENP-B containing the DNA-binding domain is sufficient enough to promote CENP-A assembly in HAC (Ohzeki et al., 2002; Okada et al., 2007).

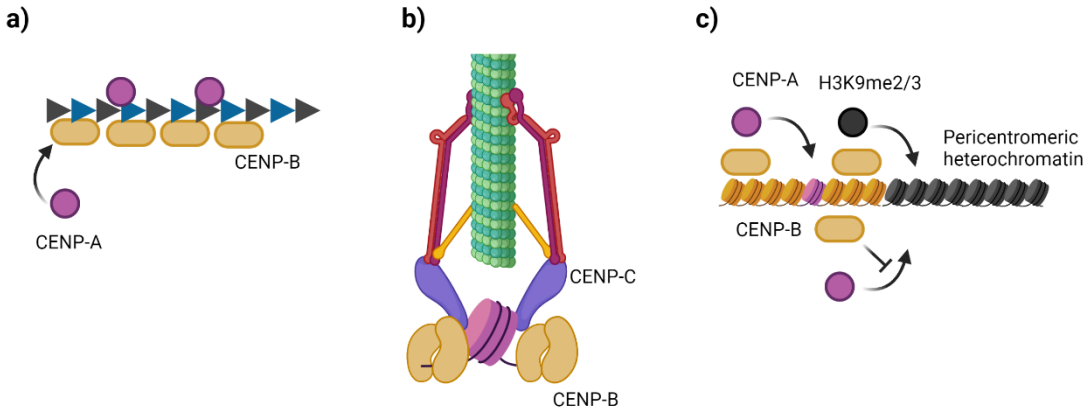


Figure 9. CENP-B protein function. (a) Formation of the human artificial chromosome is dependent on CENP-B. **(b)** CENP-B stabilizes kinetochore via direct interaction with CENP-A and CENP-C. **(c)** CENP-B facilitates CENP-A assembly in centromeric sites, and promotes heterochromatinization in non-centromeric regions, thus preventing CENP-A incorporation into ectopic sites.

Besides its function in the centromere stabilization, CENP-B was also shown to be an important epigenetic modulator. By promoting heterochromatin modifications, CENP-B can prevent *de novo* assembly of CENP-A in the ectopic sites (Figure 9). Incorporation of satellite DNA into ectopic sites in chromosomes does not lead to the formation of HAC but instead to an increased H3K9me3 modification which is directly dependent on CENP-B expression. Interestingly, expression of the N-terminal truncated fragment of CENP-B sufficient to assemble CENP-A does not promote heterochromatinization. Recently, it was shown that the acidic domains close to the C-terminus of CENP-B recruit not only heterochromatin-related factors such as Suv39h1 or HP1 but also H3K36 methyltransferase ASH1L. By promoting this open chromatin state, CENP-B can facilitate the

assembly of CENP-A. Therefore, CENP-B acts as a hub recruiting several histone modifiers and consequently controlling the balance between open and closed chromatin and, finally, proper chromosome segregation (Okada et al., 2007; Otake et al., 2020).

1.3.4 Kinetochore

The crucial function of the centromere is to create a site for the kinetochore assembly. This multiprotein complex interconnects spindle microtubules with centromere to ensure faithful segregation of chromatids during anaphase (Cheeseman and Desai, 2008). Kinetochore proteins could be categorized into inner and outer kinetochore (Figure 6). Inner kinetochore proteins, collectively referred to as constitutive centromere-associated network (CCAN), represent the interface between the centromere and outer kinetochore. They can be classified into certain subcomplexes according to their function or, more likely, their mutual interactions (CENP-C; CENP-H/I/K/M; CENP-L/M/N; CENP-O/P/Q/R/U; CENP-T/W/S/X). Among them, the most important and described is CENP-C (Hara and Fukagawa, 2017). Although CENP-C does not directly interact with all of the CCAN proteins, the localization of most of them to centromere depends on it, as CENP-C-interacting proteins mediate the recruitment of others. Depletion of CENP-C thus leads to the mislocalization of other CCAN proteins (Carroll et al., 2010; Klare et al., 2015; Przewloka et al., 2011). Moreover, CENP-C associates with CENP-A nucleosomes and creates a bridge linking the centromere with the outer kinetochore (Przewloka et al., 2011). The outer kinetochore is represented by KMN (KNL-1, Mis12 complex, and Ndc80 complex) network that directly interacts with microtubules (Cheeseman et al., 2006).

The attachment of the spindle microtubules into the centromere is one of the most crucial steps in the mitotic division. To avoid defects resulting from improper or delayed microtubule attachment, the outer kinetochore developed a checkpoint mechanism (also known as spindle assembly checkpoint; SAC). By assembling mitotic checkpoint complex (MCC), it prevents premature anaphase initiation until chromatids are correctly attached. MCC comprises proteins BUBR1, BUB3, and MAD2 that inhibit the activity of APC/C^{CDC20} ubiquitin ligase by recruiting CDC20 (cell division cycle homolog 20) (Musacchio and Salmon, 2007). Once chromosomes are bioriented on the spindle, APC/C^{CDC20} ubiquitin ligase is activated. By targeting Securin and cyclin B for degradation, it promotes the transition to anaphase. Degradation of Securin leads to

the activation of Separase protease responsible for the cleavage of cohesin that holds sister chromatids together (Pesin and Orr-Weaver, 2008).

1.4 Spermatogenesis

Spermatogenesis is a continuous and tightly regulated process of cell differentiation with final sperm production. It is localized to the testicular seminiferous tubule epithelium (Figure 10). Each tubule contains a pool of spermatogonial stem cells (SSC) that can self-renew or start to generate transit-amplifying progenitors and hence enter the differentiation program (Oatley and Brinster, 2012). These undifferentiated spermatogonia (in a mouse collectively referred to as A_{undiff}) undergo several divisions to produce differentiating A_1 spermatogonia that undergo five subsequent divisions (producing A_2, A_3, A_4, Intermediate - In, and B-type spermatogonia) to finally enter

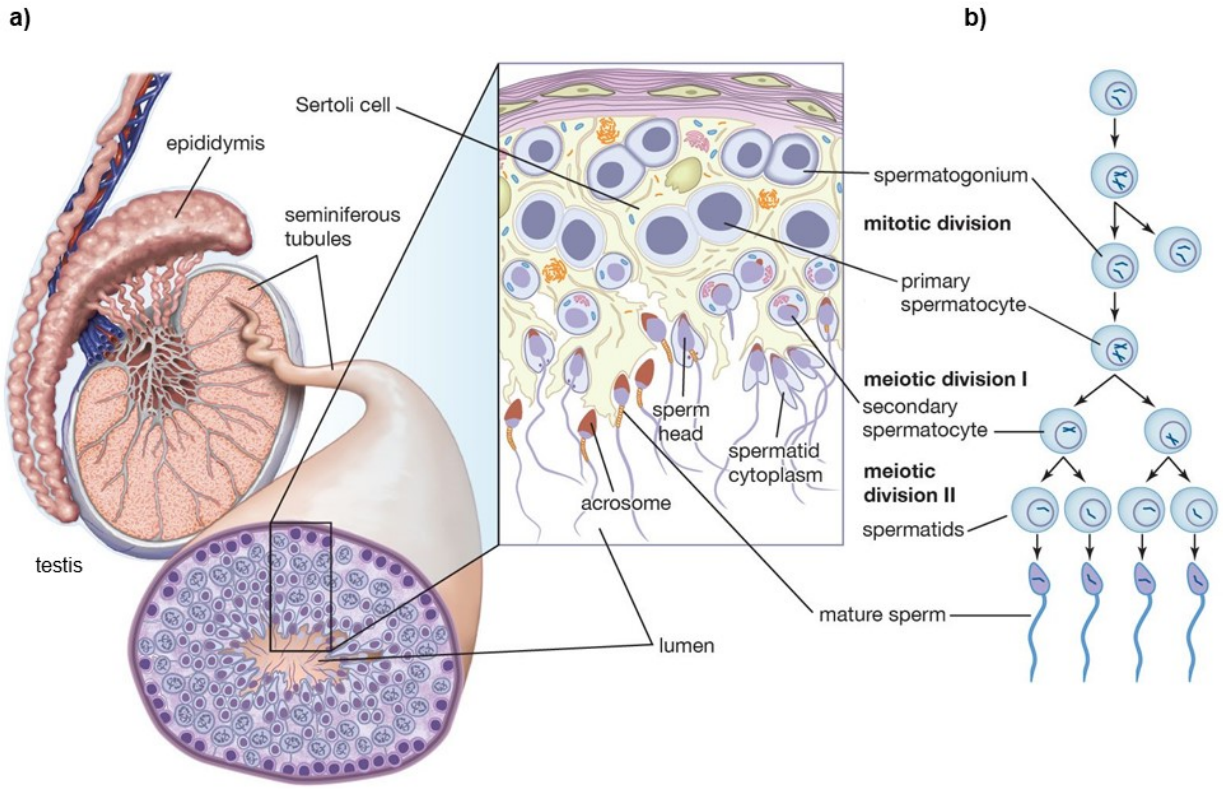


Figure 10. Spermatogenesis. Seminiferous tubules arranged in testes are the site of spermatogenesis. **(a)** Testis and seminiferous tubule cross-sections with depicted Sertoli cells and germ cell populations. **(b)** Spermatogonial stem cells give rise to undifferentiated spermatogonia that undergo several mitotic divisions. Differentiated spermatogonia give rise to primary spermatocytes that undergo two meiotic divisions and result in haploid spermatids. After a series of morphological changes, the resulting spermatozoa are ready to be released from the epithelium. Adapted from Encyclopaedia Britannica.

meiosis. Preleptotene spermatocytes proceed with meiosis I, the prophase of which involves leptotene, zygotene, pachytene, and diplotene stages that include the critical event of homologous recombination. Resulting secondary spermatocytes then undergo the second meiotic division, finally giving rise to haploid round spermatids. In the last step, spermatids differentiate into mature spermatozoa (Figure 10). This process of spermiogenesis involves morphogenetic changes, chromatin condensation, including replacing histones with protamines, and acrosome and axoneme formation. Finally, mature elongated spermatozoa are released from the seminiferous epithelium (Griswold, 2015). This complete process, the spermatogenic cycle, takes approximately 35 days in mice (64 days in humans). Since it is necessary to produce sperms continuously, more differentiation stages are present simultaneously in different parts of the testes along the seminiferous tubules. In mice, the cycles of seminiferous epithelium can be classified into twelve stages based on the presence of individual cell types (O'Donnell et al., 2021).

1.4.1 Hormonal Regulation of Spermatogenesis

The process of spermatogenesis is tightly regulated by the interplay of hormones acting via paracrine and endocrine pathways. Production of these hormones comprising gonadotropin-releasing hormone (GnRH), luteinizing hormone (LH), follicle-stimulating hormone (FSH), and testosterone is controlled via the hypothalamic-pituitary-testis pathway. Testosterone is the major orchestrator of spermatogenesis, responsible for both its initiation and maintenance. Production of androgens, especially testosterone, is the main function of Leydig cells, a somatic population located in interstitial space outside tubules (McLachlan et al., 2002). For testosterone production, the GnRH produced by the hypothalamus stimulates LH secretion from the pituitary gland. LH binding to its corresponding receptor (LHR) present on Leydig cells drives the production of cyclic AMP (cAMP), which triggers a signaling cascade resulting in cholesterol translocation into the mitochondria. By the consecutive action of several enzymes, cholesterol is converted to pregnenolone, progesterone, and finally testosterone. Testosterone then binds to androgen receptors (AR) in Sertoli, Leydig, and peritubular myoid cells, activates it, and triggers its translocation to the nucleus, where AR executes its function (Zhou et al., 2019b; Zirkin and Papadopoulos, 2018) (Figure 11).

Hypothalamic secreted GnRH also stimulates the production of FSH from the pituitary gland. FSH is a glycoprotein that acts via binding to the FSH receptor (FSHR) from the G protein-coupled family expressed in males only in Sertoli cells, a somatic population inside tubules. Sertoli cells perform various functions and thus are crucial for the whole process of spermatogenesis. Although FSH is not essential for spermatogenesis, it has a significant role in Sertoli cell proliferation during maturation and affects Sertoli cell number in adulthood. Lack of FSH or defects in FSHR leads to reduced testis size and sperm number. FSH triggers and modulates the activity of many transcription regulators, such as c-Myc and HIF2, and it also activates PI3K/Akt/mTORC1 and cAMP/PKA/ERK1/2 pathways (Meroni et al., 2019). As a response to FHS, Sertoli cells produce Inhibin B, which acts in a feedback loop by inhibiting the secretion of FSH from the pituitary gland (Figure 11) (O'Connor and De Kretser, 2004).

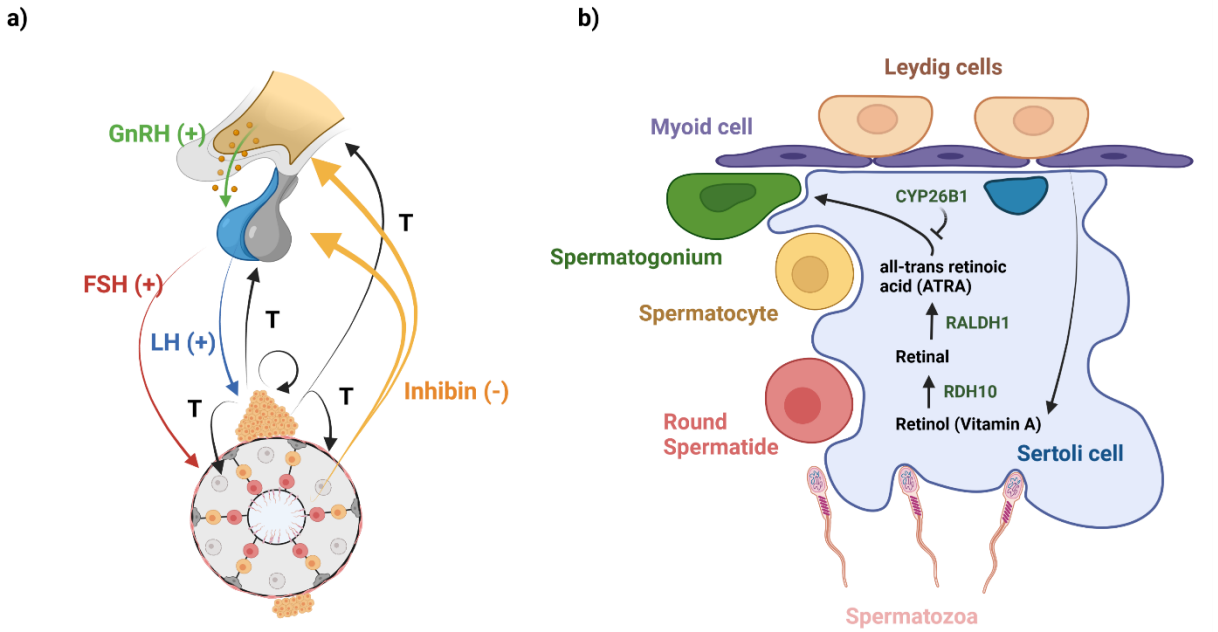


Figure 11. The Regulation of Spermatogenesis. (a) Spermatogenesis is hormonally controlled by the hypothalamic-pituitary-testis pathway. Hypothalamic-produced gonadotropin-releasing hormone (GnRH) stimulates luteinizing hormone (LH) production from the pituitary gland. LH binding to receptors on Leydig cells triggers a cascade resulting in testosterone production (T). T positively regulates Sertoli, Leydig, and peritubular myoid cells. GnRH stimulates also the production of follicle-stimulating hormone (FSH) from the pituitary gland. FSH by binding to its receptor in Sertoli cells triggers various pathways. As a response, Sertoli cells produce Inhibin B that inhibits FSH secretion from pituitary gland. **(b)** Spermatogenesis is initiated by the action of retinoic acid. In Sertoli cells, retinol from vitamin A is converted to retinaldehyde by retinol dehydrogenase 10 (RDH10) and then to all-trans retinoic acid (ATRA) by retinaldehyde dehydrogenase 1 (RALDH1). ATRA stimulates differentiation of spermatogonia. The level of ATRA is controlled by the enzymatic action of CYP26B1.

1.4.2 Retinoic Acid Pathway

One of the essential compounds in spermatogenesis establishment is retinoic acid (RA), the active metabolite of vitamin A, which is synthesized in the testes mainly by Sertoli cells. In the testes, RA has two functions – it initiates spermatogonia differentiation and spermatocyte meiotic entry. A precise balance of RA production and deactivation is required to ensure a proper spermatogenic process. Briefly, vitamin A from the diet is converted to retinol by retinyl ester hydrolases in the intestine. Then, retinol is transported to the liver, where it either binds to transport retinol-binding protein 4 (RBP4) and is secreted into plasma or remains stored in hepatocytes in the form of retinyl esters. Circulating retinol bound to RBP4 is internalized by the membrane receptor stimulated by retinoic acid 6 (STRA6) in the Sertoli cells, where it is converted to RA by a series of oxidative reactions (Kawaguchi et al., 2007). First, retinol is oxidized to retinaldehyde by retinol dehydrogenase 10 (RDH10) and then to RA by retinaldehyde dehydrogenase 1 (RALDH1, encoded by *ALDH1A1*) (Figure 11). Although two other retinaldehyde dehydrogenases (RALDH2 and RALDH3) exist within the testis, RALDH1 represents the predominant enzyme in RA production in Sertoli cells {Arnold, 2015 #355}. Synthesized RA in the form of all-trans (ATRA) or 9-cis then binds to its corresponding nuclear receptors (α, β or γ isotypes of RAR or RXR) in the target cells and, by interacting with retinoic acid response elements (RARE) located close to the vicinity of gene promoters, modulates gene expression (Chambon, 1996). However, the local levels of RA are controlled by the family 26 of cytochrome P450 enzymes (CYP26) expressed by peritubular myoid cells in adults. CYP26B1 degrades RA into inactive metabolites, which provides a counterbalance in the RA signaling (Vernet et al., 2006; White et al., 1997). One of the most significant targets of RA signaling is *stimulated by retinoic acid 8* (*STRA8*) gene. The expression of STRA8 is not only necessary for the initiation of meiosis by induction of meiotic markers, but it also promotes the differentiation of spermatogonia (Endo et al., 2015; Oulad-Abdelghani et al., 1996).

1.4.3 Sertoli Cells

Sertoli cells exhibit huge cytoplasm extending from the basement membrane to the lumen of the tubules, thus providing physical support to the developing germ cells (Griswold, 2018). Moreover, they divide the seminiferous epithelium into basal and apical compartments by the formation of the blood-testis barrier (BTB) between two adjacent Sertoli cells. This physical barrier

regulates nutrient transport and prevents diffusion, and is essential to creating the environment for germ cell differentiation by protecting them from the innate immune system. The BTB complexes sequester spermatogonia and spermatocytes. They are formed in puberty when Sertoli cells differentiate and reach their mature state. The BTB complexes consist of several types of cell junctions, including tight, adherens, and gap junctions, and alterations in the proteins constituting them often lead to disruption of spermatogenesis (Cheng and Mruk, 2012; Stanton, 2016). Since many differentiating germ cells undergo apoptosis during spermatogenesis, Sertoli cells are responsible for their recognition and elimination by phagocytosis. Similarly, they also remove residual bodies originating from the detached cytoplasm of developing spermatozoa and facilitate the release of spermatozoa into the lumen (Kerr and de Kretser, 1974; Nakanishi and Shiratsuchi, 2004; O'Donnell et al., 2011). Importantly, Sertoli cells provide growth factors and hormones necessary for spermatogenesis control and testicular somatic cell function and represent the major contributor to the SSC niche (Petersen and Soder, 2006).

1.4.4 Sertoli Cells in Testis Development

Sertoli cells are the first specified somatic cell type during embryonic development and hence play an essential role in testicular development and the establishment of spermatogenesis. Testicular differentiation relies on the expression of the Y chromosome gene *sex-determining region Y* (*SRY*). The developing gonads remain bipotential, able to give rise to a testis or an ovary, until the transient expression of the *SRY* gene in a small pool of somatic cells, which triggers the expression of *SRY-related high-mobility group* (*HMG*) *box 9* (*SOX9*) in pre-Sertoli cells (Rotgers et al., 2018; Sinclair et al., 1990). This leads to gonad commitment to the male sex and initiation of testis cord formation that promotes the sexual development of the entire embryo. Interestingly, expression of the *Sry* gene in mouse XX embryos results in the normal development of testis; however, spermatogenesis in adults is impaired (Koopman et al., 1991). After initiation of SOX9 expression, pre-Sertoli cells polarize and start to acquire their typical shape and form testis cords by surrounding clusters of gonocytes – precursors of SSC, that will establish seminiferous tubules. During this period, Sertoli cells massively proliferate. Interestingly, the number of Sertoli cells determines the testis size and spermatogenesis efficiency in adulthood, since every Sertoli cell is able to support only a limited number of germ cells. Sertoli cells proliferate even after birth, but they reach terminal differentiation during puberty, which is connected with the formation of the

BTB (Furuya et al., 1978; Orth et al., 1988; Schmahl et al., 2000). Although prospermatogonia (spermatogonia precursors) proliferate actively around embryonic day 14 (E14), they stop dividing around E16 and remain quiescent in G_0/G_1 phase until birth in mice (Vergouwen et al., 1991). Preventing the premature entry of prospermatogonia into the differentiation program represents one of the key processes in testis development. Since RA is highly produced by mesonephroi during embryogenesis, it has to be eliminated from the developing testes in order to prevent the initiation of meiosis. This is ensured by the activity of CYP26B1, specifically expressed downstream of SRY and SOX9 by Sertoli cells (Bowles et al., 2018; Bowles et al., 2006; Koubova et al., 2006). Interestingly, embryonic testes of mice deficient in *Cyp26b1* exhibit an increased level of RA that leads to premature meiosis entry and increased apoptosis of germ cells after E13.5 (MacLean et al., 2007). However, other signals contribute to maintaining germ cell quiescence until birth. Fibroblast growth factor 9 (FGF9) inhibits germ cell meiosis by antagonizing *Stra8* expression, and controls the expression of pluripotency genes (Bowles et al., 2010). Similarly, NANOS2 suppresses meiotic initiation in fetal testes. As it was shown that the expression of CYP26B1 decreases during embryonic development in males, increasing the expression of NANOS2 could prevent the initiation of RA signaling (Kato et al., 2016; Suzuki and Saga, 2008).

The first spermatogenesis, also known as the first wave of spermatogenesis, is initiated shortly after birth in mice. It proceeds in a synchronized fashion resulting in the production of the first spermatozoa around day 35 after birth. Notably, the efficiency of the first wave dictates spermatogenesis in adulthood (Ernst et al., 2019; Janca et al., 1986). Spermatogenesis is initiated by the migration of prospermatogonia towards the basal membrane of the seminiferous tubules, where they subsequently resume their mitotic program (Vergouwen et al., 1991). Some of the resulting spermatogonia similar to the A_{undiff} type become SSC that produce progenitor spermatogonia giving rise to differentiated spermatogonia (Oatley and Brinster, 2012). During this period, Sertoli cells provide a stem cell niche for developing spermatogonia by producing stem cell factor or glial cell-line-derived neurotrophic factor (GDNF) (Dadoune, 2007). Moreover, Sertoli cell-provided ATRA signaling triggers the expression of STRA8 necessary for spermatogonia differentiation and meiotic initiation (Endo et al., 2015). Furthermore, Sertoli cells terminate their mitotic program and reach their mature state, followed by the formation of BTB around day 15 after birth (Sharpe et al., 2003).

2. Objectives

The goal of this project was to characterize the function of the SCF^{FBXO38} ubiquitin ligase *in vitro* and *in vivo*.

The main aims were to:

1. Identify substrates of the SCF^{FBXO38} ubiquitin ligase and the mechanism of their recognition
2. Characterize the biological function of the SCF^{FBXO38}-dependent protein degradation
3. Develop the mouse model of *Fbxo38* deficiency and describe its phenotype
4. Confirm the results obtained from *in vitro* experiments in the mouse model

3. Publications

The thesis was based on the publications listed below. The full text of the publications can be found in the following section.

Dibus, N., Korinek, V., and Cermak, L. (2022a). FBXO38 Ubiquitin Ligase Controls Centromere Integrity via ZXDA/B Stability. Frontiers in Cell and Developmental Biology *10*.

Dibus, N., Zobalova, E., Monleon, M.A.M., Korinek, V., Filipp, D., Petrusova, J., Sedlacek, R., Kasparek, P., and Cermak, L. (2022b). FBXO38 Ubiquitin Ligase Controls Sertoli Cell Maturation. Frontiers in Cell and Developmental Biology *10*.

Author contribution:
The author of this thesis performed the majority of the experiments and contributed extensively to the writing of both manuscripts. Isolation of Sertoli cells was performed in collaboration with the laboratory of Dr. Filipp from the Institute of Molecular Genetics of the Czech Academy of Sciences (IMG CAS). Specific experiments and analyzes were performed in collaboration with several research facilities. Mass spectrometric analysis was performed in the Laboratory of Mass Spectrometry, Charles University. RNA-seq, microarray, and ChIP-seq analyzes were performed at the Genomics and Bioinformatics Facility, IMG CAS. The mouse model was established in the Transgenic and Archiving Module, IMG CAS. The exact authors' contributions are stated in the manuscripts.

Baloghova, N., Lidak, T., and Cermak, L. (2019). Ubiquitin Ligases Involved in the Regulation of Wnt, TGF-beta, and Notch Signaling Pathways and Their Roles in Mouse Development and Homeostasis. Genes (Basel) *10*

Author contribution:
The author of this thesis contributed equally to the writing of this review. The review is enclosed as an appendix.

frontiers | Frontiers in Cell and Developmental Biology

ORIGINAL RESEARCH
published: 23 June 2022
doi: 10.3389/fcell.2022.929288

FBXO38 Ubiquitin Ligase Controls Centromere Integrity via ZXDA/B Stability

Nikol Dibus[1], *Vladimir Korinek*[2] *and Lukas Cermak*[1]*

[1]*Laboratory of Cancer Biology, Institute of Molecular Genetics of the Czech Academy of Sciences, Vestec, Czechia,* [2]*Laboratory of Cell and Developmental Biology, Institute of Molecular Genetics of the Czech Academy of Sciences, Prague, Czechia*

Alterations in the gene encoding the E3 ubiquitin ligase substrate receptor FBXO38 have been associated with several diseases, including early-onset motor neuronopathy. However, the cellular processes affected by the enzymatic action of FBXO38 are not yet known. Here, we identify the zinc finger proteins ZXDA/B as its interaction partners. FBXO38 controls the stability of ZXDA/B proteins via ubiquitination and proteasome-dependent degradation. We show that ZXDA/B proteins associate with the centromeric protein CENP-B and that the interaction between ZXDA/B and FBXO38 or CENP-B is mutually exclusive. Functionally, ZXDA/B factors control the protein level of chromatin-associated CENP-B. Furthermore, their inappropriate stabilization leads to upregulation of CENP-A and CENP-B positive centromeric chromatin. Thus we demonstrate a previously unknown role of cullin-dependent protein degradation in the control of centromeric chromatin integrity.

Keywords: proteasome, ubiquitin ligase, protein degradation, cullin, zinc finger protein, centromere

OPEN ACCESS

Edited by:
Tadashi Nakagawa, Tohoku University, Japan

Reviewed by:
Yohei Niikura, Nanjing University, China
Alexei Arnaoutov, Eunice Kennedy Shriver National Institute of Child Health and Human Development (NIH), United States

***Correspondence:**
Lukas Cermak
lukas.cermak@img.cas.cz

Specialty section:
This article was submitted to Cellular Biochemistry, a section of the journal Frontiers in Cell and Developmental Biology

Received: *26 April 2022*
Accepted: *02 June 2022*
Published: *23 June 2022*

Citation:
Dibus N, Korinek V and Cermak L (2022) FBXO38 Ubiquitin Ligase Controls Centromere Integrity via ZXDA/B Stability. Front. Cell Dev. Biol. 10:929288. doi: 10.3389/fcell.2022.929288

INTRODUCTION

The ubiquitin-proteasome pathway is a cellular system that shapes the temporal and spatial proteome via targeted protein degradation. This control is achieved via the specific recognition of targeted proteins by ubiquitin ligases (Senft et al., 2018). Multi-subunit E3 ubiquitin ligases allow system versatility by using separate modules for substrate recognition and ubiquitination (Skaar et al., 2014). F-box containing protein 38 (FBXO38; also known as MoKA) is a substrate receptor for SKP1-CUL1-dependent ubiquitin ligase (SCF). Initially, it was discovered as a modulator of transcription factor Krüppel-like factor 7 (KLF7) activity (Smaldone et al., 2004). In addition, FBXO38 stability is controlled via ubiquitin-specific peptidase 7 (USP7), and FBXO38 protein expression was shown to be required for proper cytokinesis (Georges et al., 2019). However, as a ubiquitin ligase, SCF^{FBXO38} is still insufficiently characterized. So far, the only potential substrate identified is programmed cell death 1 (PD-1) (Meng et al., 2018).

Significantly, two FBXO38 gene mutations were found in patients with early-onset distal hereditary motor neuronopathy, indicating its role in the homeostasis of the nervous system (Sumner et al., 2013; Akcimen et al., 2019). Interestingly, another mutation was discovered in the study of monozygotic twins with discordant development of gender dysphoria (Morimoto et al., 2017).

Proteins zinc finger X-linked duplicated A and B (ZXDA/B) have no sufficiently described function. Their close homolog and interacting partner ZXDC has been shown to play a role in the transcription control of major histocompatibility complex class II (Al-Kandari et al., 2007). However, there is no significant evidence supporting the role of ZXDA/B in this process.

Centromeres serve as a platform for microtubule attachment during chromosome segregation. They are defined by the tandem arrays of α-satellite DNA repeats and by the epigenetic signature, characterized by substituting histone H3 with its variant centromere protein A (CENP-A) (Earnshaw and Rothfield, 1985; Palmer et al., 1987). CENP-A nucleosomes are assembled during mitotic exit and the G1 phase of the cell cycle (Jansen et al., 2007). CENP-A depletion, once the kinetochore is already tethered to the centromere, does not disrupt chromosome segregation since its fidelity is ensured by the CENP-B DNA binding protein (Hoffmann et al., 2016). CENP-B protein, homologous to transposases, binds DNA motif (CENP-B box) frequently found in centromeric repetitions (Masumoto et al., 1989; Muro et al., 1992). Functionally, it supports the stabilization of the kinetochore structure through direct binding to CENP-A and by maintaining the CENP-C protein at the centromeres (Fachinetti et al., 2015; Fujita et al., 2015). Moreover, studies on human artificial chromosomes show that forming a functional centromere requires CENP-B protein-dependent CENP-A loading (Ohzeki et al., 2002; Okada et al., 2007). Interestingly, CENP-B is missing from the Y chromosome due to the absence of CENP-B boxes (Masumoto et al., 1989) and from ectopically-derived neocentromeres (du Sart et al., 1997). As a possible consequence, the Y chromosome exhibits an increased missegregation rate compared to other chromosomes (Fachinetti et al., 2015). Furthermore, CENP-B controls the epigenetic signature of centromeres by recruiting various histone modifiers, including tethering histone H3.3 chaperone DAXX to pericentric regions in a SUMO2-dependent manner (Okada et al., 2007; Drane et al., 2010; Morozov et al., 2017; Otake et al., 2020). Notably, Cenp-B-deficient mice are viable, but they exhibit decreased body weight, lower sperm count, and age-dependent deterioration of female reproductive organs (Hudson et al., 1998; Kapoor et al., 1998; Perez-Castro et al., 1998; Fowler et al., 2000; Fowler et al., 2004).

Here, we have revealed the previously unknown role of SCF^{FBXO38} ubiquitin ligase. We identified ZXDA/B zinc finger proteins as its substrates. Furthermore, we show that ZXDA/B proteins are responsible for CENP-B protein stabilization at centromeres, a process negatively controlled by FBXO38.

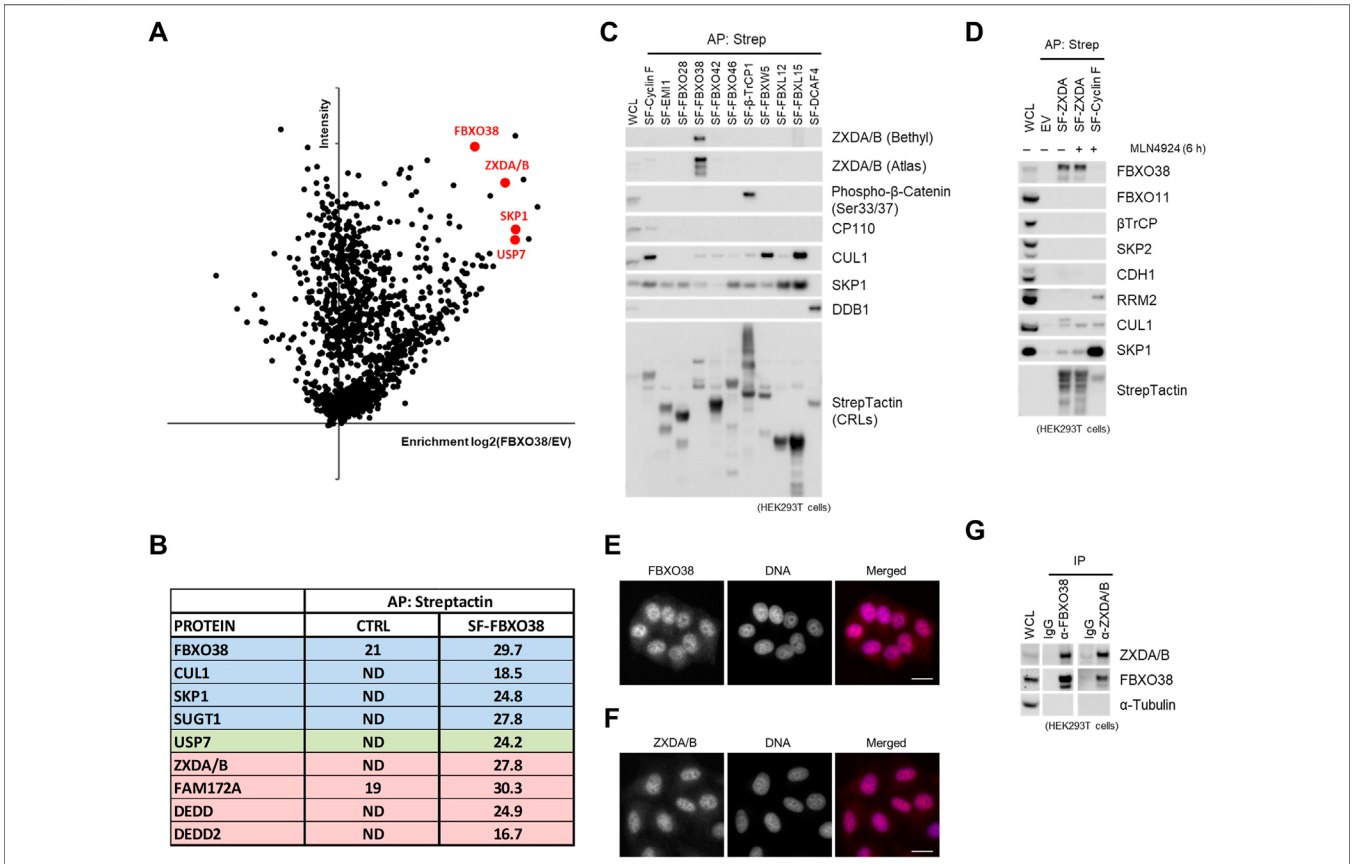
RESULTS

FBXO38 Interacts With ZXDA/B in the Nucleus

To identify substrates of SCF^{FBXO38}, we performed affinity purification of the FBXO38 protein. Mass spectrometry analysis of the FBXO38 interactome revealed peptides corresponding to canonical subunits of SCF^{FBXO38} (SKP1, SUGT1, and CUL1) and previously identified FBXO38 interaction partner USP7 deubiquitinase (Zhang M. et al., 2008; Skaar et al., 2013; Georges et al., 2019). Additionally, the list of co-purified proteins contained a family of small DED-containing proteins DEDD and DEDD2, transcription co-regulator FAM172A, and zinc finger X-linked duplicated A and B proteins (ZXDA/B) (**Figures 1A,B**). ZXDA/B proteins were selected for further studies as their protein level increased upon FBXO38 knockdown, suggesting that they represent potential substrates of SCF^{FBXO38} ubiquitin ligase (**Supplementary Figure S1A**). ZXDA/B encoding genes evolved in two steps. First, *ZXDA* appeared as a retrogene from the *ZXDC* gene in placental mammals (**Supplementary Figure S1B**). Later, in the Boreoeutheria clade, *ZXDA* was duplicated, and *ZXDB* appeared in an inverted position on chromosome X (**Supplementary Figure S1C**). Translational products of *ZXDA* and *ZXDB* genes are almost identical, sharing 98% similarity in primary sequence (**Supplementary Figure S1D**; in the following text we will refer to endogenous proteins as ZXDA/B and exogenous recombinant protein as ZXDA). We screened a small panel of Cullin-RING ligase substrate receptors to confirm that the interaction between FBXO38 and ZXDA/B is specific (**Figure 1C**). In a complementary approach, we purified StrepII-FLAG-tagged ZXDA (SF-ZXDA) and found that endogenous FBXO38, CUL1, and SKP1, but not other tested F-box proteins, interacted specifically with ZXDA (**Figure 1D**). Finally, we confirmed that endogenous FBXO38 and ZXDA/B proteins localized into the nucleoplasm (**Figures 1E,F**, **Supplementary Figure S1E**) and mutually interacted (**Figure 1G**).

FBXO38 Mediates Ubiquitination and Controls the Stability of ZXDA/B

To assess whether ZXDA/B proteins are targeted for protein degradation by Cullin-dependent ubiquitin ligases, we first utilized the neddylation inhibitor MLN4924, since NEDD8-cojugation to Cullin proteins is prerequisite for SCF activity (Baek et al., 2020). At two different time points after treatment, an increase in ZXDA/B protein levels was observed, similar to other well-characterized CUL1-dependent substrates REST, p21, and FBXO28 (**Figure 2A**) (Yu et al., 1998; Guardavaccaro et al., 2008; Cai et al., 2020). Upon neddylation or proteasome (MG-132) inhibition, the ZXDA/B proteins accumulated in the nuclear compartment specifically (**Figure 2B**). To test whether these effects are FBXO38-dependent, we silenced endogenous FBXO38 in HeLa and RPE-1 cell lines. Acute knockdown of FBXO38 led to the increased protein level of ZXDA/B compared to the control cells (**Figure 2C**). To further validate the effect of FBXO38 on ZXDA/B proteins stability, $FBXO38^{\Delta Ex3/\Delta Ex3}$ HCT116 and RPE-1 cell lines lacking full-length protein were generated (FBXO38 knockout; KO). As expected, we observed an increased protein level of ZXDA/B in the nuclei of the FBXO38 KO cells (**Figure 2D**). By treating KO cells with translation inhibitor cycloheximide (CHX), we confirmed the increased stability of ZXDA/B in the absence of FBXO38. This effect was rescued by the expression of exogenous FBXO38, which led to the destabilization of ZXDA/B. At the same time, another target of CUL1-dependent degradation, p21, did not show any change in stability upon FBXO38 expression (**Figure 2E**). Using the HCT116 cell line with an inducible expression of exogenous ZXDA, we confirmed that these effects are transcriptionally



	AP: Streptactin	
PROTEIN	CTRL	SF-FBXO38
FBXO38	21	29.7
CUL1	ND	18.5
SKP1	ND	24.8
SUGT1	ND	27.8
USP7	ND	24.2
ZXDA/B	ND	27.8
FAM172A	19	30.3
DEDD	ND	24.9
DEDD2	ND	16.7

FIGURE 1 | FBXO38 interacts with ZXDA/B in the nucleus. **(A)** Schematic representation of mass-spectrometry identification of FBXO38-interacting proteins. Affinity-purified proteins from HeLa cells expressing StrepII-FLAG-tagged FBXO38 (SF-FBXO38) were identified by Liquid Chromatography with Tandem Mass-Spectrometry (LC-MS/MS). Parental HeLa cells without FBXO38 expression were used as a negative control. Proteins that were significantly enriched in FBXO38 purifications compared to the control are in red. The graph represents maximum intensity and the enrichment calculated from the ratio of intensities of identified proteins. **(B)** The list of specific hits enriched in FBXO38 purifications identified by the LC-MS/MS analysis as in **(A)**. Log_2 intensities from FBXO38 purifications or the control are shown. Components of SCF^{FBXO38} are depicted in blue, putative substrates in red, and other associated proteins in green. **(C)** HEK293T cells were transfected with SF-tagged Cullin-RING ligase substrate receptors (CRLs). Cells were treated with the MLN4924 inhibitor 6 h prior to collecting. Whole-cell lysates (WCL) were affinity purified (AP) using Strep-Tactin resin and immunoblotted as indicated. As positive controls, phospho-β-catenin is shown to interact with β-TrCP, and CP110 is shown to interact with Cyclin **(F)**. Two anti-ZXDA/B antibodies were used to ensure interaction specificity. **(D)** HEK293T cells were transfected with SF-ZXDA or SF-Cyclin F and subjected to lysis and AP as in **(C)**. An empty vector (EV) was used as a negative control. Where indicated, the MLN4924 inhibitor was added to the cells 6 h prior to collecting. RRM2 is shown to interact with Cyclin F as a positive control. **(E)** FBXO38 localizes to the nucleus. HeLa cells were fixed, permeabilized, and incubated with an anti-FBXO38 antibody. DNA was stained with DAPI. Scale bar, 20 μm **(F)** ZXDA/B localizes to the nucleus. HeLa cells were treated as in **(F)** and incubated with an anti-ZXDA/B antibody. DNA was stained with DAPI. Scale bar, 20 μm. **(G)** Endogenous FBXO38 or endogenous ZXDA/B were immunoprecipitated from HEK293T cells using either FBXO38 or a ZXDA/B antibody. Non-specific IgG was used as a negative control. Whole-cell lysates (WCL) and immunoprecipitations (IP) were immunoblotted as indicated.

independent. Both the neddylation inhibition and FBXO38 knockdown increased exogenous ZXDA protein level and stability (**Figures 2F,G**). Finally, affinity-purified FBXO38 promoted *in vitro* ubiquitination of endogenous ZXDA/B (**Figure 2H**). Overall, these results show that SCF^{FBXO38} controls ZXDA/B proteins stability via Cullin-dependent protein degradation.

FBXO38 Associates With ZXDA/B via Zinc Finger Linker Motif

FBXO38 contains three structurally different domains (**Figure 3A** and **Supplementary Figure S3A**). Although initially described as an F-box lacking the typical WD40 or leucine repeats (thus designated FBXO) (Jin et al., 2004), detailed analysis using the Leucine-rich-repeats (LRR) and AlphaFold predictors showed that it is rather a typical F-box protein containing leucine-rich repeats (FBXL) (Martin et al., 2020; Jumper et al., 2021). The F-box motif, essential for SCF complex formation, and C-terminal domain were indispensable for FBXO38 interaction with ZXDA/B. In contrast, the loss of these motifs did not affect the interaction with deubiquitinase USP7 (**Figure 3B**). Mutants of FBXO38 found in patients with muscular atrophy interacted with ZXDA/B more strongly, especially after MLN4924 treatment (**Supplementary Figure S3B**).

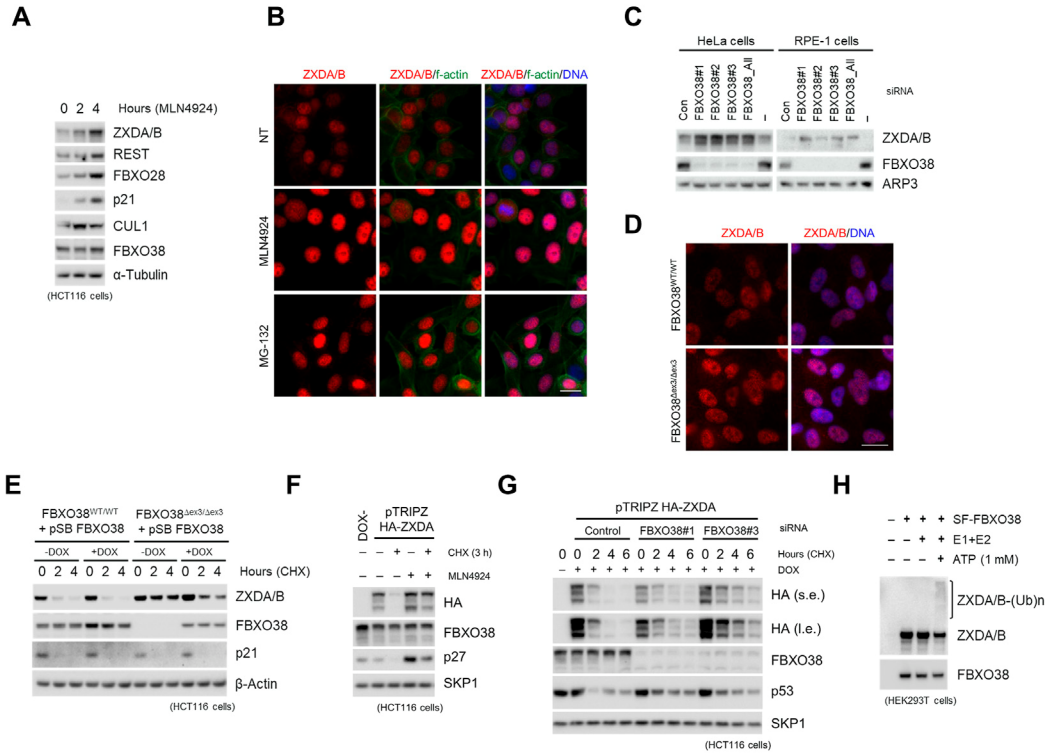


FIGURE 2 | FBXO38 mediates ubiquitination and controls the stability of ZXDA/B. **(A)** HCT116 cells were treated with MLN4924 for 2 and 4 h, lysed and immunoblotted as indicated **(B)** HeLa cells were grown on slides and treated with MLN4924 or MG-132 for 12 h where indicated. The cells were fixed and immunostained with an anti-ZXDA/B antibody. DNA was stained with DAPI, and f-actin was visualized using phalloidin. Scale bar, 20 μm. **(C)** HeLa and RPE-1 cells were transfected with three different siRNAs targeting FBXO38, and whole-cell lysates were immunoblotted as indicated. Non-targeting siRNA (Con) or no siRNA were used as negative controls. **(D)** Wild-type (WT) or FBXO38 knockout RPE-1 cells (FBXO38$^{\Delta ex3/\Delta ex3}$; KO) were grown on slides, fixed, and immunostained with the ZXDA/B antibody. DNA was stained with DAPI. Scale bar, 20 μm. **(E)** StrepII-FLAG-tagged FBXO38 (SF-FBXO38) was inducibly expressed in FBXO38 WT and KO HCT116 cells using the Sleeping Beauty Transposon System. Where indicated, the expression of FBXO38 was induced with doxycycline for 24 h. Cells were treated with cycloheximide (CHX) for the indicated time. Whole-cell lysates were immunoblotted as indicated. **(F)** HCT116 cells with doxycycline-inducible expression of HA-tagged ZXDA were treated with doxycycline for 24 h and then treated with CHX for 3 h. Where indicated, cells were pre-treated with MLN4924 for 3 h. Non-treated cells (DOX-) were used as a negative control. Whole-cell lysates were immunoblotted as indicated. **(G)** HCT116 cells with doxycycline-inducible expression of HA-tagged ZXDA were transfected with two different siRNAs targeting FBXO38. Expression of ZXDA was induced by doxycycline 18 h after transfection. Cells were treated with CHX for the indicated time and collected 48 h after transfection. Whole-cell lysates were immunoblotted as indicated **(H)** SF-FBXO38 was overexpressed in HEK293T cells and isolated using Strep-Tactin resin. Eluate was subjected to *in vitro* ubiquitination in the presence of E1 and E2 enzymes or E1, E2, and ATP. An empty vector (EV) was used as a negative control. ZXDA/B antibody was used to detect polyubiquitinated forms of co-purified endogenous ZXDA/B proteins.

A series of ZXDA mutants immunopurifications revealed that FBXO38 recognizes a motif encompassing amino acid residues 386–408 of ZXDA (**Supplementary Figure S3C–S3J**). We chose Y389A and ERP386-388AAA mutants for further experiments (**Figure 3C,D**, **Supplementary Figure S3K,L**). Tandem purification of the FBXO38-ZXDA complex revealed that their interaction is independent of posttranslational modification of this motif, as we did not detect any modification in the identified peptides covering the essential region (**Supplementary Figure S3M,N**). Furthermore, we confirmed increased stability of selected mutants compared to wild-type ZXDA (**Figure 3E**). An *in silico* search revealed that only ZXDA/B/C proteins contain this motif (**Supplementary Figure S3O,P**). Importantly, we observed that ZXDC, heterodimer partner of ZXDA/B (Al-Kandari et al., 2007), interacted with FBXO38 only upon proteasome or neddylation inhibition and that this interaction correlated with ZXDA/B stabilization (**Supplementary Figure S3Q,R**). Moreover, the ZXDC protein level was not elevated upon the FBXO38 siRNA-mediated knockdown, and *in silico* homology modeling of ZXDA/B/C zinc fingers revealed that minor differences in the FBXO38 interacting region can affect the orientation of amino acids essential for the interaction (**Supplementary Figure S3S,T**) (Wang et al., 2018; Waterhouse et al., 2018).

Finally, an analysis of The Cancer Genome Atlas (TCGA) revealed that *ZXDA/B* are significantly mutated in several tumor types and that a large portion of these ZXDA/B cancer-associated mutations is located in the vicinity of the FBXO38-dependent degron (**Figure 3F** and **Supplementary Figure S3U**).

ZXDA/B Do Not Act as Transcription Factors

To further understand ZXDA/B protein function, we determined whether its DNA-binding activity affects the transcriptional level

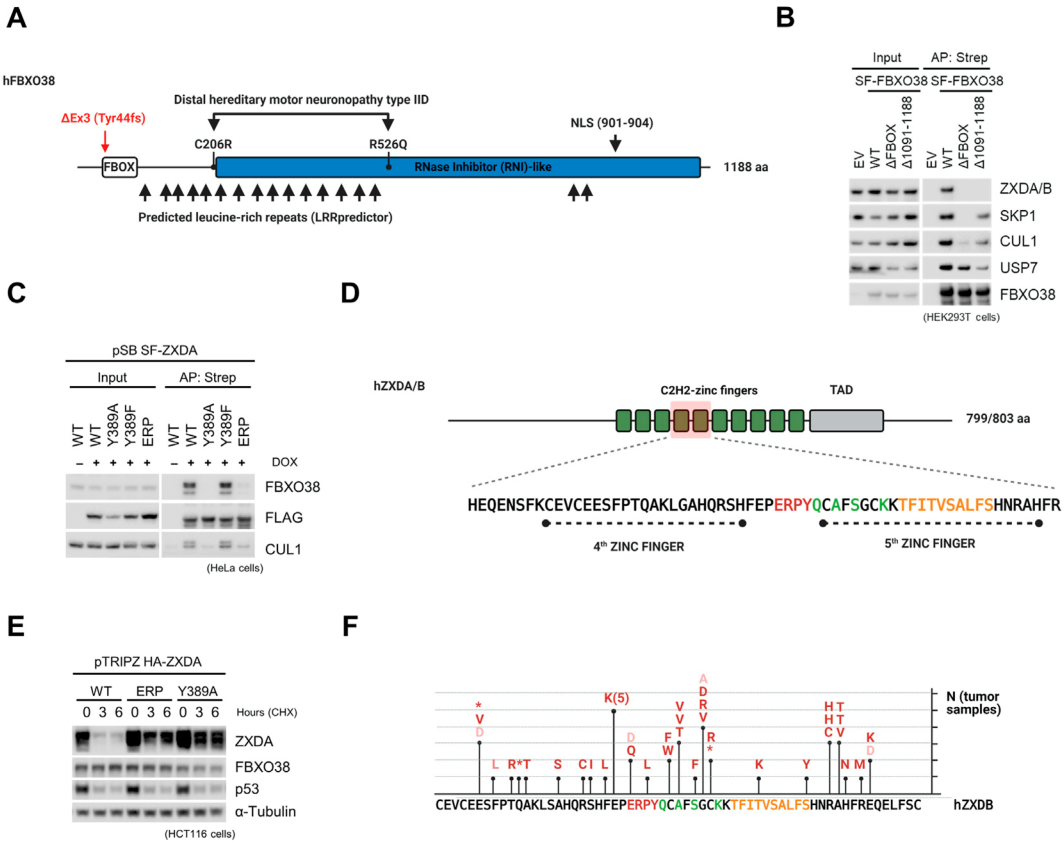


FIGURE 3 | FBXO38 associates with ZXDA/B via the zinc finger linker motif. **(A)** A scheme illustrating human FBXO38 structural features and disease-associated mutations. The F-box motif is located in the N-terminus followed by predicted leucine-rich repeats. Locations of the two mutations (C206R and R526Q) found in patients with distal hereditary motor neuronopathy type IID are depicted. The previously confirmed nuclear localization sequence (NLS) is located in the C-terminal part. Red arrowhead indicates the site of frameshift in FBXO38$^{\Delta ex3/\Delta ex3}$. **(B)** HEK293T cells were transfected with StrepII-FLAG-tagged wild-type FBXO38 (SF-FBXO38 WT), FBXO38 lacking the F-box motif (FBXO38$^{\Delta FBOX}$) or C-terminus (FBXO38$^{\Delta 1091\text{-}1188}$), treated with MLN4924 6 h prior to collecting, lysed, and subjected to affinity purification (AP) using Strep-Tactin resin. Inputs represent 1% of the whole-cell lysates subjected to AP. **(C)** HeLa cells with the inducible expression of SF-ZXDA and its mutants were treated with doxycycline for 24 h where indicated. Whole-cell lysates were subjected to affinity purification (AP) using Strep-Tactin resin and immunoblotted as indicated. Inputs represent 1% of the whole-cell lysate subjected to AP. **(D)** A schematic representation of human ZXDA and ZXDB proteins. Both contain ten C2H2 Zinc fingers (green boxes) followed by a previously reported transcriptional activation domain (TAD) (Al-Kandari et al., 2007). The zinc fingers important for FBXO38-interaction are red-tinted. Amino acids encompassing this region are depicted below, with a zinc finger linker necessary for FBXO38-interaction highlighted in red. Mutations of amino acids marked in yellow had a negative effect on FBXO38 interaction (degron). The green-labeled amino acids differ between ZXDA/B and ZXDC. **(E)** HCT116 cells with inducible expression of HA-tagged ZXDA and its mutated forms were incubated in the presence of doxycycline for 24 h and then treated with cycloheximide (CHX) for the indicated time. **(F)** ZXDB mutations identified in tumor samples (The Cancer Genome Atlas cohort). Mutations found in the vicinity of the FBXO38-dependent degron are depicted (deleterious mutations—red; synonymous or conservative mutations—orange). The ZXDB sequence is outlined below with amino acids highlighted as in **(D)**.

of genes located nearby its binding sites. As already mentioned, ZXDA/B are nuclear proteins. Detergent pre-extraction or soluble fraction analysis via western blot showed that a significant portion of the ZXDA/B proteins is nucleoplasmic, not associated with chromatin (**Figures 4A,B**). To determine the DNA-binding specificity of ZXDA/B, we performed chromatin immunoprecipitation using an anti-ZXDA/B antibody followed by next-generation sequencing (ChIP-seq) in the HCT116 cells. An analysis of the normalized data showed that the ZXDA/B proteins bind the chromatin in numerous gene promoters. Most of the ZXDA/B-associated loci were located nearby transcription starting sites (**Supplementary Table S1**), and previously designated as CpG islands and DNase I hypersensitive sites (**Figure 4C** and **Supplementary Figure S4A**). Furthermore, the analysis of MACS2-called peaks using regulatory sequence analysis tools (RSAT) software revealed significant GC-enrichment in close vicinity to the peak summits (**Supplementary Figure S4B,C**) (Zhang Y. et al., 2008; Thomas-Chollier et al., 2012). ChIP-seq data and ZXDA/B binding specificity were confirmed using publicly available data from the Encode and GEO databases (GSE91872). Genes with strong enrichment of ZXDA/B in their promoters belong to several gene ontology groups, including genes encoding ribosomal and stress granule proteins (**Supplementary Figure S4D**). Surprisingly, neither overexpression of ZXDA (WT and ERP mutant) nor ZXDA/B knockdown showed any significant

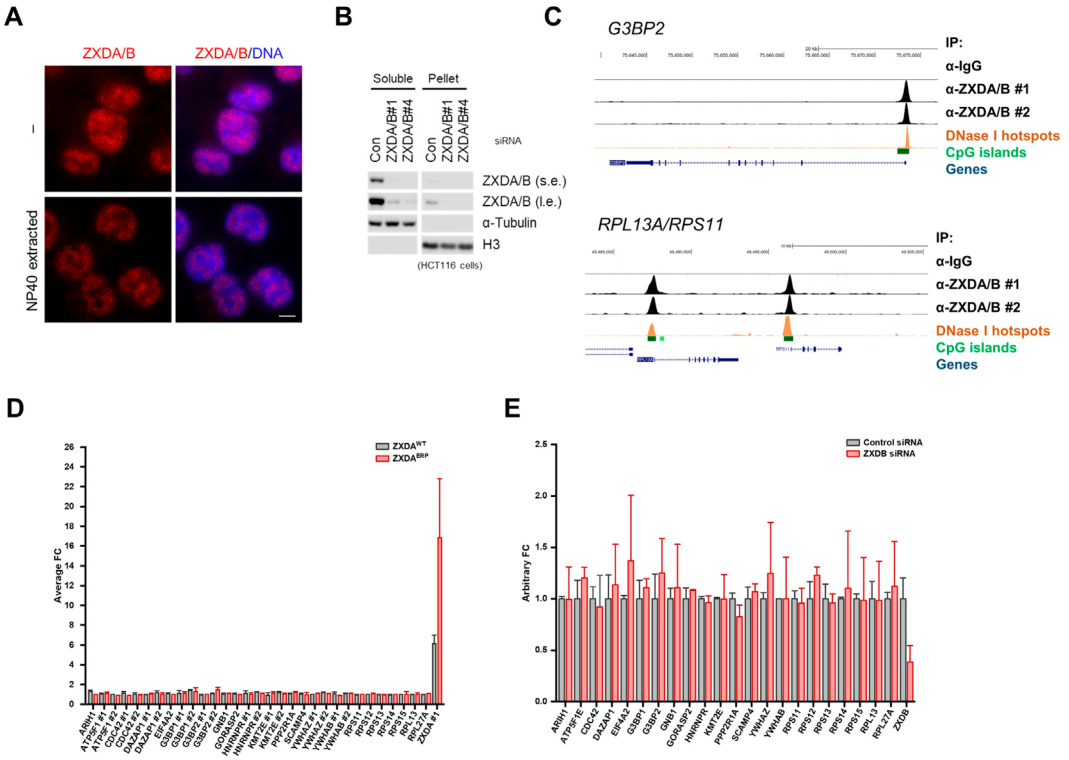


FIGURE 4 | ZXDA/B do not act as transcription factors. **(A)** Representative images of DNA-associated ZXDA/B in HCT116 cells. Cells were either directly fixed or the soluble proteins were pre-extracted using a CSK buffer with 0.5% NP-40 for 10 min. DNA was visualized using DAPI. Scale bar, 5 μm **(B)** The HCT116 cells were subjected to isotonic lysis, soluble fractions were collected and the pellets were further lysed in the presence of Benzonase nuclease and subsequently heat denatured in the presence of 1% SDS for insoluble fractions. Comparable amounts of soluble and insoluble fractions were loaded and immunoblotted as indicated. Both sides of the panel represent the same exposure time; l. e. stands for long exposure, s. e. short exposure. **(C)** ChIP-seq tag profiles covering *G3BP2* (upper panel), *RPS11*, and *RPL13A* (lower panel) loci showing a high correlation between two independent ZXDA/B ChIP-seq samples. The upper tag profiles represent the control and two anti-ZXDA/B ChIP-seq samples. The lower panels show the location of the genes, DNase I hypersensitivity regions, and CpG islands. The scheme was generated using a UCSC Genome Browser (Kent et al., 2002). **(D)** Microarray analysis of gene expression in the HCT116 cell line with inducible expression of wild-type (WT) or mutant (ERP) ZXDA. The cells were incubated in doxycycline for 24 h. Only genes with ZXDB-associated promoters are shown. All numbers were compared to the mean value obtained in untreated (non-induced) control. The final value represents the mean calculated from two independent experiments. **(E)** RNA-seq analysis of the HCT116 cell line transfected with two different control siRNAs and two siRNAs targeting ZXDB. All counts (FKPM) were compared to the average count obtained in control samples. Only genes with ZXDB-associated promoters are shown.

changes in the expression of genes with ZXDA/B-associated promoters (**Figures 4D,E**).

ZXDA/B Are CENP-B Associated Proteins

To clarify the biological function of ZXDA/B proteins, a series of affinity purifications of ZXDA were performed to determine its interactome in stably transfected HeLa cells and transiently transfected HEK293T cells. First, whole-cell lysates were prepared with turbonuclease to include chromatin-associated proteins. Subsequently, proteins co-purified with ZXDA were identified by mass-spectrometry analysis. In addition to the SCF^{FBXO38} subunits, ZXDA was associated with casein kinase 2 (CK2), protein phosphatase 2/6, and centromere protein B (CENP-B) (**Figures 5A–C**). By small-scale immunopurification, we confirmed that CENP-B, as well as CK2α and CK2β, interacted specifically with ZXDA and not with another interactor of FBXO38, DEDD2, that was used as a negative control (**Figure 5D**). As CENP-B is rarely found as a contaminant in mass-spectrometry analyzed purifications, we aspired to verify its interaction with ZXDA/B further. We revealed that the fifth and sixth zinc fingers of ZXDA protein are required for the interaction with CENP-B (**Figure 5E**). A comparison of the interaction profile of FBXO38 and CENP-B with ZXDA revealed that they bind overlapping regions (**Figure 5F**). Next, we established HeLa cells stably expressing eGFP-tagged CENP-B. We revealed that endogenous ZXDA/B co-precipitated with GFP-tagged CENP-B and that their interaction is enhanced by neddylation inhibition, most probably because ZXDA/B proteins level increased upon neddylation inhibition. Interestingly, FBXO38 did not interact with CENP-B, suggesting that their binding to ZXDA/B is mutually exclusive (**Figure 5G**). This observation was further confirmed by analysis of proteins co-purified with FBXO38 (**Figure 5H**).

Finally, to answer the question whether ZXDA/B are constitutive centromeric proteins, we analyzed different cancer cell lines using immunofluorescence. We did not observe any enrichment of endogenous ZXDA/B in distinct centromeric spots

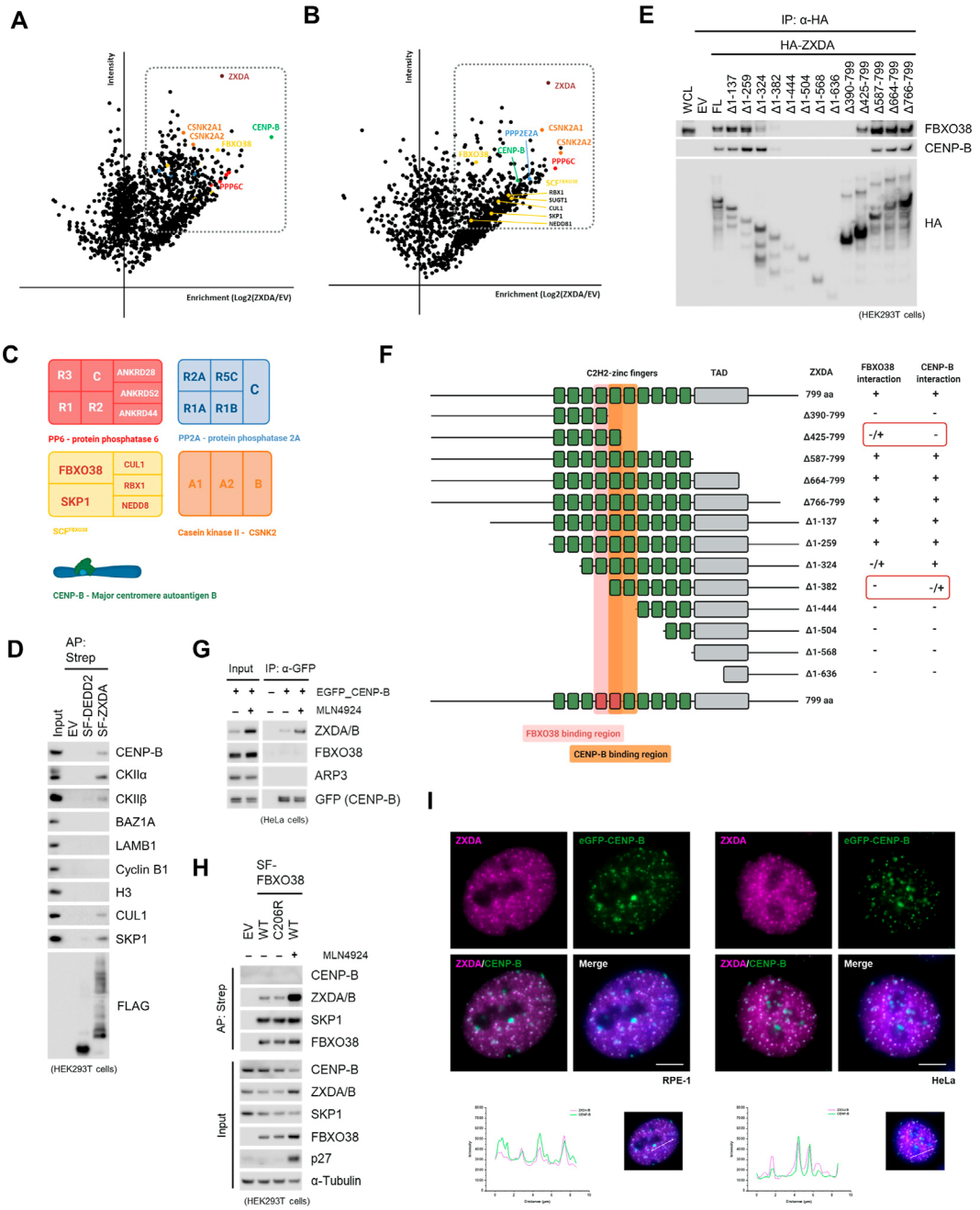


FIGURE 5 | ZXDA/B are CENP-B associated proteins. **(A)** Schematic representation of mass-spectrometry identification of ZXDA-interacting proteins. Affinity-purified proteins from HEK293T cells expressing StrepII-FLAG-tagged ZXDA (SF-ZXDA) were identified by Liquid Chromatography with Tandem Mass-Spectrometry (LC-MS/MS). Proteins that were significantly enriched in ZXDA purifications compared to the controls are highlighted in box. The graph represents maximum intensity and the enrichment calculated from ratio of intensities of identified proteins. Colors represent the identity of proteins to different complexes as it is depicted in **(C)**. **(B)** Schematic representation of mass-spectrometry identification of ZXDA-interacting proteins. Affinity purified proteins from HeLa cells with inducible expression of SF-ZXDA were identified by LC-MS/MS as in **(A)**. **(C)** Schematic composition of proteins and protein complexes enriched in ZXDA interactome from **(A)** and **(B)**. **(D)** HEK293T cells were transfected with SF-tagged ZXDA or DEDD2, and whole-cell lysates were subjected to affinity purification (AP) and subsequently immunoblotted as indicated. An empty vector (EV) was used as a negative control. The input represents 1% of the lysate subjected to AP. **(E)** HEK293T cells were transfected with HA-tagged full-length (FL) ZXDA or its deletion variants. Cells were treated with the MLN4924 inhibitor 6 h prior to collecting. Whole-cell lysates (WCL) were subjected to immunoprecipitation (IP) using anti-HA beads. Empty vector (EV) was used as a negative control. **(F)** Schematic representation of full-length ZXDA (1–799 aa) or its N- and C-terminally truncated variants. Zinc fingers are depicted as green boxes, those essential for interaction with FBXO38 are red-tinted, with CENP-B are orange-tinted. The middle panel indicates deleted amino acid positions in ZXDA. Interacting variants are indicated by the symbol (+) (+/-) denotes reduced binding, and (-) denotes a lack of binding. TAD; transcriptional activation domain. **(G)** HeLa cells expressing eGFP-CENP-B were treated with MLN4924 for 6 h where indicated. Soluble protein fraction

(*Continued*)

FIGURE 5 | was subjected to immunoprecipitation (IP) using GFP-Trap magnetic beads. Parental cells were used as negative control. Input represents 1% of the lysate subjected to IP. **(H)** HEK293T cells were transfected with WT or mutant (C206R) SF-FBXO38 and subjected to lysis and AP. An empty vector (EV) was used as a negative control. Where indicated, the MLN4924 inhibitor was added to the cells 16 h prior to collecting. p27 expression is shown as a positive control for neddylation inhibition. **(I)** Representative images of RPE-1 (left panel) and HeLa (right panel) cells with inducible expression of SF-ZXDA and stable expression of eGFP-CENP-B. The cells were incubated in the presence of doxycycline for 3 h. Scale bar, 5 μm.

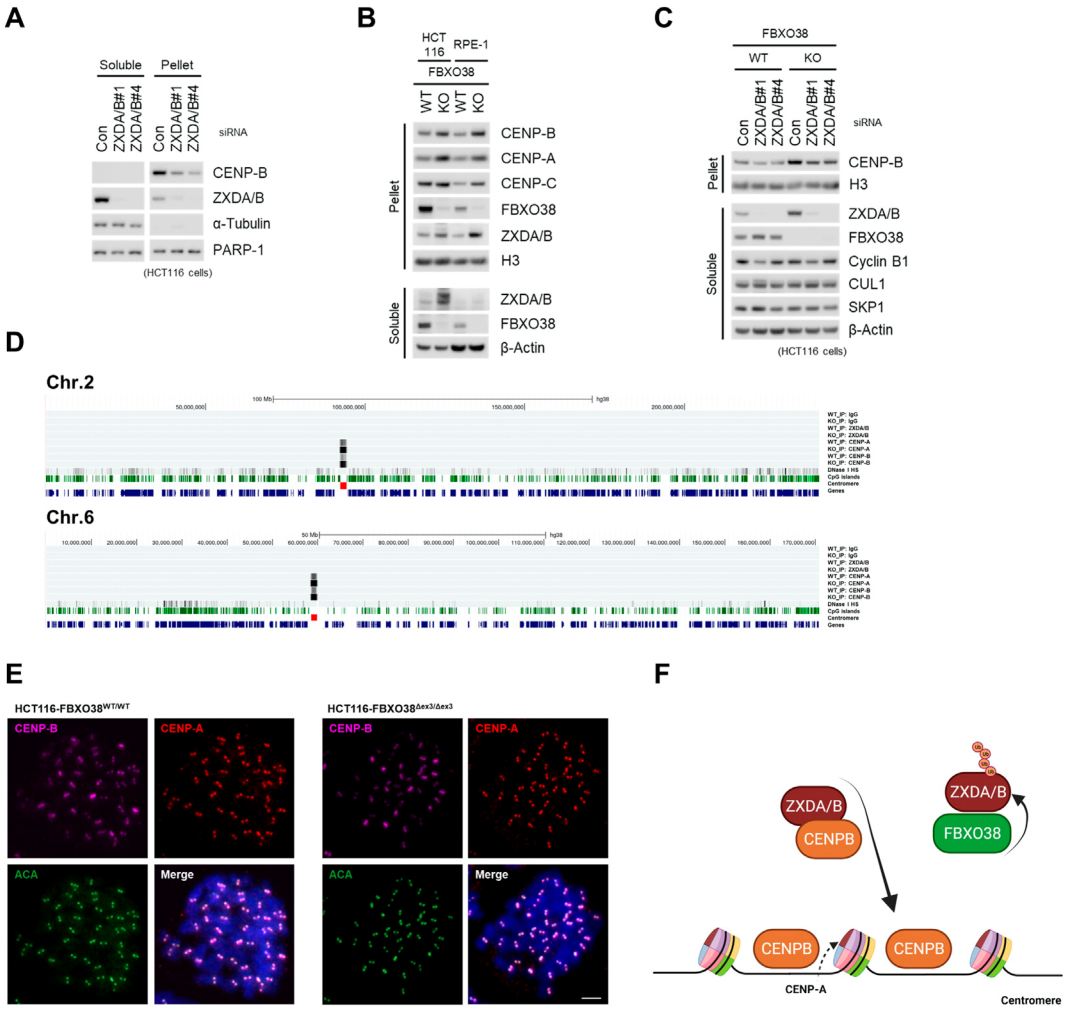


FIGURE 6 | FBXO38 controls centromeric signature via ZXDA/B stability. **(A)** HCT116 cells were transfected with two different siRNAs targeting ZXDA/B, or with control siRNA. The cells were subjected to isotonic lysis 48 h after transfection, soluble fractions were collected and the pellets were further lysed in the presence of Benzonase nuclease and subsequently heat denatured in the presence of 1% SDS for insoluble fractions. Lysates were immunoblotted as indicated **(B)** FBXO38 wild type (WT) and knockout (KO) HCT116 or RPE-1 cells were subjected to fractionation as in **(A)** and immunoblotted as indicated. **(C)** FBXO38 WT and KO HCT116 cells were transfected with two different siRNAs targeting ZXDA/B, or with control siRNA, lysed and immunoblotted as in **(A)**. The longer exposure of CENP-B immunostaining is available as **Supplementary Figure S6A**. **(D)** ChIP-Seq analysis of chromatin-bound proteins in FBXO38 WT and KO HCT116 cell line. Fragmented chromatin was immunopurified with either non-specific IgG, or ZXDA/B, CENP-A, and CENP-B polyclonal antibodies. Trimmed reads were aligned using the Bowtie2 program and further normalized with bamCoverage utility (Galaxy—DeepTools) to obtain counts per million (CPM) values. Coverage of the human genome (hg38) was visualized in the UCSC genome browser. The figure shows two chromosomes (2 and 6) coverage with other chromosomes depicted in (**Supplementary Figure S6D**). The quantity of precipitated chromatin is shown as a density graph using autoscale to highlight the centromeric enrichment. The single lines below the chromosome range ruler represent ChIP results from IgG control, ZXDA/B, CENP-A, and CENP-B (in FBXO38 WT and KO HCT116 cells). These lines are followed by a density graph of DNase I hypersensitivity, CpG islands (green), centromere (red), and genes locations. **(E)** Representative images of a mitotic spread of FBXO38 WT (left) and KO (right) HCT116 cell line. The cells were pre-treated with colchicine and spun onto slides. Permeabilized cells were fixed and immunostained with anti-centromere antibodies (ACA) and anti-CENP-A and CENP-B antibodies. Chromosomes were visualized with DAPI. Scale bar, 5 μm **(F)** Model of FBXO38-dependent regulation of the ZXDA/B protein. ZXDA/B proteins controls centromeric CENP-B protein level. FBXO38 is responsible for ZXDA/B degradation and limits CENP-B chromatin loading.

(data not shown). This result was not surprising, as we did not detect any centromeric chromatin DNA enrichment in ZXDA/B ChIP-seq. However, we found that brief inducible expression of exogenous ZXDA transiently colocalized in centromeric regions marked by eGFP-tagged CENP-B (**Figure 5I**).

FBXO38 Controls Centromeric Signature via ZXDA/B Stability

To clarify the physiologic role of ZXDA/B in centromeric chromatin control, we assessed the impact of their knockdown on the CENP-B protein level. Independent siRNAs targeting ZXDA/B significantly decreased the CENP-B protein level in chromatin (pellet) fraction (**Figure 6A**). Next, we assessed the effect of FBXO38 depletion on CENP-B expression and localization. As expected, FBXO38 deficiency led to increased levels of the ZXDA/B protein in immortalized RPE-1 and HCT116 cells. Accordingly to our previous observation, ZXDA/B acted as positive regulators of centromeric chromatin, and FBXO38 deficiency increased CENP-A, -B, and -C protein levels (**Figure 6B**). Our next goal was to rescue the effect of FBXO38 knockdown with simultaneous ZXDA/B inactivation. Since constitutive ZXDA/B KO cells were not viable, we proceeded with an acute knockdown of their expression using siRNAs. This inactivation led to the rescue of the CENP-B protein to the control level in the FBXO38-deficient HCT116 cells. To exclude cell cycle-related artifacts, the expression of cyclin B was assessed. Despite a slight change in the level of cyclin B in cells transfected with one of the ZXDA/B siRNAs, the pattern did not generally correlate with any significant cell cycle disruption (**Figure 6C** and **Supplementary Figure S6A**). Subsequently, we focused on the subgenomic localization of centromeric chromatin proteins. As it was shown that both CENP-A and CENP-B proteins could be deposited into extra-centromeric chromatin, such as neocentromeres, DNA damage sites, and transcription factor hotspots (Zeitlin et al., 2009; Scott and Sullivan, 2014; Athwal et al., 2015), we were interested in whether the loss of FBXO38 leads to these aberrations. For this purpose, ChIP-seq analyses of endogenous CENP-A/B proteins were performed. In FBXO38-deficient HCT116 cells, we did not detect any enrichment of previously described ZXDA/B binding sites in ChIP using CENP-A/B antibodies (**Supplementary Table S1**; examples in **Supplementary Figure S6B**), nor did we observe any CENP-A/B binding to the non-centromeric regions described previously (examples in **Supplementary Figure S6C**) (Athwal et al., 2015). Moreover, ChIP-seq results showed that the FBXO38 deficiency in HCT116 cells led to significant upregulation of CENP-A/B proteins in centromeric regions across the genome (**Figure 6D**, **Supplementary Figure S6D**). Finally, we visualized the subchromosomal localization of centromeres by immunofluorescence staining of CENP-A/B proteins in mitotic cell spreads. Both FBXO38 WT and KO cells had the same number of chromosomes (~45) and we observed no ectopic centromere formation (**Figure 6E**). These results suggest that the endogenous ZXDA/B proteins act as positive regulators of chromatin CENP-B protein loading and thus represent previously unknown controllers of the epigenetic signature of the centromeres. Finally, we proved that FBXO38-dependent ZXDA/B degradation regulates this process and controls the composition of centromeric chromatin and integrity (**Figure 6F**).

DISCUSSION

Here we show that FBXO38 ubiquitin ligase substrate receptor interacts with the zinc finger proteins ZXDA and ZXDB and targets them for degradation. FBXO38 recognizes a zinc finger linker in ZXDA/B, which represents a consensus motif found in many commonly expressed zinc finger proteins. Surprisingly, none of them had ever been detected in any of our proteomic analyses of FBXO38-associated proteins, indicating the hidden complexity of how FBXO38 recognizes this degron. Interestingly, we found that ZXDC, a very close homolog of ZXDA/B that shares an identical motif in the zinc finger linker, did not interact with FBXO38. Homology modeling revealed a significant difference in the structural positioning of essential tyrosine due to different amino acid compositions surrounding this motif. Although these *in silico* results support our *in vitro* observations, we cannot exclude the possibility that FBXO38 also controls ZXDC under certain conditions. Furthermore, we proved that phosphorylation of this motif is not required, but it is also plausible that phosphorylation of degron residues and surrounding amino acids may have an inhibitory impact on the interaction between ZXDA/B and FBXO38. Similarly positioned tyrosine in the Yin Yang 1 protein (YY1) is the target of Src tyrosine kinases, and its phosphorylation interferes with the DNA and RNA binding of YY1 protein (Wang and Goff, 2015). Importantly, threonine and serine residues adjacent to C2H2 zinc finger linkers are globally phosphorylated during mitosis (Rizkallah et al., 2011). This phosphorylation was shown to be inhibitory towards their DNA-binding and represents cellular control of the transcription factor function during mitosis (Dovat et al., 2002). Interestingly, ZXDA/B proteins contain glutamate residue at the corresponding position (hZXDA/B Glu384/388), indicating that these zinc fingers may not be involved in DNA binding since glutamate mimics phosphorylated threonine.

The ZXDA/B/C proteins were shown to act as transcriptional regulators (Al-Kandari et al., 2007). Here we demonstrated that ZXDA/B proteins are in complex with CENP-B, an enigmatic DNA-binding centromeric protein controlling the centromere integrity and preventing aneuploidy (Fachinetti et al., 2015; Gamba and Fachinetti, 2020). We propose that the interaction of ZXDA/B with FBXO38 and CENP-B is mutually exclusive since we have neither detected the CENP-B protein in FBXO38 purifications nor observed FBXO38 in CENP-B pulldowns. The underlying reason could be the partial overlap of FBXO38 and CENP-B interaction motifs in ZXDA/B. Although we have not studied the region in CENP-B required for ZXDA/B binding, we observed that they interact preferentially in the soluble fraction. This observation is supported by the fact that we have not seen localization of endogenous ZXDA/B in centromeric regions, nor have we observed precipitation of centromeric chromatin using

the ZXDA/B antibody. In fact, ZXDA colocalizes with CENP B only transiently after a brief induction of exogenous ZXDA expression.

We proposed that ZXDA/B proteins positively affect CENP-B loading into the centromere region. ZXDA/B stabilization in FBXO38 KO cells led to increased CENP-A/B/C protein levels. There is growing evidence that centromere chromatin is dynamically regulated upon stress conditions, viral infection, or during the differentiation process (Everett et al., 1999; Hedouin et al., 2017; Hou et al., 2021). However, we do not currently understand the cellular mechanisms governing FBXO38/ZXDA/B-dependent regulation of centromeric chromatin. In FBXO38-deficient cell lines, FBXO38 appears to control steady-state levels of ZXDA/B proteins, but we cannot rule out the possibility of a signaling pathway controlling this interaction. In addition, the physiological role of human FBXO38 seems unclear. FBXO38-deficient mice are growth-retarded with a defect in the maturation of Sertoli cells, the postmitotic somatic population required for germ cell nurturing. FBXO38 deficiency leads to ZXDA/B stabilization and increased centromeric CENP-A/B protein levels in Sertoli cells. As a result, mouse testes exhibit disorganized spermatogenesis and decreased fertility (Dibus et al., 2022). Another hint for the physiological role of FBXO38 comes from discoveries that several mutations in the FBXO38 gene drive early-onset distal muscular dystrophy (Sumner et al., 2013; Akcimen et al., 2019). Increased anterior horn motor neuron loss was observed in the spinal cord of these patients. Although it was not our aim to identify the role of FBXO38 in neural tissue, ZXDA/B proteins and centromeres can be deregulated in these patient motor neurons similarly to cancer cell lines or the previously mentioned Sertoli cells. This biochemical pathway could thus link centromere integrity to the development of a subset of neurodegenerative syndromes.

Since ZXDA/B/C nuclear factors have previously been identified as transcriptional regulators, we expected that their binding to DNA would affect the expression of nearby genes (Al-Kandari et al., 2007; Aleksandrova et al., 2010). However, we did not observe any differences in the expression of these genes after ZXDA-inducible overexpression or ZXDA/B siRNA-mediated knockdown. This could be due to a functional uncoupling of the ZXDA/B proteins from the transcription machinery or because the effect of ZXDA/B expression on transcription is not immediate. Unfortunately, we were unable to generate CRISPR-mediated ZXDA/B knockdown (in mouse or cancer cell lines) and thus analyze the long-term effects of ZXDA/B expression. Finally, ZXDA/B might have context-specific partners that would affect the transcription of downstream genes, but we are currently unaware of any such ZXDA/B interaction partners.

The frequency of CENP-A positive nucleosomes in centromere chromatin is tightly regulated and dependent on various factors, including CENP-B itself, as shown in human artificial chromosome experiments (Ohzeki et al., 2002). Human epithelial diploid cells have been reported to contain ~400 molecules of CENP-A in their centromeres. This observation is in striking contrast to a large number of CENP-B box-containing satellite repeats in the human genome, particularly in centromeric regions (Bodor et al., 2014; McNulty and Sullivan, 2018). Such paradox suggests that the CENP-B box is essential but not sufficient for CENP-A nucleosome *de novo* assembly, and there have to exist controlling mechanisms involved in this process. Our results suggest that the FBXO38-ZXDA/B biochemical pathway could be one of these mechanisms, as we demonstrated that FBXO38 KO cells exhibited stabilized centromeric chromatin proteins. To understand the nature of this stabilization, we performed a ChIP-seq analysis to clarify differences in CENP-A/B proteins DNA interaction upon the loss of FBXO38. As shown previously, CENP-A centromeric histone can be transiently present at the DNA damage sites and transcription factor hotspots (Zeitlin et al., 2009; Scott and Sullivan, 2014; Athwal et al., 2015). This might suggest that FBXO38 controls centromere chromatin deposition at these sites, potentially blocking the formation of neocentromeres. However, we did not observe any ectopic CENP-A/B proteins in FBXO38 knockout cells, implying that ZXDA/B controls the deposition of these chromatin proteins primarily in the centromeres themselves.

Interestingly, a similar complex, centromere binding factor 3 (CBF3), controls the centromere chromatin establishment and kinetochore assembly in budding yeast (Lechner and Carbon, 1991). The point centromere in budding yeast consists of three short DNA elements CDE I, CDE II and CDE III, and the CBF3 complex binds to the CCG motif in CDE III. CBF3 complex consists of leucine-rich repeats containing F-box proteins Ctf13, $Skp1^{SKP1}$, zinc finger protein Cep3, and the kinetochore protein Ndc10 (Yan et al., 2018). In addition, Skp1 chaperone $Sgt1^{SUGT1}$ is also essential for the function of the CBF3 complex (Kitagawa et al., 1999). Importantly, the CBF3 complex controls centromere chromatin loading of $Cbf1^{CENP-B}$ and $Cse4^{CENP-A}$, similarly to FBXO38/ZXDA/B complex (Hemmerich et al., 2000; Zhang et al., 2007). However, there are no identified mammalian homologs for Ctf13 ubiquitin ligase and Cep3 zinc finger protein, and the similarity to FBXO38/ZXDA/B is based on structural and functional protein motifs. Moreover, we did not observe a tertiary complex between CENP-B/ZXDA/B and FBXO38, and FBXO38 did not localize to nor interact with centromeric DNA.

Aberrant centromere chromatin composition frequently results in improper kinetochore formation and aneuploidy, one of the hallmarks of cancer (Vasudevan et al., 2021). As previously mentioned, CENP-B protein is required for faithful chromosome segregation (Fachinetti et al., 2015). On the other hand, increased CENP-B expression leads to its non-specific DNA binding (Tachiwana, Miya et al., 2013) and the consequent increase in chromatin CENP-A and CENP-C levels (Okada et al., 2007; Fachinetti et al., 2015). Importantly, overexpression of CENP-A has been shown to affect the fidelity of mitosis and promote tumorigenesis (Tomonaga et al., 2003; Jeffery et al., 2021). Given that such misexpression of centromeric chromatin may lead to chromosomal aberrations and possibly cancer-related malformations, there is a possibility that FBXO38 may provide a fine-tuning mechanism to avoid these anomalies. In support of this hypothesis, it has been shown that FBXO38 prevents cytokinesis and mitotic defects and that cancer cells lacking FBXO38 exhibited an increased frequency of multinucleated cells (Georges et al., 2019).

MATERIALS AND METHODS

Cell Culture Procedures

Human cell lines HEK293T (female), hTERT RPE-1 (female), HCT 116 (male), U-2 OS (female), HeLa (female) were maintained in Dulbecco's Modified Eagle's Medium (DMEM) supplemented with 10% fetal bovine serum (FBS) and penicillin, streptomycin, and gentamicin. All cell lines were cultured in a humidified incubator at 37°C with 5% CO_2. Cycloheximide (100 μg/ml), MLN4924 (2 μM), or MG-132 (10 μM) were used where indicated. If not stated otherwise, doxycycline hyclate (Sigma Aldrich) was used at 1 μg/ml concentration. Cells were regularly screened for *Mycoplasma* contamination.

Plasmid Construction

cDNAs of human *FBX O 38* (Origene #RC204380), *ZXDA* (TransOMIC Technologies, #BC059356), or *ZXDC* (kind gift from Dr. Joseph D. Fontes.) genes were cloned into pcDNA3.1 containing either N-terminal twinStrepII-FLAG-tag (pcDNA3.1—NSF) or an N-terminal hemagglutinin-tag (pcDNA 3.1—HA). For mutated and truncated variants of these genes, PCR mutagenesis was carried out using primers designed with QuikChange® Primer Design Program (Agilent) with subsequent DpnI digestion. All the constructs created were verified by sequencing. For inducible expression, cDNAs of selected genes were cloned into lentiviral pTRIPZ™ (Dharmacon) or pSBtet vectors. A retroviral construct expressing eGFP-CENPB was a gift from Iain Cheeseman (pKG141-eGFP-CENPB; Addgene plasmid #69759). The cDNA library of the ubiquitin ligases was prepared as described previously (Lidak et al., 2021).

For FBXO38$^{\Delta Ex3/\Delta Ex3}$ cell line generation (HCT116 and RPE-1 FBXO38 KO), single guide RNAs (sgRNAs) were cloned into the LentiCRISPR (pXPR_001; Addgene, #49535) containing dual sgRNA and hSpCas9 expression cassettes. Optimal sgRNA sequences were designed using http://crispr.mit.edu/and the targeted sequences were: AAGCTGTATGACCGTATGTGT GG, GATGCATGTTTTCCGGTGAATGG. Successful deletion was confirmed by PCR and sequencing.

Transient Transfections

HEK293T cells were transfected using polyethylenimine (PEI MW 25000, Polysciences). All other cell lines were transfected using Lipofectamine 2000 (Invitrogen) according to the manufacturer's protocol. For transient transfections, the cells were collected 48 h after transfection. Where indicated, MLN4924 or MG-132 was used.

Stable Cell Line Generation

For lentiviral particles production, HEK293T cells were co-transfected with the lentiviral vector containing HA-tagged ZXDA (pTRIPZ_HA-ZXDA) along with pCMV-dR8.2 (Addgene, #8455) and pCMV-VSV-G (Addgene, #8454). The lentiviral media was collected 48 h after transfection, mixed with Polybrene (Sigma Aldrich), and used for infecting the cells of interest. The stable clones were selected using puromycin.

For the transposition-based gene transfer, the cells were transfected with pSBtet containing SF-tagged ZXDA (pSB_NSF-ZXDA) along with the transposase-containing pSB100X. The selection of stable clones was carried out using puromycin 24 h after transfection.

HeLa cells stably expressing eGFP-CENP-B were generated by co-transfection of pKG141-eGFP-CENPB along with pCMV-VSV-G (Addgene, #8454) and gag/pol plasmid (Addgene, #14887) into HEK293T cells. The viral containing media was collected 48 h after transfection and used for infecting HeLa cells. CENP-B-expressing clones were selected according to eGFP positivity.

To generate FBXO38 knockout cell lines, the LentiCRISPR containing sgRNA targeting sequences were transfected into the previously subcloned HCT116 and RPE-1 cells. Two days after transfection, the cells were briefly selected with puromycin and sorted to get single-cell clones. Genomic DNA was extracted using a DNA-isolation buffer (0.2% Tween, 0.2% Triton-X100, Proteinase K 200 μg/ml) and genotyped by PCR using primers surrounding the targeted sequence. The PCR products were purified and sequenced to confirm the deletion.

Gene Silencing

Small interfering RNAs (Sigma Aldrich) were transfected into the subconfluent cell lines using Lipofectamine RNAiMAX (Invitrogen) according to the manufacturer's protocol. The sequences of the oligonucleotides targeting FBXO38 were GGGUGUAUUUCAGCGAGUAUU (#1), GGACUCGAU UGGUUGAUAUUU (#2), and GAGCGAAGCUGUUUGAGU AUU (#3). The sequences of the oligonucleotides targeting ZXDA/B were GCUCUGUGGUGUUGGAUAAUU (#1), CUG AAAGGCCACAGCAUAAUU (#2), CCAAGAAGCACCAGC UGAAUU (#3), and ACACAUAAGUCUUGGAAAUUU (#4). Non-targeting siRNAs were used as negative controls.

Immunoblotting

For whole-cell lysates, cells were washed with ice-cold PBS and lysed in a lysis buffer (150 mM NaCl, 50 mM Tris pH 7.5, 0.4% Triton X-100, 2 mM CaCl2, 2mM MgCl2, 1 mM EDTA) in the presence of phosphatase a protease inhibitor cocktail (MedChem Express) and Benzonase nuclease (0.125 U/μl; Santa Cruz) for 30 min on ice. Lysates were mixed with an equal volume of 2% SDS in 50 mM Tris-HCl, pH 8, heated for 5 min in 95°C, and cleared by centrifugation. For soluble fraction, washed cells were lysed for 10 min in the same buffer without Benzonase nuclease, centrifuged for 5 min, 3,000 rpm, and the fraction was separated. The leftover insoluble fraction was further lysed for 15 min in the same buffer with the addition of Benzonase nuclease (1.25 U/μl), mixed with 2% SDS in 50 mM Tris-HCl, pH 8, to the final concentration 1%, heated for 5 min in 95°C and cleared by centrifugation.

Protein concentration was determined by the BCA method (Thermo Fisher Scientific). Samples were prepared by mixing with Bolt™ LDS Sample Buffer (Thermo Fisher Scientific) supplemented with 10% β-mercaptoethanol (Sigma Aldrich), heated for 5 min at 95°C, and then separated using NuPAGE™ 4–12% gradient Bis-Tris gel (Invitrogen). Afterward, the samples

were transferred to PVDF membrane (Amersham), blocked with 5% milk (ChemCruz), and incubated with indicated antibodies diluted in 3% BSA (PanReac Applichem) in TBS-T overnight at 4°C. The HRP-conjugated secondary antibodies (Cell Signaling) were diluted in 5% milk in TBS-T. The membranes were developed using WesternBright ECL (Advansta) or SuperSignal™ West Femto Maximum Sensitivity Substrate (Thermo Fisher Scientific).

Protein Immunoprecipitation and Affinity Purification

The cells were collected and lysed in the lysis buffer (150 mM NaCl, 50 mM Tris pH 7.5, 0.4% Triton X-100, 2 mM CaCl2, 2 mM MgCl2, 1 mM EDTA, supplemented with phosphatase and protease inhibitors) in the presence of Benzonase nuclease (0.125 U/µl; Santa Cruz) for 30 min on ice. The lysates cleared by centrifugation were then incubated with either Strep-Tactin® Sepharose resin (IBA Lifesciences) for SF-tagged proteins or with Pierce™ anti-HA Magnetic Beads (Thermo Fisher Scientific) or GFP-Trap® Magnetic Beads (ChromoTek) Purified Strep-tagged proteins were then eluted by desthiobiotin using Buffer E (IBA Lifesciences) and subsequently prepared for immunoblotting as described above. Elution of immunoprecipitated HA-tagged and eGFP-tagged proteins was carried out with 1x Bolt™ LDS Sample Buffer (Thermo Fisher Scientific). Eluates were then supplemented with β-mercaptoethanol (Sigma Aldrich) and incubated at 95 °C for 5 min. For immunoprecipitation of endogenous proteins, lysates were incubated with the indicated antibodies and mixed with Dynabeads® Protein G. Rabbit IgG was used as a negative control. Elution of immunoprecipitated proteins was carried out under the same conditions as for anti-HA immunoprecipitation. For tandem affinity purification, HEK293T cells were co-transfected with constructs encoding SF-tagged and HA-tagged proteins. Cells were collected and lysed in the same lysis buffer as described above. The lysates were incubated with Strep-Tactin® Sepharose resin and eluted as described above. A portion of the eluate was subsequently used for HA-immunoprecipitation. Precipitated proteins were eluted by 3M NaSCN.

Mass Spectrometry

Protein Digestion. Desthiobiotine and NaSCN eluates were acetone precipitated and resuspended in 100 mM TEAB containing 1% SDC. Cysteins were reduced with 5 mM final concentration of TCEP (60°C for 60 min) and blocked with 10 mM final concentration of MMTS (10 min Room Temperature). Samples were cleaved on beads with 1 µg of trypsine at 37°C overnight. After digestion samples were centrifuged and supernatants were collected and acidified with TFA to 1% final concentration. SDC was removed by extraction to ethylacetate (Masuda et al., 2008). Peptides were desalted using in-house made stage tips packed with C18 disks (Empore) according to (Rappsilber et al., 2007).

nLC-MS 2 Analysis. Nano Reversed phase column (EASY-Spray column, 50 cm × 75 µm ID, PepMap C18, 2 µm particles, 100 Å pore size) was used for LC/MS analysis. Mobile phase buffer A was composed of water and 0.1% formic acid. Mobile phase B was composed of acetonitrile and 0.1% formic acid. Samples were loaded onto the trap column (Acclaim PepMap300, C18, 5 µm, 300 Å Wide Pore, 300 µm × 5 mm, 5 Cartridges) for 4 min at 15 µl/min. Loading buffer was composed of water, 2% acetonitrile and 0.1% trifluoroacetic acid. Peptides were eluted with Mobile phase B gradient from 4 to 35% B in 60 min. Eluting peptide cations were converted to gas-phase ions by electrospray ionization and analyzed on a Thermo Orbitrap Fusion (Q-OT-qIT, Thermo). Survey scans of peptide precursors from 400 to 1,600 m/z were performed at 120K resolution (at 200 m/z) with a 5×10^5 ion count target. Tandem MS was performed by isolation at 1, 5 Th with the quadrupole, HCD fragmentation with normalized collision energy of 30, and rapid scan MS analysis in the ion trap. The MS 2 ion count target was set to 10^4 and the max injection time was 35 ms. Only those precursors with charge state 2–6 were sampled for MS 2. The dynamic exclusion duration was set to 45 s with a 10 ppm tolerance around the selected precursor and its isotopes. Monoisotopic precursor selection was turned on. The instrument was run in top speed mode with 2 s cycles (Hebert et al., 2014).

Data analysis. All data were analyzed ans quantified with the MaxQuant software (version 1.5.3.8) (Cox et al., 2014). The false discovery rate (FDR) was set to 1% for both proteins and peptides and we specified a minimum length of seven amino acids. The Andromeda search engine was used for the MS/MS spectra search against the *Caenorhabditis elegans* database (downloaded from Uniprot on April 2015, containing 25,527 entries). Enzyme specificity was set as C-terminal to Arg and Lys, also allowing cleavage at proline bonds and a maximum of two missed cleavages. Dithiomethylation of cysteine was selected as fixed modification and N- terminal protein acetylation, methionine oxidation na serine/threonine/tyrosine phosphorylation as variable modifications. The "match between runs" feature of MaxQuant was used to transfer identifications to other LC-MS/MS runs based on their masses and retention time (maximum deviation 0.7 min) and this was also used in quantification experiments. Quantifications were performed with the label-free algorithms described recently. Data analysis was performed using Perseus 1.5.2.4 software (Tyanova et al., 2016).

In vitro Ubiquitination Assay

HEK293T cells were transfected with pNSF-FBXO38 and lysed using an isotonic buffer containing Benzonase (0.125 U/µl). Lysates were precleared with 0.40 µm filters and Strep-tagged complexes were isolated using Strep-Tactin® Sepharose resins. *In vitro* ubiquitination assays were performed as described previously (Horn et al., 2014). Briefly, resins with affinity-purified FBXO38 were mixed with 30 µl of ubiquitination assay buffer containing 0.1 µM UBE1, 10 ng/ml Ubch3, 10 ng/ml Ubch5c, 1 µM ubiquitin aldehyde (all Boston Biochem), 2.5 µg/µl ubiquitin (Sigma Aldrich), 50 mM Tris (pH 7.6), ±2 mM ATP, 5 mM MgCl2, 0.6 mM DTT for 45 min at 37°C. Complexes were eluted by competition with 3.5 µl desthiobiotin containing Buffer E (IBA Lifesciences).

Immunocytochemistry

Cells were washed with PBS, fixed with 4% PFA in PBS for 20 min, permeabilized with 0.2% Triton X-100 in PBS for 10 min, and blocked for 1 h (3% BSA, 0.1% Triton X-100 in PBS). Incubation with indicated primary antibodies was carried out for 2 h at RT followed by incubation with Alexa Fluor-conjugated secondary antibodies (Abcam) for 30 min at RT. DAPI was used to stain DNA. To visualize F-actin, Phalloidin-iFluor 488 Reagent (Abcam) was used. Slides were mounted with ProLong Gold Antifade Mountant (Invitrogen). Images were acquired using Axio Imager Zeiss 2 (EC Plan—Nefluar objectives) and analyzed with ZEN 2.3 or ImageJ software.

Mitotic Spreads

HCT116 cells were incubated with colchicine (5 μg/ml; Sigma Aldrich) for 90 min. Trypsinized cells were then swelled in a hypotonic solution of 75 mM KCl for 15 min at 37°C. StatSpin Cytofuge2 was used for spinning cells for 5 min at 800 rpm onto slides pre-treated with poly-L-lysine, followed by permeabilization with 0.2% Triton-X100 for 2 min and subsequent fixation with 4% paraformaldehyde for 4 min. Slides were then washed three times with PBS and blocked for 1 h (3% BSA, 0.1% Triton X-100 in PBS). Antibodies incubation was carried out as described above.

Chromatin Immunoprecipitation

Growing cells were fixed with 1% formaldehyde for 10 min. The reaction was stopped using 125 mM glycine, cells were washed twice with PBS and collected. Afterward, the cells were lysed in a sonication buffer (50 mM Tris pH 7.5, 140 mM NaCl, 1 mM EDTA pH 8, 0.1% Triton X-100, 0.1% SDS, protease inhibitor cocktail), incubated for 10 min on ice, centrifuged and the pellets were resuspended in an identical buffer. The subsequent sonication was performed for 10 min to generate a fragment size distribution of 100–800 bp (Covaris ME220 Focused-Ultrasonicator, Peak-Power: 75 W, Duty factor: 15%, Cycle/Burst 1,000, water temperature: 6°C). The sonicated chromatin was precleared by centrifugation, diluted with an IP buffer (as described above) and immunoprecipitated with the corresponding antibodies overnight at 4°C, followed by incubation with Dynabeads-Protein G (ThermoFisher Scientific). Precipitated DNA/protein complexes were eluted from stringently washed beads using buffer containing 1% SDS and 100 mM NaHCO3. Reverse cross-linking of eluates were performed in presence of 200 mM NaCl and RnaseA (ThermoFisher Scientific; 0.15 μg/μl) overnight at 65°C, followed by 1 hour incubation with Proteinase K (Santa Cruz; 0.3 μg/μl) and subsequent purification of DNA with QIAquick PCR Purification Kit (Qiagen).

ChIP-Seq Analysis

The quantity and quality of immunoprecipitated DNA was measured using Qubit (ThermoFisher Scientific) and analysed by Agilent 2,100 Bioanalyser (Agilent Technologies). Sequencing libraries were prepared with NEBNext Ultra II DNA (New England Biolabs) library preparation kit. Libraries were sequenced on the Illumina NextSeq 500 instrument using 76 bp single-end configuration yielding on average 27 million reads per sample.

Sequencing reads were mapped against the hg38 genome with Bowtie2 by using Galaxy Version 2.4.2 + galaxy0) with the following settings: D 20 -R 3 -N 0 -L 20 -i S,1,0.50. The resulting bam files were normalized and compared in the bamCompare utility (Galaxy), and bigwig or bam files were visualized in the UCSC genome browser. Peaks were called with MACS2 using version (2.1.1.20160309). Enriched Motifs were searched using RSAT (rsat.sb-roscoff.fr).

RNA-Seq Analysis

Total RNA was isolated using an RNeasy Micro kit (Qiagen Sciences, Inc., Gaithersburg, Md, United States) according to the manufacturer's protocol. The quantity and quality of isolated RNA was measured using Qubit (ThermoFisher Scientific) and analysed by Agilent 2,100 Bioanalyser (Agilent Technologies). Sequencing libraries were prepared with Takara Smarter Stranded Total RNA-seq Kit v2 Pico Input Mammalian (PN 634413). The protocol includes depletion of ribosomal RNA. Libraries were sequenced on the Illumina NextSeq® 500 instrument using 76bp single-end configuration yielding on average 1.4×10^7 reads per sample.

For subsequent read processing, a bioinformatic pipeline nf-core/rnaseq version 1.4.2, was used (Ewels et al., 2019). Individual steps included removing sequencing adaptors and low-quality reads with Trim Galore! (http://www.bioinformatics.babraham.ac.uk/projects/trim_galore/), mapping to reference genome GRCm38 (Ensembl annotation version 98) with HISAT2 and quantifying expression on gene level with featureCounts (Liao et al., 2014; Kim et al., 2015; Cunningham et al., 2019). Per gene mapped counts served as input for differential expression analysis using DESeq2 R Bioconductor package (Love et al., 2014). Prior to the analysis, genes not expressed in at least two samples were discarded. We supplied experimental model assuming sample group as main effect. Resulting per gene expression log2-fold changes were used for differential expression analysis. Genes exhibiting minimal absolute log2-fold change value of log2 (1.5) and statistical significance (FDR <0.05) between compared groups of samples were considered as differentially expressed. As next, gene set over representation analysis was done using gene length bias aware algorithm implemented in goseq R Bioconductor package with KEGG pathways and GO terms gene sets (Young et al., 2010).

For individual genes expression comparison, raw read counts were normalized using fragment counts per kilobase of feature length per million mapped reads (FPKM) based on sum of lengths of all gene exons.

Microarrays

Total RNA was isolated using an RNeasy Micro kit (Qiagen Sciences, Inc., Gaithersburg, Md, United States) according to the manufacturer's protocol. Quality and concentration of RNA were measured with a Nanodrop 2000 spectrophotometer (Thermo Fisher Scientific, Inc.). RNA integrity was analysed using an Agilent Bioanalyzer 2,100 (Agilent Technologies, Inc.). Only samples with an intact RNA profile were used for microarray analyses (RNA Integrity Number >9).

Illumina HumanHT-12 v4 Expression BeadChips (Illumina, Inc., San Diego, CA, United States) were used for the microarray analysis following the standard protocol. Briefly, 250 ng RNA was

amplified with the Illumina TotalPrep RNA Amplification kit (Ambion; Thermo Fisher Scientific, Inc.) and 750 ng labelled RNA was hybridized on the chip according to the manufacturer's protocol. Analysis was performed in indicated replicates per group. The raw data were preprocessed using GenomeStudio software (version 1.9.0.24624; Illumina, Inc.). The transcription profiles were background corrected using an Illumina proprietary correction, quantile normalized and variance stabilized using base 2 logarithmic transformation.

Swiss Model Prediction

Models were computed by the SWISS-MODEL server homology modeling pipeline (Waterhouse et al., 2018), using ZXDB (amino acids: 361–419) and ZXDC (amino acid: 265–323) as a query. As a template Wilms' tumor 1 (WT1) zinc finger structure (6-blw.1.A) was selected. The results of the prediction will be available in the Mendeley database.

Quantification and Statistical Analysis

Graphs were generated using OriginPro 2021. Protein identity and similarity was assessed by MegAlign Pro (DNAStar). The mass spectrometry results are presented as a dot-plot graph with enrichment calculated as log2 differences between control and experimental samples on the *x*-axis and maximal intensity on the *y*-axis. Only proteins identified in biological replicates are indicated.

DATA AVAILABILITY STATEMENT

The datasets presented in this study can be found in online repositories. The names of the repository/repositories and accession number(s) can be found below: ArrayExpress accession number: E-MTAB-11272, E-MTAB-11269, E-MTAB-11270.

AUTHOR CONTRIBUTIONS

Conceptualization, LC and ND; investigation, ND and LC; Writing—original draft preparation, ND and LC; writing—review and editing, ND, VK, and LC; supervision, LC; funding acquisition, LC and VK. All authors have read and agreed to the published version of the manuscript.

FUNDING

This work was supported by the Czech Science Foundation (18-27408S) and the Czech Academy of Sciences. LC was supported by Marie Skłodowska-Curie Fellowship (LIGER) and by Czech Health Research Council (AZV: NU21-08-00312). The work of the Genomics and Bioinformatics facility in IMG was supported by ELIXIR CZ research infrastructure (MEYS Grant No: LM2018131). VK was supported by The project National Institute for Cancer Research (Programme EXCELES, ID Project No. LX22NPO5102)—Funded by the European Union—Next Generation EU.

ACKNOWLEDGMENTS

We acknowledge Karel Harant and Pavel Talacko from Laboratory of Mass Spectrometry, Biocev, Charles University, Faculty of Science, where proteomic and mass spectrometric analysis had been done. We thank the Light Microscopy Core Facility, IMG CAS, Prague, the Czech Republic, for their support with the imaging presented herein, particularly to Ivan Novotny and Jan Valecka. We acknowledge Jan Kubovciak for RNA-seq, microarray and ChIP-seq analysis. We are also thankful to Michal Dibus and Hynek Wichterle for comments on the manuscript, Leslie F. Ryan for proofreading the manuscript. Illustrations were created with BioRender.com.

SUPPLEMENTARY MATERIAL

The Supplementary Material for this article can be found online at: https://www.frontiersin.org/articles/10.3389/fcell.2022.929288/full#supplementary-material

REFERENCES

Akçimen, F., Vural, A., Durmuş, H., Çakar, A., Houlden, H., Parman, Y. G., et al. (2019). A Novel Homozygous FBXO38 Variant Causes an Early-Onset Distal Hereditary Motor Neuronopathy Type IID. *J. Hum. Genet.* 64 (11), 1141–1144. doi:10.1038/s10038-019-0652-y

Al-Kandari, W., Koneni, R., Navalgund, V., Aleksandrova, A., Jambunathan, S., and Fontes, J. D. (2007). The Zinc Finger Proteins ZXDA and ZXDC Form a Complex that Binds CIITA and Regulates MHC II Gene Transcription. *J. Mol. Biol.* 369 (5), 1175–1187. doi:10.1016/j.jmb.2007.04.033

Aleksandrova, A., Galkin, O., Koneni, R., and Fontes, J. D. (2010). An N- and C-Terminal Truncated Isoform of Zinc Finger X-Linked Duplicated C Protein Represses MHC Class II Transcription. *Mol. Cell Biochem.* 337 (1-2), 1–7. doi:10.1007/s11010-009-0280-5

Athwal, R. K., Walkiewicz, M. P., Baek, S., Fu, S., Bui, M., Camps, J., et al. (2015). CENP-A Nucleosomes Localize to Transcription Factor Hotspots and Subtelomeric Sites in Human Cancer Cells. *Epigenetics Chromatin* 8, 2. doi:10.1186/1756-8935-8-2

Baek, K., Krist, D. T., Prabu, J. R., Hill, S., Klügel, M., Neumaier, L.-M., et al. (2020). NEDD8 Nucleates a Multivalent Cullin-RING-Ube2d Ubiquitin Ligation Assembly. *Nature* 578 (7795), 461–466. doi:10.1038/s41586-020-2000-y

Bodor, D. L., Mata, J. F., Sergeev, M., David, A. F., Salimian, K. J., Panchenko, T., et al. (2014). The Quantitative Architecture of Centromeric Chromatin. *Elife* 3, e02137. doi:10.7554/eLife.02137

Cai, L., Liu, L., Li, L., and Jia, L. (2020). SCFFBXO28-mediated Self-Ubiquitination of FBXO28 Promotes its Degradation. *Cell. Signal.* 65, 109440. doi:10.1016/j.cellsig.2019.109440

Cox, J., Hein, M. Y., Luber, C. A., Paron, I., Nagaraj, N., and Mann, M. (2014). Accurate Proteome-wide Label-free Quantification by Delayed Normalization and Maximal Peptide Ratio Extraction, Termed MaxLFQ. *Mol. Cell. Proteomics* 13 (9), 2513–2526. doi:10.1074/mcp.M113.031591

Cunningham, F., Achuthan, P., Akanni, W., Allen, J., Amode, M. R., Armean, I. M., et al. (2019). Ensembl 2019. *Nucleic Acids Res.* 47 (D1), D745–D751. doi:10.1093/nar/gky1113

Dibus, N., Zobalova, E., Monleon, M. A. M., Korinek, V., Filipp, D., Petrusova, J., et al. (2022). FBXO38 Ubiquitin Ligase Controls Sertoli Cell Maturation. *Front. Cell Dev. Biol.* 10. doi:10.3389/fcell.2022.914053

Dovat, S., Ronni, T., Russell, D., Ferrini, R., Cobb, B. S., and Smale, S. T. (2002). A Common Mechanism for Mitotic Inactivation of C2H2 Zinc Finger DNA-Binding Domains. *Genes Dev.* 16 (23), 2985–2990. doi:10.1101/gad.1040502

Drané, P., Ouararhni, K., Depaux, A., Shuaib, M., and Hamiche, A. (2010). The Death-Associated Protein DAXX Is a Novel Histone Chaperone Involved in the Replication-independent Deposition of H3.3. *Genes Dev.* 24 (12), 1253–1265. doi:10.1101/gad.566910

Earnshaw, W. C., and Rothfield, N. (1985). Identification of a Family of Human Centromere Proteins Using Autoimmune Sera from Patients with Scleroderma. *Chromosoma* 91 (3-4), 313–321. doi:10.1007/BF00328227

Everett, R. D., Earnshaw, W. C., Findlay, J., and Lomonte, P. (1999). Specific Destruction of Kinetochore Protein CENP-C and Disruption of Cell Division by Herpes Simplex Virus Immediate-Early Protein Vmw110. *EMBO J.* 18 (6), 1526–1538. doi:10.1093/emboj/18.6.1526

Ewels, P., Hammarén, R., Peltzer, A., Moreno, D., Garcia, M., and Wang, C. (2019). *Nf-core/rnaseq: Nf-core/rnaseq Version 1.4.2 (Version 1.4.2)*. Zenodo. doi:10.5281/zenodo.1400710

Fachinetti, D., Han, J. S., McMahon, M. A., Ly, P., Abdullah, A., Wong, A. J., et al. (2015). DNA Sequence-specific Binding of CENP-B Enhances the Fidelity of Human Centromere Function. *Dev. Cell* 33 (3), 314–327. doi:10.1016/j.devcel.2015.03.020

Fowler, K. J., Hudson, D. F., Salamonsen, L. A., Edmondson, S. R., Earle, E., Sibson, M. C., et al. (2000). Uterine Dysfunction and Genetic Modifiers in Centromere Protein B-Deficient Mice. *Genome Res.* 10 (1), 30–41.

Fowler, K. J., Wong, L. H., Griffiths, B. K., Sibson, M. C., Reed, S., and Choo, K. H. A. (2004). Centromere Protein B-Null Mice Display Decreasing Reproductive Performance through Successive Generations of Breeding Due to Diminishing Endometrial Glands. *Reproduction* 127 (3), 367–377. doi:10.1530/rep.1.00102

Fujita, R., Otake, K., Arimura, Y., Horikoshi, N., Miya, Y., Shiga, T., et al. (2015). Stable Complex Formation of CENP-B with the CENP-A Nucleosome. *Nucleic Acids Res.* 43 (10), 4909–4922. doi:10.1093/nar/gkv405

Gamba, R., and Fachinetti, D. (2020). From Evolution to Function: Two Sides of the Same CENP-B Coin? *Exp. Cell Res.* 390 (2), 111959. doi:10.1016/j.yexcr.2020.111959

Georges, A., Coyaud, E., Marcon, E., Greenblatt, J., Raught, B., and Frappier, L. (2019). USP7 Regulates Cytokinesis through FBXO38 and KIF20B. *Sci. Rep.* 9 (1), 2724. doi:10.1038/s41598-019-39368-y

Guardavaccaro, D., Frescas, D., Dorrello, N. V., Peschiaroli, A., Multani, A. S., Cardozo, T., et al. (2008). Control of Chromosome Stability by the β-TrCP-REST-Mad2 axis. *Nature* 452 (7185), 365–369. doi:10.1038/nature06641

Hebert, A. S., Richards, A. L., Bailey, D. J., Ulbrich, A., Coughlin, E. E., Westphall, M. S., et al. (2014). The One Hour Yeast Proteome. *Mol. Cell. Proteomics* 13 (1), 339–347. doi:10.1074/mcp.M113.034769

Hédouin, S., Grillo, G., Ivkovic, I., Velasco, G., and Francastel, C. (2017). CENP-A Chromatin Disassembly in Stressed and Senescent Murine Cells. *Sci. Rep.* 7, 42520. doi:10.1038/srep42520

Hemmerich, P., Stoyan, T., Wieland, G., Koch, M., Lechner, J., and Diekmann, S. (2000). Interaction of Yeast Kinetochore Proteins with Centromere-Protein/transcription Factor Cbf1. *Proc. Natl. Acad. Sci. U.S.A.* 97 (23), 12583–12588. doi:10.1073/pnas.97.23.12583

Hoffmann, S., Dumont, M., Barra, V., Ly, P., Nechemia-Arbely, Y., McMahon, M. A., et al. (2016). CENP-A Is Dispensable for Mitotic Centromere Function after Initial Centromere/Kinetochore Assembly. *Cell Rep.* 17 (9), 2394–2404. doi:10.1016/j.celrep.2016.10.084

Horn, M., Geisen, C., Cermak, L., Becker, B., Nakamura, S., Klein, C., et al. (2014). DRE-1/FBXO11-dependent Degradation of BLMP-1/BLIMP-1 Governs C Elegans Developmental Timing and Maturation. *Dev. Cell* 28 (6), 697–710. doi:10.1016/j.devcel.2014.01.028

Hou, H., Kyriacou, E., Thadani, R., Klutstein, M., Chapman, J. H., and Cooper, J. P. (2021). Centromeres Are Dismantled by Foundational Meiotic Proteins Spo11 and Rec8. *Nature* 591 (7851), 671–676. doi:10.1038/s41586-021-03279-8

Hudson, D. F., Fowler, K. J., Earle, E., Saffery, R., Kalitsis, P., Trowell, H., et al. (1998). Centromere Protein B Null Mice Are Mitotically and Meiotically Normal but Have Lower Body and Testis Weights. *J. Cell Biol.* 141 (2), 309–319. doi:10.1083/jcb.141.2.309

Jansen, L. E. T., Black, B. E., Foltz, D. R., and Cleveland, D. W. (2007). Propagation of Centromeric Chromatin Requires Exit from Mitosis. *J. Cell Biol.* 176 (6), 795–805. doi:10.1083/jcb.200701066

Jeffery, D., Gatto, A., Podsypanina, K., Renaud-Pageot, C., Ponce Landete, R., Bonneville, L., et al. (2021). CENP-A Overexpression Promotes Distinct Fates in Human Cells, Depending on P53 Status. *Commun. Biol.* 4 (1), 417. doi:10.1038/s42003-021-01941-5

Jin, J., Cardozo, T., Lovering, R. C., Elledge, S. J., Pagano, M., and Harper, J. W. (2004). Systematic Analysis and Nomenclature of Mammalian F-Box Proteins. *Genes Dev.* 18 (21), 2573–2580. doi:10.1101/gad.1255304

Jumper, J., Evans, R., Pritzel, A., Green, T., Figurnov, M., Ronneberger, O., et al. (2021). Highly Accurate Protein Structure Prediction with AlphaFold. *Nature* 596 (7873), 583–589. doi:10.1038/s41586-021-03819-2

Kapoor, M., Montes de Oca Luna, R., Liu, G., Lozano, G., Cummings, C., Mancini, M., et al. (1998). The cenpB Gene Is Not Essential in Mice. *Chromosoma* 107 (8), 570–576. doi:10.1007/s004120050343

Kent, W. J., Sugnet, C. W., Furey, T. S., Roskin, K. M., Pringle, T. H., Zahler, A. M., et al. (2002). The Human Genome Browser at UCSC. *Genome Res.* 12 (6), 996–1006. doi:10.1101/gr.229102

Kim, D., Langmead, B., and Salzberg, S. L. (2015). HISAT: a Fast Spliced Aligner with Low Memory Requirements. *Nat. Methods* 12 (4), 357–360. doi:10.1038/nmeth.3317

Kitagawa, K., Skowyra, D., Elledge, S. J., Harper, J. W., and Hieter, P. (1999). SGT1 Encodes an Essential Component of the Yeast Kinetochore Assembly Pathway and a Novel Subunit of the SCF Ubiquitin Ligase Complex. *Mol. Cell* 4 (1), 21–33. doi:10.1016/s1097-2765(00)80184-7

Lechner, J., and Carbon, J. (1991). A 240 Kd Multisubunit Protein Complex, CBF3, Is a Major Component of the Budding Yeast Centromere. *Cell* 64 (4), 717–725. doi:10.1016/0092-8674(91)90501-o

Liao, Y., Smyth, G. K., and Shi, W. (2014). featureCounts: an Efficient General Purpose Program for Assigning Sequence Reads to Genomic Features. *Bioinformatics* 30 (7), 923–930. doi:10.1093/bioinformatics/btt656

Lidak, T., Baloghova, N., Korinek, V., Sedlacek, R., Balounova, J., Kasparek, P., et al. (2021). CRL4-DCAF12 Ubiquitin Ligase Controls MOV10 RNA Helicase during Spermatogenesis and T Cell Activation. *Ijms* 22 (10), 5394. doi:10.3390/ijms22105394

Love, M. I., Huber, W., and Anders, S. (2014). Moderated Estimation of Fold Change and Dispersion for RNA-Seq Data with DESeq2. *Genome Biol.* 15 (12), 550. doi:10.1186/s13059-014-0550-8

Martin, E. C., Sukarta, O. C. A., Spiridon, L., Grigore, L. G., Constantinescu, V., Tacutu, R., et al. (2020). LRRpredictor-A New LRR Motif Detection Method for Irregular Motifs of Plant NLR Proteins Using an Ensemble of Classifiers. *Genes* 11 (3), 286. doi:10.3390/genes11030286

Masuda, T., Tomita, M., and Ishihama, Y. (2008). Phase Transfer Surfactant-Aided Trypsin Digestion for Membrane Proteome Analysis. *J. Proteome Res.* 7 (2), 731–740. doi:10.1021/pr700658q

Masumoto, H., Masukata, H., Muro, Y., Nozaki, N., and Okazaki, T. (1989). A Human Centromere Antigen (CENP-B) Interacts with a Short Specific Sequence in Alphoid DNA, a Human Centromeric Satellite. *J. Cell Biol.* 109 (5), 1963–1973. doi:10.1083/jcb.109.5.1963

McNulty, S. M., and Sullivan, B. A. (2018). Alpha Satellite DNA Biology: Finding Function in the Recesses of the Genome. *Chromosome Res.* 26 (3), 115–138. doi:10.1007/s10577-018-9582-3

Meng, X., Liu, X., Guo, X., Jiang, S., Chen, T., Hu, Z., et al. (2018). FBXO38 Mediates PD-1 Ubiquitination and Regulates Anti-tumour Immunity of T Cells. *Nature* 564 (7734), 130–135. doi:10.1038/s41586-018-0756-0

Morimoto, Y., Ono, S., Imamura, A., Okazaki, Y., Kinoshita, A., Mishima, H., et al. (2017). Deep Sequencing Reveals Variations in Somatic Cell Mosaic Mutations between Monozygotic Twins with Discordant Psychiatric Disease. *Hum. Genome Var.* 4, 17032. doi:10.1038/hgv.2017.32

Morozov, V. M., Giovinazzi, S., and Ishov, A. M. (2017). CENP-B Protects Centromere Chromatin Integrity by Facilitating Histone Deposition via the H3.3-specific Chaperone Daxx. *Epigenetics Chromatin* 10 (1), 63. doi:10.1186/s13072-017-0164-y

Muro, Y., Masumoto, H., Yoda, K., Nozaki, N., Ohashi, M., and Okazaki, T. (1992). Centromere Protein B Assembles Human Centromeric Alpha-Satellite DNA at the 17-bp Sequence, CENP-B Box. *J. Cell Biol.* 116 (3), 585–596. doi:10.1083/jcb.116.3.585

Ohzeki, J.-i., Nakano, M., Okada, T., and Masumoto, H. (2002). CENP-B Box Is Required for De Novo Centromere Chromatin Assembly on Human Alphoid DNA. *J. Cell Biol.* 159 (5), 765–775. doi:10.1083/jcb.200207112

Okada, T., Ohzeki, J.-i., Nakano, M., Yoda, K., Brinkley, W. R., Larionov, V., et al. (2007). CENP-B Controls Centromere Formation Depending on the Chromatin Context. *Cell* 131 (7), 1287–1300. doi:10.1016/j.cell.2007.10.045

Otake, K., Ohzeki, J.-i., Shono, N., Kugou, K., Okazaki, K., Nagase, T., et al. (2020). CENP-B Creates Alternative Epigenetic Chromatin States Permissive for CENP-A or Heterochromatin Assembly. *J. Cell Sci.* 133 (15). doi:10.1242/jcs.243303

Palmer, D., O'Day, K., Wener, M., Andrews, B., and Margolis, R. (1987). A 17-kD Centromere Protein (CENP-A) Copurifies with Nucleosome Core Particles and with Histones. *J. Cell Biol.* 104 (4), 805–815. doi:10.1083/jcb.104.4.805

Perez-Castro, A. V., Shamanski, F. L., Meneses, J. J., Lovato, T. L., Vogel, K. G., Moyzis, R. K., et al. (1998). Centromeric Protein B Null Mice Are Viable with No Apparent Abnormalities. *Dev. Biol.* 201 (2), 135–143. doi:10.1006/dbio.1998.9005

Rappsilber, J., Mann, M., and Ishihama, Y. (2007). Protocol for Micro-purification, Enrichment, Pre-fractionation and Storage of Peptides for Proteomics Using StageTips. *Nat. Protoc.* 2 (8), 1896–1906. doi:10.1038/nprot.2007.261

Rizkallah, R., Alexander, K. E., and Hurt, M. M. (2011). Global Mitotic Phosphorylation of C2H2zinc Finger Protein Linker Peptides. *Cell Cycle* 10 (19), 3327–3336. doi:10.4161/cc.10.19.17619

Sart, D. d., Cancilla, M. R., Earle, E., Mao, J.-i., Saffery, R., Tainton, K. M., et al. (1997). A Functional Neo-Centromere Formed through Activation of a Latent Human Centromere and Consisting of Non-alpha-satellite DNA. *Nat. Genet.* 16 (2), 144–153. doi:10.1038/ng0697-144

Scott, K. C., and Sullivan, B. A. (2014). Neocentromeres: a Place for Everything and Everything in its Place. *Trends Genet.* 30 (2), 66–74. doi:10.1016/j.tig.2013.11.003

Senft, D., Qi, J., and Ronai, Z. e. A. (2018). Ubiquitin Ligases in Oncogenic Transformation and Cancer Therapy. *Nat. Rev. Cancer* 18 (2), 69–88. doi:10.1038/nrc.2017.105

Skaar, J. R., Pagan, J. K., and Pagano, M. (2013). Mechanisms and Function of Substrate Recruitment by F-Box Proteins. *Nat. Rev. Mol. Cell Biol.* 14 (6), 369–381. doi:10.1038/nrm3582

Skaar, J. R., Pagan, J. K., and Pagano, M. (2014). SCF Ubiquitin Ligase-Targeted Therapies. *Nat. Rev. Drug Discov.* 13 (12), 889–903. doi:10.1038/nrd4432

Smaldone, S., Laub, F., Else, C., Dragomir, C., and Ramirez, F. (2004). Identification of MoKA, a Novel F-Box Protein that Modulates Kruppel-like Transcription Factor 7 Activity. *Mol. Cell Biol.* 24 (3), 1058–1069. doi:10.1128/mcb.24.3.1058-1069.2004

Sumner, C. J., d'Ydewalle, C., Wooley, J., Fawcett, K. A., Hernandez, D., Gardiner, A. R., et al. (2013). A Dominant Mutation in FBXO38 Causes Distal Spinal Muscular Atrophy with Calf Predominance. *Am. J. Hum. Genet.* 93 (5), 976–983. doi:10.1016/j.ajhg.2013.10.006

Thomas-Chollier, M., Darbo, E., Herrmann, C., Defrance, M., Thieffry, D., and van Helden, J. (2012). A Complete Workflow for the Analysis of Full-Size ChIP-Seq (And Similar) Data Sets Using Peak-Motifs. *Nat. Protoc.* 7 (8), 1551–1568. doi:10.1038/nprot.2012.088

Tomonaga, T., Matsushita, K., Yamaguchi, S., Oohashi, T., Shimada, H., Ochiai, T., et al. (2003). Overexpression and Mistargeting of Centromere Protein-A in Human Primary Colorectal Cancer. *Cancer Res.* 63 (13), 3511–3516.

Tyanova, S., Temu, T., Sinitcyn, P., Carlson, A., Hein, M. Y., Geiger, T., et al. (2016). The Perseus Computational Platform for Comprehensive Analysis of (Prote) omics Data. *Nat. Methods* 13 (9), 731–740. doi:10.1038/nmeth.3901

Vasudevan, A., Schukken, K. M., Sausville, E. L., Girish, V., Adebambo, O. A., and Sheltzer, J. M. (2021). Aneuploidy as a Promoter and Suppressor of Malignant Growth. *Nat. Rev. Cancer* 21 (2), 89–103. doi:10.1038/s41568-020-00321-1

Wang, D., Horton, J. R., Zheng, Y., Blumenthal, R. M., Zhang, X., and Cheng, X. (2018). Role for First Zinc Finger of WT1 in DNA Sequence Specificity: Denys-Drash Syndrome-Associated WT1 Mutant in ZF1 Enhances Affinity for a Subset of WT1 Binding Sites. *Nucleic Acids Res.* 46 (8), 3864–3877. doi:10.1093/nar/gkx1274

Wang, G. Z., and Goff, S. P. (2015). Regulation of Yin Yang 1 by Tyrosine Phosphorylation. *J. Biol. Chem.* 290 (36), 21890–21900. doi:10.1074/jbc.M115.660621

Waterhouse, A., Bertoni, M., Bienert, S., Studer, G., Tauriello, G., Gumienny, R., et al. (2018). SWISS-MODEL: Homology Modelling of Protein Structures and Complexes. *Nucleic Acids Res.* 46 (W1), W296–W303. doi:10.1093/nar/gky427

Yan, K., Zhang, Z., Yang, J., McLaughlin, S. H., and Barford, D. (2018). Architecture of the CBF3-Centromere Complex of the Budding Yeast Kinetochore. *Nat. Struct. Mol. Biol.* 25 (12), 1103–1110. doi:10.1038/s41594-018-0154-1

Young, M. D., Wakefield, M. J., Smyth, G. K., and Oshlack, A. (2010). Gene Ontology Analysis for RNA-Seq: Accounting for Selection Bias. *Genome Biol.* 11 (2), R14. doi:10.1186/gb-2010-11-2-r14

Yu, Z.-K., Gervais, J. L. M., and Zhang, H. (1998). Human CUL-1 Associates with the SKP1/SKP2 Complex and Regulates P21 CIP1/WAF1 and Cyclin D Proteins. *Proc. Natl. Acad. Sci. U.S.A.* 95 (19), 11324–11329. doi:10.1073/pnas.95.19.11324

Zeitlin, S. G., Baker, N. M., Chapados, B. R., Soutoglou, E., Wang, J. Y. J., Berns, M. W., et al. (2009). Double-strand DNA Breaks Recruit the Centromeric Histone CENP-A. *Proc. Natl. Acad. Sci. U.S.A.* 106 (37), 15762–15767. doi:10.1073/pnas.0908233106

Zhang, M., Botër, M., Li, K., Kadota, Y., Panaretou, B., Prodromou, C., et al. (2008a). Structural and Functional Coupling of Hsp90- and Sgt1-Centred Multi-Protein Complexes. *EMBO J.* 27 (20), 2789–2798. doi:10.1038/emboj.2008.190

Zhang, W., Mellone, B. G., and Karpen, G. H. (2007). A Specialized Nucleosome Has a "point" to Make. *Cell* 129 (6), 1047–1049. doi:10.1016/j.cell.2007.05.054

Zhang, Y., Liu, T., Meyer, C. A., Eeckhoute, J., Johnson, D. S., Bernstein, B. E., et al. (2008b). Model-based Analysis of ChIP-Seq (MACS). *Genome Biol.* 9 (9), R137. doi:10.1186/gb-2008-9-9-r137

Conflict of Interest: The authors declare that the research was conducted in the absence of any commercial or financial relationships that could be construed as a potential conflict of interest.

Publisher's Note: All claims expressed in this article are solely those of the authors and do not necessarily represent those of their affiliated organizations, or those of the publisher, the editors and the reviewers. Any product that may be evaluated in this article, or claim that may be made by its manufacturer, is not guaranteed or endorsed by the publisher.

Copyright © 2022 Dibus, Korinek and Cermak. This is an open-access article distributed under the terms of the Creative Commons Attribution License (CC BY). The use, distribution or reproduction in other forums is permitted, provided the original author(s) and the copyright owner(s) are credited and that the original publication in this journal is cited, in accordance with accepted academic practice. No use, distribution or reproduction is permitted which does not comply with these terms.

frontiers

Supplementary Material

FBXO38 Ubiquitin Ligase Controls Centromere Integrity via ZXDA/B Stability

Nikol Dibus[1,2], Vladimir Korinek[3] and Lukas Cermak[1*]

* Correspondence:
Lukas Cermak, Ph.D.
lukas.cermak@img.cas.cz

Contents

Supplementary Figures 2
Figure S1. FBXO38 interacts with ZXDA/B in the nucleus 3
Figure S3. FBXO38 associates with ZXDA via zinc-finger linker motif 6
Figure S4. ZXDA/B do not act as transcriptional factors 9
Figure S6. FBXO38 controls centromeric signature via ZXDA/B stability 11
Supplementary table 12
Dataset S1. (separate file) MACS2-called peaks in ZXDA/B ChIP-seq analysis 12
List of reagents 13
Chemicals 13
Antibodies 14
Vectors 15
siRNAs 16
Oligos 17

Supplementary Figures

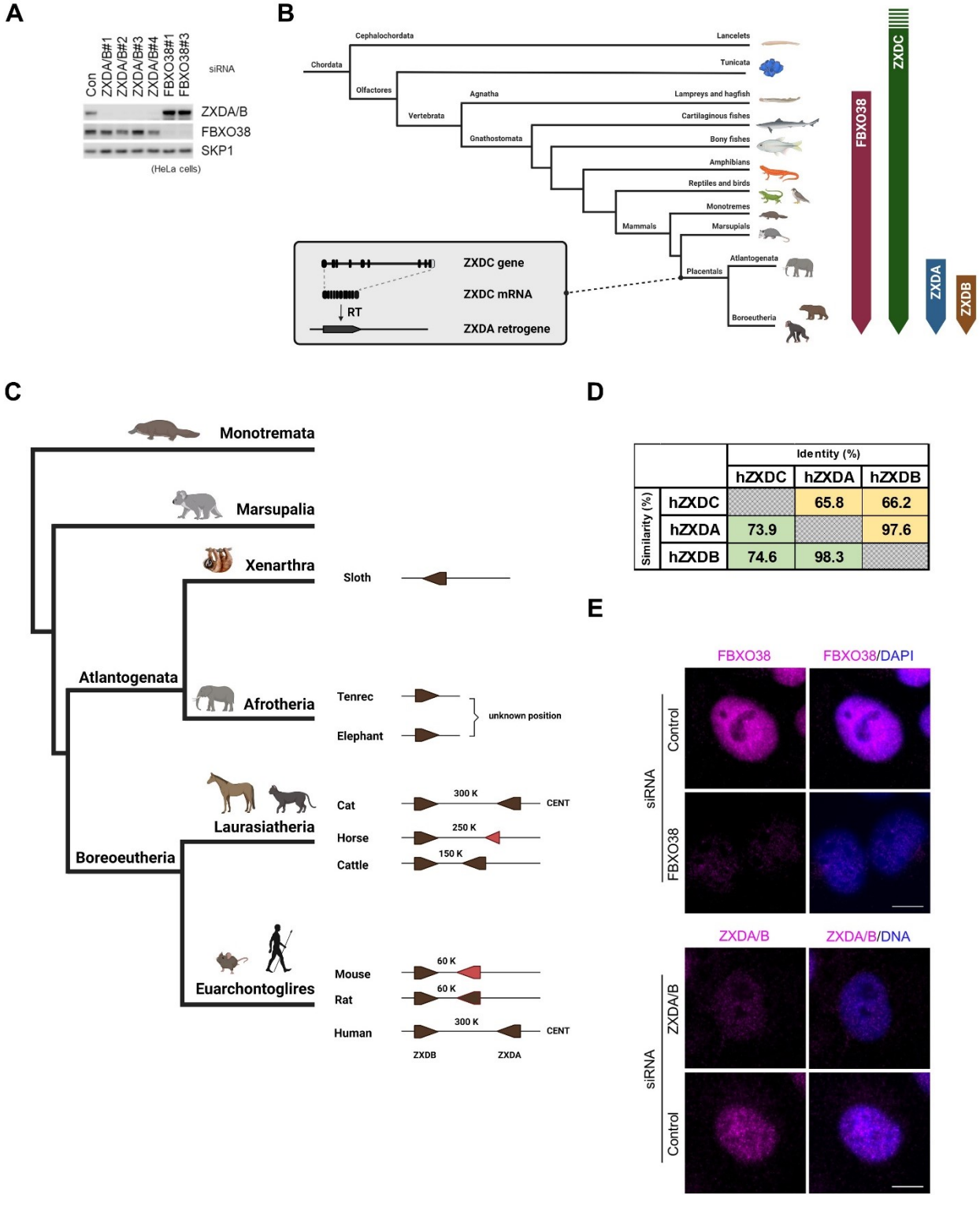


Figure S1. FBXO38 interacts with ZXDA/B in the nucleus

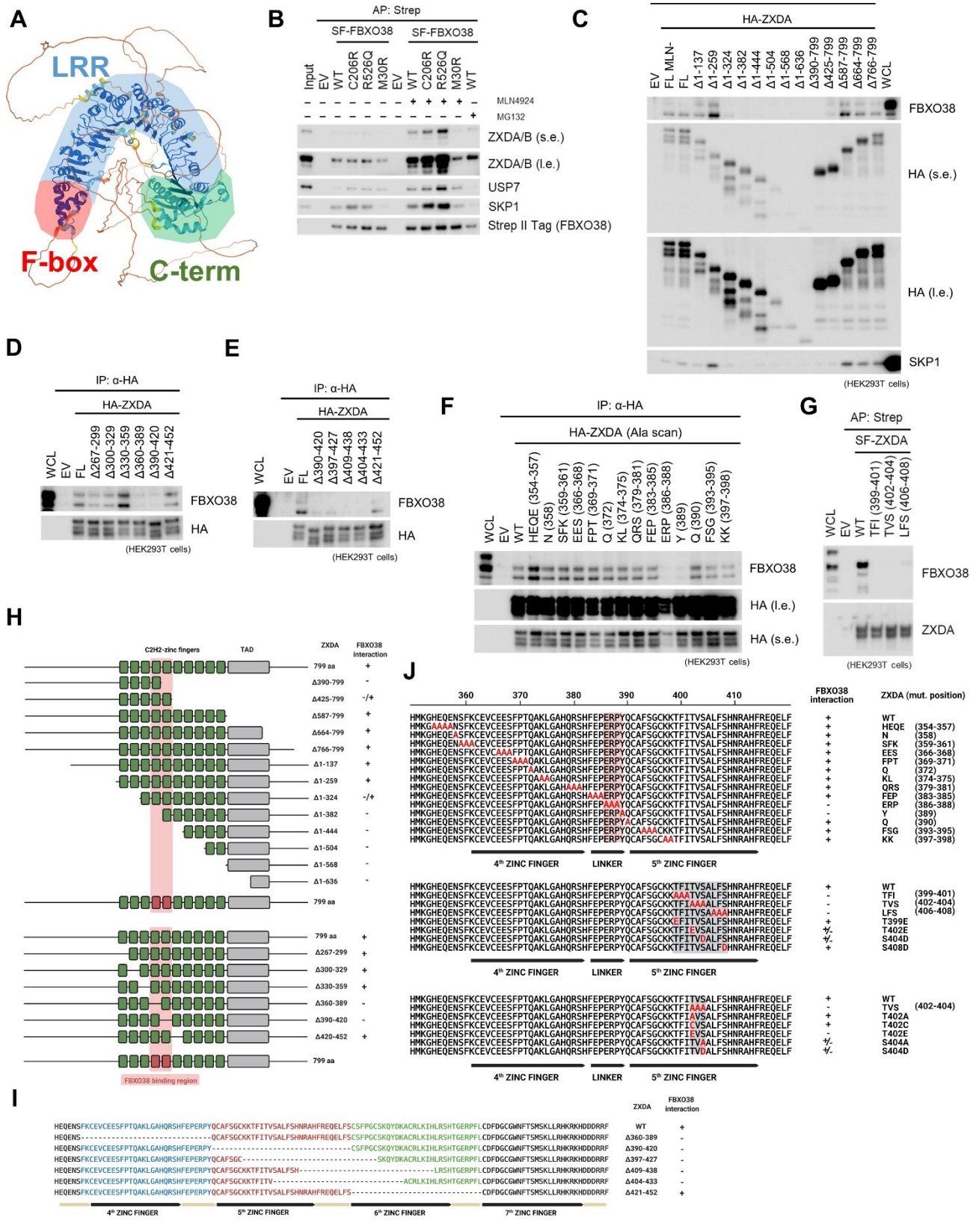
(A) HeLa cells were transfected with different siRNAs targeting ZXDA/B or FBXO38, and whole-cell lysates were immunoblotted as indicated. Non-targeting siRNA (Con) was used as a negative control.

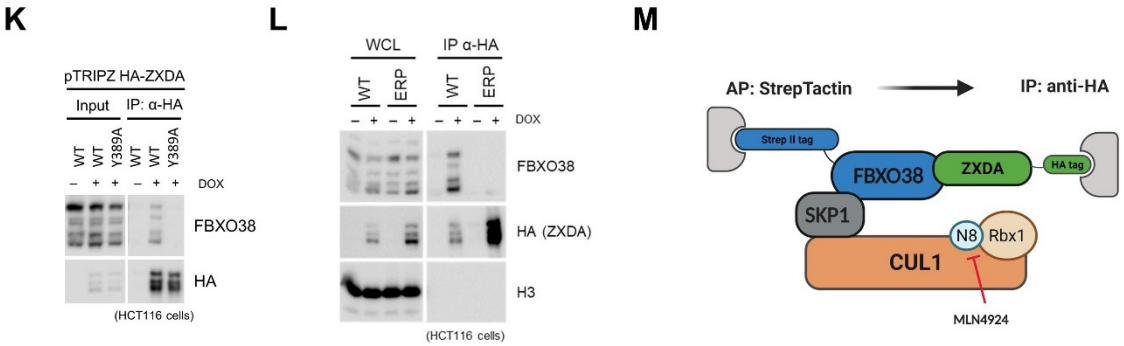
(B) A simplified evolutionary scheme illustrating the emergence of *FBXO38, ZXDA, ZXDB, and ZXDC* genes in animals. *Zxdc* gene appeared in early animals (UniProt: Porifera - A0A1X7UJN7; Cnidaria - A7RPS8). *Zxda* and *Zxdb* genes are retrogenes that appeared in placental animals, and the *Fbxo38* gene is vertebrate-specific.

(C) A simplified evolutionary scheme illustrating the emergence of *ZXDA* and *ZXDB* genes in mammals. *ZXDA* appeared as an X-chromosome located retrogene in placental animals. In Boreoeutheria mammals, *ZXDA* duplicated and *ZXDB* appeared in an inverted position on chromosome X. In some mammals (e.g., mouse or horse), original *ZXDA* contains nonsense mutation resulting in predicted shorter protein length (in red). CENT; centromere position.

(D) Table showing the similarity and identity of human ZXD proteins calculated by MegAlign Pro.

(E) U2-OS cells were transfected with siRNA targeting FBXO38 (upper panel) or ZXDA/B (lower panel), fixed and incubated with an anti-FBXO38 (upper panel) or anti-ZXDA/B (lower panel) antibody. DNA was stained with DAPI. Scale bar, 10 μm.

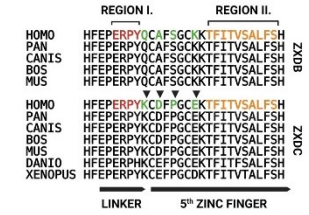

A
LRR
F-box
C-term
B
AP: Strep
SF-FBXO38
SF-FBXO38
Input
EV
WT
C206R
R526Q
M30R
EV
WT
C206R
R526Q
M30R
WT
MLN4924
MG132
ZXDA/B (s.e.)
ZXDA/B (l.e.)
USP7
SKP1
Strep II Tag (FBXO38)
C
HA-ZXDA
EV
FL MLN-
FL
Δ1-137
Δ1-259
Δ1-324
Δ1-382
Δ1-444
Δ1-504
Δ1-568
Δ1-636
Δ390-799
Δ425-799
Δ587-799
Δ664-799
Δ766-799
WCL
FBXO38
HA (s.e.)
HA (l.e.)
SKP1
(HEK293T cells)
D
IP: α-HA
HA-ZXDA
WCL
EV
FL
Δ267-299
Δ300-329
Δ330-359
Δ360-389
Δ390-420
Δ421-452
FBXO38
HA
(HEK293T cells)
E
IP: α-HA
HA-ZXDA
WCL
EV
FL
Δ390-420
Δ397-427
Δ409-438
Δ404-433
Δ421-452
FBXO38
HA
(HEK293T cells)
F
IP: α-HA
HA-ZXDA (Ala scan)
WCL
EV
WT
HEQE (354-357)
N (358)
SFK (359-361)
EES (366-368)
FPT (369-371)
Q (372)
KL (374-375)
QRS (379-381)
FEP (383-385)
ERP (386-388)
Y (389)
Q (390)
FSG (393-395)
KK (397-398)
FBXO38
HA (l.e.)
HA (s.e.)
(HEK293T cells)
G
AP: Strep
SF-ZXDA
WCL
EV
WT
TFI (399-401)
TVS (402-404)
LFS (406-408)
FBXO38
ZXDA
(HEK293T cells)
H
C2H2-zinc fingers
TAD
ZXDA
FBXO38 interaction
799 aa +
Δ390-799 -
Δ425-799 -/+
Δ587-799 +
Δ664-799 +
Δ766-799 +
Δ1-137 +
Δ1-259 +
Δ1-324 -/+
Δ1-382 -
Δ1-444 -
Δ1-504 -
Δ1-568 -
Δ1-636 -
799 aa
799 aa +
Δ267-299 +
Δ300-329 +
Δ330-359 +
Δ360-389 -
Δ390-420 -
Δ420-452 +
799 aa
FBXO38 binding region
I
ZXDA
FBXO38 interaction
WT +
Δ360-389 -
Δ390-420 -
Δ397-427 -
Δ409-438 -
Δ404-433 -
Δ421-452 +
4th ZINC FINGER
5th ZINC FINGER
6th ZINC FINGER
7th ZINC FINGER
J
360 370 380 390 400 410
FBXO38 interaction
ZXDA (mut. position)
WT
HEQE (354-357)
N (358)
SFK (359-361)
EES (366-368)
FPT (369-371)
Q (372)
KL (374-375)
QRS (379-381)
FEP (383-385)
ERP (386-388)
Y (389)
Q (390)
FSG (393-395)
KK (397-398)
4th ZINC FINGER
LINKER
5th ZINC FINGER
WT
TFI (399-401)
TVS (402-404)
LFS (406-408)
T399E
T402E
S404D
S408D
WT
TVS (402-404)
T402A
T402C
T402E
S404A
S404D



N

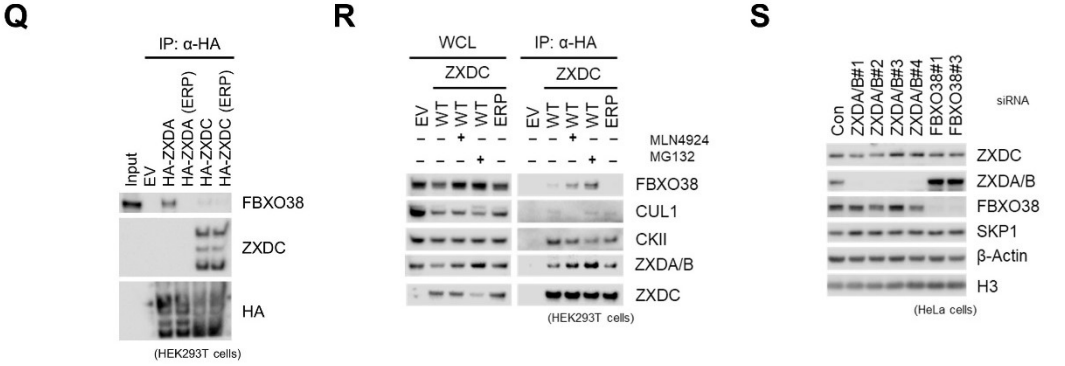
```
CEVCEESFPTQAKLGAHQRSHFEPERPYQCAFSGCKKTFITVSALFSHNRAHFREQELFSCSFPGCSK    hZXDA
CEVCEESFPTQAK        SHFEPERPYQCAFSGCK TFITVSALFSH      EQELFSCSFPGCSK    unmodified
                     SHFEPERPYQCAFSGCK TFITVSALFSHNR                      peptides
                                       TFITVSALFSHNR
```

	coverage (%)	peptides (N)	modified (N)	type/location	mod:unmod
ZXDA	34	33	2	pS714	2:2
FBXO38	70	91	0		
CUL1	45	56	0		
SKP1	52	12	0		



P

Protein ID	Description	Position	Sequence
79364	ZXDC, ZXDL; ZXD family zinc finger C	290..304	HFEPERPYKCDFPGC
7789	ZXDA, ZNF896; zinc finger X-linked duplicated A	382..396	HFEPERPYQCAFSGC
158586	ZXDB, ZNF905; zinc finger X-linked duplicated B	386..400	HFEPERPYQCAFSGC



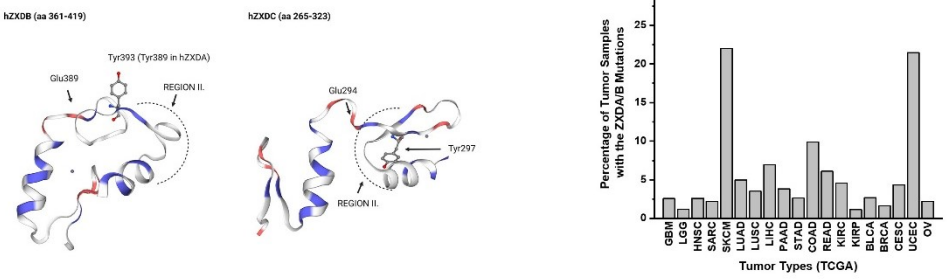


Figure S3. FBXO38 associates with ZXDA via zinc-finger linker motif

(A) Prediction of FBXO38 protein structure using AlphaFold (Jumper, Evans et al., 2021). The N-terminal part contains the F-box motif and N-terminally located leucine-rich repeats (LRRs). The C-terminal part consists of the region containing the second part of LRRs and the C-terminal domain. Mentioned parts are predicted with high accuracy (based on available AlphaFold data).

(B) HEK293T cells were transfected with StrepII-FLAG-tagged wild-type (WT) FBXO38 (SF-FBXO38 WT) or its mutated variants found in patients with motor neuronopathy (C206R; R526Q), or in twins with gender dysphoria (M30R). Where indicated, cells were treated with MLN4924 or MG-132 inhibitors for 6 hours prior to collecting. Whole-cell lysates (WCL) were subjected to affinity purification (AP) using Strep-Tactin resin and immunoblotted as indicated. Empty vector (EV) was used as a negative control; l.e. stands for long exposure, s.e. for short exposure.

(C) – (E) HEK293T cells were transfected with HA-tagged full-length (FL) ZXDA or its deletion mutants. Cells were treated with the MLN4924 inhibitor 6 hours prior to collecting. Whole-cell lysates (WCL) were subjected to immunoprecipitation (IP) using anti-HA beads. Empty vector (EV) was used as a negative control; l.e. long exposure, s.e. short exposure.

(F) HEK293T cells were transfected with HA-tagged full-length (FL) ZXDA or its mutated variants. Cells were treated, and whole-cell lysates (WCL) were subjected to immunoprecipitation as in (C). Empty vector (EV) was used as a negative control. l.e. long exposure, s.e. short exposure.

(G) HEK293T cells were transfected with SF-tagged wild-type (WT) ZXDA or its constructs with mutations of indicated amino acids. Cells were treated as in (C). Whole-cell lysates (WCL) were subjected to affinity purification (AP) using Strep-Tactin resin and immunoblotted as indicated. Empty vector (EV) was used as a negative control.

(H) Schematic representation of full-length ZXDA (1-799 aa) or its N- and C-terminally truncated variants (upper panel) or zinc finger deletion mutants (lower panel). Zinc fingers are depicted as green boxes, zinc fingers essential for interaction with FBXO38 are red-tinted. The middle panel indicates deleted amino acid positions. FBXO38-interacting variants of ZXDA are indicated by the symbol (+), (+/-) denotes reduced binding, and (-) denotes a lack of binding. TAD; transcriptional activation domain.

(I) Detail of the sequence surrounding the 4th-7th zinc fingers of ZXDA protein and their deletions used in the study (S3E). Deleted zinc fingers and the following linkers are color-coded. The lower line shows the position of the zinc fingers (black) and linkers (ocher). The middle panel indicates deleted amino acid positions. Mutants interacting with FBXO38 are designated with (+) in the right part of the panel.

(J) Schematic representation of ZXDA mutants. ZXDA mutants found to interact with FBXO38 are indicated by the symbol (+). (+/-) denotes reduced binding, and (-) denotes a lack of binding. Positions and amino acids mutated are depicted in the right panel.

(K) – (L) HCT116 cells with inducible expression of HA-tagged wild-type (WT) ZXDA or its mutants were treated with doxycycline where indicated. Whole-cell lysates (WCL) were subjected to immunoprecipitation (IP) using anti-HA beads.

(M) Schematic representation of the tandem affinity purification strategy and proteomic analysis of ZXDA modifications encompassing the FBXO38-interacting region. SF-tagged FBXO38 and HA-tagged ZXDA were co-expressed in HEK293T cells. The cells were treated with the MLN4924 inhibitor 6 hours prior to collecting and subjected to isotonic lysis and affinity purification (AP) using Strep-Tactin resin followed by elution with desthiobiotin and subsequent immunoprecipitation (IP) using anti-HA magnetic beads. The composition and modifications of

purified peptides were analyzed using Liquid Chromatography with Tandem Mass-Spectrometry (LC-MS/MS).

(N) Identified peptides (from S3M) covering the FBXO38-interacting ZXDA region (upper panel). The table (lower panel) summarizes the LC-MS/MS analysis results showing the coverage of sequences, the total number of identified peptides, and their modifications. The rightmost columns indicate the identified phosphorylation of ZXDA in position S714 and the ratio between modified and unmodified peptides identified in tandem purification of FBXO38-ZXDA complex.

(O) Alignment of ZXDA/B and ZXDC sequences encompassing the region of the linker and the 5th zinc finger. The regions indicated above represent essential motifs involved in ZXDA/B interaction with FBXO38 – zinc finger linker (Region I.) and amino acids located in 5th zinc finger (Region II.). Arrowheads point to amino acids that differ between ZXDA/B and ZXDC. Amino acids encompassing this region are depicted below, with a zinc-finger linker necessary for FBXO38-interaction highlighted in red (degron). Mutations of amino acids marked in yellow had a negative effect on FBXO38-interaction. The green-labeled amino acids differ between ZXDA/B and ZXDC.

(P) Analysis of degenerate motif H-X(3)-[ED]-[RK]-P-[YF]-x-C-x(3,5)-C occurrence using MOTIF Search (https://www.genome.jp/tools/motif/MOTIF2.html) and human Kyoto Encyclopedia of Genes and Genomes database (KEGG). Specific sequences and their positions are indicated on the right side of the table.

(Q) HEK293T cells were transfected with HA-tagged ZXDA or ZXDC or their ERP mutants. Cells were treated with the MLN4924 inhibitor 6 hours prior to collecting. Whole-cell lysates (WCL) were subjected to immunoprecipitation (IP) using anti-HA beads. Empty vector (EV) was used as a negative control.

(R) HEK293T cells were transfected with HA-tagged ZXDC or its ERP mutant. Where indicated, cells were treated with either MG-132 or the MLN4924 inhibitor 6 hours prior to collecting. Whole-cell lysates (WCL) were subjected to immunoprecipitation (IP) using anti-HA beads. Empty vector (EV) was used as a negative control.

(S) HeLa cells were transfected with different siRNAs targeting ZXDB or FBXO38, and whole-cell lysates were immunoblotted as indicated. Non-targeting siRNA (Con) was used as a negative control. The blot is the same used for the siRNA efficiency test in Figure (S1E).

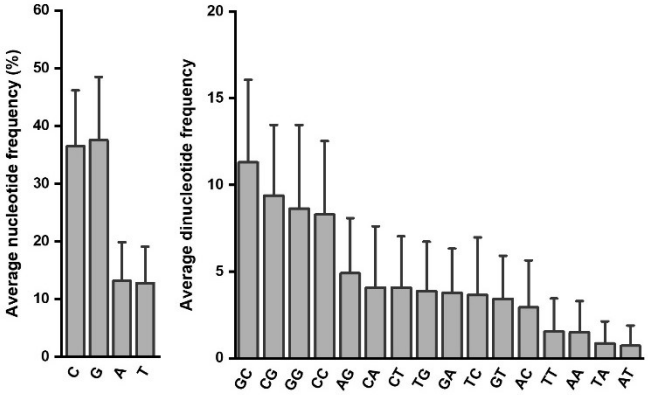
(T) The protein structure prediction of hZXDB and hZXDC 4th and 5th zinc fingers. SWISS MODEL-based (https://swissmodel.expasy.org/) homology modeling was used to predict the structure of the zinc-finger region containing FBXO38-dependent degron. hZXDB with essential glutamate (E389), tyrosine (Y393), and the fifth zinc finger region highlighted are shown (left). The prediction of the homologous region in hZXDC with identical amino acids and regions highlighted (right).

(U) Frequency of tumor samples with ZXDA/B mutations identified in The Cancer Genome Atlas (TCGA) cohort. Single abbreviations represent different groups of cancers (e.g., Skin Cutaneous Melanoma – SKCM). The results are based upon data generated by the TCGA Research Network (https://www.cancer.gov/tcga).

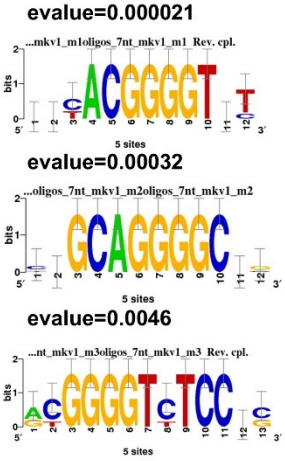
A


KMT2E
ARIH1
DAZAP1
YWHAB
IP:
α-IgG
α-ZXDA/B #1
α-ZXDA/B #2
DNase I hotspots
CpG islands
Genes

B


Average nucleotide frequency (%)
C
G
A
T
Average dinucleotide frequency
GC
CG
GG
CC
AG
CA
CT
TG
GA
TC
GT
AC
TT
AA
TA
AT

C


evalue=0.000021
...mkv1_m1oligos_7nt_mkv1_m1 Rev. cpl.
bits
5 sites
evalue=0.00032
...oligos_7nt_mkv1_m2oligos_7nt_mkv1_m2
5 sites
evalue=0.0046
...nt_mkv1_m3oligos_7nt_mkv1_m3 Rev. cpl.
5 sites

D

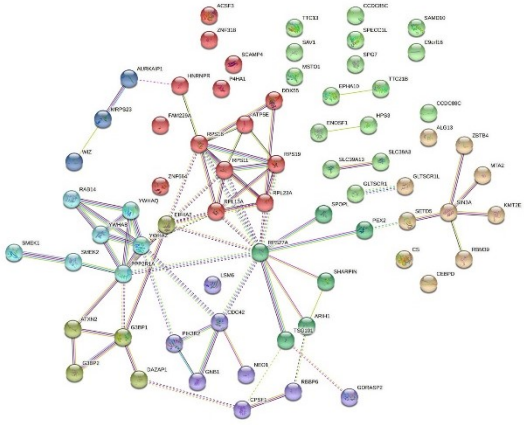


Figure S4. ZXDA/B do not act as transcriptional factors

(A) Selected ChIP-seq tag profiles of two independent ZXDB ChIP-seq samples. Five peaks selected as significant called by the MACS2 program are shown. Lower panels show DNase I hypersensitivity regions (orange), CpG islands (green), and exon-intron structure of genes (blue). The scheme was generated using UCSC Genome Browser (Kent, Sugnet et al., 2002).

(B) Nucleotide composition of ZXDB-precipitated chromatin peaks. Twenty base pairs surrounding peaks called by MACS2 were analyzed using RSAT software for nucleotide and motifs enrichment.

(C) Significant cis-motifs identified by RSAT oligo-analyzer motif discovery tool. Three motifs with the lowest expectation (E)-values and high log-likelihood ratio are shown. The X- and Y-axes show the position of nucleotides and the bits score, respectively.

(D) Protein/genes interaction map. Only genes with promoters significantly enriched in ZXDB ChIP samples were analyzed. The map was constructed using the STRING 11.5 web tool (Szklarczyk, Gable et al., 2019). Colored lines denote interactions: green (text mining), blue (curated database), purple (experimentally determined), and black (co-expression).

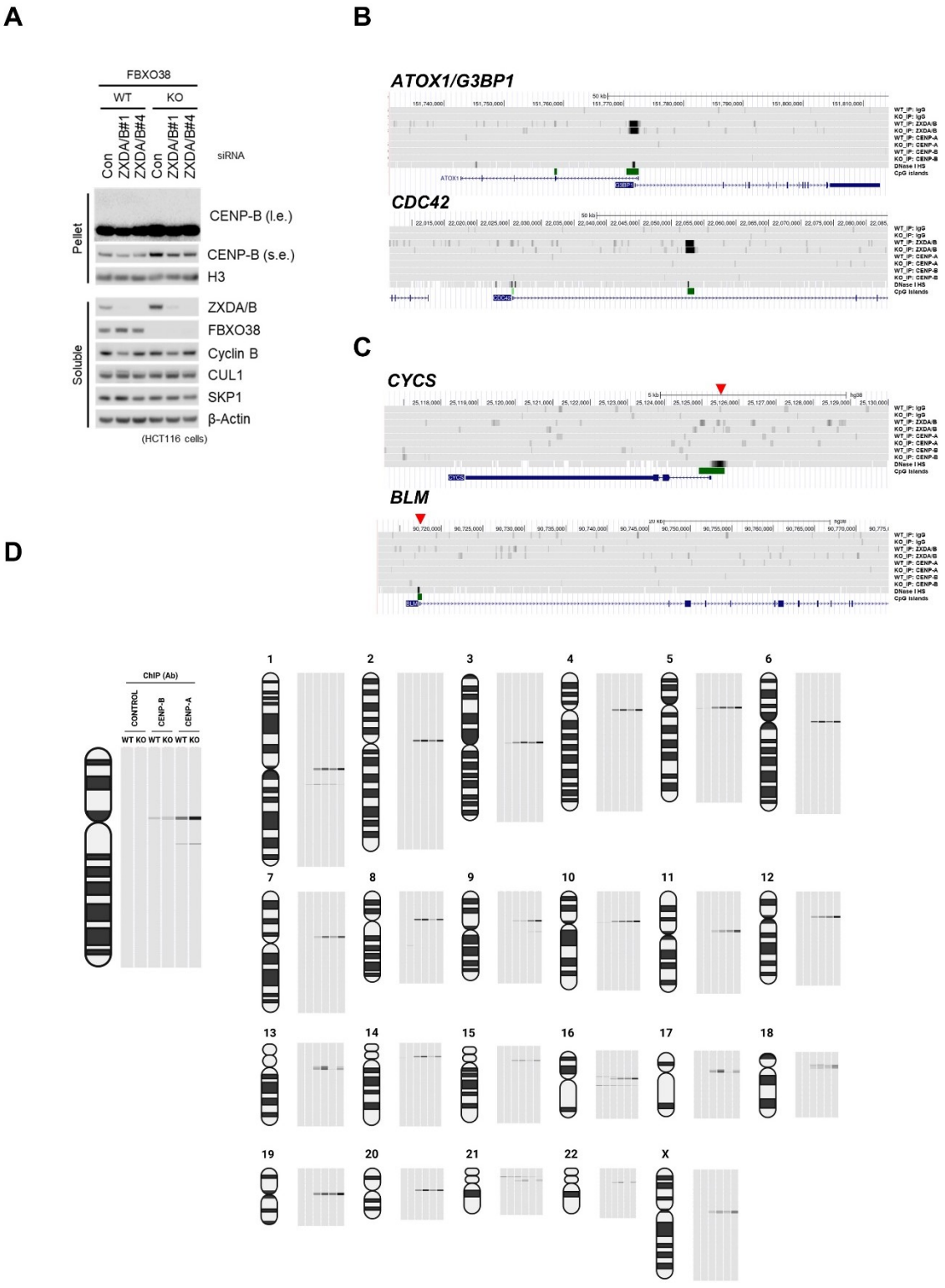

A
FBXO38
WT
KO
Con
ZXDA/B#1
ZXDA/B#4
Con
ZXDA/B#1
ZXDA/B#4
siRNA
Pellet
CENP-B (l.e.)
CENP-B (s.e.)
H3
Soluble
ZXDA/B
FBXO38
Cyclin B
CUL1
SKP1
β-Actin
(HCT116 cells)
B
ATOX1/G3BP1
CDC42
C
CYCS
BLM
D
ChIP (Ab)
CONTROL
CENP-B
CENP-A
WT KO WT KO WT KO
1
2
3
4
5
6
7
8
9
10
11
12
13
14
15
16
17
18
19
20
21
22
X

Figure S6. FBXO38 controls centromeric signature via ZXDA/B stability

(A) FBXO38 wild type (WT) and knockout (KO) HCT116 cells were transfected with two different siRNAs targeting ZXDA/B, or with control siRNA. The cells were subjected to isotonic lysis 48 hours after transfection, soluble fractions were collected and the pellets were further lysed in the presence of Benzonase nuclease and subsequently heat-denatured in the presence of 1% SDS for insoluble fractions. Lysates were immunoblotted as indicated. This image represents the longer exposure of CENP-B immunostaining of the blot found in (Figure 6C).

(B) Examples of ChIP-Seq analysis in FBXO38 WT and KO HCT116 cell line. ZXDA/B-associated *G3BP1* (promoter localized) and *CDC42* (intron localized) loci were selected. Fragmented chromatin was immunopurified with either non-specific IgG, or ZXDA/B, CENP-A, and CENP-B polyclonal antibodies. Trimmed reads were aligned using the Bowtie2 program and further normalized with bamCoverage utility (Galaxy – DeepTools) to obtain counts per million (CPM) values. Coverage of the human genome (hg38) was visualized in the UCSC genome browser (Kent et al., 2002). The quantity of precipitated chromatin is shown as a density graph using autoscale to highlight the enrichment. The upper two lines represent the control profiles, followed by anti-ZXDA/B, anti-CENP-A, and anti-CENP-B ChIP-seq samples. For each antibody, data from FBXO38 WT and KO cell lines are present. Lower panels show the location of genes (blue), DNase I hypersensitivity regions, and CpG islands.

(C) The quantity of precipitated chromatin is shown as a density graph of *CYCS* and *BLM* loci using autoscale to highlight the enrichment. Red arrowheads indicate previously described CENP-A depositions at the DNase I hypersensitive sites. Data are generated and visualized as in (B).

(D) The quantity of precipitated chromatin is shown as a density graph using autoscale to highlight the centromeric enrichment. All human chromosomes (except Y) are present. The single lines next to the chromosome schemes represent ChIP results using IgG control, CENP-B, and CENP-A antibodies (in FBXO38 WT and KO HCT116 cells). Data are generated and visualized as in (B).

Supplementary table

Dataset S1. (separate file) MACS2-called peaks in ZXDA/B ChIP-seq analysis

MACS2-called ZXDA-associated annotated peaks (version 2.1.1.20160309). Q-values were calculated from p-values using Benjamini-Hochberg procedure (--qvalue). Galaxy MACS2 callpeak app was used for calling peaks and calculating q-values. Peaks were annotated by PAVIS online software (https://manticore.niehs.nih.gov/pavis2/annotate).

List of reagents

Chemicals

Name	Company	CAT#
2-mercaptoethanol	Sigma	M6250
4',6-diamidin-2-fenylindol (DAPI)	Sigma	D9542
ATP	Sigma	A26209
Benzonase	Santa Cruz	sc-391121
Blasticidin	Sigma	15205
Colchicine	Sigma	C3915
Cycloheximide	Sigma	C7698
Doxycycline hyclate	Sigma	D9891
Dithiothreitol	Sigma	10197777001
Formaldehyde	Thermo Fisher Scientific	28908
Lipofectamine 2000	Thermo Fisher Scientific	11668019
Methanol	Penta	67-56-1
MG132	Medchemexpresss	HY-13259
MLN4924	Medchemexpresss	HY-70062
Sodium fluoride	Sigma	S7920
Sodium thiocyanate	Sigma	251410
Sodium orthovanadate	Sigma	450243
Paraformaldehyde	Electron Microscopy Sciences	15710
Polybrene	Sigma	107689
Polyethyleneimine (MW 25 000)	Polysciences	23966
Protease Inhibitors Mini Tablets	Pierce	A32955
Proteinase K	Sigma	P2308
Puromycin	Sigma	P8833
RNAiMax	Thermo Fisher Scientific	13778150
Sodium dodecyl sulfate (SDS)	Sigma	71736
UBE1	Boston Biochem/R&D Systems	E-305-025
UBCH3	Boston Biochem/R&D Systems	E2-610-100
Ubch5c	Boston Biochem/R&D Systems	E2-627-100
ubiquitin aldehyde	Boston Biochem/R&D Systems	U-201-050
Ubiquitin	Boston Biochem/R&D Systems	U-100H-10M

Antibodies

Primary antibodies	Source	CAT#	RRID	LINK
Anti-centromere antibodies	Antibodies Incorporated	15-234		
ARP3	Santa Cruz	ab49671	AB_2257830	AB_2257830
BAZ1A	Santa Cruz	sc-393164		
CDH1	Thermo Fisher Scientific	34-2000	AB_2533160	AB_2533160
CENP-A	Cell Signaling	2186	AB_10828491	AB_10828491
CENP-B	Santa Cruz	sc-376283	AB_10988421	AB_10988421
CENP-B	Santa Cruz	sc-376392	AB_11151020	AB_11151020
CENP-B	Atlas Antibodies	HPA054405	AB_2682477	AB_2682477
CENP-C	Atlas Antibodies	HPA058252	AB_2683654	AB_2683654
CK-IIα	Santa Cruz	sc-514403	AB_2894823	AB_2894823
CKII-β	Santa Cruz	sc-12739	AB_626792	AB_626792
CP110	Bethyl	A301-343A	AB_937760	AB_937760
CUL1	Thermo Fisher Scientific	32-2400	AB_2533070	AB_2533070
Cyclin B1	Santa Cruz	sc-245	AB_627338	AB_627338
DDB1	Santa Cruz	sc-376860	AB_2894825	AB_2894825
FBXO11	Novus Biologicals	NB100-59825	AB_892468	AB_892468
FBXO28	Bethyl	A302-377A	AB_1907260	AB_1907260
FBXO38	Atlas Antibodies	HPA041444	AB_2677484	AB_2677484
FLAG	Cell Signaling	14793	AB_2572291	AB_2572291
GFP	Cell Signaling	2956	AB_1196615	AB_1196615
H3	Abcam	ab1791	AB_302613	AB_302613
HA	Cell Signaling	3724	AB_1549585	AB_1549585
Lamin B	Santa Cruz	sc-6216	AB_648156	AB_648156
p21	Santa Cruz	sc-397	AB_632126	AB_632126
p27	Santa Cruz	sc-528	AB_632129	AB_632129
p53	Cell Signaling	2527	AB_10695803	AB_10695803
PARP-1	Santa Cruz	sc-8007	AB_628105	AB_628105
Phospho-β-Catenin (Ser33/37)	Cell Signaling	2009	AB_2088238	AB_2088238
REST	Millipore	07-579	AB_11211936	AB_11211936
RRM2	Santa Cruz	sc-398294	AB_2894824	AB_2894824
SKP1	Cell Signaling	12248	AB_2754993	AB_2754993
SKP2	Thermo Fisher Scientific	32-3300	AB_2533074	AB_2533074
Strep II Tag	Novus Biologicals	NBP2-43735		
StrepTactin HRP	Bio-Rad	1610381		
USP7	Bethyl	A303-943A	AB_2620292	AB_2620292
ZXDA/B	Bethyl	A303-656A	AB_11205808	AB_11205808
ZXDA/B	Atlas Antibodies	HPA043789	AB_2678673	AB_2678673
α-Tubulin	Proteintech	66031-1-Ig	AB_11042766	AB_11042766
β-Actin	Santa Cruz	sc-69879	AB_1119529	AB_1119529
β-TrCP2	Cell Signaling	4394	AB_10545763	AB_10545763

Secondary antibodies	Source	CAT#	RRID	LINK
Anti-Rabbit IgG (Alexa Fluor® 647)	Abcam	ab150067	AB_2894821	AB_2894821
Anti-Rabbit IgG (Alexa Fluor® 555)	Abcam	ab150070	AB_2783636	AB_2783636
Anti-Human IgG (Alexa Fluor 488)	Thermo Fisher Scientific	A11013	AB_2534080	AB_2534080
Anti-Mouse IgG (Alexa Fluor 647)	Abcam	ab150115	AB_2687948	AB_2687948

Fluorescence probes	Source	CAT#
Phalloidin - Fluor 488	Abcam	ab176753

Beads for protein purification	Source	CAT#
anti-HA (magnetic)	Pierce	88837
Strep-Tactin® Superflow resin	IBA	2-1206-025
Protein G (magnetic)	Dynabeads	10004D
ChromoTek GFP-Trap® (magnetic)	Chromotek	gtma-20

Vectors

Expression vectors	Backbone	N-term. tag
ZXDA	pCDNA3	2xStrep-1xFLAG
ZXDA	pCDNA3	1xHA
ZXDA	pSB	2xStrep-1xFLAG
ZXDA	pTRIPZ	1xHA
ZXDC	pCDNA3	2xStrep-1xFLAG
FBXO38	pCDNA3	2xStrep-1xFLAG
FBXO38	pSB	2xStrep-1xFLAG
DEDD2	pCDNA3	2xStrep-1xFLAG
CUL1	pCDNA3	1xHA
CENP-B	pKG141	GFP

Sleeping Beauty System	Company	Cat. Number
pSBtet-Pur	Addgene	60507
pSB100X	Addgene	34879

Lentiviral packaging vectors	Company	Cat. Number
pLenti CMV/TO SV40 Small and Large T antigen	Addgene	22298
pCMV-dR8.2	Addgene	8455
pCMV-VSV-G	Addgene	8454

CRISPR system	Company	Insert	Targeted cells
pXPR001	Addgene	FBXO38_5' #1	HCT116
pXPR001	Addgene	FBXO38_5' #2	RPE-1
pXPR001	Addgene	FBXO38_3' #1	HCT116/RPE-1

siRNAs

Name	Sequence	Target	Position
FBXO38#1	GGGUGUAUUUCAGCGAGUAUU	FBXO38	TR
FBXO38#2	GGACUCGAUUGGUUGAUAUUU	FBXO38	TR
FBXO38#3	GAGCGAAGCUGUUUGAGUAUU	FBXO38	UTR
ZXDA/B (#1)	GCUCUGUGGUGUUGGAUAAUU	ZXDB*	UTR
ZXDA/B (#2)	CUGAAAGGCCACAGCAUAAUU	ZXDA/B/C	TR
ZXDA/B (#3)	CCAAGAAGCACCAGCUGAAUU	ZXDA/B/C	TR
ZXDA/B (#4)	ACACAUAAGUCUUGGAAAUUU	ZXDB*	UTR

*Oligos were used in HeLa cells (Figure S1A) and HCT116 (Figure S6A) that express only ZXDB.

Oligonucleotides

Cloning oligonucleotides

Gene	Orientation	Position	Sequence	RE SITE
FBXO38	FWD	FL	CGAGAAAGGAGCTAGCGGGCCACGAAAGAAAAGTG	NHE1
FBXO38	REV	FL	GGGGTCGACTTAAATGTAGTCATCTTCAA	SAL1
X38_1090_REV	REV	1090	GGGGTCGACTCAAAATACACCCTTCTTCATCTG	SAL1
CUL1	FWD	FL	GGGGATCCTCGTCAACCCGGAGCCAGAA	BAMH1
CUL1	REV	FL	GGGGCGGCCGCTTAAGCCAAGTAACTGTAGGTGT	NOT1
DEDD2	FWD	FL	GGGGATCCGCGCTATCCGGGTCGAC	BAMH1
DEDD2	REV	FL	GGCTCGAGTCAGGAGGCCTCTGTCGGG	XHO1
ZXDA	FWD	FL	GGGGATCCGAAATCCCGAAGCTGCTCCC	BAMH1
ZXDA	REV	FL	GGCTCGAGTCATACCAAAAATGAGCTGCCAG	XHO1
ZXDA	FWD	138	GGGGATCCCAGGGCCCCCACTGCCTGTC	BAMH1
ZXDA	FWD	260	GGGGATCCTCTGGTCCAGGCGTGGTGCT	BAMH1
ZXDA	FWD	325	GGGGATCCGATAAACTGCGGCCCTTCGG	BAMH1
ZXDA	FWD	383	GGGGATCCTTCGAACCCGAGAGGCCTTA	BAMH1
ZXDA	FWD	445	GGGGATCCACCGGCGAGAGACCTTTCCT	BAMH1
ZXDA	FWD	505	GGGGATCCCTGGGCACAAAGCCTTTCGT	BAMH1
ZXDA	FWD	569	GGGGATCCAAGGTGGGCCAGGATCTCTT	BAMH1
ZXDA	FWD	637	GGGGATCCAGCTCGACTCTGGCAGGGCA	BAMH1
ZXDA	REV	389	GGCTCGAGTCAGTAAGGCCTCTCGGGTTCGA	XHO1
ZXDA	REV	424	GGCTCGAGTTAAAACAGTTCCTGTTCCCTGAAAT	XHO1
ZXDA	REV	586	GGCTCGAGTCAGGGTGTAAGAGAATTTGCTGC	XHO1
ZXDA	REV	663	GGCTCGAGTCAGCCATCAAGGACGGAGGGTC	XHO1
ZXDA	REV	765	GGCTCGAGTCATGGTGTCAGTAGTTCTGAGA	XHO1
ZXDC	FWD	FL	GGGGATCCGACCTCCCGGCGCTGCTCCC	BAMH1
ZXDC	REV	FL	GGCTCGAGTCACTGCAGATCCTGCAGGTTGA	XHO1

Mutagenesis oligonucleotides

Gene	Mutation	Sequence
FBXO38	M30A	CAGCAGATGAAACAAAGGACTATAGGAATCAACTTTCACATGAAG
FBXO38	C206R	TGCCTTAGCATTGGGATACGAGGAATTTCAGGAACATTC
FBXO38	R526Q	CGAGGAGAATGACTTTCAGCAAGATCTGCAGCCAG
FBXO38	Δ30-65 (ΔFBOX)	TCTCACAACTCGCAGATATAGATAGTCCTTTGTTTCATCTGC
ZXDA	HEQE354-357AAAA	CTCAAGGCGCACATGAAGGGCGCGGCCGCCGCGAACTCGTTCAAATGTGAGGT
ZXDA	N358A	GAAGGGCCATGAGCAGGAGGCCTCGTTCAAATGTGAGGTG
ZXDA	SFK359-361AAA	GGGCCATGAGCAGGAGAACGCGGCCGCCTGTGAGGTGTGCGAGGAG
ZXDA	EES366-368AAA	TCAAATGTGAGGTGTGCGCGGCCGCCTTCCCCACGCAGGCCAA
ZXDA	FPT369-371AAA	GTGTGCGAGGAGAGCGCGGCCGCCCAGGCCAAACTCG
ZXDA	Q372A	GAGAGCTTCCCCACGGCGGCCAAACTCGGCGC
ZXDA	AKL373-5AAA	GCTTCCCCACGCAGGCGGCCGCCGGCGCCCACCAGCGC
ZXDA	QRS379-381AAA	GCCAAACTCGGCGCCCACGCGGCCGCCCACTTCGAACCCGAGAG
ZXDA	FEP383-5AAA	CACCAGCGCAGCCACGCGGCCGCCGAGAGGCCTTACC
ZXDA	ERP386-388AAA	AGCCACTTCGAACCCGCGGCCGCTTACCAGTGCGCGTT
ZXDA	Y389A	AAAACGCGCACTGGGCAGGCCTCTCGGGTTCG
ZXDA	Y389F	ACGCGCACTGGAAAGGCCTCTCGGG
ZXDA	Q390A	AACCCGAGAGGCCTTACGCGTGCGCGTTTTCTGGCT
ZXDA	FSG393-395AAA	AGAGGCCTTACCAGTGCGCGGCCGCTGCCTGCAAGAAGACATTTATCAC
ZXDA	TFI399-401AAA	GTGCGCGTTTTCTGGCTGCAAGAAGGCGGCCGCCACAGTGAGTGCTCTGTTTTCCCAT
ZXDA	TVS402-404AAA	GCGTTTTCTGGCTGCAAGAAGACATTTATCGCGGCCGCTGCTCTGTTTTCCCATAACCGC
ZXDA	LFS406-408AAA	TGCAAGAAGACATTTATCACAGTGAGTGCGGCCGCTGCCCATAACCGCGCCCATTTCAGG
ZXDA	KK397-398AA	ACCAGTGCGCGTTTTCTGGCTGCGCGGCGACATTTATCACAGTGAGTGCTC
ZXDA	Δ266-330	AGGCGTGGTGCTGTTCGGCTGCCCTG
ZXDA	Δ267-299	CCAGGCGTGGTGCTGTTCAAATGCCCCCTG
ZXDA	Δ299-360	ACACCTCACATTTGAAGGGCCTCTGGCCCTG
ZXDA	Δ300-329	AGGGCAGCCGAAGGGCCTCTGGCC
ZXDA	Δ329-389	CGATAAACTGCGGCCCTACCAGTGCGCGTTTT
ZXDA	Δ330-359	ACGATAAACTGCGGCCCTTCAAATGTGAGGTGTG
ZXDA	Δ360-389	TGAGCAGGAGAACTCGCAGTGCGCGTTTTCTG
ZXDA	Δ397-427	CCTTGTCATATTGCTTGCTGCAGCCAGAAAACGCGCAC
ZXDA	Δ404-433	CAGGTGAATTTTCAGCCTACAAGCCACTGTGATAAATGTCTTCTTGCA
ZXDA	Δ409-438	GTGACTCCGCAGGTGAATGGAAAACAGAGCACTCAC
ZXDA	Δ421-452	AGCCACAGCCATCAAAGTCGCAGGAAAACAGTTCCTGT
ZXDC	ERP294-296AAA	GCGCAGCCACTTCGAGCCCGCGGCCGCTTACAAGTGTGACTTTCC

CRISPR cloning oligonucleotides

Name	Orientation	Sequence
FBXO38_5' #1	FWD	CACCGAAGCTGTATGACCGTATGTG
FBXO38_5' #1	REV	AAACCACATACGGTCATACAGCTTC
FBXO38_5' #2	FWD	CACCGAGAAACTCGTATTTATCAAG
FBXO38_5' #2	REV	AAACCTTGATAAATACGAGTTTCTC
FBXO38_3' #1	FWD	CACCGGATGCATGTTTTCCGGTGAA
FBXO38_3' #1	REV	AAACTTCACCGGAAAACATGCATCC

CRISPR verification oligonucleotides

Name	Orientation	Sequence
FBXO38	FWD	CCTGTGGAGGGAGCTCAATA
FBXO38	REV	GGTGCAGTTTAGTTGCAGAGG

frontiers | Frontiers in Cell and Developmental Biology

ORIGINAL RESEARCH
published: 13 June 2022
doi: 10.3389/fcell.2022.914053

FBXO38 Ubiquitin Ligase Controls Sertoli Cell Maturation

*Nikol Dibus[1,2], Eliska Zobalova[1], Mario A. M. Monleon[1], Vladimir Korinek[3], Dominik Filipp[4], Jana Petrusova[4], Radislav Sedlacek[5], Petr Kasparek[5] and Lukas Cermak[1]**

[1]Laboratory of Cancer Biology, Institute of Molecular Genetics of the Czech Academy of Sciences, Vestec, Czechia, [2]Faculty of Science, Charles University, Prague, Czechia, [3]Laboratory of Cell and Developmental Biology, Institute of Molecular Genetics of the Czech Academy of Sciences, Prague, Czechia, [4]Laboratory of Immunobiology, Institute of Molecular Genetics of the Czech Academy of Sciences, Prague, Czechia, [5]Czech Centre for Phenogenomics, Institute of Molecular Genetics of the Czech Academy of Sciences, Vestec, Czechia

The ubiquitin ligase SCF^{FBXO38} controls centromeric chromatin by promoting the degradation of the ZXDB protein. To determine the importance of this pathway during development, *Fbxo38*-deficient mice were generated. The loss of FBXO38 resulted in growth retardation affecting several organs, including the male reproductive system. A detailed analysis of the mutant testes revealed pathological changes in the seminiferous tubules, accompanied by a significant decrease in sperm production and reduced fertility. In adult testes, FBXO38 was specifically expressed in Sertoli cells, a somatic population essential for spermatogenesis initiation and progression. Sertoli cells lacking FBXO38 exhibited stabilized ZXDB protein and upregulated centromeric chromatin. Furthermore, the gene expression profile revealed that the absence of FBXO38 led to a defect in Sertoli cell maturation, specifically characterized by dysregulation in genes controlling retinoic acid metabolism and intercellular communication. Consequently, we documented significant changes in their ability to initiate spermatogonial differentiation. In conclusion, we show that FBXO38 acts as a Sertoli cell maturation factor, affecting the Sertoli cell transcription program, centromere integrity, and, subsequently, the ability to control spermatogenesis.

Keywords: proteasome, ubiquitin, ubiquitin ligase, spermatogenesis, sertoli cell, centromere, retinoic acid

OPEN ACCESS

Edited by:
João Ramalho-Santos, University of Coimbra, Portugal

Reviewed by:
Qi-En Yang, Northwest Institute of Plateau Biology (CAS), China
Luís Crisóstomo, Universidade do Porto, Portugal
Luca Busino, University of Pennsylvania, United States

****Correspondence:***
Lukas Cermak
lukas.cermak@img.cas.cz

Specialty section:
This article was submitted to Molecular and Cellular Reproduction, a section of the journal Frontiers in Cell and Developmental Biology

Received: *06 April 2022*
Accepted: *19 May 2022*
Published: *13 June 2022*

Citation:
Dibus N, Zobalova E, Monleon MAM, Korinek V, Filipp D, Petrusova J, Sedlacek R, Kasparek P and Cermak L (2022) FBXO38 Ubiquitin Ligase Controls Sertoli Cell Maturation. Front. Cell Dev. Biol. 10:914053. doi: 10.3389/fcell.2022.914053

INTRODUCTION

F-box-containing protein 38 (FBXO38), a member of the F-box family, was initially discovered as a co-activator of the transcription factor Krüppel-like factor 7 (KLF7) (Smaldone et al., 2004). FBXO38 acts as a substrate-binding receptor for multi-subunit ubiquitin ligase SCF^{FBXO38} (SKP1-CUL1-FBXO38). In this complex, a CUL1 scaffold protein separates substrate recognition and ubiquitination modules. The protein adaptor SKP1 connects CUL1 to different F-box-containing proteins, thus providing versatility to the ubiquitin-mediated degradation system (Skaar et al., 2013; Baek et al., 2021). Although several studies showed FBXO38 might act both as a part or independently of the SCF complex, the only substrate of SCF^{FBXO38} identified, so far, was the T-cell-specific transmembrane receptor programmed cell death 1 (PD1) (Meng et al., 2018; Georges et al., 2019). Recently, we have shown that FBXO38 controls the stability of ZXDA/B zinc finger proteins. ZXDA/B are encoded by an intronless retroposed gene (retrogene) derived from their homolog ZXDC (Greig et al., 1993; Aleksandrova et al., 2010). In mouse genome, *Zxda* gene contains frameshift mutation and thus *Zxdb* gene is the only functional mouse ortholog. In addition, we discovered that FBXO38-dependent degradation of ZXDB was responsible for the dynamic control

of the centromeric chromatin, particularly the centromeric protein CENP-B (manuscript co-submitted). Interestingly, mutations in the FBXO38 gene were found in three families with early-onset distal hereditary motor neuronopathy (Sumner et al., 2013; Akçimen et al., 2019). Other genetic studies showed FBXO38 gene polymorphism in patients suffering from severe chronic periodontitis and chronic obstructive pulmonary disease (Shang et al., 2015; Saferali et al., 2019). Moreover, a genetic analysis of monozygotic twins with discordant development of gender dysphoria revealed the potential role of FBXO38 in the control of gender identity (Morimoto et al., 2017).

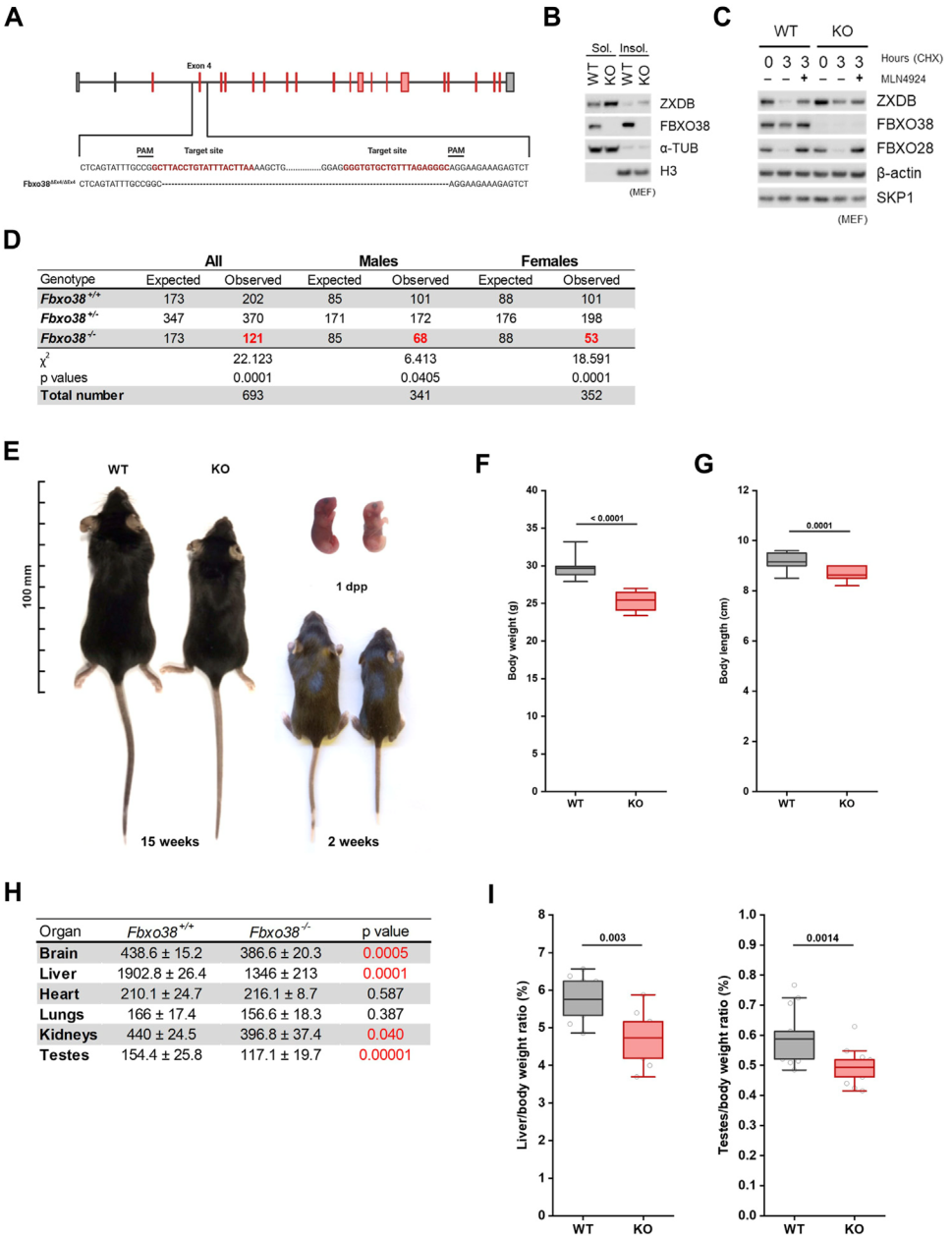
Spermatogenesis represents a well-documented and straightforward system of stem cell differentiation. Spermatogonial stem cell division is controlled by a stem cell niche composed of cellular and cell-free components (Oatley and Brinster, 2012; Griswold, 2016). Spermatogonial precursor cells undergo several mitotic divisions, giving rise to spermatocytes that divide meiotically, resulting in the formation of haploid germ cells that are further transformed into mature spermatozoa. The process of spermatogenesis is localized to the seminiferous tubules arranged in the testes. Each tubule is surrounded by a basal lamina formed by an extracellular matrix with the peritubular myoid cells providing structural support. The interstitial space contains Leydig cells responsible for testosterone production. Inside the tubules, somatic Sertoli cells are essential for the whole process of spermatogenesis (Griswold, 2018). During embryogenesis, fetal Sertoli cells surround the gonocytes (spermatogonial precursors), proliferate, and drive the tubule formation. Interestingly, Sertoli cell proliferation occurs rarely after the onset of puberty when Sertoli cells undergo a complex change in gene expression and finally reach terminal differentiation (Figueiredo et al., 2016; Meroni et al., 2019). Since each Sertoli cell is capable of supporting a limited number of germ and Leydig cells, testis size is determined by the proliferation potential of the Sertoli cell population. In adults, Sertoli cells provide paracrine (niche) support to differentiating germ stem cells. Additionally, a "web" of interconnected Sertoli cells constitutes the blood-testis barrier (BTB). Moreover, the cells are involved in seminiferous tubule clearance from apoptotic and cytosolic residues (Wu et al., 2022). To control spermatogonial differentiation, Sertoli cells transmit signals generated by the hypothalamic-pituitary-Leydig cell system. Interestingly, the activity of this hormonal germ cell differentiation axis is negatively regulated by Sertoli cells through the secretion of serum inhibins (Krause, 1977). Upon activation, Sertoli cells produce several morphogens that provide paracrine control of spermatogenic events across the tubule. One of the most important morphogenic compounds is all-trans retinoic acid (ATRA), responsible for spermatogenesis initiation (Griswold, 2016). Serum retinol (or vitamin A) is actively transported to Sertoli cells, where it is metabolically modified into retinaldehyde and, finally, to ATRA. Upon release from the Sertoli cells, it enters spermatogonia and activates the pro-mitotic program. ATRA is actively degraded in Sertoli cells during early postnatal development of the testes by cytochrome P450 family 26 subfamily B member 1 (CYP26B1), the enzyme preventing premature initiation of differentiation. In the first wave of spermatogenesis, CYP26B1 activity ensures the coordinated entry of spermatogonia into meiosis, a process required for continuous sperm production in adulthood (MacLean et al., 2007; Griswold, 2016).

Here, we investigated the role of FBXO38 in mouse development. FBXO38 controls the growth of several organs, including testes, where it is specifically expressed by stem cell-supporting Sertoli cells. Sertoli cells lacking FBXO38 exhibit a defect in maturation resulting in improper spermatogonia stimulation and disrupted sperm production. This pathologic process is accompanied by stabilization of the FBXO38 substrate ZXDB and alteration in CENP-A/B positive centromeric regions.

RESULTS

FBXO38 Deficiency Leads to Growth Retardation

Ubiquitin substrate receptor FBXO38 is highly conserved in vertebrates, with ~95% amino acid identity between the mouse and human orthologs (**Supplementary Figures S1A,B**). Identically to human FBXO38 protein, its mouse ortholog binds ZXDA/B proteins *via* degron located in between their fourth and fifth zinc fingers (**Supplementary Figure S1C**). To uncover the physiological role of FBXO38, we generated a mouse model with a targeted deletion of exon four of the *Fbxo38* gene ($Fbxo38^{\Delta Ex4}$). Mutated allele encodes prematurely terminated protein without any functional domain, including the F-box motif (**Figure 1A**, **Supplementary Figure S1D**). As expected, lysates from immortalized $Fbxo38^{\Delta Ex4/\Delta Ex4}$ (KO) mouse embryonic fibroblasts (MEF) lacked any detectable FBXO38 protein. The effect of FBXO38 inactivation was a stabilization of its substrate ZXDB (**Figures 1B,C**). While heterozygous $Fbxo38^{WT/\Delta Ex4}$ (HT) animals were fertile with normal gross morphology, the offspring of heterozygous breeding pairs were not born in the expected (Mendelian) ratio. Compared to wild-type (WT) pups, the frequency of birth of *Fbxo38*-deficient mice was reduced by 40% (32%—males; 52% females) (**Figure 1D**). Surviving newborn *Fbxo38*-deficient mice were smaller and exhibited reduced body weight compared to their littermates. This growth retardation phenotype began to manifest during embryonic development, as KO pups were already smaller at birth (**Figure 1E**, **Supplementary Figure S1E**). The phenotype persisted throughout the lifespan—mature adult *Fbxo38* KO mice exhibited reduced body weight and decreased body length (**Figures 1E–G**). A detailed analysis showed differences in their organ size. We observed a significant decrease in the weight of the liver, brain, testes, and kidneys of KO males when compared to their WT littermates, although the heart and lungs were not affected (**Figure 1H**, **Supplementary Figure S1F**). Differences in liver and testes weight between WT and KO were significant, even when normalized to total body weight (**Figure 1I**). Moreover, the observed differences in organ size were confirmed in the female cohort (**Supplementary Figure S1G**).



D

	All		Males		Females	
Genotype	Expected	Observed	Expected	Observed	Expected	Observed
Fbxo38 $^{+/+}$	173	202	85	101	88	101
Fbxo38 $^{+/-}$	347	370	171	172	176	198
Fbxo38 $^{-/-}$	173	121	85	68	88	53
χ^2		22.123		6.413		18.591
p values		0.0001		0.0405		0.0001
Total number		693		341		352

H

Organ	*Fbxo38* $^{+/+}$	*Fbxo38* $^{-/-}$	p value
Brain	438.6 ± 15.2	386.6 ± 20.3	0.0005
Liver	1902.8 ± 26.4	1346 ± 213	0.0001
Heart	210.1 ± 24.7	216.1 ± 8.7	0.587
Lungs	166 ± 17.4	156.6 ± 18.3	0.387
Kidneys	440 ± 24.5	396.8 ± 37.4	0.040
Testes	154.4 ± 25.8	117.1 ± 19.7	0.00001

FIGURE 1 | FBXO38 deficiency leads to growth retardation in mouse. **(A)** Scheme illustrating mouse Fbxo38 gene structure and its targeted disruption using a CRISPR/Cas9 genome-editing system. Two single guide RNAs (sgRNAs) were designed to target intron sequences (sequence in red) flanking exon four of the *Fbxo38* gene. Translated exons are depicted in red color. PAM; protospacer adjacent motif, dashed line indicates deleted nucleotides in *Fbxo38*$^{\Delta Ex4/\Delta Ex4}$ animals. **(B)** SV40 immortalized MEF generated from *Fbxo38* wild-type (WT) and knockout (KO) E13.5 embryos were subjected to lysis. Soluble and insoluble fractions were immunoblotted as indicated; α-tubulin and histone H3 were used as loading and fractionation controls. **(C)** MEF (as in C) were treated with cycloheximide (CHX) for 3 h and pre-treated with MLN4924 for 1 h where indicated. Whole-cell lysates were immunoblotted as indicated. Staining of FBXO28 was used as a control for CUL1-dependent degradation. **(D)** Observed and expected mouse genotypes of weaned pups from heterozygous breedings. The proportion of mice with different genotypes was compared to expected Mendelian ratios by the Chi-square test. Significant deviations from the expected numbers are shown in red. **(E)** Representative images of Fbxo38 WT and KO littermate males of indicated age. Dpp; days postpartum. **(F)** Body weight of adult (17–21 weeks) *Fbxo38* WT and KO males. Age distribution in both groups was the same (n = 15). Statistical significance was assessed by an unpaired two-tailed t-test. **(G)** Body length of animals as in (E). **(H)** Means ± standard deviations and p-values of organ weights of *Fbxo38* WT and KO males as in (E) are summarized in the table. Statistical significance was assessed by an unpaired two-tailed t-test. Statistically significant p-values are highlighted in red (p-value < 0.05). **(I)** Liver (left) and testes (right) weight to body weight ratio of adult *Fbxo38* WT and KO males (liver: n = 9; testes: n = 14). Individual data points are shown. Horizontal bars show mean values, boxes represent 25th and 75th percentiles. Statistical significance was assessed by an unpaired two-tailed t-test.

Altogether, these findings demonstrate that, although *Fbxo38* is not essential for mouse survival, it is important for proper growth and fitness.

Reproduction and Spermatogenesis Are Impaired in FBXO38-Deficient Animals

Due to significant differences in the weight of testes between *Fbxo38* WT and KO animals (**Figures 1H,I**, **Supplementary Figure S1F**), we decided to determine whether FBXO38 is critical for male reproduction. We conducted breeding experiments where WT female mice were allowed to mate with KO males. In each cage, one female was housed with one male. Mice had free access to food and water. In the first approach, females were checked everyday and once they produced vaginal plug, males were separated (**Supplementary Figure S2A**). Examining a small-scale cohort of males ($n = 5$), no defects in the mating behavior of KO males were observed and vaginal plugs appeared during the first week of breeding, with no apparent difference between WT and KO males. However, none of the females bred to KO males became pregnant and gave birth to pups, which was in accordance with International Mouse Phenotyping Consortium (IMPC) data (Dickinson et al., 2016). In contrast to this observation, allowing WT females to mate with KO males without separation up to 3 months revealed that KO males are capable of reproduction (**Supplementary Figure S2A**). However, their reproductive fitness was impaired with significantly smaller litter size (**Figure 2A**). Furthermore, smaller testes of KO animals correlated with lower spermatid and spermatozoa production (**Figure 2B**) and a significant decrease in epididymal sperm count (**Figure 2C**). Despite fewer mature sperms in cauda, the epididymis had a typical gross morphology (**Supplementary Figure S2B**).

Both young and mature adult KO males showed morphological anomalies in the testes. A histological examination revealed disorganized seminiferous tubules with reduced cellularity at spermatocyte, spermatid, and sperm levels in FBXO38-deficient males (**Figure 2D**, **Supplementary Figure S2C**). The disorganized structure of KO seminiferous tubules did not allow us to determine the exact stages of spermatogenesis. However, the height of tubular epithelium was significantly reduced compared to WT testes (**Figure 2E**). Interestingly, we detected a dramatic increase in the number of multinucleated cells (**Supplementary Figures S2C–E**).

The histological observation was confirmed using specific antibodies to mark different spermatogenesis populations (The scheme of the antibodies used and publicly available testicular single-cell expression data analysis can be seen in **Supplementary Figures S2F,G**) (Hermann et al., 2018). First, Sertoli cells were visualized by co-staining of nuclear factor Wilms' tumor 1 (WT1) and cytosolic intermediate filament vimentin (**Figure 2F**). We did not observe any differences in Sertoli cell number (**Figure 2G**). However, compared to WT animal testes, WT1 staining was weaker in the nuclei of the KO Sertoli cells (**Supplementary Figure S2H**). Markers of the spermatogonial stem cell compartment, Promyelocytic leukemia zinc finger protein (PLZF), and Spalt-like transcription factor 4 (SALL4), did not reveal any significant differences in the number of these cells and the intensity of the staining (**Supplementary Figure S2I**). Synaptonemal complex protein 3 (SCP3) staining confirmed the disruption of spermatogenesis progression characterized by a reduced number of meiotic spermatocytes (**Figure 2H**). Immunofluorescence staining with the Stimulated by retinoic acid 8 (STRA8) antibody, the marker of differentiating spermatogonia and target of retinoic acid signaling, allowed us to recognize the distinct stages of spermatogenesis (stage VII-VIII) (Endo et al., 2015). In tubules positive for STRA8, we observed a decreased number of spermatocytes (detected by staining Pituitary homeobox 2; PITX2) and spermatids (detected by peanut agglutinin; PNA), supporting the observation of defects in spermatogenesis. Of note, we observed a weaker signal of STRA8 staining but an undisturbed number of STRA8 positive cells, suggesting a potential disturbance in retinoic acid signaling (**Figure 2I**).

The Timing of the First Wave of Spermatogenesis Depends on FBXO38

Decreased sperm counts in adult KO males indicate the importance of FBXO38 in spermatogenesis. Adult mouse spermatogenesis depends on the progression of its first wave characterized by the synchronous initiation of cell divisions, germ cell apoptosis, and, finally, production of the first spermatozoa by 6 weeks of age (**Figure 3A**). To determine whether this process is affected by FBXO38 deficiency, we first focused on identifying the cellular population expressing FBXO38 protein. We isolated juvenile testes and noticed that, as with adult animals, KO mice testes were smaller in size (example in **Supplementary Figure S3D**). Initially, FBXO38 protein was expressed predominantly by spermatogonia. However, the staining of testes from two-week-old animals, revealed that its expression broadened also to Sertoli cells, a population of somatic cells essential for testis formation and spermatogenesis (co-stained with WT1) (**Figures 3B,C**, and detail in 3D). Moreover, immunofluorescence staining showed that many individual tubules lacking FBXO38, did not enter the meiotic stage, suggesting asynchronicity of the first wave of KO animals (**Figure 3E**). Similar results were obtained by analysis of total testicular protein, which showed a significant decrease in the SCP3 meiotic marker expression in KO testis lysates. As expected, ZXDB was stabilized in KO testes, while WT1 was decreased in accordance with the immunofluorescence staining. Interestingly, we observed a higher expression of SALL4A, a marker of differentiating spermatogonia (**Figure 3F**). Although this transcription factor contains two zinc-finger linkers bearing the "signature" of a ZXDB-like FBXO38-dependent degron (**Supplementary Figure S3A**), we could not detect the interaction between FBXO38 and SALL4A (**Supplementary Figure S3B**).

To support our observation indicating that KO males have a delay in the first wave of spermatogenesis, we visualized spermatids in 4.5-week-old testes. In contrast to WT tubules, which showed the synchronous emergence of spermatids at this age, KO tubules mostly lacked any positivity, suggesting an

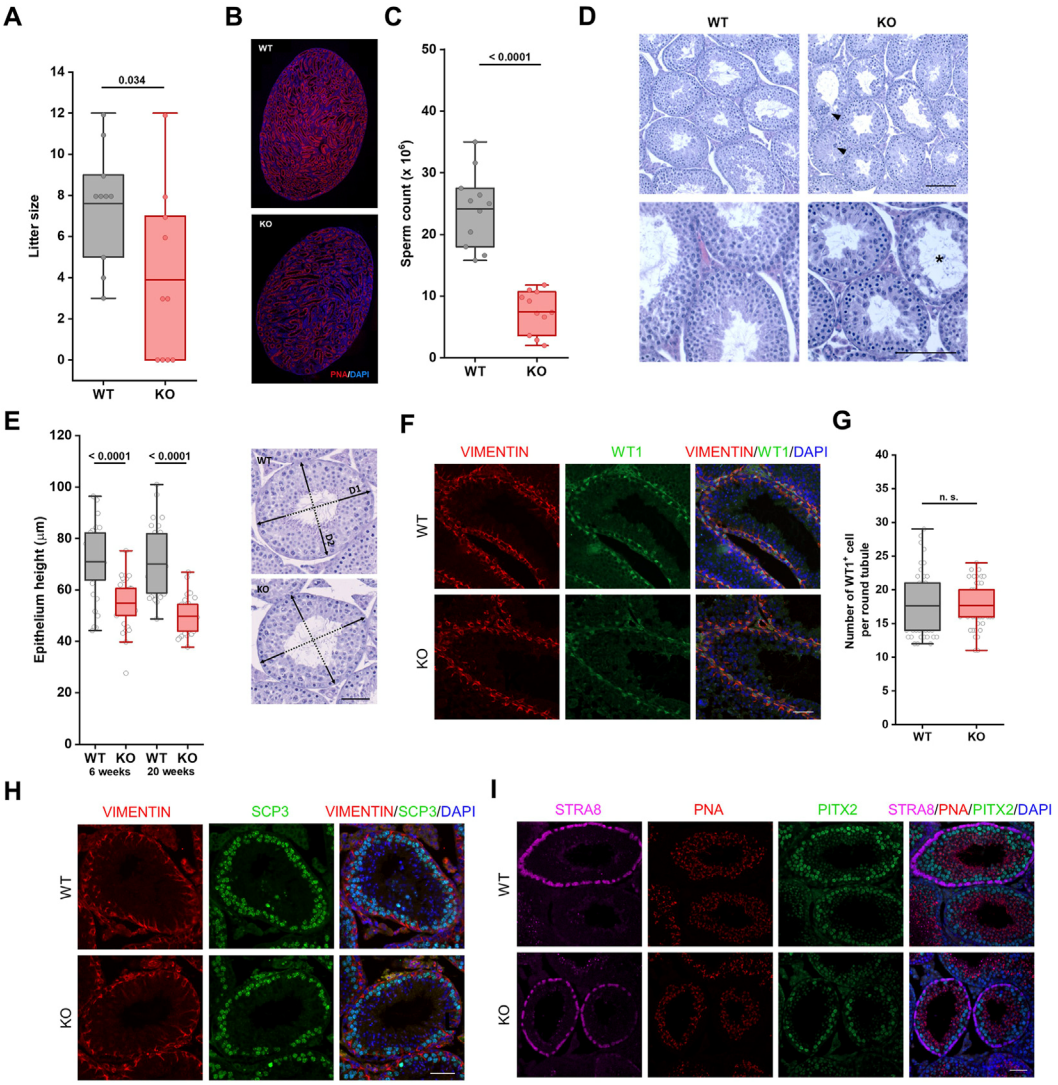


FIGURE 2 | Reproduction and spermatogenesis are impaired in *Fbxo38*-deficient animals. **(A)** Litter size of WT females bred to *Fbxo38* WT or KO males. Litters were recorded for the time period of 18–21 days after monitored vaginal plugs. Number of pups per litter are shown as individual data points, horizontal bars show mean values, boxes represent the 25th and 75th percentiles. Statistical significance was assessed by an unpaired two-tailed *t*-test. **(B)** Composite pictures of sagittal sections of *Fbxo38* WT and KO testes labeled with peanut agglutinin (PNA) lectin and counterstained with DAPI. **(C)** Sperm counts of adult (17–21 weeks) *Fbxo38* WT and KO males with the same age distribution in both groups. Spermatozoa were isolated from both caudae epididymides. Individual data points are shown, horizontal bars show mean values, boxes represent the 25th and 75th percentiles. Statistical significance was assessed by an unpaired two-tailed *t*-test. **(D)** Hematoxylin and eosin-stained testicular sections from 9-week-old *Fbxo38* WT and KO males. Arrowheads point to atypical multinucleated cells, asterisks show disrupted tubules. Scale bar, 100 µm. **(E)** Height of germinal epithelium from young and adult *Fbxo38* WT and KO animals (left) and methodological approach of measurement (right). Average height of germinal layer in two perpendicular axes was measured for each tubule (35 randomly selected round tubules from transversal section per animal). Horizontal bars show mean values, boxes represent the 25th and 75th percentiles. Statistical significance was assessed by an unpaired two-tailed *t*-test. Scale bar, 50 µm. **(F)** Seminiferous tubule sections of young adult (10 weeks) *Fbxo38* WT and KO mice stained for Vimentin and WT1. DNA was visualized with DAPI. Scale bar, 50 µm. **(G)** The number of WT1-positive cells in round seminiferous tubules from sections of *Fbxo38* WT and KO testes ($n = 2$; 24 tubules per animal). Horizontal bars show mean values, boxes represent the 25th and 75th percentiles. Statistical significance was assessed by an unpaired two-tailed *t*-test. **(H)** Seminiferous tubule sections of young adult (10 weeks) *Fbxo38* WT and KO mice stained for Vimentin and SCP3. DNA was visualized with DAPI. Scale bar, 50 µm. **(I)** Seminiferous tubule sections of 17-week-old *Fbxo38* WT and KO mice co-stained with antibodies against STRA8 and PITX2 and labeled with PNA. DNA was visualized using DAPI. Scale bar, 50 µm.

apparent arrest or delay in the final stages of spermatogenesis. (**Figure 3G**). Finally, we measured sperm counts of six-week-old males. Although the significance of lower sperm counts from KO males is not strong (due to the smaller sample size; $n = 3$), there is a clear trend showing that the first wave of spermatogenesis is weaker compared to WT littermates (**Figure 3H**). Additionally, a detailed analysis of the sperm shows no difference in sperm structure or motility (**Supplementary Figure S3C + Supplementary Movies S1-WT, S2-KO**). Furthermore, we did not observe any differences in the numbers of spermatogonia

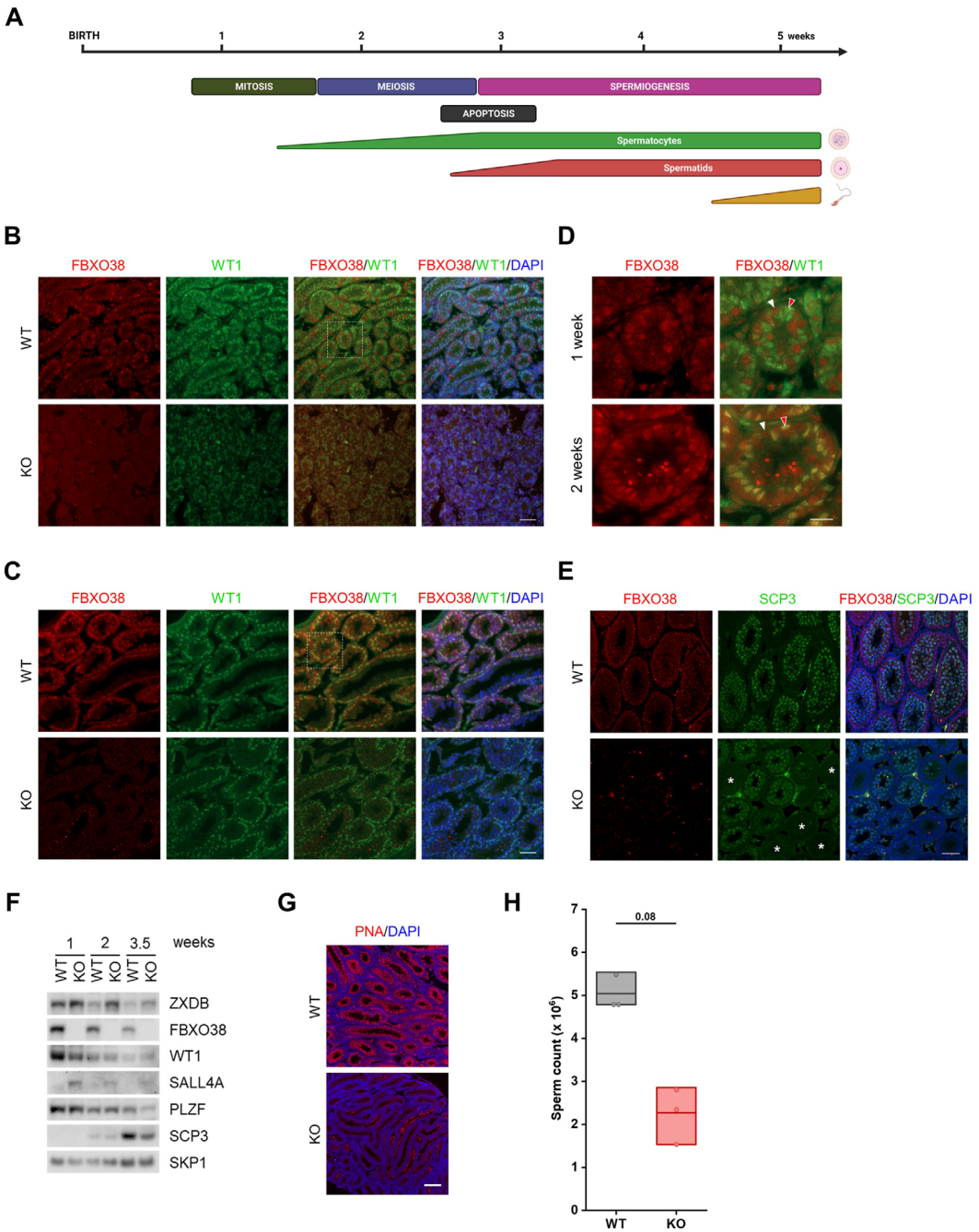
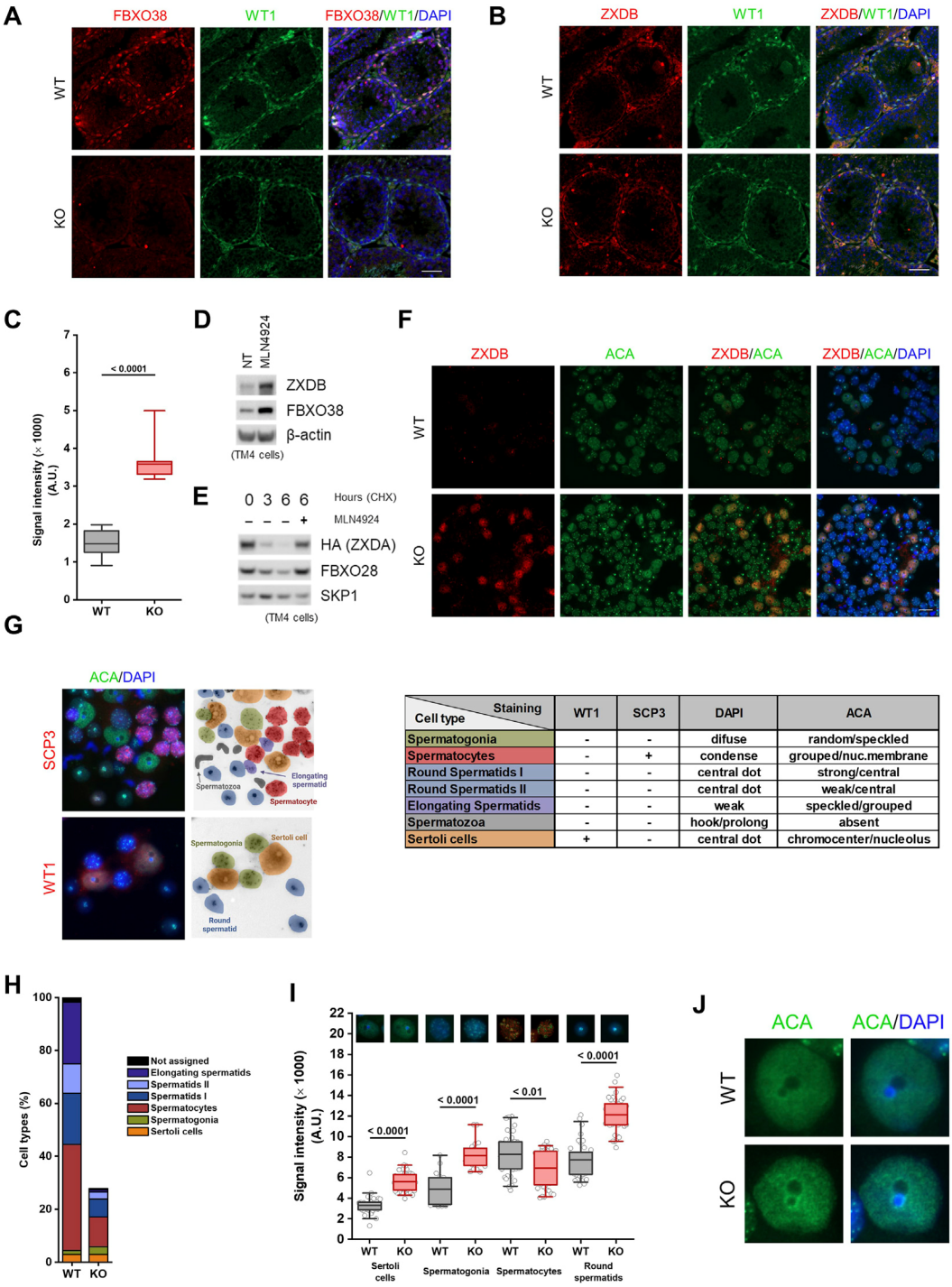


FIGURE 3 | The timing of the first wave of spermatogenesis depends on FBXO38. **(A)** Schematic illustration of major events in the first wave of spermatogenesis. The timeline in the upper panel indicates postnatal age in weeks. The middle panel shows the occurrence of the individual processes in spermatogenesis and the lower panel indicates the time course of the formation of spermatogenic differentiation stages. **(B,C)** Testis sections of infant *Fbxo38* wild-type (WT) and knockout (KO) littermate males at the age of 1 (B) and 2 weeks (C) postpartum stained for FBXO38 and WT1. DNA was visualized with DAPI. Scale bar, 50 µm. **(D)** Details of FBXO38 and WT1 localization in seminiferous tubule sections from WT mice at the age of 1 and 2 weeks from **(B,C)**. White arrowheads show spermatogonia, red arrowheads point to Sertoli cells. Scale bar, 20 µm. **(E)** Co-immunofluorescence staining for FBXO38 and SCP3 of testis sections from *Fbxo38* WT and KO mice at the age of 2 weeks. DAPI was used to stain DNA. Asterisks show tubules with negative SCP3 staining. Scale bar, 50 µm. **(F)** Western blot analysis of whole testes protein lysates from *Fbxo38* WT and KO littermate males at the indicated age. Testes without tunica albuginea were homogenized and lysed in the presence of Benzonase nuclease and lysates were immunoblotted as indicated **(G)** Testis sections of *Fbxo38* WT and KO littermate males at the age of 4.5 weeks labeled with peanut agglutinin (PNA) lectin and counterstained with DAPI. Scale bar, 200 µm. **(H)** Sperm counts of juvenile *Fbxo38* WT and KO mice at the age of 6 weeks. Spermatozoa were isolated from the caudae epididymides. Individual data points are shown, horizontal bars show mean values, boxes represent the 25th and 75th percentiles. Statistical significance was assessed by the Mann-Whitney *U* test.



Cell type \ Staining	WT1	SCP3	DAPI	ACA
Spermatogonia	-	-	difuse	random/speckled
Spermatocytes	-	+	condense	grouped/nuc.membrane
Round Spermatids I	-	-	central dot	strong/central
Round Spermatids II	-	-	central dot	weak/central
Elongating Spermatids	-	-	weak	speckled/grouped
Spermatozoa	-	-	hook/prolong	absent
Sertoli cells	+	-	central dot	chromocenter/nucleolus

FIGURE 4 | FBXO38 controls ZXDB protein and the centromeric chromatin in adult Sertoli cells. **(A,B)** Seminiferous tubule sections of young adult (10 weeks old) *Fbxo38* wild-type (WT) and knockout (KO) mice co-stained for WT1 and FBXO38 (A) or ZXDB (B). DNA was visualized with DAPI. Scale bar, 50 μm. **(C)** Signal intensity of Sertoli cells from testicular sections of *Fbxo38* WT and KO stained for ZXDB as in (B). The maximum normalized intensity of cells (n = 2; 15 Sertoli cells per animal) was measured. Horizontal bars show mean values, boxes represent the 25th and 75th percentiles. Statistical significance was assessed by an unpaired two-tailed t-test. **(D)** TM4 cells were either non-treated or treated with MLN4924 for 22 h. Whole-cell lysates were immunoblotted as indicated. **(E)** TM4 stably expressing HA-tagged ZXDA were subjected to cycloheximide chase. Where indicated, cells were pre-treated with MLN4924 for 1 h. Whole-cell lysates were immunoblotted as indicated. **(F)** Seminiferous tubule squash from adult *Fbxo38* WT and KO mice stained with ZXDB antibody and anti-centromere antibodies (ACA). DNA was visualized with DAPI. Scale bar, 20 μm. **(G)** Representative images of testicular cell types (from KO animals) and staining for their characteristic markers used to identify the cell populations in a seminiferous tubule squash. The middle scheme illustrates the position and cell type shown in the left pictures. The table on the right depicts combination

(*Continued*)

FIGURE 4 | of the markers and features used for identification. **(H)** Composition of cell types in a seminiferous tubule squash as in (D). Each fraction is displayed as a percentage from the WT whole-squash count. Sertoli cell count was used for normalization between KO and WT animals. **(I)** The signal intensity of ACA staining in indicated cell types from testicular sections of *Fbxo38* WT and KO mice as in (D). Maximum normalized intensity was measured. Individual data points from two independent experiments are shown. Horizontal bars show mean values, boxes represent the 25th and 75th percentiles. Statistical significance was assessed by an unpaired two-tailed *t*-test. **(J)** Representative magnified images of Sertoli cells from a seminiferous tubule squash from *Fbxo38* WT and KO mice stained with ACA.

(**Supplementary Figure S3D**) or apoptotic cells detected by TUNEL assay staining (**Supplementary Figure S3E**).

In summary, the analysis of prepubertal testes showed that the localization of FBXO38 expression changes in the early stages of spermatogenesis. Furthermore, our results revealed that the absence of FBXO38 led to a delay in meiotic entry and, consequently, to a lower sperm count.

FBXO38 Controls ZXDB Protein and the Centromeric Chromatin in Adult Sertoli Cells

Since we established that FBXO38 protein expression shifts from spermatogonia to Sertoli cells during testicular maturation, we decided to determine its expression in adult animals. An analysis of publicly available scRNA-seq data revealed that *Fbxo38* is preferentially expressed in spermatogonia, spermatocytes, Sertoli, and Leydig cells, while *Zxdb* is expressed only in Sertoli cells (**Supplementary Figures S4A,B**) (Hermann et al., 2018; Ernst et al., 2019). Testicular tubules were first stained with the FBXO38-specific antibody to confirm these data. As with older pups, Sertoli cells showed the highest FBXO38 protein positivity, while spermatogonial cells, but no other stages, expressed FBXO38 slightly above the background level (**Figure 4A**). In agreement with our previous data, the FBXO38 substrate ZXDB was significantly stabilized in *Fbxo38* KO Sertoli cells in which both genes are co-expressed (**Figures 4B,C**). Moreover, endogenous ZXDB protein level increased in mouse Sertoli-derived cell line TM4 treated with Neddylation inhibitor MLN4924 which prevents all cullin-dependent ubiquitination (**Figure 4D**). Additionally, exogenous ZXDA expressed in TM4 cells was quickly degraded upon ribosomal inhibition in the cullin-dependent manner (**Figure 4E**). Considering our previous observations that ZXDB controls the centromeric chromatin proteins, we optimized their staining in distinct spermatogenic cell types using anti-centromeric antibodies (ACA) and the tubule squash method (Earnshaw and Cooke, 1989; Page et al., 1998; Parra et al., 2003). We confirmed that the ZXDB protein is uniquely stabilized in FBXO38-deficient Sertoli cells (**Figure 4F**). Analyzing scRNA-seq data revealed that *Cenpa* is expressed strongly by spermatogonia and weakly by Sertoli cells. On the other hand, *Cenpb* is specifically expressed by Sertoli and Leydig cells (**Supplementary Figures S4A,C**) (Hermann et al., 2018; Ernst et al., 2019). Testicular spreads were co-stained with SCP3 and WT1 markers and ACA to quantify centromeric chromatin signals. This staining allowed us to distinguish spermatogonial cells, Sertoli cells, spermatocytes, round spermatids I, round spermatids II, and elongating spermatids (**Figure 4G**). We confirmed that KO testes exhibit a lower ratio of spermatocytes and spermatids to Sertoli cells (**Figure 4H**). *Via* detailed analysis of ACA staining, we showed that the absence of FBXO38 leads to the stabilization of centromeric chromatin proteins, similar to the extent observed in human cancer cell lines (**Figure 4I**). In Sertoli cells, centromere staining was not concentrated in distinct dots but displayed rather diffuse signals centered around nucleoli-associated chromocenters (**Figure 4J**). As shown previously, chromocenter association with nucleoli impacts ribosomal gene transcription (Haaf et al., 1990). To assess whether KO Sertoli cells exhibit differentially active nucleoli, we employed staining of B23 (nucleophosmin) protein, previously used as a marker of ribosomal activity (Yung et al., 1985; Maggi et al., 2008). Analysis of B23 fluorescence signal in WT and KO animals showed a significant decrease in mutant Sertoli cells (**Supplementary Figures S4D,E**).

FBXO38-Deficient Sertoli Cells Exhibit a Maturation Defect

To investigate the molecular consequences of the loss of FBXO38 in Sertoli cells in greater detail, we isolated the cells from 8-week-old WT and KO testes using fluorescence-activated cell sorting (FACS) (Lakpour et al., 2017) (**Supplementary Figures S5A,B**). Next, we performed a transcriptomic analysis using RNA-seq methodology. A comparison of transcriptomes from *Fbxo38* WT and KO animals revealed significant transcriptional changes (**Figure 5A**; detail in **Supplementary Figures S5C**). One of the most significantly upregulated genes in KO Sertoli cells was *Cyp26b1* which encodes an inhibitor of retinoic acid metabolism (**Supplementary Figures S5C**, marked in **Figure 5A** with arrowhead). *Cyp26b1* is the marker of immature Sertoli cells, and its transcriptional level declines postnatally (Edelsztein et al., 2020). To assess whether FBXO38 deficiency results in a maturation defect in Sertoli cells, we profiled publicly available data from Sertoli cells isolated during the maturation period. Side-by-side correlation between genes significantly up- or downregulated in FBXO38-deficient Sertoli cells shows an apparent shift toward an immature profile in KO cells (**Figures 5A,B**). This defect is highlighted in the expression level of genes associated with the maturation of Sertoli cells (**Figure 5C**) (Baumal et al., 1989; Birk et al., 2000; Pellegrini et al., 2003; Jiang et al., 2015).

An important process associated with maturation is the activation of retinoic acid signaling. As mentioned above, CYP26B1 acts as an inhibitor of retinoic acid signaling by actively metabolizing all-trans retinoic acid (ATRA) into its inactive forms. A short ATRA presence is necessary for the coordinated activation of spermatogonial mitotic division. However, *Cyp26b1* was upregulated in FBXO38-deficient cells, suggesting a disruption in the timed activation of this morphogen

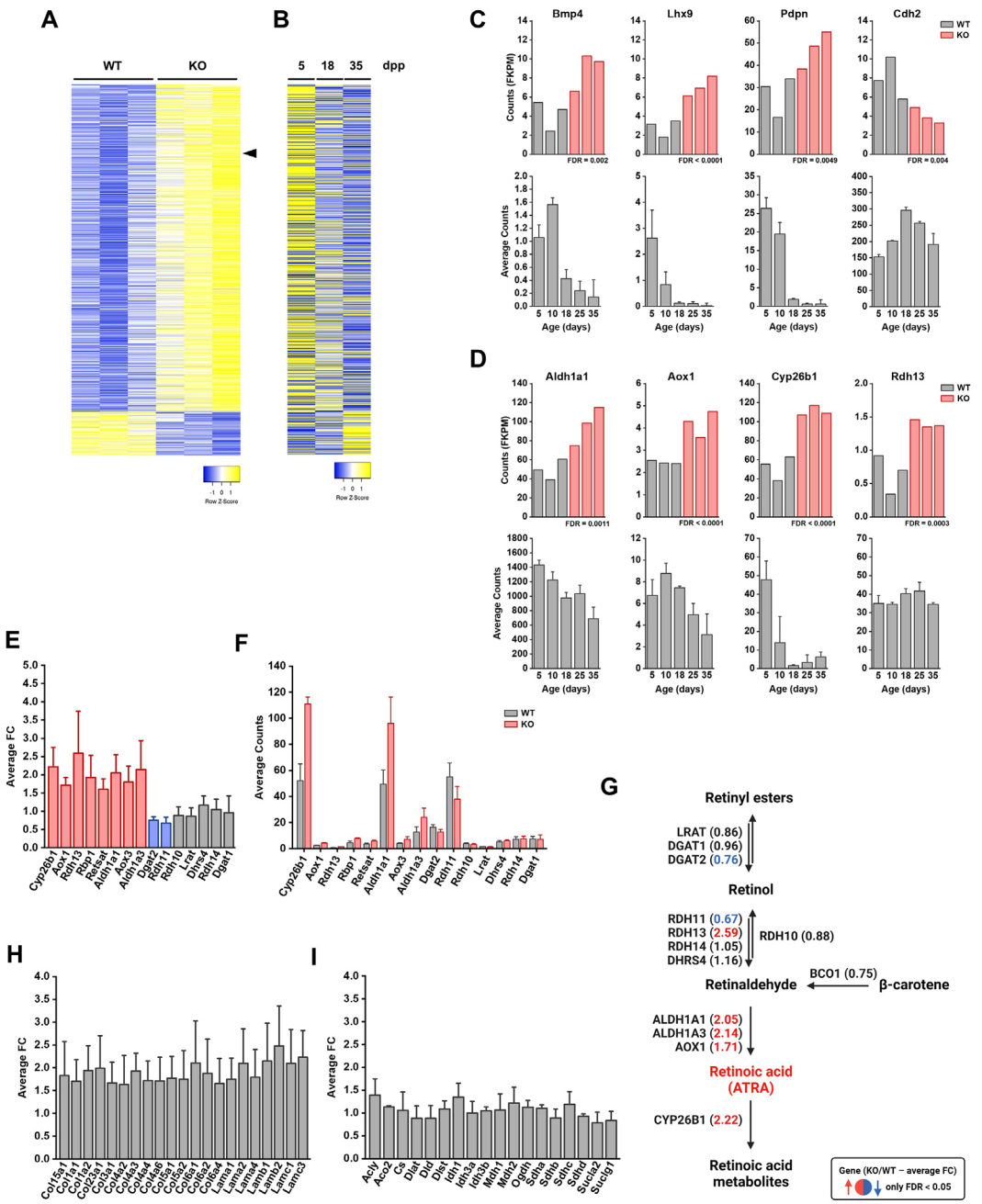


FIGURE 5 | FBXO38-deficient Sertoli cells exhibit a maturation defect. **(A)** Normalized counts (fragments per kilobase million, FKPM) from RNA-seq analysis of *Fbxo38* wild-type (WT) and knockout (KO) young adult (8 weeks old) Sertoli cells were visualized as a heat map showing gene expression normalized to the highest and lowest obtained count. Only 1,170 significantly regulated genes (FDR <0.05) are shown. The arrowhead points to Cyp26b1 gene. **(B)** Publicly available data of gene expressions in Sertoli cells from a different age of juvenile mouse males. The same set of genes as in (A) was visualized as a heat map showing gene expression normalized to the highest and lowest obtained count. Each time point represents the mean value of three different Sertoli cells isolations (GEO accession number GSE59698) (Zimmermann et al., 2015). Publicly available data were normalized using a GREIN application (http://www.ilincs.org/apps/grein/) (Mahi et al., 2019); dpp, days postpartum. **(C)** Upper panel: Expression (FKPM) of four markers of Sertoli cell maturation (Bmp4, Lhx9, Pdpn, and Cdh2) in *Fbxo38* WT (grey) and KO (red) Sertoli cells (dataset as in A). Lower panel: Time course of publicly available gene expression of the same set of genes during Sertoli cell maturation. Each time point represents the mean value obtained from three different Sertoli cell isolations. Publicly available data were obtained and normalized as in (B). **(D)** Upper panel: Expression (FKPM) of four genes involved in retinoic acid metabolism (Aldh1a1, Aox1, Cyp26b1, and Rdh13) in *Fbxo38* WT and KO Sertoli cells (dataset as in A). Lower panel: Time course of publicly available gene expression of the same set of genes during Sertoli cell maturation. Each time point represents the mean value obtained from three different Sertoli cell isolations. Publicly available data were obtained and normalized as in (B). **(E)** An average fold change (KO/WT; $n = 3$) of genes involved in retinoic acid metabolism. The graph represents an excerpt from the dataset shown in (A). Red columns show significantly upregulated genes in KO Sertoli cells (FDR <0.05). The blue columns show significantly downregulated genes in KO Sertoli cells (FDR <0.05). **(F)** An average count (FKPM) of genes involved in retinoic acid metabolism. The graph represents

(*Continued*)

FIGURE 5 | an excerpt from the dataset shown in (A). Each bar represents the mean value (WT—grey; KO—red; *n* = 3). **(G)** Schematic representation of retinoic acid metabolism with depicted fold changes in brackets—as in (D). The red font was used to highlight significantly upregulated genes in KO Sertoli cells (FDR <0.05). The blue font was used to highlight significantly downregulated genes in KO Sertoli cells (FDR <0.05). **(H)** Average fold changes (KO/WT; *n* = 3) of genes encoding laminins and collagens. The graph represents an excerpt from the dataset shown in (A). **(I)** Average fold changes (KO/WT; *n* = 3) of genes involved in the citric acid (Krebs) cycle. The graph represents an excerpt from the dataset shown in (A).

signaling pathway (**Figure 5D**). To obtain a complete picture of this pathway, we profiled an entire set of genes associated with retinoic acid signaling, and this analysis showed the scale of disruption of ATRA metabolism in KO testes (**Figures 5D–F**). Significant changes are highlighted in the illustrative scheme of this signaling pathway (**Figure 5G**). Furthermore, the gene ontology (GO) and over-representation analysis (ORA) revealed substantial changes in other signaling pathways and gene clusters (**Supplementary Figures S5D,E**). We identified a significant upregulation in the genes encoding extracellular matrix components of the basal lamina surrounding the seminiferous tubules (**Figure 5H**). Moreover, several targets of the Hippo signaling pathway, a sensor of intercellular and cell-to-extracellular matrix interactions, were deregulated (**Supplementary Figures S5F**).

Other metabolic and signaling pathways were also profiled to characterize the activity of KO Sertoli cells. While genes involved in the TCA (or Krebs) cycle were not altered between WT and KO cells (**Figure 5I**, **Supplementary Figures S5**), components and transcriptional targets of the Wnt and Hedgehog signaling pathways were upregulated (**Supplementary Figures S5G**). To obtain a complete picture of the paracrine activity of mutant Sertoli cells, we profiled the expression of secreted ligands known to be active and vital in Sertoli cell-dependent regulation of spermatogenesis. In addition to previously mentioned factors, such as *Wnt5* and *Wnt6*, and Bone morphogenetic protein 4 (*Bmp4*), changes in expression of an array of these secreted ligands, including Inhibin A, a negative spermatogenesis inhibitor secreted by Sertoli cells, were observed (**Supplementary Figures S5H**). Importantly, genes upregulated by follicle-stimulating hormone (FSH) or testosterone signaling were not altered in mutant Sertoli cells, suggesting that their differential gene expression profile is not the result of an endocrine imbalance (**Supplementary Figures S5F**) (Chaudhary and Skinner, 1999; Hu et al., 2010).

In summary, we have shown that the absence of FBXO38 disrupts maturation processes in Sertoli cells, a phenotype correlating with pathological changes observed in seminiferous tubules of FBXO38-deficient mice.

DISCUSSION

In our study focused on the role of FBXO38 *in vivo*, we demonstrate that loss of FBXO38 results in reduced prenatal and postnatal growth of several organs and tissues, especially male reproductive organs. To determine how FBXO38 acts on the cellular level, we focused on postnatal testicular development, as male reproduction and the testicular epithelium are severely affected in FBXO38-deficient mice.

In early postnatal development, we show that FBXO38 is expressed predominantly in spermatogonial stem cells. These cells start to divide and differentiate during the first wave of spermatogenesis, giving rise to a group of progenitor cells and, consequently, spermatocytes and spermatids. Although we did not observe a general decrease in spermatogonia number in individual *Fbxo38* KO tubules compared to WT, the smaller size of juvenile KO testes implied the their overall number would be lower. Importantly, FBXO38 seems to be predominantly expressed by Sertoli cells in adult testis, although we cannot rule out that FBXO38 expression in adult spermatogonia is below the immunodetection limit and they might still be affected by its loss. Moreover, we observed that the SALL4A protein, suppressor of spermatogonia differentiation (Yamaguchi et al., 2015), is upregulated during the first wave of spermatogenesis in FBXO38-deficient testes, suggesting either deregulation of its gene expression or its aberrant protein degradation. Such aberrant SALL4A expression could alter the dynamic of spermatocyte emergence, as we observed in juvenile testes of FBXO38-deficient mice. Moreover, a comparable effect of aberrant *Sall4* expression on stem cells differentiation was observed in the hematopoietic system (Milanovich et al., 2015). Interestingly, *Sall4a* expression is controlled by all-trans retinoic acid (ATRA) signaling (Gely-Pernot et al., 2015), which is crucial for the regulation of spermatogenesis (Gewiss et al., 2020). ATRA is released from Sertoli cells, and it activates a pro-mitotic program in spermatogonia (Endo et al., 2017). In differentiated spermatogonia, ATRA promotes the expression of an essential gatekeeper of meiotic initiation *Stra8* (Koubova et al., 2006). As it is activated only during a distinct spermatogenic tubule stage, STRA8 is commonly used as a marker for ATRA activity and to determine a specific stage (VII-VIII) in tubule development (Gewiss et al., 2020). By using this staging method, we revealed that *Fbxo38* KO animals consistently show weaker STRA8 staining and, at the same time, a significant reduction in the $SCP3^{+}$ spermatocyte population. Taken together, these observations strongly suggest that FBXO38-deficiency results in defective differentiation of spermatogonia.

Testes isolated from FBXO38-deficient mice were substantially smaller when compared to WT. Since we found that FBXO38 is predominantly expressed in Sertoli cells in adult testes, the major determinant of testis size (O'Donnell et al., 2022), we decided to focus on FBXO38 function in this somatic cell type. By detailed transcriptomic analysis of WT and KO Sertoli cells, we discovered that RA metabolism was one of the most affected pathways. *Aldh1a1* and *Aldh1a3* (otherwise known as *Raldh1/2*), both upregulated in KO Sertoli cells, are the genes responsible for the metabolic conversion of retinaldehyde and ATRA. They were shown to be necessary for spermatogonia differentiation, and their overexpression should lead to an

increased amount of ATRA (Raverdeau et al., 2012). As the activation of RA-dependent genes has to be under strict spatiotemporal control, ATRA-mediated signaling leads to transcriptional activation of the *CYP26B1* gene. This enzyme is required for the accelerated clearance of ATRA from cells, and its expression decreases with the onset of puberty (Li et al., 2009). It is noteworthy that *Cyp26b1* is one of the most upregulated genes in *Fbxo38* KO Sertoli cells. Significantly, a high and precise level of Sertoli cell delivered RA is necessary for spermatogonia mitotic entry (Gewiss et al., 2020) and, accordingly, deletion of the *Cyp26b1* gene or its pharmacological inhibition leads to the premature entry of germ cells into meiosis (Bowles et al., 2006; Koubova et al., 2006). Therefore, we hypothesize that FBXO38 deficiency could disrupt ATRA production control and, thus, inappropriate spermatogonial stimulation. In addition to RA signaling, we observed upregulation of several signaling pathways, such as Wnt, Hedgehog, and Hippo. Moreover, an aberrant expression of the extracellular matrix components could impair spermatogonia activation (Siu and Cheng, 2004). Thus, the significantly different transcriptional landscape of KO Sertoli cells results in spermatogenesis defects in adult FBXO38-deficient animals. Analysis of this profile showed a striking resemblance to the gene expression signature of immature Sertoli cells. However, we did not observe any significant structural differences in mutant Sertoli cells, although the nuclei of adult KO cells seemed smaller in volume, which is one of the characteristics of their immaturity as shown in different mammals (Auharek and de França, 2010; Avelar et al., 2010). Nonetheless, Sertoli cell immaturity is a broad term, and the nucleus shape could be a result of complex changes in seminiferous tubule architecture and its cellular composition. To this point, further studies are needed to show the impact of altered gene expression of KO Sertoli cells on their biology and whether this altered gene expression is the result of maturation arrest or dedifferentiation process.

As with FBXO38, its substrate ZXDB zinc finger protein expression is restricted to Sertoli cells, where it is significantly stabilized in *Fbxo38* KO animals. We have recently discovered that ZXDB acts as a positive regulator of centromeric protein CENP-B. Interestingly, as in the case of *Fbxo38*, *Cenpb* KO mice are growth retarded and have reduced testicular weight (Hudson et al., 1998). In accordance with our data from cancer cell lines, we observed an increased centromeric signal in KO Sertoli cells. Sertoli cells do not have distinguished centromeric signals but rather a diffuse one surrounding chromocenters associated with the nucleolus. The number of chromocenters and the localization and genomic regions associated with them undergo dynamic control during differentiation, as described in different systems, including hematopoietic and Sertoli cells (Krzanowska and Bilinska, 2000; Wijchers et al., 2015). It was shown that the forced location of gene loci to chromocenters leads to their heterochromatinization and subsequent transcriptional silencing (Francastel et al., 1999; Brown et al., 2001). The previous report suggests a correlation between the localization of centromeres to chromocenters and rRNA expression in nucleoli (Haaf et al., 1990). Although we did not specifically measure rRNA production in FBXO38-deficient cells, we observed a significant decrease in their nucleophosmin signal. Notably, the levels of nucleophosmin were previously used to indirectly measure rRNA production in nucleoli (Yung et al., 1985; Maggi et al., 2008). The activity of rRNA genes has an enormous effect on cell function and its differentiation potential. For example, in oocytes, distributions of pericentromeric chromatin around nucleoli (speckled or ring-type) distinguish not only nucleoli activity but also the pluripotent potential of fertilized oocytes. Like the one observed in Sertoli cells, ring-type distribution was associated with silenced rRNA genes and full pluripotency potential (Bonnet-Garnier et al., 2012; Kresoja-Rakic and Santoro, 2019). Interestingly, Sertoli cells are giant cells with an abundant rough endoplasmic reticulum. We hypothesized that their function would require higher production of ribosomes, as shown in other large cell types, including neuronal ones (Lipshultz et al., 1982). Moreover, other factors regulating centromere and pericentromeric chromatin have already been shown to impact adult and fetal testes. Alpha-thalassemia/mental retardation, X-linked (ATRX), which controls the establishment of pericentromeric heterochromatin regions, is essential for Sertoli cell proliferation and survival. Mice deficient in *Atrx* have reduced tubule expansion, ultimately impacting the testicular size and its architecture in adulthood (Bagheri-Fam et al., 2011).

In summary, we have described the impact of FBXO38 loss on murine development. This understudied ubiquitin ligase acts as an important factor in the control of organ size, including the male reproductive system. Specifically, we show that FBXO38 is functionally expressed in Sertoli cells and is required for transcriptional control of their maturation and spermatogonia stimulation.

MATERIALS AND METHODS

Mouse Model

Fbxo38 KO mice (Δexon 4) were generated in a C57BL/6N background using the CRISPR/Cas9 genome-editing system. For this purpose, the Cas9 protein and gene-specific sgRNAs (Integrated DNA Technologies) were used for zygote electroporation using a protocol described previously (Chen et al., 2016). Single guide RNA sequences with the a protospacer adjacent motif (PAM) in underlined bold (3′end) were as follows:

sgRNA target 1: TTAAGTAAATACAGGTAAGC**CGG**
sgRNA target 2: GGGTGTGCTGTTTAGAGGGC**AGG**.

The genome editing was confirmed in the founder mouse using primers: 5′-GGCTGTTCTCCTCTTTGTG-3′ and 5′-TCC TTCCTCCTGCTAGACTCT-3’. The mutant allele was backcrossed for two generations to C57BL/6N mice to obtain homozygous animals. Animals were maintained in a controlled, specific pathogen-free environment at the Animal Facility of the Czech Center for Phenogenomics in Vestec, Institute of Molecular Genetics of the Czech Academy of Sciences, Czech Republic. All animal experiments were approved by the Animal Care and Use Committee of the Institute of Molecular Genetics of the CAS (protocol 115/2016) and were in accordance with the

Czech Act No. 246/1992 Coll. and European directive 2010/63/EU.

Organs were collected from the mice after euthanasia. Most experiments were carried out on samples collected from adult mice. To enrich certain cell populations in spermatogenesis and to monitor the first wave of spermatogenesis, we used infant and juvenile littermate mice. The age and number of the mice used in this study is indicated in the figure legends. For mouse embryonic fibroblasts (MEFs) preparation, heterozygous animals were bred until females produced vaginal plugs. At the embryonic day (E) 13.5, females were euthanized and embryos were dissected. For examination of female reproductive organs, females from the same litter were housed in the same cages until dissection, in order to avoid differences in the estrous cycle.

Sperm Count

To evaluate epididymal sperm counts, both caudae epididymides were dissected, placed into 1 ml of PBS, minced, and shaken to allow the sperms to swim out. After 5 min of incubation, suspensions were diluted for quantitative assessments, and individual counts were determined using the Bürker chamber. For sperm morphology and motility assessment, the sperms were released from cauda and incubated in a medium containing methyl-β-cyclodextrin (0.75 mM) for 30 min at 37°C and observed under Zen Axio Vert. A1 microscope (Zeiss).

Cell Culture

NIH/3T3 and HEK293T (both American Type Culture Collection, ATCC) cell lines were cultured in Dulbecco′s Modified Eagle′s Medium (DMEM) media supplemented with 10% fetal bovine serum (FBS), and antibiotics (penicillin, streptomycin, and gentamicin). TM4 (ATCC) cell line was cultured in a 1:1 mixture of Ham'S F12 and DMEM supplemented with 5% horse serum and 2.5% FBS and antibiotics. Primary MEFs were isolated from E13.5 mouse embryos. After dissection, head and internal organs were removed, and embryos were minced in 0.05% trypsin/EDTA. After 30 min of incubation, dissociated cells were washed, and cultured DMEM supplemented with 10% fetal bovine serum (FBS), non-essential amino acids, L-glutamine, and antibiotics. For immortalization of MEFs, human cell line HEK293T was co-transfected with pLenti CMV/TO SV40 Small and Large T antigen (Addgene, #22298) along with pCMV-dR8.2 (Addgene, #8455) and pCMV-VSV-G (Addgene, #8454). The cells were transfected using polyethylenimine (PEI MW 25000, Polysciences) and maintained in DMEM supplemented with 10% FBS and antibiotics. The lentivirus containing media was collected 48 h after transfection, mixed with Polybrene (Sigma Aldrich), and used for infecting the primary fibroblasts. TM4 cells stably expressing HA-tagged ZXDA were generated by co-transfection of pBABE-HA-ZXDA along with pCMV-VSV-G (Addgene, #8454) and gag/pol plasmid (Addgene, #14887) into HEK293T cells. The viral containing media was collected 48 h after transfection and used for infecting TM4 cells. Cells were selected in a medium containing puromycin (1 μg/ml). For transient transfection, HEK293T cells were transfected with HA-tagged ZXDA or SALL4 using polyethylenimine (PEI MW 25000, Polysciences) and collected 48 h after transfection. All the cells and cell lines were cultured in a humidified incubator at 37°C with 5% CO2. Cycloheximide (100 μg/ml) or MLN4924 (2 μM) were used where indicated.

Immunoblotting

For whole testes protein lysates, tunica was mechanically removed, and the tissue was placed in a lysis buffer (150 mM NaCl, 50 mM Tris pH 7.5, 0.4% Triton X-100, 2 mM CaCl2, 2mM MgCl2, 1 mM EDTA with addition of phosphatase and protease inhibitor cocktail (MedChem Express) and Benzonase nuclease (0.125 U/μl; Santa Cruz) and homogenized using TissueLyser (Qiagen). After 30 min of incubation on ice, lysates were mixed with an equal volume of 2% SDS in 50 mM Tris-HCl, pH 8, heated for 5 min at 95°C, and cleared by centrifugation.

For the fractionation of MEF protein lysates, cells were washed with ice-cold PBS and lysed for 10 min in the lysis buffer without Benzonase nuclease, centrifuged for 5 min, at 3,000 rpm, and the soluble fraction was separated. The remaining chromatin fraction was further lysed for 10 min in the same buffer with the addition of Benzonase nuclease (1.25 U/μl), mixed with 2% SDS in 50 mM Tris-HCl, pH 8, to final concentration, 1%, heated for 5 min at 95°C and cleared by centrifugation. Protein concentration was determined by the BCA method (ThermoFisher). Samples were prepared by mixing with Bolt™ LDS Sample Buffer (Thermo Fisher Scientific) supplemented with 10% β-mercaptoethanol (Sigma Aldrich), heated for 5 min at 95°C and then separated using a NuPAGE™ 4–12% gradient Bis-Tris gel (Invitrogen). Afterward, the samples were transferred to a PVDF membrane (Amersham), blocked with 5% milk (ChemCruz), and incubated with indicated antibodies diluted in 3% BSA (PanReac Applichem) in TBS-T overnight at 4°C. The HRP-conjugated secondary antibodies (Cell Signaling) were diluted in 5% milk in TBS-T. The membranes were developed using WesternBright ECL (Advansta) or SuperSignal™ West Femto Maximum Sensitivity Substrate (Thermo Scientific).

Protein Immunoprecipitation and Affinity Purification

Transfected cells were collected and lysed in the lysis buffer (150 mM NaCl, 50 mM Tris pH 7.5, 0.4% Triton X-100, 2 mM CaCl2, 2 mM MgCl2, 1 mM EDTA, supplemented with phosphatase and protease inhibitors) in the presence of Benzonase nuclease (0.125 U/μl) for 30 min on ice. The lysates precleared by centrifugation were then incubated with Pierce™ anti-HA Magnetic Beads (Thermo Fisher Scientific). After series of washes, immunoprecipitated HA-tagged proteins were eluted with 1x Bolt™ LDS Sample Buffer (Thermo Fisher Scientific). Eluates were then supplemented with β-mercaptoethanol (Sigma Aldrich) and incubated at 95°C for 5 min.

MEF with inducible expression of Strep-FLAG-tagged ZXDA were collected 24 h after doxycycline treatment and lysed in the identical buffer. The lysates precleared by centrifugation were then incubated with Strep-Tactin® Sepharose resin (IBA Lifesciences). Purified Strep-tagged proteins were then eluted

by desthiobiotin using Buffer E (IBA Lifesciences) and subsequently prepared for immunoblotting as described above.

Seminiferous Tubule Squash

Squashed seminiferous tubules were prepared according to the previously published protocol (Page et al., 1998). Isolated testes without tunica albuginea were fixed in 2% formaldehyde in PBS containing 0.05% Triton X-100 for 10 min at room temperature. Isolated tubules were placed on a slide with the fixative, gently minced, and squashed with coverslip. Slides were frozen in liquid nitrogen, the coverslips were removed and slides were three times washed with PBS before immunolabeling.

Histology and Immunofluorescence Staining

Tissues were fixed in modified Davidson's fluid for 24 h, dehydrated, and processed in automated tissue processor (Leica) prior to paraffin embedding on paraffin station (Leica). Paraffin sections of 4 µm thickness were deparaffinized, hydrated, and stained with hematoxylin and eosin (H&E) or periodic acid-Schiff (PAS) using Ventana Symphony Slide Stainer (Roche).

Antigen retrieval for immunofluorescence staining was performed in 0.01 M citrate buffer, pH 6, in a steam bath for 18 min. Afterward, slides were permeabilized with 0.2% Triton X-100 in PBS for 10 min and blocked with 5% goat and 5% horse serum for 1 h. The samples were incubated with the indicated primary antibodies in a humidified chamber O/N at 4°C. The signal was visualized using AlexaFluor-conjugated secondary antibodies (Abcam). DAPI was used to counterstain DNA. Slides were mounted with ProLong Gold Antifade Mountant (Invitrogen). For staining of testicular squashes, the slides were washed with PBS and blocked with 3% BSA with 0.1% Triton X-100 in PBS for 45 min. Incubation with the indicated primary antibodies was carried out for 2 h in RT followed by washes. Secondary antibodies incubation, DNA staining and mounting was performed as described above. Images were acquired using Axio Imager Zeiss 2 (EC Plan—Neofluar objectives) and analyzed with ZEN2.3 or ImageJ software. ImageJ macro, used for normalization and quantification of centromeric signal, was developed by IMG microscopy facility and is available upon request. Composite images of H&E or PAS-stained organs were obtained by scanning using Axio Scan. Z1 slide scanner (Zeiss). Composite images of fluorescent-stained testes were obtained on DMi8 inverted microscope (Leica). The apoptotic cells in the tissue sections were determined by a terminal deoxynucleotidyl transferase-mediated dUTP nick-end labeling (TUNEL) assay, using the TACS 2 TdT-DAB *In Situ* Apoptosis Detection Kit (Trevigen) according to the protocol.

Sertoli Cell RNA Isolation

Dissected testes were decapsulated and processed into a single-cell suspension using a previously described protocol (Bellvé et al., 1977). Briefly, seminiferous tubules were submerged in EKRB medium (120.1 mM NaCl, 4.8mM KCl, 25.2 mM NaHCO3, 1.2 mM KH2PO2, 1.2 mM MgSO4, 1.3 mM CaCl2, 11 mM glucose, 1 mM L-glutamine, 4.4 mM sodium lactate, 6.5 mM sodium pyruvate, 20 mM HEPES, non-essential amino acid and penicillin-streptomycin) with collagenase (0.5 mg/ml) and incubated for 20 min at 32°C. Tubules were disrupted by gently pipetting up and down, followed by filtration through a 100 µm strainer. Cells were sedimented at 300 g for 10 min and resuspended in fresh EKRB medium. To identify the Sertoli cells, the cell suspension was stained with a commercially available antibody against the follicle-stimulating hormone receptor (FSHR) conjugated with phycoerythrin (Bioss, BS-20658R-PE) for 1 h. FSHR-positive Sertoli cells were sorted (Influx; BD Biosciences) into the RLT buffer (Qiagen) supplemented with β-mercaptoethanol. The RNA from the cells was isolated using an RNeasy Micro Kit (Qiagen) according to the manufacturer's protocol. FACS data were analyzed by FlowJo v10 software.

RNA-Seq

The quantity and quality of isolated RNA was measured using Qubit (ThermoFisher Scientific) and analyzed by Agilent 2,100 Bioanalyser (Agilent Technologies). Sequencing libraries were prepared with Takara Smarter Stranded Total RNA-seq Kit v2 Pico Input Mammalian (PN 634413). Libraries were sequenced on the Illumina NextSeq® 500 instrument using the 76bp single-end configuration.

For subsequent read processing, a bioinformatics pipeline nf-core/rnaseq version 1.4.2, was used (Ewels, 2019). Individual steps included removing sequencing adaptors and low-quality reads with Trim Galore! (http://www.bioinformatics.babraham.ac.uk/projects/trim_galore/), mapping to reference genome GRCm38 (Ensembl annotation version 98) with HISAT2 and quantifying expression on gene level with featureCounts (Liao et al., 2014; Kim et al., 2015; Cunningham et al., 2019). Per gene mapped counts served as input for differential expression analysis using DESeq2 R Bioconductor package (Love et al., 2014). Prior to the analysis, genes not expressed in at least two samples were discarded. We supplied experimental model assuming sample group as main effect. Resulting per gene expression log2-fold changes were used for differential expression analysis. Genes exhibiting minimal absolute log2-fold change value of log2 (1.5) and statistical significance (FDR <0.05) between compared groups of samples were considered as differentially expressed. As next, gene set over representation analysis was done using gene length bias aware algorithm implemented in goseq R Bioconductor package with KEGG pathways and GO terms gene sets (Young et al., 2010).

For individual genes expression comparison, raw read counts were normalized using fragment counts per kilobase of feature length per million mapped reads (FPKM) based on sum of lengths of all gene exons.

Gene set enrichment analysis (GSEA) was performed using GSEA v.4.1.0 software. Over-Representation Analysis (ORA) was performed using the WEB-based GEne SeT AnaLysis Toolkit (http://www.webgestalt.org/). Publicly available data from the GEO database were normalized using the GREIN

application (http://www.ilincs.org/apps/grein/) (Edgar et al., 2002; Mahi et al., 2019).

Quantification and Statistical Analysis

A heatmap was created with Heatmapper (www.heatmapper.ca) (Babicki et al., 2016); scRNA-seq data were visualized using the Loupe cell browser (https://www.10xgenomics.com/products/loupe-browser). Differences between Fbxo38 WT and KO groups were evaluated by an unpaired two-tailed *t*-test, while a chi-square test was used to assess the mouse offspring ratios. p-value < 0.05 was considered significant. To calculate the statistical significance of young male sperm count difference, the non-parametric Mann-Whitney *U* test was performed. For RNA-seq data, p-values and FDR were calculated; FDR <0.05 was considered significant. Individual data points and group means are shown in figures. The statistical analyses were performed using OriginPro 2021 (OriginLab). Protein identity and similarity, and MUSCLE alignment was assessed by MegAlign Pro (DNAStar).

The maximum normalized signal intensity was determined by measuring the intensity in a circle corresponding to the diameter of the signal. The average background value (measured in four areas) was subtracted from the obtained signal intensity value. Intensity of cells (the number is specified in each figure) was measured from at least two animals of each genotype. For ACA staining intensity in testicular squashes, the cell types were grouped according to specific features, and at least 20 cells of each cell type were measured in two animals of each genotype in two independent experiments. The number of specifically stained cells was determined by counting these cells from all round tubules obtained from the middle cross-sections and shown as the number of positive cells per round tubule. The number of positive cells from at least two animals of each genotype were measured in two independent experiments. Epithelial height was determined by measuring the diameter of round tubules in two perpendicular axes with subtracting the diameter of the lumen. At least 120 tubules from two animals of each genotype were measured in two independent experiments. All the analyses of microscopy images were performed by ImageJ software or ZEN2.3 (Zeiss). The composition of cell types in a seminiferous tubule squash was determined by counting the cells and grouping them according to specific staining. Fractions were shown as a percentage of the number of whole testis squash from wild-type animals. Sertoli cell count was used as a reference for normalization between genotypes.

Litter size was determined by monitoring the birth within 18–21 days after recording vaginal plug.

DATA AVAILABILITY STATEMENT

RNA-seq data are deposited at the ArrayExpress database under accession number E-MTAB-11271.

ETHICS STATEMENT

All animal experiments were approved by the Animal Care and Use Committee of the Institute of Molecular Genetics of the CAS (protocol 115/2016) and were in accordance with the Czech Act No. 246/1992 Coll. and European directive 2010/63/EU.

AUTHOR CONTRIBUTIONS

Conceptualization, LC, and ND; investigation, ND, EZ, and MM; writing-original draft preparation, ND, and LC; writing-review and editing, ND, VK, and LC; methodology, RS, PK, JP, and DF; supervision, LC; funding acquisition, LC, and VK. All authors have read and agreed to the published version of the manuscript.

FUNDING

This work was supported by the Czech Science Foundation (18-27408S) and the Czech Academy of Sciences. All experimental work was performed at IMG. ND was partially supported by the Charles University Grant Agency (406317). Animal work was partially supported by LM2018126 (Czech Centre for Phenogenomics provided by MEYS CR).

ACKNOWLEDGMENTS

We thank the Light Microscopy Core Facility, IMG CAS, Prague, Czech Republic, for their support with the imaging presented herein, particularly Jan Valečka for designing ImageJ macro. We are also thankful to Michal Dibus and Hynek Wichterle for comments on the manuscript and Leslie F. Ryan for proofreading the manuscript. Illustrations were created with BioRender.com.

SUPPLEMENTARY MATERIAL

The Supplementary Material for this article can be found online at: https://www.frontiersin.org/articles/10.3389/fcell.2022.914053/full#supplementary-material

REFERENCES

Akçimen, F., Vural, A., Durmuş, H., Çakar, A., Houlden, H., Parman, Y. G., et al. (2019). A Novel Homozygous FBXO38 Variant Causes an Early-Onset Distal Hereditary Motor Neuronopathy Type IID. *J. Hum. Genet.* 64 (11), 1141–1144. doi:10.1038/s10038-019-0652-y

Aleksandrova, A., Galkin, O., Koneni, R., and Fontes, J. D. (2010). An N- and C-Terminal Truncated Isoform of Zinc Finger X-Linked Duplicated C Protein Represses MHC Class II Transcription. *Mol. Cell Biochem.* 337 (1-2), 1–7. doi:10.1007/s11010-009-0280-5

Auharek, S. A., and de França, L. R. (2010). Postnatal Testis Development, Sertoli Cell Proliferation and Number of Different Spermatogonial Types in C57BL/6J Mice Made Transiently Hypo- and Hyperthyroidic during the Neonatal Period. *J. Anat.* 216 (5), 577–588. doi:10.1111/j.1469-7580.2010.01219.x

Avelar, G. F., Oliveira, C. F. A., Soares, J. M., Silva, I. J., Dobrinski, I., Hess, R. A., et al. (2010). Postnatal Somatic Cell Proliferation and Seminiferous Tubule Maturation in Pigs: A Non-random Event. *Theriogenology* 74 (1), 11–23. doi:10.1016/j.theriogenology.2009.12.014

Babicki, S., Arndt, D., Marcu, A., Liang, Y., Grant, J. R., Maciejewski, A., et al. (2016). Heatmapper: Web-Enabled Heat Mapping for All. *Nucleic Acids Res.* 44 (W1), W147–W153. doi:10.1093/nar/gkw419

Baek, K., Scott, D. C., and Schulman, B. A. (2021). NEDD8 and Ubiquitin Ligation by Cullin-RING E3 Ligases. *Curr. Opin. Struct. Biol.* 67, 101–109. doi:10.1016/j.sbi.2020.10.007

Bagheri-Fam, S., Argentaro, A., Svingen, T., Combes, A. N., Sinclair, A. H., Koopman, P., et al. (2011). Defective Survival of Proliferating Sertoli Cells and Androgen Receptor Function in a Mouse Model of the ATR-X Syndrome. *Hum. Mol. Genet.* 20 (11), 2213–2224. doi:10.1093/hmg/ddr109

Baumal, R., Bailey, D., Giwercman, A., Skakkebaek, N., Stratis, M., and Marks, A. (1989). A Novel Maturation Marker for Human Sertoli Cells. *Int. J. Androl.* 12 (5), 354–359. doi:10.1111/j.1365-2605.1989.tb01324.x

Bellvé, A. R., Millette, C. F., Bhatnagar, Y. M., and O'Brien, D. A. (1977). Dissociation of the Mouse Testis and Characterization of Isolated Spermatogenic Cells. *J. Histochem Cytochem.* 25 (7), 480–494. doi:10.1177/25.7.893996

Birk, O. S., Casiano, D. E., Wassif, C. A., Cogliati, T., Zhao, L., Zhao, Y., et al. (2000). The LIM Homeobox Gene Lhx9 is Essential for Mouse Gonad Formation. *Nature* 403 (6772), 909–913. doi:10.1038/35002622

Bonnet-Garnier, A., Feuerstein, P., Chebrout, M., Fleurot, R., Jan, H. U., Debey, P., et al. (2012). Genome Organization and Epigenetic Marks in Mouse Germinal Vesicle Oocytes. *Int. J. Dev. Biol.* 56 (10-12), 877–887. doi:10.1387/ijdb.120149ab

Bowles, J., Knight, D., Smith, C., Wilhelm, D., Richman, J., Mamiya, S., et al. (2006). Retinoid Signaling Determines Germ Cell Fate in Mice. *Science* 312 (5773), 596–600. doi:10.1126/science.1125691

Brown, K. E., Amoils, S., Horn, J. M., Buckle, V. J., Higgs, D. R., Merkenschlager, M., et al. (2001). Expression of α- and β-globin Genes Occurs within Different Nuclear Domains in Haemopoietic Cells. *Nat. Cell Biol.* 3 (6), 602–606. doi:10.1038/35078577

Chaudhary, J., and Skinner, M. K. (1999). E-box and Cyclic Adenosine Monophosphate Response Elements are Both Required for Follicle-Stimulating Hormone-Induced Transferrin Promoter Activation in Sertoli Cells. *Endocrinology* 140 (3), 1262–1271. doi:10.1210/endo.140.3.6597

Chen, S., Lee, B., Lee, A. Y.-F., Modzelewski, A. J., and He, L. (2016). Highly Efficient Mouse Genome Editing by CRISPR Ribonucleoprotein Electroporation of Zygotes. *J. Biol. Chem.* 291 (28), 14457–14467. doi:10.1074/jbc.m116.733154

Cunningham, F., Achuthan, P., Akanni, W., Allen, J., Amode, M. R., Armean, I. M., et al. (2019). Ensembl 2019. *Nucleic Acids Res.* 47 (D1), D745–D751. doi:10.1093/nar/gky1113

Dickinson, M. E., Flenniken, A. M., Flenniken, A. M., Ji, X., Teboul, L., Wong, M. D., et al. (2016). High-throughput Discovery of Novel Developmental Phenotypes. *Nature* 537 (7621), 508–514. doi:10.1038/nature19356

Earnshaw, W. C., and Cooke, C. A. (1989). Proteins of the Inner and Outer Centromere of Mitotic Chromosomes. *Genome* 31 (2), 541–552. doi:10.1139/g89-103

Edelsztein, N. Y., Kashimada, K., Schteingart, H. F., and Rey, R. A. (2020). CYP26B1 Declines Postnatally in Sertoli Cells Independently of Androgen Action in the Mouse Testis. *Mol. Reprod. Dev.* 87 (1), 66–77. doi:10.1002/mrd.23302

Edgar, R., Domrachev, M., and Lash, A. E. (2002). Gene Expression Omnibus: NCBI Gene Expression and Hybridization Array Data Repository. *Nucleic Acids Res.* 30 (1), 207–210. doi:10.1093/nar/30.1.207

Endo, T., Romer, K. A., Anderson, E. L., Baltus, A. E., de Rooij, D. G., and Page, D. C. (2015). Periodic Retinoic Acid-STRA8 Signaling Intersects with Periodic Germ-Cell Competencies to Regulate Spermatogenesis. *Proc. Natl. Acad. Sci. U. S. A.* 112 (18), E2347–E2356. doi:10.1073/pnas.1505683112

Endo, T., Freinkman, E., de Rooij, D. G., and Page, D. C. (2017). Periodic Production of Retinoic Acid by Meiotic and Somatic Cells Coordinates Four Transitions in Mouse Spermatogenesis. *Proc. Natl. Acad. Sci. U. S. A.* 114 (47), E10132–E41. doi:10.1073/pnas.1710837114

Ernst, C., Eling, N., Martinez-Jimenez, C. P., Marioni, J. C., and Odom, D. T. (2019). Staged Developmental Mapping and X Chromosome Transcriptional Dynamics during Mouse Spermatogenesis. *Nat. Commun.* 10 (1), 1251. doi:10.1038/s41467-019-09182-1

Ewels, P. H. R., Peltzer, A., Moreno, D., Garcia, M., and Wang, C. (2019). nf-core/rnaseq: nf-core/rnaseq version 1.4.2 (Version 1.4.2). *Zenodo*.

Figueiredo, A. F. A., França, L. R., Hess, R. A., and Costa, G. M. J. (2016). Sertoli Cells are Capable of Proliferation into Adulthood in the Transition Region between the Seminiferous Tubules and the Rete Testis in Wistar Rats. *Cell Cycle* 15 (18), 2486–2496. doi:10.1080/15384101.2016.1207835

Francastel, C., Walters, M. C., Groudine, M., and Martin, D. I. K. (1999). A Functional Enhancer Suppresses Silencing of a Transgene and Prevents its Localization Close to Centromeric Heterochromatin. *Cell* 99 (3), 259–269. doi:10.1016/s0092-8674(00)81657-8

Gely-Pernot, A., Raverdeau, M., Teletin, M., Vernet, N., Féret, B., Klopfenstein, M., et al. (2015). Retinoic Acid Receptors Control Spermatogonia Cell-Fate and Induce Expression of the SALL4A Transcription Factor. *PLoS Genet.* 11 (10), e1005501. doi:10.1371/journal.pgen.1005501

Georges, A., Coyaud, E., Marcon, E., Greenblatt, J., Raught, B., and Frappier, L. (2019). USP7 Regulates Cytokinesis through FBXO38 and KIF20B. *Sci. Rep.* 9 (1), 2724. doi:10.1038/s41598-019-39368-y

Gewiss, R., Topping, T., and Griswold, M. D. (2020). Cycles, Waves, and Pulses: Retinoic Acid and the Organization of Spermatogenesis. *Andrology* 8 (4), 892–897. doi:10.1111/andr.12722

Greig, G. M., Sharp, C. B., Carrel, L., and Willard, H. F. (1993). Duplicated Zinc Finger Protein Genes on the Proximal Short Arm of the Human X Chromosome: Isolation, Characterization and X-Inactivation Studies. *Hum. Mol. Genet.* 2 (10), 1611–1618. doi:10.1093/hmg/2.10.1611

Griswold, M. D. (2016). Spermatogenesis: The Commitment to Meiosis. *Physiol. Rev.* 96 (1), 1–17. doi:10.1152/physrev.00013.2015

Griswold, M. D. (2018). 50 Years of Spermatogenesis: Sertoli Cells and Their Interactions with Germ Cells. *Biol. Reprod.* 99 (1), 87–100. doi:10.1093/biolre/ioy027

Haaf, T., Steinlein, C., and Schmid, M. (1990). Nucleolar Transcriptional Activity in Mouse Sertoli Cells Is Dependent on Centromere Arrangement. *Exp. Cell Res.* 191 (1), 157–160. doi:10.1016/0014-4827(90)90051-b

Hermann, B. P., Cheng, K., Singh, A., Roa-De La Cruz, L., Mutoji, K. N., Chen, I.-C., et al. (2018). The Mammalian Spermatogenesis Single-Cell Transcriptome, from Spermatogonial Stem Cells to Spermatids. *Cell Rep.* 25 (6), 1650–1667. doi:10.1016/j.celrep.2018.10.026

Hu, Z., Dandekar, D., O'Shaughnessy, P. J., De Gendt, K., Verhoeven, G., and Wilkinson, M. F. (2010). Androgen-induced Rhox Homeobox Genes Modulate the Expression of AR-regulated Genes. *Mol. Endocrinol.* 24 (1), 60–75. doi:10.1210/me.2009-0303

Hudson, D. F., Fowler, K. J., Earle, E., Saffery, R., Kalitsis, P., Trowell, H., et al. (1998). Centromere Protein B Null Mice are Mitotically and Meiotically Normal but Have Lower Body and Testis Weights. *J. Cell Biol.* 141 (2), 309–319. doi:10.1083/jcb.141.2.309

Jiang, X., Ma, T., Zhang, Y., Zhang, H., Yin, S., Zheng, W., et al. (2015). Specific Deletion of Cdh2 in Sertoli Cells Leads to Altered Meiotic Progression and Subfertility of Mice. *Biol. Reprod.* 92 (3), 79. doi:10.1095/biolreprod.114.126334

Kim, D., Langmead, B., and Salzberg, S. L. (2015). HISAT: A Fast Spliced Aligner with Low Memory Requirements. *Nat. Methods* 12 (4), 357–360. doi:10.1038/nmeth.3317

Koubova, J., Menke, D. B., Zhou, Q., Capel, B., Griswold, M. D., and Page, D. C. (2006). Retinoic Acid Regulates Sex-specific Timing of Meiotic Initiation in Mice. *Proc. Natl. Acad. Sci. U.S.A.* 103 (8), 2474–2479. doi:10.1073/pnas.0510813103

Krause, W. (1977). Serum Gonadotropins in the Rat after Prenatal Damage to the Testes by Busulfan and Their Reaction to Cryptorchidism, Castration and Administration of Testosterone. *Arzneimittelforschung* 27 (2), 401–403.

Kresoja-Rakic, J., and Santoro, R. (2019). Nucleolus and rRNA Gene Chromatin in Early Embryo Development. *Trends Genet.* 35 (11), 868–879. doi:10.1016/j.tig.2019.06.005

Krzanowska, H., and Bilinska, B. (2000). Number of Chromocentres in the Nuclei of Mouse Sertoli Cells in Relation to the Strain and Age of Males from Puberty to Senescence. *J. Reprod. Fertil.* 118 (2), 343–350. doi:10.1530/reprod/118.2.343

Lakpour, M. R., Aghajanpour, S., Koruji, M., Shahverdi, A., Sadighi-Gilani, M. A., Sabbaghian, M., et al. (2017). Isolation, Culture and Characterization of Human Sertoli Cells by Flow Cytometry: Development of Procedure. *J. Reprod. Infertil.* 18 (2), 213–217.

Li, H., MacLean, G., Cameron, D., Clagett-Dame, M., and Petkovich, M. (2009). Cyp26b1 Expression in Murine Sertoli Cells is Required to Maintain Male Germ Cells in an Undifferentiated State during Embryogenesis. *PLoS One* 4 (10), e7501. doi:10.1371/journal.pone.0007501

Liao, Y., Smyth, G. K., and Shi, W. (2014). FeatureCounts: An Efficient General Purpose Program for Assigning Sequence Reads to Genomic Features. *Bioinformatics* 30 (7), 923–930. doi:10.1093/bioinformatics/btt656

Lipshultz, L. I., Murthy, L., and Tindall, D. J. (1982). Characterization of Human Sertoli Cells *In Vitro*. *J. Clin. Endocrinol. Metabolism* 55 (2), 228–237. doi:10.1210/jcem-55-2-228

Love, M. I., Huber, W., and Anders, S. (2014). Moderated Estimation of Fold Change and Dispersion for RNA-Seq Data with DESeq2. *Genome Biol.* 15 (12), 550. doi:10.1186/s13059-014-0550-8

MacLean, G., Li, H., Metzger, D., Chambon, P., and Petkovich, M. (2007). Apoptotic Extinction of Germ Cells in Testes of Cyp26b1 Knockout Mice. *Endocrinology* 148 (10), 4560–4567. doi:10.1210/en.2007-0492

Maggi, L. B., Kuchenruether, M., Dadey, D. Y. A., Schwope, R. M., Grisendi, S., Townsend, R. R., et al. (2008). Nucleophosmin Serves as a Rate-Limiting Nuclear Export Chaperone for the Mammalian Ribosome. *Mol. Cell Biol.* 28 (23), 7050–7065. doi:10.1128/mcb.01548-07

Mahi, N. A., Najafabadi, M. F., Pilarczyk, M., Kouril, M., and Medvedovic, M. (2019). GREIN: An Interactive Web Platform for Re-analyzing GEO RNA-Seq Data. *Sci. Rep.* 9 (1), 7580. doi:10.1038/s41598-019-43935-8

Meng, X., Liu, X., Guo, X., Jiang, S., Chen, T., Hu, Z., et al. (2018). FBXO38 Mediates PD-1 Ubiquitination and Regulates Anti-tumour Immunity of T Cells. *Nature* 564 (7734), 130–135. doi:10.1038/s41586-018-0756-0

Meroni, S. B., Galardo, M. N., Rindone, G., Gorga, A., Riera, M. F., and Cigorraga, S. B. (2019). Molecular Mechanisms and Signaling Pathways Involved in Sertoli Cell Proliferation. *Front. Endocrinol.* 10, 224. doi:10.3389/fendo.2019.00224

Milanovich, S., Peterson, J., Allred, J., Stelloh, C., Rajasekaran, K., Fisher, J., et al. (2015). Sall4 Overexpression Blocks Murine Hematopoiesis in a Dose-dependent Manner. *Exp. Hematol.* 43 (1), 53–64. doi:10.1016/j.exphem.2014.09.004

Morimoto, Y., Ono, S., Imamura, A., Okazaki, Y., Kinoshita, A., Mishima, H., et al. (2017). Deep Sequencing Reveals Variations in Somatic Cell Mosaic Mutations between Monozygotic Twins with Discordant Psychiatric Disease. *Hum. Genome Var.* 4, 17032. doi:10.1038/hgv.2017.32

Oatley, J. M., and Brinster, R. L. (2012). The Germline Stem Cell Niche Unit in Mammalian Testes. *Physiol. Rev.* 92 (2), 577–595. doi:10.1152/physrev.00025.2011

O'Donnell, L., Smith, L. B., and Rebourcet, D. (2022). Sertoli Cells as Key Drivers of Testis Function. *Semin. Cell Dev. Biol.* 121, 2–9. doi:10.1016/j.semcdb.2021.06.016

Page, J., Suja, J. A., Santos, J. L., and Rufas, J. S. (1998). Squash Procedure for Protein Immunolocalization in Meiotic Cells. *Chromosome Res.* 6 (8), 639–642. doi:10.1023/a:1009209628300

Parra, M. T., Viera, A., Gómez, R., Page, J., Carmena, M., Earnshaw, W. C., et al. (2003). Dynamic Relocalization of the Chromosomal Passenger Complex Proteins Inner Centromere Protein (INCENP) and Aurora-B Kinase during Male Mouse Meiosis. *J. Cell Sci.* 116 (Pt 6), 961–974. doi:10.1242/jcs.00330

Pellegrini, M., Grimaldi, P., Rossi, P., Geremia, R., and Dolci, S. (2003). Developmental Expression of BMP4/ALK3/SMAD5 Signaling Pathway in the Mouse Testis: A Potential Role of BMP4 in Spermatogonia Differentiation. *J. Cell Sci.* 116 (Pt 16), 3363–3372. doi:10.1242/jcs.00650

Raverdeau, M., Gely-Pernot, A., Féret, B., Dennefeld, C., Benoit, G., Davidson, I., et al. (2012). Retinoic Acid Induces Sertoli Cell Paracrine Signals for Spermatogonia Differentiation but Cell Autonomously Drives Spermatocyte Meiosis. *Proc. Natl. Acad. Sci. U.S.A.* 109 (41), 16582–16587. doi:10.1073/pnas.1214936109

Saferali, A., Yun, J. H., Parker, M. M., Sakornsakolpat, P., Chase, R. P., Lamb, A., et al. (2019). Analysis of Genetically Driven Alternative Splicing Identifies FBXO38 as a Novel COPD Susceptibility Gene. *PLoS Genet.* 15 (7), e1008229. doi:10.1371/journal.pgen.1008229

Shang, D., Dong, L., Zeng, L., Yang, R., Xu, J., Wu, Y., et al. (2015). Two-stage Comprehensive Evaluation of Genetic Susceptibility of Common Variants in FBXO38, AP3B2 and WHAMM to Severe Chronic Periodontitis. *Sci. Rep.* 5, 17882. doi:10.1038/srep17882

Siu, M. K. Y., and Cheng, C. Y. (2004). Extracellular Matrix: Recent Advances on its Role in Junction Dynamics in the Seminiferous Epithelium during Spermatogenesis. *Biol. Reprod.* 71 (2), 375–391. doi:10.1095/biolreprod.104.028225

Skaar, J. R., Pagan, J. K., and Pagano, M. (2013). Mechanisms and Function of Substrate Recruitment by F-Box Proteins. *Nat. Rev. Mol. Cell Biol.* 14 (6), 369–381. doi:10.1038/nrm3582

Smaldone, S., Laub, F., Else, C., Dragomir, C., and Ramirez, F. (2004). Identification of MoKA, a Novel F-Box Protein that Modulates Krüppel-like Transcription Factor 7 Activity. *Mol. Cell Biol.* 24 (3), 1058–1069. doi:10.1128/mcb.24.3.1058-1069.2004

Sumner, C. J., d'Ydewalle, C., Wooley, J., Fawcett, K. A., Hernandez, D., Gardiner, A. R., et al. (2013). A Dominant Mutation in FBXO38 Causes Distal Spinal Muscular Atrophy with Calf Predominance. *Am. J. Hum. Genet.* 93 (5), 976–983. doi:10.1016/j.ajhg.2013.10.006

Wijchers, P. J., Geeven, G., Eyres, M., Bergsma, A. J., Janssen, M., Verstegen, M., et al. (2015). Characterization and Dynamics of Pericentromere-Associated Domains in Mice. *Genome Res.* 25 (7), 958–969. doi:10.1101/gr.186643.114

Wu, X., Gao, S., Wang, L., Bu, T., Wu, S., Zhou, L., et al. (2022). Role of Laminin and Collagen Chains in Human Spermatogenesis - Insights from Studies in Rodents and scRNA-Seq Transcriptome Profiling. *Semin. Cell Dev. Biol.* 121, 125–132. doi:10.1016/j.semcdb.2021.07.011

Yamaguchi, Y. L., Tanaka, S. S., Kumagai, M., Fujimoto, Y., Terabayashi, T., Matsui, Y., et al. (2015). Sall4 is Essential for Mouse Primordial Germ Cell Specification by Suppressing Somatic Cell Program Genes. *Stem Cells* 33 (1), 289–300. doi:10.1002/stem.1853

Young, M. D., Wakefield, M. J., Smyth, G. K., and Oshlack, A. (2010). Gene Ontology Analysis for RNA-seq: Accounting for Selection Bias. *Genome Biol.* 11 (2), R14. doi:10.1186/gb-2010-11-2-r14

Yung, B. Y.-M., Busch, R. K., Busch, H., Mauger, A. B., and Chan, P.-K. (1985). Effects of Actinomycin D Analogs on Nucleolar Phosphoprotein B23 (37,000 daltons/pI 5.1). *Biochem. Pharmacol.* 34 (22), 4059–4063. doi:10.1016/0006-2952(85)90387-9

Zimmermann, C., Stévant, I., Borel, C., Conne, B., Pitetti, J.-L., Calvel, P., et al. (2015). Research Resource: The Dynamic Transcriptional Profile of Sertoli Cells during the Progression of Spermatogenesis. *Mol. Endocrinol.* 29 (4), 627–642. doi:10.1210/me.2014-1356

Conflict of Interest: The authors declare that the research was conducted in the absence of any commercial or financial relationships that could be construed as a potential conflict of interest.

Publisher's Note: All claims expressed in this article are solely those of the authors and do not necessarily represent those of their affiliated organizations, or those of the publisher, the editors and the reviewers. Any product that may be evaluated in this article, or claim that may be made by its manufacturer, is not guaranteed or endorsed by the publisher.

Copyright © 2022 Dibus, Zobalova, Monleon, Korinek, Filipp, Petrusova, Sedlacek, Kasparek and Cermak. This is an open-access article distributed under the terms of the Creative Commons Attribution License (CC BY). The use, distribution or reproduction in other forums is permitted, provided the original author(s) and the copyright owner(s) are credited and that the original publication in this journal is cited, in accordance with accepted academic practice. No use, distribution or reproduction is permitted which does not comply with these terms.

Supplementary Material

FBXO38 Ubiquitin Ligase Controls Sertoli Cell Maturation.

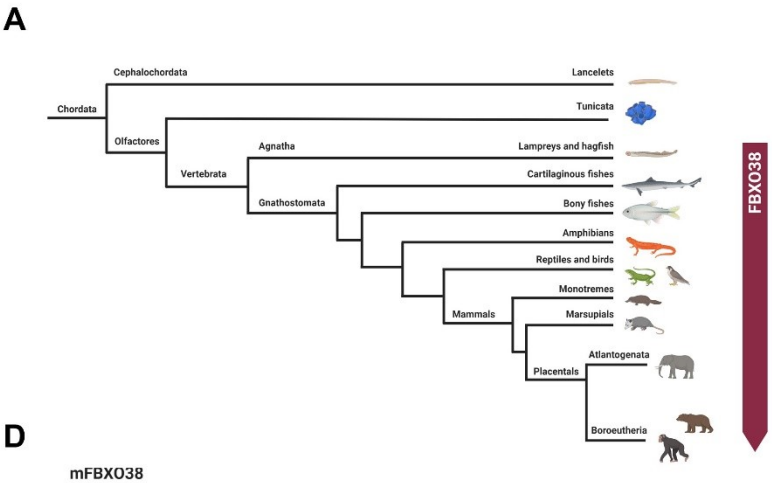
Nikol Dibus[1,2], Eliska Zobalova[1], Mario A.M. Monleon[1], Vladimir Korinek[3], Dominik Filipp[4], Jana Petrusova[4], Radislav Sedlacek[5], Petr Kasparek[5] and Lukas Cermak[1]*

* Corresponding author: Lukas Cermak, lukas.cermak@img.cas.cz

Table of Contents

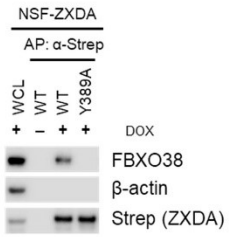
Supplementary figures and legends 2
Figure S1. FBXO38 deficiency leads to growth retardation in mouse 3
Figure S2. Reproduction and spermatogenesis are impaired in Fbxo38-deficient animals 5
Figure S3. The timing of the first wave of spermatogenesis depends on FBXO38 7
Figure S4. FBXO38 controls ZXDB protein and the centromeric chromatin in adult Sertoli cells 9
Figure S5. FBXO38-deficient Sertoli cells exhibit a maturation defect 11
Supplementary movies legends 12
Movie S1 and S2 (separate files). Sperm motility 12
List of reagents 12
Chemicals 12
Antibodies 13
Vectors 14
References 14

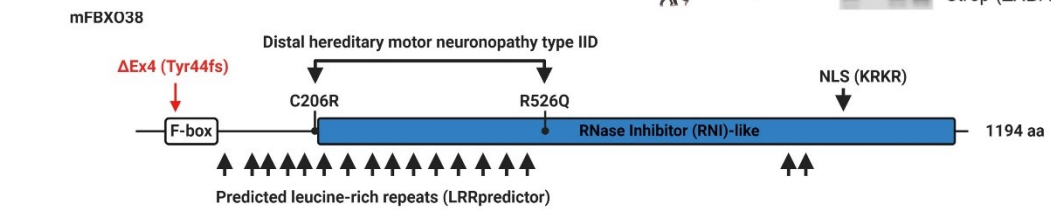
Supplementary figures and legends

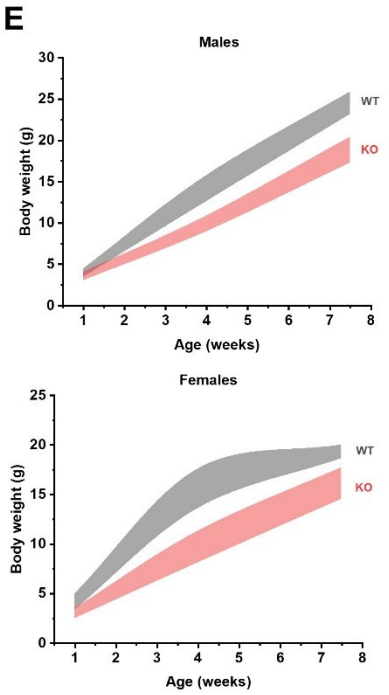


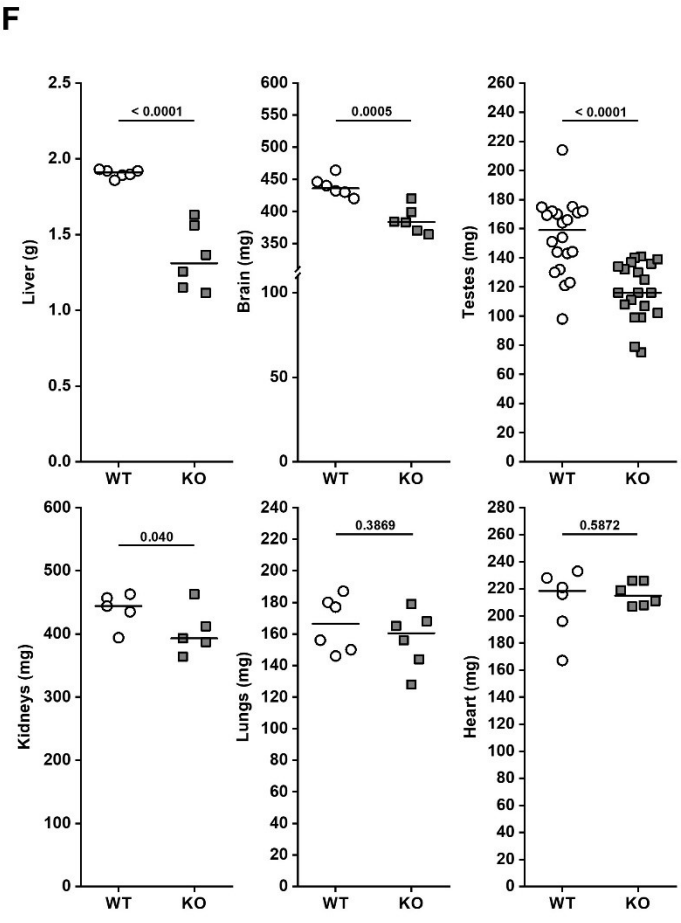
B

		Identity (%)				
		Homo	Mus	Columba	Xenopus	Danio
Similarity (%)	Homo	0	94.837	83.7862	77.9891	73.6413
	Mus	96.9203	0	82.7899	77.5362	72.8261
	Columba	90.308	89.8551	0	81.1594	74.4565
	Xenopus	87.3188	86.0507	88.0435	0	73.4601
	Danio	82.5181	81.9746	83.2428	81.4312	0









G

Organ	*Fbxo38*$^{+/+}$	*Fbxo38*$^{-/-}$	p value
Brain	407.1 ± 28.8	370.8 ± 31	0.062
Liver	1371.4 ± 225.7	1012.6 ± 100	0.012
Heart	175.6 ± 55.9	153.5 ± 31.4	0.418
Lungs	174 ± 37	154.5 ± 29.2	0.335
Kidneys	353.3 ± 59.1	292.3 ± 44.3	0.071

Figure S1. FBXO38 deficiency leads to growth retardation in mouse

(A) A simplified evolutionary scheme illustrating the emergence of *Fbxo38* gene.

(B) Table showing the similarity and identity of FBXO38 proteins in different vertebrate species.

(C) Mouse embryonic fibroblasts (MEF) with the inducible expression of StrepII-FLAG-tagged ZXDA (SF-ZXDA) and its mutant (Y389A) were treated with doxycycline for 24 hours where indicated. Whole-cell lysates (WCL) were subjected to affinity purification (AP) using Strep-Tactin resin and immunoblotted as indicated. WCL represent 1 % input subjected to AP.

(D) A scheme illustrating mouse FBXO38 structural features and disease-associated mutations found in patients with distal hereditary motor neuronopathy IID. The F-Box motif is located in the N-terminus followed by the predicted leucine-rich repeats. Locations of the two mutations (C206R and R526Q) found in patients. The previously confirmed nuclear localization sequence (NLS) is located in the C-terminal part. Red arrow points to frameshift resulting from targeted deletion of exon 4 in mouse model.

(E) Growth curves of infant and juvenile *Fbxo38* wild-type (WT) and knockout (KO) males (left) and females (right). Body weights were measured at 1, 4, 7, and 8 weeks of age ($n^{♂} \geq 6$; $n^{♀} \geq 3$). Curves represent mean values ± standard deviations.

(F) Total weight of the liver, brain, testes, both kidneys, lungs and heart of *Fbxo38* WT and KO males. Age distribution in both groups was the same (17-21 weeks). Individual data points and group means are shown. Statistical significance was assessed by an unpaired two-tailed t-test.

(G) Means ± standard deviations and p-values of organ weights of adult (25 weeks) *Fbxo38* WT and KO females are summarized in the table. Statistical significance was assessed by an unpaired two-tailed t-test. Statistically significant p-values are highlighted in red (p-value < 0.05).

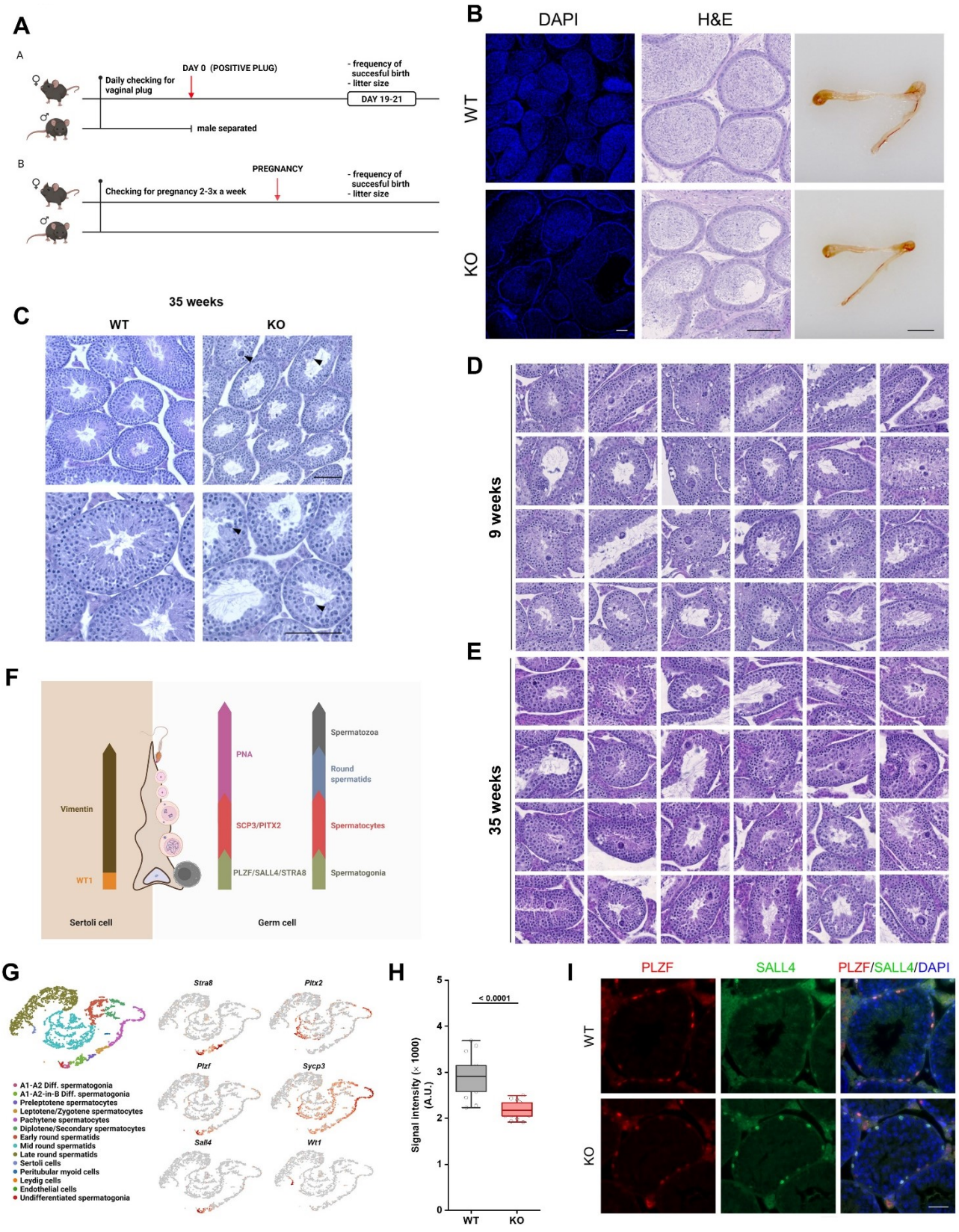

A
A
DAY 0 (POSITIVE PLUG)
Daily checking for vaginal plug
- frequency of succesful birth
- litter size
DAY 19-21
male separated
B
PREGNANCY
Checking for pregnancy 2-3x a week
- frequency of succesful birth
- litter size
B
DAPI
H&E
WT
KO
C
35 weeks
WT
KO
D
9 weeks
E
35 weeks
F
Vimentin
WT1
Sertoli cell
PNA
SCP3/PITX2
PLZF/SALL4/STRA8
Germ cell
Spermatozoa
Round spermatids
Spermatocytes
Spermatogonia
G
A1-A2 Diff. spermatogonia
A1-A2-in-B Diff. spermatogonia
Preleptotene spermatocytes
Leptotene/Zygotene spermatocytes
Pachytene spermatocytes
Diplotene/Secondary spermatocytes
Early round spermatids
Mid round spermatids
Late round spermatids
Sertoli cells
Peritubular myoid cells
Leydig cells
Endothelial cells
Undifferentiated spermatogonia
Stra8
Pitx2
Plzf
Sycp3
Sall4
Wt1
H
< 0.0001
Signal intensity (× 1000) (A.U.)
0
1
2
3
4
5
WT
KO
I
PLZF
SALL4
PLZF/SALL4/DAPI
WT
KO

Figure S2. Reproduction and spermatogenesis are impaired in Fbxo38-deficient animals

(A) Schematic representation of strategies used for assessing male fertility.

(B) Cauda epididymis of 17-week-old *Fbxo38* wild-type (WT) and knockout (KO) males stained with DAPI (left), or hematoxylin and eosin (H&E; middle). Scale bars, 100 μm. Representative images of *Fbxo38* WT and KO epididymis (right). Scale bar, 500 μm.

(C) H&E-stained testicular sections from *Fbxo38* WT and KO males (35 weeks). Arrowheads point to atypical multinucleated cells. Scale bar, 100 μm.

(D) – **(E)** Examples of H&E-stained cross-sections of seminiferous tubules bearing multinucleated giant cells from adult *Fbxo38* KO mice – 9 weeks (D), 35 weeks (E).

(F) Scheme of antibodies used to visualize different somatic and germ cell populations in testicular cross-sections.

(G) tSNE representation of gene expression in adult mouse unselected spermatogenic cells where the color represents the log2-transformed, normalized counts. The enlarged panel on the left shows different spermatogenic populations. The panels on the right show the expression of spermatogonial markers: *Stra8, Plzf,* and *Sall4,* Spermatocytes markers: *Pitx2* and *Sycp3,* and Sertoli cell marker *Wt1*. Publicly available data were uploaded from https://data.mendeley.com/datasets/kxd5f8vpt4/1 and analyzed using the Loupe cell browser (1).

(H) The signal intensity of WT1 staining in sections from *Fbxo38* WT and KO testes. The maximum normalized intensity of cells (n=2; 15 Sertoli cells per animal) was measured. Horizontal bars show mean values, boxes represent the 25th and 75th percentiles.

(I) Seminiferous tubule sections of adult (15 weeks) *Fbxo38* WT and KO mice stained for PLZF and SALL4. DNA was visualized with DAPI. Scale bar, 50 μm.

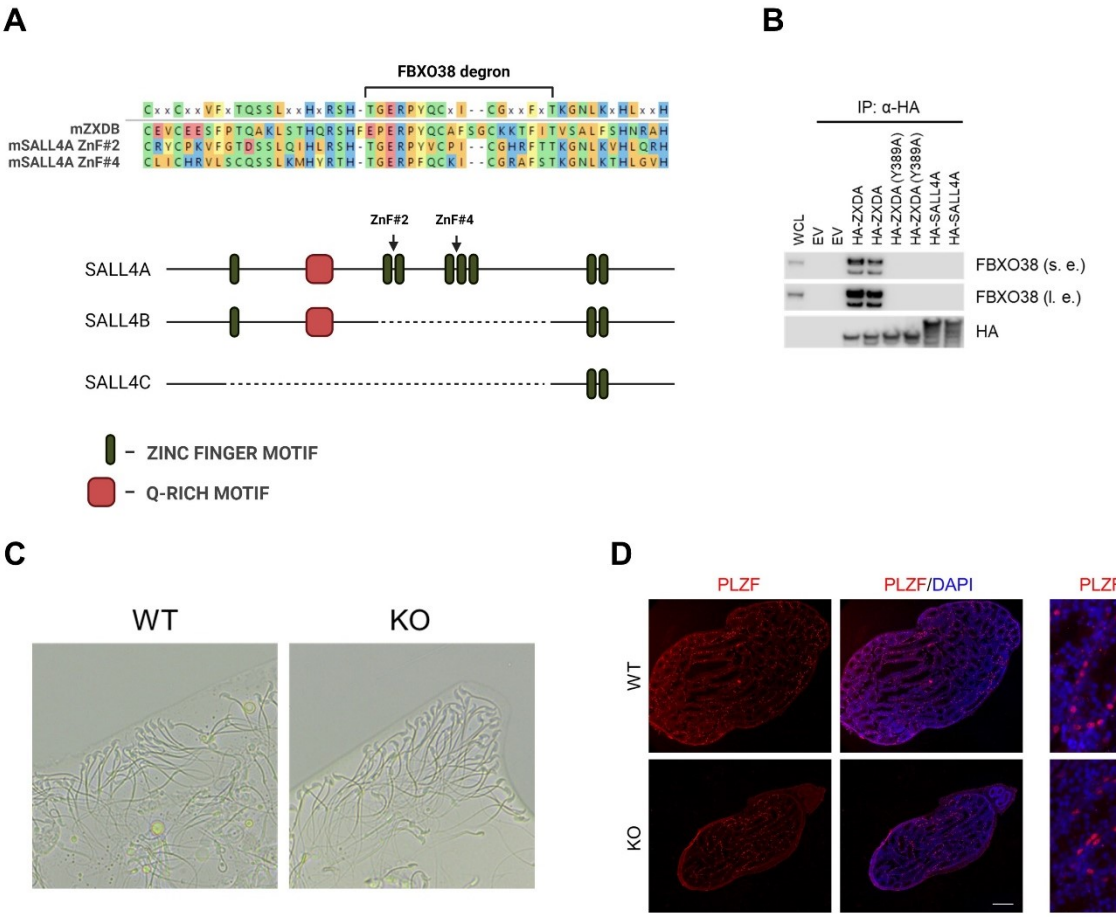

A
FBXO38 degron
mZXDB
mSALL4A ZnF#2
mSALL4A ZnF#4
ZnF#2
ZnF#4
SALL4A
SALL4B
SALL4C
ZINC FINGER MOTIF
Q-RICH MOTIF
B
IP: α-HA
W/CL
EV
EV
HA-ZXDA
HA-ZXDA
HA-ZXDA (Y389A)
HA-ZXDA (Y389A)
HA-SALL4A
HA-SALL4A
FBXO38 (s. e.)
FBXO38 (l. e.)
HA
C
WT
KO
D
PLZF
PLZF/DAPI
PLZF/DAPI
WT
KO
E
Number of TUNEL Positive Cells
25
20
15
10
5
0
0.8224
0.2066
WT
KO
WT
KO
2 weeks
3.5 weeks

Figure S3. The timing of the first wave of spermatogenesis depends on FBXO38

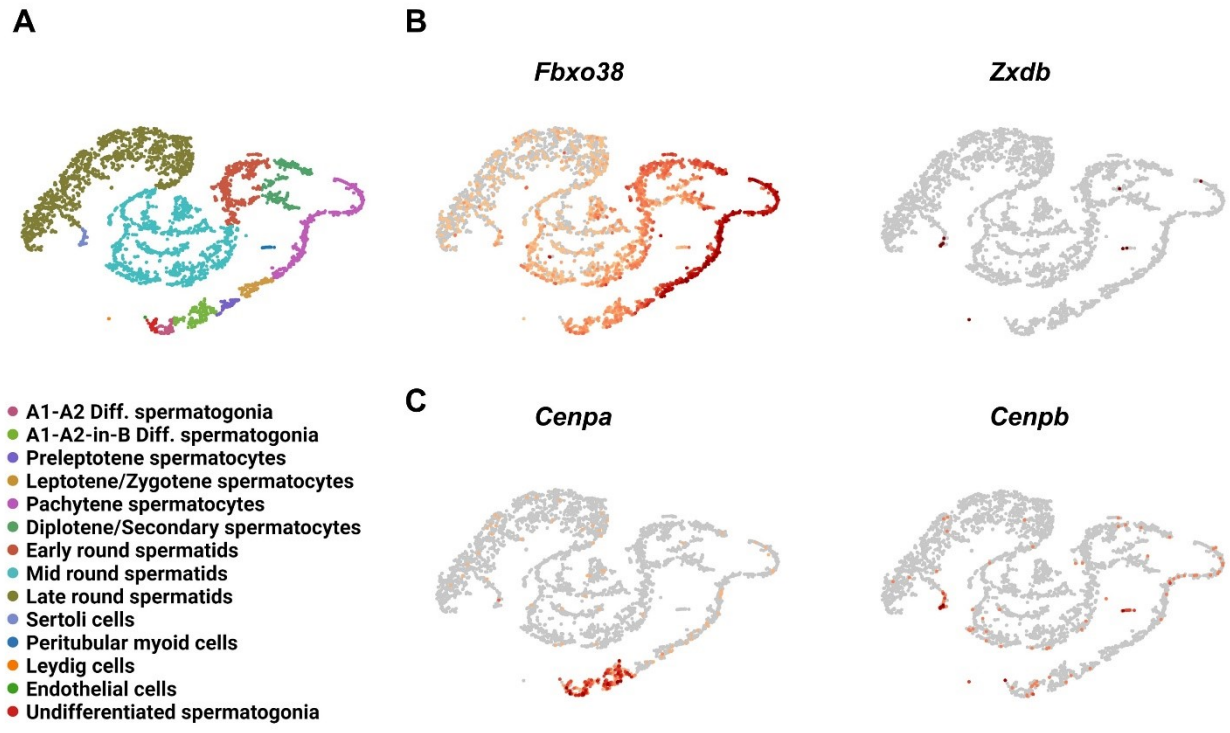
(A) Analysis of a potential FBXO38-dependent degron in the zinc-finger linkers of SALL4A. The upper panel shows the alignment between the FBXO38-dependent degron in ZXDB and two potential sites in SALL4A. The lower panel shows a comparison of SALL4 isoforms and indications of potential sites location (arrows).

(B) HEK293T cells were transfected with an empty vector (EV), HA-tagged ZXDA, ZXDA mutant Y389A, or mouse SALL4A, and treated with MLN4924 inhibitor 6 hours prior to collecting. The cells were subjected to isotonic lysis and immunopurified using anti-HA magnetic beads and immunoblotted as indicated.

(C) Representative images of sperm morphology of young adult (6 weeks) *Fbxo38* wild-type (WT) and knockout (KO) mice. Sperms were released from the cauda epididymides. Videos of motile sperms are available as a supplement.

(D) Sagittal sections of *Fbxo38* WT and KO testes at the age of 2 weeks stained for PLZF and counterstained with DAPI. Scale bar, 200 μm. Right panel shows the detail of individual tubules. Scale bar, 20 μm.

(E) Number of TUNEL-positive cells per tubule (n = 50) in sections of *Fbxo38* WT and KO littermate males at the indicated age. Individual data points are shown, horizontal bars show mean values. Statistical significance was assessed by an unpaired two-tailed t-test.


A
B
Fbxo38
Zxdb
C
Cenpa
Cenpb
A1-A2 Diff. spermatogonia
A1-A2-in-B Diff. spermatogonia
Preleptotene spermatocytes
Leptotene/Zygotene spermatocytes
Pachytene spermatocytes
Diplotene/Secondary spermatocytes
Early round spermatids
Mid round spermatids
Late round spermatids
Sertoli cells
Peritubular myoid cells
Leydig cells
Endothelial cells
Undifferentiated spermatogonia

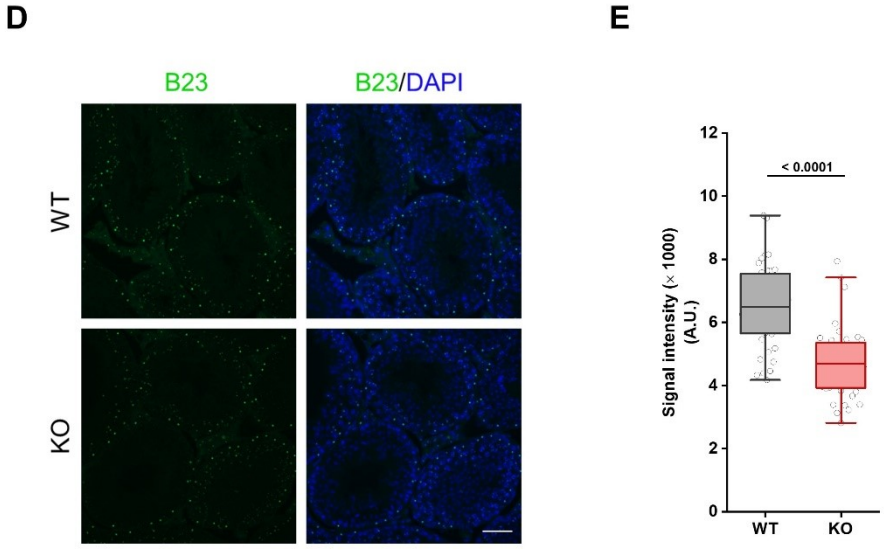

D
B23
B23/DAPI
WT
KO
E
< 0.0001
Signal intensity (× 1000) (A.U.)
12
10
8
6
4
2
0
WT
KO

Figure S4. FBXO38 controls ZXDB protein and the centromeric chromatin in adult Sertoli cells

(A) tSNE representation of adult mouse spermatogenic cells where the colors represent the different populations as described in the lower panel. Publicly available data were uploaded from https://data.mendeley.com/datasets/kxd5f8vpt4/1 and analyzed using the Loupe cell browser (1).

(B) tSNE representation of *Fbxo38* and *Zxdb* gene expression, where the color represents the log2-transformed, normalized counts. Publicly available data were uploaded and analyzed as in (A).

(C) tSNE representation of *Cenpa* and *Cenpb* gene expression analyzed and visualized as in (B).

(D) Representative images of tubule sections of adult *Fbxo38* wild-type (WT) and knockout (KO) mice stained for B23. DAPI was used to visualize DNA. Scale bar, 50 μm.

(E) Signal intensity of B23 staining in Sertoli cells. Mean normalized intensity was measured in two independent experiments. Individual data points represent a single Sertoli cell measurement (n=2; 40 Sertoli cells per animal). Horizontal bars show mean values, boxes represent the 25th and 75th percentiles. Statistical significance was assessed by an unpaired two-tailed t-test.

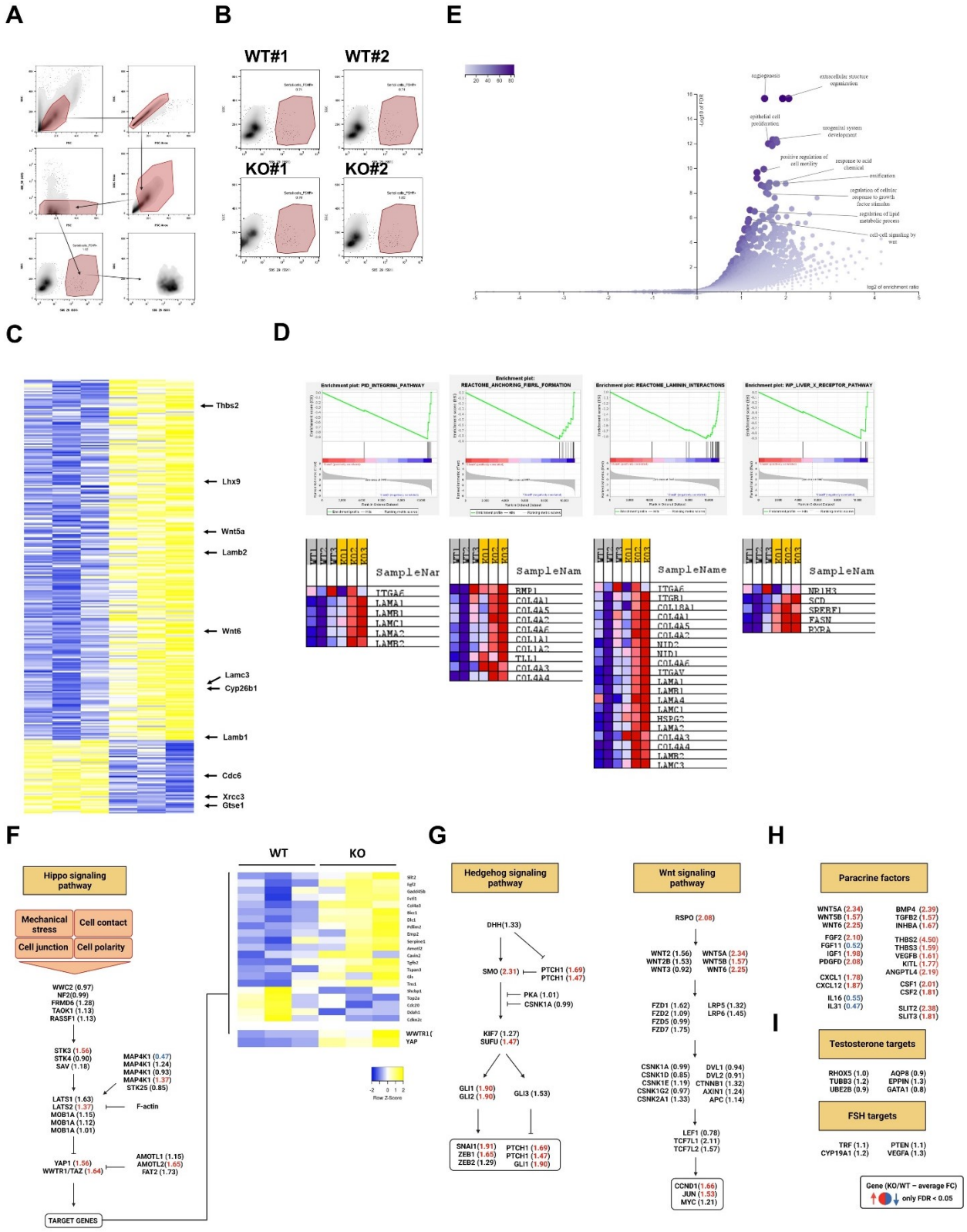

A
B
WT#1
WT#2
KO#1
KO#2
E
angiogenesis
extracellular structure organization
epithelial cell proliferation
urogenital system development
positive regulation of cell motility
response to acid chemical
ossification
regulation of cellular response to growth factor stimulus
regulation of lipid metabolic process
cell-cell signaling by wnt
log2 of enrichment ratio
C
Thbs2
Lhx9
Wnt5a
Lamb2
Wnt6
Lamc3
Cyp26b1
Lamb1
Cdc6
Xrcc3
Gtse1
D
Enrichment plot: PID_INTEGRIN4_PATHWAY
Enrichment plot: REACTOME_ANCHORING_FIBRIL_FORMATION
Enrichment plot: REACTOME_LAMININ_INTERACTIONS
Enrichment plot: WP_LIVER_X_RECEPTOR_PATHWAY
F
Hippo signaling pathway
Mechanical stress
Cell contact
Cell junction
Cell polarity
WWC2 (0.97)
NF2(0.99)
FRMD6 (1.28)
TAOK1 (1.13)
RASSF1 (1.13)
STK3 (1.56)
STK4 (0.90)
SAV (1.18)
MAP4K1 (0.47)
MAP4K1 (1.24)
MAP4K1 (0.93)
MAP4K1 (1.37)
STK25 (0.85)
LATS1 (1.63)
LATS2 (1.37)
MOB1A (1.15)
MOB1A (1.12)
MOB1A (1.01)
F-actin
YAP1 (1.56)
WWTR1/TAZ (1.64)
AMOTL1 (1.15)
AMOTL2(1.65)
FAT2 (1.73)
TARGET GENES
WT
KO
WWTR1
YAP
Row Z-Score
G
Hedgehog signaling pathway
DHH(1.33)
SMO (2.31)
PTCH1 (1.69)
PTCH1 (1.47)
PKA (1.01)
CSNK1A (0.99)
KIF7 (1.27)
SUFU (1.47)
GLI1 (1.90)
GLI2 (1.90)
GLI3 (1.53)
SNAI1(1.91)
ZEB1 (1.65)
ZEB2 (1.29)
PTCH1 (1.69)
PTCH1 (1.47)
GLI1 (1.90)
Wnt signaling pathway
RSPO (2.08)
WNT2 (1.56)
WNT2B (1.53)
WNT3 (0.92)
WNT5A (2.34)
WNT5B (1.57)
WNT6 (2.25)
FZD1 (1.62)
FZD2 (1.09)
FZD5 (0.99)
FZD7 (1.75)
LRP5 (1.32)
LRP6 (1.45)
CSNK1A (0.99)
CSNK1D (0.85)
CSNK1E (1.19)
CSNK1G2 (0.97)
CSNK2A1 (1.33)
DVL1 (0.94)
DVL2 (0.91)
CTNNB1 (1.32)
AXIN1 (1.24)
APC (1.14)
LEF1 (0.78)
TCF7L1 (2.11)
TCF7L2 (1.57)
CCND1(1.66)
JUN (1.53)
MYC (1.21)
H
Paracrine factors
WNT5A (2.34)
WNT5B (1.57)
WNT6 (2.25)
FGF2 (2.10)
FGF11 (0.52)
IGF1 (1.98)
PDGFD (2.08)
CXCL1 (1.78)
CXCL12 (1.87)
IL16 (0.55)
IL31 (0.47)
BMP4 (2.39)
TGFB2 (1.57)
INHBA (1.67)
THBS2 (4.50)
THBS3 (1.59)
VEGFB (1.61)
KITL (1.77)
ANGPTL4 (2.19)
CSF1 (2.01)
CSF2 (1.81)
SLIT2 (2.38)
SLIT3 (1.81)
I
Testosterone targets
RHOX5 (1.0)
TUBB3 (1.2)
UBE2B (0.9)
AQP8 (0.9)
EPPIN (1.3)
GATA1 (0.8)
FSH targets
TRF (1.1)
CYP19A1 (1.2)
PTEN (1.1)
VEGFA (1.3)
Gene (KO/WT − average FC)
only FDR < 0.05

Figure S5. FBXO38-deficient Sertoli cells exhibit a maturation defect

(A) Scheme of the mouse Sertoli cells sorting strategy. Adult Sertoli cells (obtained from 8-week-old animals) were isolated using enzymatic tissue digestion, followed by fluorescence-activated cell sorting with the anti-FSHR antibody.

(B) Effectivity of mouse Sertoli cells sorting from *Fbxo38* wild-type (WT) and knockout (KO) testes. Two out of the three isolations are shown.

(C) Normalized counts (fragments per kilobase million; FKPM) from the RNA-seq analysis of *Fbxo38* WT and KO young adult (8-week-old animals) Sertoli cells were visualized as a heat map showing gene expression normalized to the highest and lowest obtained count. Only 301 significantly regulated genes (FDR < 0.05; false discovery rate) are shown. Arrows point to individual genes.

(D) Gene set enrichment analysis (GSEA) of gene expression data from *Fbxo38* WT and KO Sertoli cells. GSEA enrichment plots of four gene clusters that are enriched in *Fbxo38* KO Sertoli cells are shown. Heat maps of genes from enriched clusters are shown in the lower panel.

(E) Over-Representation Analysis (ORA) of gene enrichment was prepared using the WEB-based GEne SeT AnaLysis Toolkit (http://www.webgestalt.org/). Positively enriched non-redundant gene clusters are named in the figure.

(F) Schematic representation of the Hippo signaling pathway with depicted fold changes in brackets. Data represent an average fold change (*Fbxo38* KO/WT Sertoli cells; n = 3). Significantly upregulated genes in KO Sertoli cells (FDR < 0.05) are in red. The blue font was used to highlight significantly downregulated genes in KO Sertoli cells (FDR < 0.05). Normalized counts (FKPM) of Hippo signaling pathway target genes (YAP conserved signature; GSEA: M2871) (2) from the RNA-seq analysis of *Fbxo38* WT and KO young adult (8 weeks old) Sertoli cells are shown on the right side of the panel. Data were visualized as a heat map showing gene expression normalized to the highest and lowest obtained count. Significantly regulated genes (FDR < 0.05) are depicted in the upper part of the heat map. Canonical transcription factors controlling Hippo-dependent target genes – *Yap* and *Wwtr1* (*Taz*), are shown in the lower part of the heat map.

(G) Schematic representation of the Hedgehog and Wnt signaling pathways with depicted fold changes in brackets. Data represent an average fold change (*Fbxo38* KO/WT Sertoli cells; n = 3). Significantly upregulated genes in KO Sertoli cells (FDR < 0.05) are in red. The blue font was used to highlight significantly downregulated genes in KO Sertoli cells (FDR < 0.05).

(H) List of paracrine factors with depicted fold changes in brackets. Significantly upregulated genes in KO Sertoli cells (FDR < 0.05) are in red, significantly downregulated genes (FDR < 0.05) are in blue.

(I) List of testosterone and FSH target genes with depicted fold changes in brackets. Significantly upregulated genes in KO Sertoli cells (FDR < 0.05) are in red, significantly downregulated genes (FDR < 0.05) are in blue.

Supplementary movies legends

Movie S1 and S2 (separate files). Sperm motility

Sperms of young adult (6 weeks) Fbxo38 wild-type (Movie S1) and knockout (Movie S2) mice. The sperms were released from cauda epididymides, incubated in medium containing methyl-β-cyclodextrin (0.75mM) for 30 minutes at 37 °C, and observed under Zen Axio Vert.A1 microscope (Zeiss).

List of reagents

Chemicals

Name	Company	CAT#
2-mercaptoethanol	Sigma	M6250
4',6-diamidin-2-fenylindol (DAPI)	Sigma	D9542
Benzonase	Santa Cruz	sc-391121
Cycloheximide	Sigma Aldrich	C7698
Dithiothreitol	Sigma	10197777001
Doxycycline hyclate	Sigma Aldrich	D9891
Eosin Y	VWR Qpath	10047101
Harris' Hematoxylin	VWR Qpath	10047107
Methanol	Penta	67-56-1
Paraformaldehyde	Electron Microscopy Sciences	15710
Pevonedistat (MLN4924)	Medchemexpresss	HY-70062
Polybrene	Sigma	107689
Polyethyleneimine (MW 25 000)	Polysciences	23966
ProLong Gold Antifade Mountant	Thermo Fisher Scientific	P36934
Protease Inhibitors Mini Tablets	Pierce	A32955
Proteinase K	Sigma	P2308
Puromycin	Sigma Aldrich	P8833
Sodium dodecyl sulfate (SDS)	Sigma	71736
Sodium fluoride	Sigma	S7920
Sodium orthovanadate	Sigma	450243
TACS 2 TdT-DAB (TUNEL assay)	Trevigen	4810-30-K

Antibodies

Primary antibodies and probes	Company	CAT#	RRID
Anti-centromere antibodies	Antibodies Incorporated	15-234	
B23	Santa Cruz	sc-271737	AB_10708848
FBXO28	Bethyl	A302-377A	AB_1907260
FBXO38	Atlas Antibodies	HPA041444	AB_2677484
HA	Cell Signaling	3724	AB_1549585
Histone H3	Abcam	ab1791	AB_302613
PITX2	Santa Cruz	sc-390457	
PLZF	Atlas Antibodies	HPA001499	AB_1079640
SALL4A	Santa Cruz	sc-101147	AB_1129262
SCP3	Santa Cruz	sc-74569	AB_2197353
SKP1	Cell Signaling	12248	AB_2754993
STRA8	Abcam	ab49405	AB_945677
Strep II Tag	Novus Biologicals	NBP2-43735	
Vimentin	Cell Signaling	5741	AB_10695459
WT1	Novus Biologicals	NB110-60011	AB_905863
ZXDB	Atlas Antibodies	HPA043789	AB_2678673
α-Tubulin	Proteintech	66031-1-Ig	AB_11042766
β-Actin	Santa Cruz	sc-69879	AB_1119529
FSHr (PE Conjugated)	Bioss USA	bs-20658R-PE	
Lectin PNA (AF594 Conjugated)	Thermo Fisher Scientific	L32459	

Secondary antibodies	Company	CAT#	RRID
Anti-Human IgG (Alexa Fluor 488)	Thermo Fisher Scientific	A11013	AB_2534080
Anti-Mouse IgG (Alexa Fluor 647)	Abcam	ab150115	AB_2687948
Anti-Mouse IgG (Alexa Fluor® 555)	Abcam	ab150110	AB_2783637
Anti-Mouse IgG (DyLight 488)	Thermo Fisher Scientific	35503	AB_1965946
Anti-Rabbit IgG (Alexa Fluor® 488)	Abcam	ab150061	AB_2571722
Anti-Rabbit IgG (Alexa Fluor® 555)	Abcam	ab150070	AB_2783636
Anti-Rabbit IgG (Alexa Fluor® 647)	Abcam	ab150067	AB_2894821

Beads for affinity and immunopurification	Company	CAT#
anti-HA (magnetic)	Pierce	88837
Strep-Tactin® Superflow resin	IBA	2-1206-025

Vectors

Lentiviral packaging vectors	Company	Cat#
pLenti CMV/TO SV40 Small and Large T antigen	Addgene	22298
pCMV-dR8.2	Addgene	8455
pCMV-VSV-G	Addgene	8454

cDNA	Vector	Tag
SALL4	pcDNA3	N-terminal HA
ZXDA	pcDNA3	N-terminal HA-tag
ZXDA	pcDNA3	N-terminal SF-tag

Sleeping Beauty System	Company	Cat#
pSBtet-Pur	Addgene	60507
pSB100X	Addgene	34879

References

1. Hermann BP, Cheng K, Singh A, Roa-De La Cruz L, Mutoji KN, Chen IC, et al. The Mammalian Spermatogenesis Single-Cell Transcriptome, from Spermatogonial Stem Cells to Spermatids. Cell Rep. 2018;25(6):1650-67 e8.
2. Cordenonsi M, Zanconato F, Azzolin L, Forcato M, Rosato A, Frasson C, et al. The Hippo transducer TAZ confers cancer stem cell-related traits on breast cancer cells. Cell. 2011;147(4):759-72.

4. Results and Discussion

4.1 Substrates of the SCF^{FBXO38} Ubiquitin Ligase

F-box-containing protein FBXO38 is implicated in the development of distal muscular atrophy since its mutations were found in patients suffering from this syndrome (Akcimen et al., 2019; Grunseich et al., 2021; Sumner et al., 2013). It represents a substrate receptor for SCF ubiquitin ligase with no extensively described function (Jin et al., 2004; Meng et al., 2018). Since ubiquitin ligases perform their functions through substrate ubiquitination, the identification of substrate is an essential step in characterizing ubiquitin ligase function and describing its role in the cellular context.

To identify new substrates of SCF^{FBXO38} ubiquitin ligase, we performed a proteomic screen of its interacting partners. For this purpose, we employed inhibitors of cullin-dependent ubiquitination to prevent the degradation of isolated substrates. Among the co-purified proteins, we identified the SCF complex components SKP1 and CUL1. We also detected USP7, the previously identified deubiquitinase interacting with FBXO38 (Georges et al., 2019). In addition to these expected FBXO38 interactors, we identified a set of previously unknown, specifically death effector domain-containing proteins 1 and 2 (DEDD and DEDD2), and zinc finger-containing proteins from the ZXD family. On the other hand, we did not detect PD-1, a transmembrane receptor involved in the immune checkpoint and the only SCF^{FBXO38} substrate identified so far (Meng et al., 2018). This result was expected since PD-1 is expressed specifically on the surface of T cells. Moreover, the authors of the mentioned study proposed that FBXO38 mediates the ubiquitination and subsequent degradation of internalized PD-1 in the cytoplasm. This is in contrast to our observed FBXO38 localization in the nucleus. These discrepancies could result from cell-specific regulation of FBXO38 cellular localization. Previously, FBXO38 was shown to be able to shuttle between the cytoplasm and the nucleus (Smaldone and Ramirez, 2006). In our proteomic screen, we did not detect any cytosolic proteins specifically interacting with FBXO38, which suggested that FBXO38 represents strictly nuclear protein in HEK293T and HeLa cell lines. Moreover, we did not detect the transcription factor KLF7, the other known FBXO38-associated protein, as KLF7 is predominantly expressed in neural tissues, and our studies were performed in epithelial cells (Smaldone et al., 2004).

As mentioned above, we identified DEDD and DEDD2 as potential FBXO38 substrates. They represent small nuclear factors involved in the cell cycle regulation, apoptosis, and autophagy. The nature of their interaction with FBXO38 and their role in FBXO38-dependent ubiquitination is a part of the follow-up study and will not be discussed in this work. We identified two C2H2 type zinc-finger proteins, ZXDA and ZXDB, as FBXO38 interaction partners and proved that FBXO38 mediates their ubiquitination and subsequent degradation. We found that FBXO38 recognizes a linker between the fourth and fifth zinc fingers in ZXDA/B bearing a sequence ERPY. Interestingly, already mentioned KLF7 is a transcription factor containing three C-terminally located C2H2 zinc fingers, the first and second of which are separated by the consensus linker sequence (TGEKPY). However, FBXO38 was reported to act as the co-activator of KLF7 in a ubiquitin-ligase-independent manner, and the authors did not search for the motif responsible for the interaction (Smaldone et al., 2004). Regarding PD-1 protein, FBXO38 was shown to mediate the ubiquitination of Lys233 but the authors of the study did not evaluate the degron sequence (Meng et al., 2018). A detailed analysis of the primary structure of the PD-1 intracellular part did not reveal any significant match to the FBXO38-dependent degron we discovered.

The consensus sequence (H_2-**TGEKPY/FX-**C_1**)** is the most common linker in zinc-finger proteins, although some variations occur (Jantz and Berg, 2004; Laity et al., 2000). It only slightly differs from our identified FBXO38-dependent degron (H_2-X(3)-ERPY-X-C_1). Surprisingly, we did not identify any of these zinc-finger proteins in our proteomic analyzes of FBXO38 interactors, indicating the hidden complexity of degron recognition. Moreover, by *in silico* search for the stringent degenerate motif where the second histidine of the zinc finger is followed by three amino acids with the following ERP(Y/F) linker sequence, we discovered that only ZXDA, ZXDB, and ZXDC contain this kind of linker. On the other hand, we found that ZXDA/B-close homolog ZXDC does not act as an FBXO38 substrate, as it is not stabilized either upon inhibition of proteasome and cullin neddylation, or FBXO38 silencing. Moreover, the interaction between FBXO38 and ZXDC we detected, was probably mediated via ZXDA/B, as they were shown to form a complex with ZXDC (Al-Kandari et al., 2007b). One of the reasons why FBXO38 is not able to recognize ZXDC as its substrate could originate from slight differences in the ZXDC amino acid sequence. The fifth zinc finger following the essential linker region contains a sequence that results in structural differences affecting the availability of essential tyrosine, as we discovered by homology-based modeling. Another reason could be the existence of posttranslational modification

of ZXDA/B degron, which is common in a broad spectrum of degrons recognized by CRLs. By mutational analysis, we discovered that phosphorylation of Tyr389 is not required for the interaction with FBXO38. On the other hand, we cannot exclude the possibility that phosphorylation could have a negative effect on the interaction. Phosphorylation of the zinc-finger linker sequence is quite common in many zinc-finger proteins and leads to a reduction in their DNA-binding ability (Jantz and Berg, 2004; Rizkallah et al., 2011). Despite the main target of the phosphorylation being the linker threonine, tyrosine also undergoes phosphorylation. An example represents the Ying Yang 1 (YY1) protein, a transcription factor containing four C2H2 zinc fingers. It was shown that YY1 Tyr383 positioned in the linker sequence before the fourth zinc finger is phosphorylated by members of the Src family kinases and that its phosphomimetic mutation (Y383E) affects the DNA and RNA binding abilities of YY1 (Wang and Goff, 2015).

Moreover, in our study focused on describing the *Fbxo38*-deficient mouse model, we observed increased expression of Spalt-like transcription factor 4 (SALL4), the marker of undifferentiated spermatogonia (Yamaguchi et al., 2015). This zinc-finger protein contains two zinc-finger linkers that share a high sequence identity with the FBXO38-dependent degron, which we found in ZXDA/B. Although it indicated that SALL4 could act as a substrate of FBXO38 and thus FBXO38 could be responsible for its protein level control in spermatogonia, we did not detect the interaction between FBXO38 and SALL4A even when over-expressed.

In addition to the zinc-finger linker sequence, we found that the middle part of the following zinc finger in ZXDA/B is also essential for the interaction with FBXO38. As it contains several serines and threonines, it represents a potential phosphorylation site and regulatory mechanism of ZXDA/B degradation. To prove this hypothesis, we performed several mutational experiments. We did not observe any positive effect of the phospho-mimicking mutations, but some had an inhibitory impact on the interaction (data were not shown).

Interestingly, by analyzing The Cancer Genome Atlas, we discovered that a significant number of cancer-associated mutations in ZXDA and ZXDB are found in the essential zinc-finger linker and the surrounding sequences. Given the complexity of the FBXO38-dependent degron, we hypothesized that these alterations could result in aberrant ZXDA and ZXDB degradation, thereby contributing to tumorigenesis. Indeed, alterations in the degrons affecting the protein stability were found in many proteins with annotated degron sequences leading to the inability of ubiquitin ligase to recognize these substrates (Tokheim et al., 2021).

4.2 The Biological Function of the SCF^{FBXO38}-dependent Protein Degradation

Little is known about the function of ZXDA and ZXDB proteins. They were shown to form a complex with ZXDC and thus promote the MHC class II gene expression (Al-Kandari et al., 2007b). In our pilot experiments, we did not observe any effect of ZXDA/B knockdown or overexpression on MHC class II gene expression.

In our study, we observed ZXDA/B localization in the nucleus. However, only a portion of ZXDA/B was associated with the chromatin. By chromatin immunoprecipitation using an anti-ZXDA/B antibody followed by next-generation sequencing (ChIP-seq), we discovered that ZXDA/B bind the DNA in promoters of many important highly-expressed genes. However, their expression was not affected by the overexpression of ZXDA/B or their siRNA-mediated knockdown, indicating that they do not act as transcription regulators. Although many transcription factors exist among zinc-finger proteins, they can exhibit a broad range of molecular functions (Cassandri et al., 2017). Admittedly, we cannot rule out that ZXDA/B act as transcription factors in specific tissues or under specific conditions. Notably, the effect of the manipulated ZXDA/B expression may not manifest itself instantly. The study of the long-term impact of ZXDA/B deficiency would require the generation of knockout cells. During the establishment of ZXDA/B knockouts, we encountered technical problems caused either by the essentiality of ZXDA/B or by the inability of CRISPR to target the DNA of duplicated genes.

Therefore, to uncover ZXDA and ZXDB functions, we performed a proteomic screen of their interacting partners. Among ZXDA/B co-purified proteins, we detected the subunits of the SCF^{FBXO38} ubiquitin ligase complex and centromeric protein CENP-B, which plays an important role in centromeric identity and function (Gamba and Fachinetti, 2020). Interestingly, CENP-B was reported to interact with many centromeric and noncentromeric proteins, including zinc-finger proteins, suggesting the regulation of its functions is more complex (Huttlin et al., 2021). Recently, it was shown that CENP-B interacts with ZFAT (zinc-finger protein with AT-hook) protein containing eighteen C2H2 zinc fingers, and controls its localization to centromeres. It was proposed that CENP-B recruits and stabilizes ZFAT in the α-satellite DNA, where ZFAT regulates the transcription of noncoding RNA (ncRNA) that plays an important role in centromeric function (Ishikura et al., 2021). In our studies, we detected the interaction between ZXDA/B and CENP-B in the nucleoplasm and not within the chromatin. In addition, we did not detect centromeric chromatin precipitation in our ChIP-seq analysis using the ZXDA/B antibodies suggesting that

ZXDA/B may play a role in the regulation of CENP-B before or during its loading to centromeres. As we did not detect CENP-B co-purifying with FBXO38 and *vice versa*, we proposed that ZXDA/B interact with FBXO38 and CENP-B in a mutually exclusive manner. This observation was supported by our mutational analysis revealing that CENP-B requires the fifth and sixth zinc fingers in ZXDA/B for the interaction, the region that partly overlaps with the FBXO38-dependent degron. Consistently with our hypothesis that FBXO38-ZXDA/ZXDB axis could act as a chaperone for CENP-B protein, we discovered that the stabilization of ZXDA/B resulting from FBXO38 deficiency leads to the increased protein level of CENP-B. This upregulation was accompanied by the accumulation of other centromeric proteins, supporting the previously described role of CENP-B (Fachinetti et al., 2015; Fujita et al., 2015; Hoffmann et al., 2016). In accordance, the knockdown of ZXDA/B led to the downregulation of CENP-B.

The observed upregulation of centromeric proteins could result from their ectopic depositions as newly formed neocentromeres (Scott and Sullivan, 2014). Such upregulation of centromeric chromatin could also be the result of other aberrations. It was shown that CENP-A is recruited to the double-strand breaks in DNA (Zeitlin et al., 2009). Noncentromeric CENP-A was also reported to occupy open chromatin regions mapped by DNase I hypersensitivity and transcription factor hotspots, including gene promoters (Athwal et al., 2015). Interestingly, we observed a similar binding signature in our ChIP-seq analysis with the ZXDA/B antibodies. To uncover whether centromeric protein stabilization upon FBXO38 loss could result from the mentioned aberrations, we performed a ChIP-seq analysis of endogenous CENP-A and CENP-B. In FBXO38-deficient cells, we did not detect any binding of CENP-A or CENP-B to the ectopic sites described previously (Athwal et al., 2015). Moreover, we did not observe any enrichment of the ZXDA/B binding sites in these precipitations. On the other hand, we detected strong enrichment of CENP-A and CENP-B binding in the centromeric regions of all chromosomes in FBXO38-deficient cells, finally indicating that FBXO38-ZXDA/ZXDB axis controls the deposition of centromeric proteins.

The functional centromere requires the tight control of the centromeric protein deposition and their balance. Aberrations in this system often lead to failure in the kinetochore assembly and subsequently to unfaithful chromosome segregation (Westhorpe and Straight, 2014). As already mentioned, CENP-B plays an important role in the centromere establishment and stabilization by interacting with CENP-A and promoting its assembly (Fachinetti et al., 2015; Ohzeki et al., 2002). On the contrary, overexpression of CENP-A leads to mitotic aberrations and cell cycle arrest, thus

promoting chromosomal instability (Jeffery et al., 2021; Zhang et al., 2016). On the other hand, CENP-B also promotes heterochromatin formation, which in turn inhibits CENP-A assembly (Okada et al., 2007). Therefore, dysregulation of any of the proteins involved in the centromeric maintenance could have a harmful effect on the centromeric integrity. Our data strongly suggest that the FBXO38-ZXDA/ZXDB pathway may exhibit a fine-tuning function for CENP-B regulation to prevent these aberrations. In agreement, FBXO38 was reported to prevent defects in cytokinesis by interacting with kinesin KIF20B, and the loss of FBXO38 was shown to result in the formation of multinucleated cells (Georges et al., 2019). Interestingly, in our proteomic screen of ZXDA/B interacting partners, we detected and confirmed strong interaction with the casein kinase 2 (CK2) complex. Interestingly, CK2 was shown to phosphorylate CENP-C homolog in budding yeast Mif2$^{Cenp\text{-}C}$ and thus regulate its function in kinetochore recruitment (Peng et al., 2011). In *Drosophila*, CK2 phosphorylates Ser20 in CENP-A, which governs its centromere-specific loading and protein turnover through the recognition by the SCF^{Ppa} ubiquitin ligase. In addition, overexpressed CENP-A was shown to be phosphorylated and regulated by the same mechanism to prevent its ectopic incorporation (Huang et al., 2019). Human CENP-B was also shown to be the substrate for CK2-mediated phosphorylation, but the function of this modification was not elucidated (Sugimoto and Himeno, 1992). Although we did not explore the interaction of ZXDA/B with CK2 in detail, it might be possible that it is required for ZXDA/B-dependent centromere chromatin regulation.

A complex similar to the FBXO38-ZXDA/ZXDB controls the centromere assembly in budding yeast. It is represented by the multiprotein complex called centromere-binding factor 3 (CBF3), comprising F-box protein Ctf13, Skp1^{SKP1}, zinc-finger protein Cep3, and kinetochore protein Ndc10. It directly interacts with DNA by binding the CCG region in the CDEIII centromeric DNA element of budding yeast point centromere (Yan et al., 2018). Interestingly, this complex was shown to interact with Cbf1$^{CENP\text{-}B}$ and promote its DNA binding ability and centromere loading (Hemmerich et al., 2000). However, no homologs of CBF3 subunits were identified in mammalian cells. In addition, we did not observe FBXO38 direct interaction with the chromatin. Given that CENP-B and FBXO38 interact with ZXDA/B in a mutually exclusive manner, we do not expect the formation of such a multiprotein complex.

The involvement of FBXO38 mutations found in patients with distal muscular atrophy in the regulation of centromeric proteins is quite intriguing. Since there are three independent point

mutations, it suggests that any structural alterations in the FBXO38 protein central domain containing leucine-rich repeats could affect its function (Akcimen et al., 2019; Grunseich et al., 2021; Sumner et al., 2013). Importantly, we discovered that ZXDA/B interact with FBXO38 via its C-terminal domain. However, it does not exclude the possibility that several regions might be involved in these interactions. Compared to the wild-type form, we detected stronger interaction of ZXDA/B with two FBXO38 mutants. This suggests that atrophy-associated mutants could exhibit the aberrant function of ubiquitin ligase activity and thus mediate ZXDA/B degradation more efficiently. Although we did not aspire to study atrophy-associated mutants in detail, we hypothesize that these mutations could affect FBXO38 folding and, subsequently, any substrate or cofactor binding. In agreement, we observed that adapter protein SKP1 interacted more strongly with the mutants than with wild-type FBXO38.

4.3 The Phenotype of the Mouse Model Deficient in FBXO38

The human protein FBXO38 shares approximately 95 % identity with its mouse homolog. To explore the physiological role of FBXO38, we generated a CRISPR-Cas9-mediated *Fbxo38*-deficient mouse model. We deleted the fourth exon of the *Fbxo38* locus, resulting in a frameshift, subsequently leading *to Fbxo38* gene inactivation. Although this disruption revealed that *Fbxo38* is not essential for embryonic development, the homozygous mice were born in the lower than expected ratio. By analyzing the phenotype of *Fbxo38*-deficient mice, we observed reduced body weight and growth of several organs in both males and females. Growth retardation and increased perinatal lethality is not an uncommon phenotype upon loss of ubiquitin ligases. For example, mice deficient in SKP2 are viable, but exhibit decreased body weight caused by the accumulation of its substrates, CDK inhibitors (Nakayama et al., 2000). Similarly, a significant number of mice lacking another substrate receptor, FBXW7, die perinatally due to respiratory failure, and the surviving pups exhibit lower body weight (Tsutsumi et al., 2008). In the *Fbxo38*-deficient mouse model, we observed significant differences in the weight of several but not all organs. In addition to the liver, the male reproductive system, especially the testes, was most affected by growth retardation, which was accompanied by decreased fertility.

For this reason, we focused on investigating the role of FBXO38 in mouse spermatogenesis. As with the body weight, spermatogenesis defects were observed by several mouse models deficient in ubiquitin ligase receptors. For instance, loss of β-TrCP1 does not affect mouse viability

or lead to tissue anomalies but causes defects in spermatogenesis due to meiotic errors in spermatocytes caused by stabilization of its substrates (Guardavaccaro et al., 2003). Even though β-TrCP1 targets various substrates, the phenotype resulting from its loss is mild thanks to compensation by its paralog β-TrCP2. However, inducible loss of both leads to severe disruptions in the seminiferous epithelium (Kanarek et al., 2010). Another example could be the loss of the DCAF17 substrate receptor that leads to defects in spermiogenesis and thus to lower and abnormal sperm production (Ali et al., 2018). By histological examination, we revealed a pathological organization of the epithelium of seminiferous tubules of *Fbxo38*-deficient males. This was accompanied by a significant decrease in the number of spermatozoa; however, no alterations in their morphology or motility were observed. The disruption of the seminiferous epithelium was evident also from lower cellularity on the spermatocyte level. Besides the lower number, we did not detect any structural defects in spermatocyte morphology or structure of the synaptonemal complex, which suggested disruptions in spermatogonia differentiation. This process of spermatogonia stem cell differentiation to spermatogonia to spermatocytes is tightly regulated by paracrine signals provided by testicular somatic cells (Smith and Walker, 2014). Indeed, we found that in adults, FBXO38 is expressed mostly by Sertoli cells. Interestingly, Sertoli cell active proliferation, which ceases during puberty, is the major determinant of the testis size and spermatogenesis efficiency in adulthood (O'Donnell et al., 2021). This is consistent with the observed smaller size of testes from *Fbxo38*-deficient mice. In addition, we observed a smaller size of testes of knockout animals already in embryonic development, suggesting that smaller size is not a result of lower sperm numbers.

Given that Sertoli cells bear various functions and thus are crucial for the whole process of spermatogenesis, we focused on describing the function of FBXO38 in this cell type (Griswold, 2018). By performing RNA-seq in sorted Sertoli cells of FBXO38 wild-type and knockout adult males, we revealed significant differences in their transcriptomes. Interestingly, the loss of FBXO38 mostly affected the RA metabolism. One of the most upregulated genes in *Fbxo38*-deficient Sertoli cells was *Cyp26b1*, encoding the enzyme responsible for the RA degradation into inactive metabolites (White et al., 1997). Expression of CYP26B1 is essential during testicular development in order to eliminate RA signaling and thus prevent the premature entry of germ cells into meiosis (Bowles et al., 2018; Bowles et al., 2006; Koubova et al., 2006). However, its expression in Sertoli cells declines after birth to allow the germ cells to enter the

differentiation program in puberty (Edelsztein et al., 2020). We also detected upregulation of *Aldh1a1* and *Aldh1a3* encoding dehydrogenases important for RA conversion in Sertoli cells (Arnold et al., 2015). Increased ATRA production upregulates CYP26B1, which controls and potentially inactivates the whole RA-mediated signaling. Importantly, spermatogenesis requires the precise balance of RA production and elimination, and the activation of genes involved in its signaling thus has to be strictly controlled (Gewiss et al., 2020). We, therefore, proposed that loss of FBXO38 could lead to disruption of RA metabolism control and improper stimulation of spermatogonia. As already mentioned, increased expression of *Cyp26b1* could also be a sign of immaturity in Sertoli cells. To further explore whether loss of FBXO38 could affect the maturation of Sertoli cells, we compared publicly available transcription profiles of Sertoli cells isolated from juvenile mice to our obtained data. The analysis confirmed that the differentially expressed genes in knockout Sertoli cells mimic the transcription profiles of immature cells. Indeed, the inability of Sertoli cells to functionally mature leads to defects in spermatogenesis, affecting the production of spermatozoa (Sharpe et al., 2003). Besides, we detected upregulation of Wnt signaling pathway components. In agreement with our data, it was shown that increased activity of Wnt signaling in Sertoli cells interferes with their maturation (Tanwar et al., 2010).

By histologic examination of seminiferous tubules of young males, we detected FBXO38 expression mainly in the spermatogonial compartment and not in Sertoli cells. The deficiency of FBXO38 in the testes of juvenile mice was accompanied by an increased protein level of SALL4A, a marker of undifferentiated spermatogonia. As mentioned above, we ruled out that the SALL4A zinc-finger protein represents the FBXO38-dependent substrate. Interestingly, its upregulation could also result from defects in RA metabolism, as it was shown to be positively regulated by RA signaling (Gely-Pernot et al., 2015). Due to the observed switch in FBXO38 expression from spermatogonia to Sertoli cells during the first two weeks after birth, we focused on the initiation of spermatogenesis. The first wave of spermatogenesis is characterized by the synchronous entry of spermatogonia into the differentiation process that dictates spermatogenesis efficiency in adulthood. In mice, it starts shortly after birth when progenitor prospermatogonia re-enter the mitotic program (Kubota and Brinster, 2018). The transition from prospermatogonia to spermatogonia is again triggered by RA signaling (Busada et al., 2014). In testes of *Fbxo38*-deficient mice, we observed a decrease in the level of meiotic marker synaptonemal complex protein 3 (SCP3). We also detected many seminiferous tubules lacking SCP3-positive

cells, indicating a rather asynchronous initiation of the first wave in *Fbxo38*-deficient males. Consequently, knockout pups exhibited a lower number of testicular spermatozoa (at four weeks) as well as lower epididymal sperm counts (at six weeks). Interestingly, this could result from the imbalance in RA metabolism, similarly to adult spermatogenesis.

Regarding FBXO38 expression, we observed its localization switching from spermatogonia to Sertoli cells during the second week after birth. During this period in mice, the first meiotic prophase is initiated. Primary spermatocytes at preleptotene stages are present at postnatal day 10, and spermatocytes at zygotene stage appear on day 12, reaching the early pachytene stage by day 14 (Bellve et al., 1977; Ernst et al., 2019). Initiation of the meiotic phase requires RA signaling that triggers the expression of STRA8. Moreover, STRA8 is necessary not only for meiotic initiation but also for spermatogonia differentiation (Endo et al., 2015). This could suggest that FBXO38 is involved in the regulation of RA metabolism since the early postnatal period.

Moreover, by day 15, Sertoli cells reach their mature state, as they stop proliferating and terminally differentiate. During this transition, Sertoli cells undergo several alterations in the expression of their genes, such as downregulation of anti-Müllerian hormone (AMH) or upregulation of the interleukin-1α (Petersen and Soder, 2006). Sertoli cell maturation is also accompanied by morphological changes represented by more prominent nucleolus and enlargement of the nucleus and its reshaping into a triangle (Sharpe et al., 2003). In *Fbxo38*-deficient Sertoli cells, we detected less prominent morphological changes of the nucleus; however, further quantification is needed to confirm this observation. Moreover, the formation of BTB represents one of the features of mature Sertoli cells. BTB divides the seminiferous tubules into basal and apical compartments by establishment of junctions between adjacent Sertoli cells. Loss or dysregulation of proteins involved in the formation of BTB leads to disruptions in spermatogenesis (Jiang et al., 2014). Although we did not observe any severe disturbances in the BTB, spermatogenesis defects in *Fbxo38*-deficient mice may result from imbalances in the regulation of BTB formation during Sertoli cell maturation. Interestingly, perturbations in RA signaling were shown to affect not only the proliferation of Sertoli cells but also the formation of BTB (Nicholls et al., 2013).

4.4 Confirmation of *in vitro* Results in the Mouse Model

Since we found that FBXO38 is expressed predominantly by Sertoli cells in adults, we confirmed the stabilization of its substrate ZXDB in this cell type of *Fbxo38*-deficient males. By comparing the transcription profile of Sertoli cells from wild-type and knockout males, we did not detect any alterations in the expression of genes whose promoters we previously identified to be bound by ZXDB in ChIP-seq. This observation confirmed that ZXDB does not act as a typical transcription factor.

Similar to human cancer cell lines, we showed that loss of FBXO38 leads to the upregulation of centromeric proteins in testes. Centromeric staining may be used as a marker to distinguish certain spermatogenesis cell populations, as we showed by anti-centromeric antibodies (ACA) in testicular squashes. Spermatogonia exhibit centromeric dots randomly distributed across the nucleus. Meiotic spermatocytes show telocentric chromosomes with the centromeres attached to the nuclear membrane. Interestingly, as adult Sertoli cells are differentiated and not proliferating, they show unique localization of centromeric proteins. Rather than being centralized in distinct spots, they are diffusely distributed throughout the nucleus with upregulation around the nucleolus and adjacent chromocenters. As loss of FBXO38 led to the increase of centromeric proteins around the nucleoli, it opened an interesting question about the relationship between their centromeres, chromocenters, and nucleoli. The higher CENP-B occupancy could lead to unfavorable heterochromatinization that results in transcriptional silencing (Francastel et al., 1999; Okada et al., 2007; Otake et al., 2020). Sertoli cells exhibit prominent nucleolus flanked by two chromocenters, where all the centromeric heterochromatin is located (Jean et al., 1983). There are several observations that centromere rearrangements leading to their association with nucleoli could affect rRNA gene transcription (Haaf et al., 1990). One of the methods how to assess rRNA production can be the measurement of nucleophosmin (NPM) signal intensity (Maggi et al., 2008; Yung et al., 1985). Accordingly, we observed a decrease in NPM signal in *Fbxo38*-deficient Sertoli cells, suggesting downregulation of rRNA production, which can affect other cellular functions. Production of ribosomes is a tightly regulated process sensitive to stress that immediately ceases rRNA transcription, followed by p53 activation (Golomb et al., 2014). Whether our observed decrease in rRNA leads to cellular stress with subsequent p53 activation would require further research.

5. Conclusions

The ubiquitin-proteasome system is a cellular mechanism that shapes the temporal and spatial proteome through targeted protein degradation. This control is achieved by specific recognition of target proteins by ubiquitin ligases. The presented project focused on the functional characterization of the SCF^{FBXO38} ubiquitin ligase *in vitro* and *in vivo*.

We identified several proteins specifically interacting with FBXO38 and proved that zinc-finger proteins ZXDA and ZXDB act as the substrates of SCF^{FBXO38} ubiquitin ligase. By detailed biochemical analysis, we showed that a short stretch of amino acids between the fourth and fifth zinc fingers is required for the ZXDA/B interaction with FBXO38 and thus represents the novel FBXO38-dependent degron. Since the molecular function of ZXDA/B proteins is largely unknown, we performed a series of interaction and functional studies. We showed that they are novel regulators of centromere chromatin integrity due to their direct interaction with the centromeric protein CENP-B. Furthermore, we demonstrated that CENP-B recognizes ZXDA/B independently on FBXO38 and that the formation of these complexes is mutually exclusive.

In conclusion, we have discovered that FBXO38 controls the integrity of the centromere through the stability of ZXDA/B and that inappropriate stabilization of the ZXDA/B proteins leads to increased occupancy of centromere regions with CENP-A and CENP-B (Figure 12). To the best of our knowledge, this is the first observation of ubiquitin ligase mutated in a neurodegenerative syndrome showing its involvement in epigenetic signature control of centromeric regions. Thus, it is important not only for future basic research but also for understanding the pathologic consequences of hereditary genetic alterations.

The second part of this project presents our analysis of a mouse model deficient in *Fbxo38*. A comprehensive study of this model showed that FBXO38 controls organ growth, especially in the male reproductive system. We demonstrated that spermatogenesis and the organization of seminiferous tubules are severely affected by the loss of *Fbxo38*. We detected that FBXO38 is expressed predominantly by Sertoli cells, where we confirmed that FBXO38 executes its functions by mediating the degradation of ZXDB. By analyzing the transcriptome of *Fbxo38*-deficient Sertoli cells, we showed that they resemble the immature state of this cell type. Mostly affected were genes involved in Sertoli cell-dependent spermatogonial activation and differentiation. As a result, we observed impaired meiotic initiation, lower sperm production, and partial infertility in

Fbxo38-deficient males. In addition, we confirmed the upregulation of centromeric proteins and showed alterations in their distribution in *Fbxo38*-deficient Sertoli cells.

In summary, we have shown that FBXO38 is involved in a novel biochemical pathway controlling centromere integrity. We proved that this pathway is active in cancer cell lines and *in vivo* during spermatogenesis.

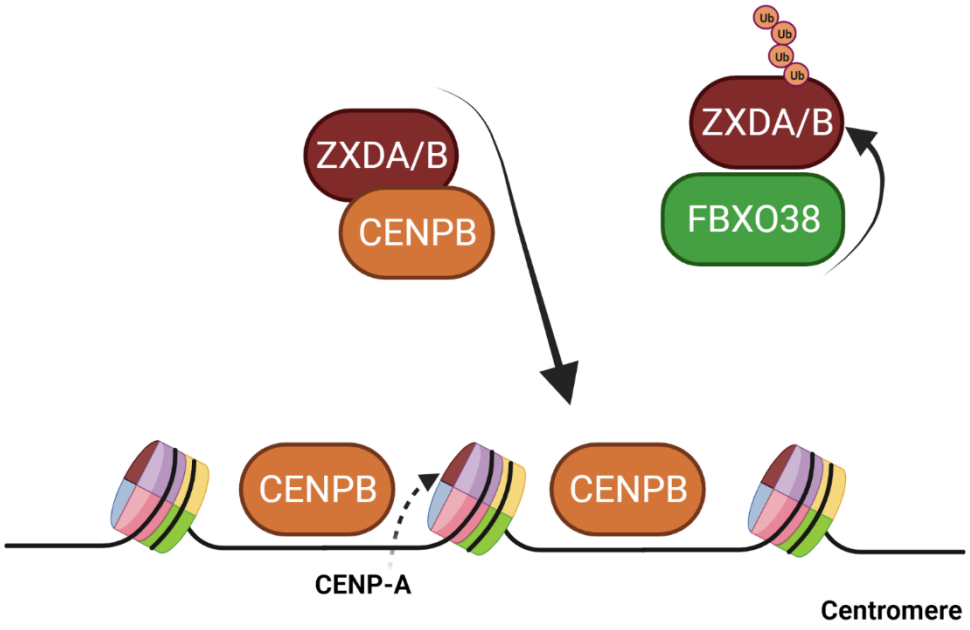


Figure 12. Model of the novel pathway controlling centromere integrity. FBXO38 mediates the degradation of ZXDA/B and thus limits CENP-B chromatin loading, as ZXDA/B proteins control CENP-B.

6. List of Publications

The doctoral thesis was based on the following publications:

Dibus, N., Korinek, V., and Cermak, L. (2022a). FBXO38 Ubiquitin Ligase Controls Centromere Integrity via ZXDA/B Stability. Frontiers in Cell and Developmental Biology *10*.

Dibus, N., Zobalova, E., Monleon, M.A.M., Korinek, V., Filipp, D., Petrusova, J., Sedlacek, R., Kasparek, P., and Cermak, L. (2022b). FBXO38 Ubiquitin Ligase Controls Sertoli Cell Maturation. Frontiers in Cell and Developmental Biology *10*.

Baloghova, N., Lidak, T., and Cermak, L. (2019). Ubiquitin Ligases Involved in the Regulation of Wnt, TGF-beta, and Notch Signaling Pathways and Their Roles in Mouse Development and Homeostasis. Genes (Basel) *10*.

Publications not included in the doctoral thesis:

Lidak, T., Baloghova, N., Korinek, V., Sedlacek, R., Balounova, J., Kasparek, P., and Cermak, L. (2021). CRL4-DCAF12 Ubiquitin Ligase Controls MOV10 RNA Helicase during Spermatogenesis and T Cell Activation. Int J Mol Sci *22*.

Janeckova, L., Kostovcikova, K., Svec, J., Stastna, M., Strnad, H., Kolar, M., Hudcovic, T., Stancikova, J., Tureckova, J., Baloghova, N., *et al.* (2019). Unique Gene Expression Signatures in the Intestinal Mucosa and Organoids Derived from Germ-Free and Monoassociated Mice. Int J Mol Sci *20*.

Janeckova, L., Kolar, M., Svec, J., Lanikova, L., Pospichalova, V., Baloghova, N., Vojtechova, M., Sloncova, E., Strnad, H., and Korinek, V. (2016). HIC1 Expression Distinguishes Intestinal Carcinomas Sensitive to Chemotherapy. Transl Oncol *9*, 99-107.

Janeckova, L., Pospichalova, V., Fafilek, B., Vojtechova, M., Tureckova, J., Dobes, J., Dubuissez, M., Leprince, D., Baloghova, N., Horazna, M., *et al.* (2015). HIC1 Tumor Suppressor Loss Potentiates TLR2/NF-kappaB Signaling and Promotes Tissue Damage-Associated Tumorigenesis. Mol Cancer Res *13*, 1139-1148.

7. References

Akcimen, F., Vural, A., Durmus, H., Cakar, A., Houlden, H., *et al.* (2019). A novel homozygous FBXO38 variant causes an early-onset distal hereditary motor neuronopathy type IID. J Hum Genet *64*, 1141-1144.

Al-Kandari, W., Jambunathan, S., Navalgund, V., Koneni, R., Freer, M., *et al.* (2007a). ZXDC, a novel zinc finger protein that binds CIITA and activates MHC gene transcription. Mol Immunol *44*, 311-321.

Al-Kandari, W., Koneni, R., Navalgund, V., Aleksandrova, A., Jambunathan, S., *et al.* (2007b). The zinc finger proteins ZXDA and ZXDC form a complex that binds CIITA and regulates MHC II gene transcription. J Mol Biol *369*, 1175-1187.

Ali, A., Mistry, B.V., Ahmed, H.A., Abdulla, R., Amer, H.A., *et al.* (2018). Deletion of DDB1- and CUL4- associated factor-17 (Dcaf17) gene causes spermatogenesis defects and male infertility in mice. Sci Rep *8*, 9202.

Altemose, N., Logsdon, G.A., Bzikadze, A.V., Sidhwani, P., Langley, S.A., *et al.* (2022). Complete genomic and epigenetic maps of human centromeres. Science *376*, eabl4178.

Arnold, S.L., Kent, T., Hogarth, C.A., Schlatt, S., Prasad, B., *et al.* (2015). Importance of ALDH1A enzymes in determining human testicular retinoic acid concentrations. J Lipid Res *56*, 342-357.

Athwal, R.K., Walkiewicz, M.P., Baek, S., Fu, S., Bui, M., *et al.* (2015). CENP-A nucleosomes localize to transcription factor hotspots and subtelomeric sites in human cancer cells. Epigenetics Chromatin *8*, 2.

Baek, K., Scott, D.C., and Schulman, B.A. (2021). NEDD8 and ubiquitin ligation by cullin-RING E3 ligases. Curr Opin Struct Biol *67*, 101-109.

Bai, C., Sen, P., Hofmann, K., Ma, L., Goebl, M., *et al.* (1996). SKP1 connects cell cycle regulators to the ubiquitin proteolysis machinery through a novel motif, the F-box. Cell *86*, 263-274.

Baloghova, N., Lidak, T., and Cermak, L. (2019). Ubiquitin Ligases Involved in the Regulation of Wnt, TGF-beta, and Notch Signaling Pathways and Their Roles in Mouse Development and Homeostasis. Genes (Basel) *10*.

Bard, J.A.M., Goodall, E.A., Greene, E.R., Jonsson, E., Dong, K.C., *et al.* (2018). Structure and Function of the 26S Proteasome. Annu Rev Biochem *87*, 697-724.

Bellve, A.R., Cavicchia, J.C., Millette, C.F., O'Brien, D.A., Bhatnagar, Y.M., *et al.* (1977). Spermatogenic cells of the prepuberal mouse. Isolation and morphological characterization. J Cell Biol *74*, 68-85.

Bergmann, J.H., Rodriguez, M.G., Martins, N.M., Kimura, H., Kelly, D.A., *et al.* (2011). Epigenetic engineering shows H3K4me2 is required for HJURP targeting and CENP-A assembly on a synthetic human kinetochore. EMBO J *30*, 328-340.

Bodor, D.L., Mata, J.F., Sergeev, M., David, A.F., Salimian, K.J., *et al.* (2014). The quantitative architecture of centromeric chromatin. Elife *3*, e02137.

Bornstein, G., Bloom, J., Sitry-Shevah, D., Nakayama, K., Pagano, M., *et al.* (2003). Role of the SCFSkp2 ubiquitin ligase in the degradation of p21Cip1 in S phase. J Biol Chem *278*, 25752-25757.

Bowles, J., Feng, C.W., Ineson, J., Miles, K., Spiller, C.M., *et al.* (2018). Retinoic Acid Antagonizes Testis Development in Mice. Cell Rep *24*, 1330-1341.

Bowles, J., Feng, C.W., Spiller, C., Davidson, T.L., Jackson, A., *et al.* (2010). FGF9 suppresses meiosis and promotes male germ cell fate in mice. Dev Cell *19*, 440-449.

Bowles, J., Knight, D., Smith, C., Wilhelm, D., Richman, J.*, et al.* (2006). Retinoid signaling determines germ cell fate in mice. Science *312*, 596-600.

Busada, J.T., Kaye, E.P., Renegar, R.H., and Geyer, C.B. (2014). Retinoic acid induces multiple hallmarks of the prospermatogonia-to-spermatogonia transition in the neonatal mouse. Biol Reprod *90*, 64.

Cardozo, T., and Pagano, M. (2004). The SCF ubiquitin ligase: insights into a molecular machine. Nat Rev Mol Cell Biol *5*, 739-751.

Carrano, A.C., Eytan, E., Hershko, A., and Pagano, M. (1999). SKP2 is required for ubiquitin-mediated degradation of the CDK inhibitor p27. Nat Cell Biol *1*, 193-199.

Carroll, C.W., Milks, K.J., and Straight, A.F. (2010). Dual recognition of CENP-A nucleosomes is required for centromere assembly. J Cell Biol *189*, 1143-1155.

Casola, C., Hucks, D., and Feschotte, C. (2008). Convergent domestication of pogo-like transposases into centromere-binding proteins in fission yeast and mammals. Mol Biol Evol *25*, 29-41.

Cassandri, M., Smirnov, A., Novelli, F., Pitolli, C., Agostini, M.*, et al.* (2017). Zinc-finger proteins in health and disease. Cell Death Discov *3*, 17071.

Chambon, P. (1996). A decade of molecular biology of retinoic acid receptors. FASEB J *10*, 940-954.

Chamoto, K., Al-Habsi, M., and Honjo, T. (2017). Role of PD-1 in Immunity and Diseases. Curr Top Microbiol Immunol *410*, 75-97.

Chau, V., Tobias, J.W., Bachmair, A., Marriott, D., Ecker, D.J.*, et al.* (1989). A multiubiquitin chain is confined to specific lysine in a targeted short-lived protein. Science *243*, 1576-1583.

Cheeseman, I.M., Chappie, J.S., Wilson-Kubalek, E.M., and Desai, A. (2006). The conserved KMN network constitutes the core microtubule-binding site of the kinetochore. Cell *127*, 983-997.

Cheeseman, I.M., and Desai, A. (2008). Molecular architecture of the kinetochore-microtubule interface. Nat Rev Mol Cell Biol *9*, 33-46.

Cheng, C.Y., and Mruk, D.D. (2012). The blood-testis barrier and its implications for male contraception. Pharmacol Rev *64*, 16-64.

Ciehanover, A., Hod, Y., and Hershko, A. (1978). A heat-stable polypeptide component of an ATP-dependent proteolytic system from reticulocytes. Biochem Biophys Res Commun *81*, 1100-1105.

Dadoune, J.P. (2007). New insights into male gametogenesis: what about the spermatogonial stem cell niche? Folia Histochem Cytobiol *45*, 141-147.

Deshaies, R.J., and Joazeiro, C.A. (2009). RING domain E3 ubiquitin ligases. Annu Rev Biochem *78*, 399-434.

du Sart, D., Cancilla, M.R., Earle, E., Mao, J.I., Saffery, R.*, et al.* (1997). A functional neo-centromere formed through activation of a latent human centromere and consisting of non-alpha-satellite DNA. Nat Genet *16*, 144-153.

Duda, D.M., Borg, L.A., Scott, D.C., Hunt, H.W., Hammel, M.*, et al.* (2008). Structural insights into NEDD8 activation of cullin-RING ligases: conformational control of conjugation. Cell *134*, 995-1006.

Dunleavy, E.M., Roche, D., Tagami, H., Lacoste, N., Ray-Gallet, D.*, et al.* (2009). HJURP is a cell-cycle-dependent maintenance and deposition factor of CENP-A at centromeres. Cell *137*, 485-497.

Earnshaw, W.C., and Rothfield, N. (1985). Identification of a family of human centromere proteins using autoimmune sera from patients with scleroderma. Chromosoma *91*, 313-321.

Edelsztein, N.Y., Kashimada, K., Schteingart, H.F., and Rey, R.A. (2020). CYP26B1 declines postnatally in Sertoli cells independently of androgen action in the mouse testis. Mol Reprod Dev *87*, 66-77.

Endo, T., Romer, K.A., Anderson, E.L., Baltus, A.E., de Rooij, D.G.*, et al.* (2015). Periodic retinoic acid-STRA8 signaling intersects with periodic germ-cell competencies to regulate spermatogenesis. Proc Natl Acad Sci U S A *112*, E2347-2356.

Ernst, C., Eling, N., Martinez-Jimenez, C.P., Marioni, J.C., and Odom, D.T. (2019). Staged developmental mapping and X chromosome transcriptional dynamics during mouse spermatogenesis. Nat Commun *10*, 1251.

Etlinger, J.D., and Goldberg, A.L. (1977). A soluble ATP-dependent proteolytic system responsible for the degradation of abnormal proteins in reticulocytes. Proc Natl Acad Sci U S A *74*, 54-58.

Fachinetti, D., Folco, H.D., Nechemia-Arbely, Y., Valente, L.P., Nguyen, K.*, et al.* (2013). A two-step mechanism for epigenetic specification of centromere identity and function. Nat Cell Biol *15*, 1056-1066.

Fachinetti, D., Han, J.S., McMahon, M.A., Ly, P., Abdullah, A.*, et al.* (2015). DNA Sequence-Specific Binding of CENP-B Enhances the Fidelity of Human Centromere Function. Dev Cell *33*, 314-327.

Finley, D. (2009). Recognition and processing of ubiquitin-protein conjugates by the proteasome. Annu Rev Biochem *78*, 477-513.

Foltz, D.R., Jansen, L.E., Bailey, A.O., Yates, J.R., 3rd, Bassett, E.A.*, et al.* (2009). Centromere-specific assembly of CENP-a nucleosomes is mediated by HJURP. Cell *137*, 472-484.

Fowler, K.J., Hudson, D.F., Salamonsen, L.A., Edmondson, S.R., Earle, E.*, et al.* (2000). Uterine dysfunction and genetic modifiers in centromere protein B-deficient mice. Genome Res *10*, 30-41.

Fowler, K.J., Wong, L.H., Griffiths, B.K., Sibson, M.C., Reed, S.*, et al.* (2004). Centromere protein b-null mice display decreasing reproductive performance through successive generations of breeding due to diminishing endometrial glands. Reproduction *127*, 367-377.

Francastel, C., Walters, M.C., Groudine, M., and Martin, D.I. (1999). A functional enhancer suppresses silencing of a transgene and prevents its localization close to centrometric heterochromatin. Cell *99*, 259-269.

Fujita, R., Otake, K., Arimura, Y., Horikoshi, N., Miya, Y.*, et al.* (2015). Stable complex formation of CENP-B with the CENP-A nucleosome. Nucleic Acids Res *43*, 4909-4922.

Fujita, Y., Hayashi, T., Kiyomitsu, T., Toyoda, Y., Kokubu, A.*, et al.* (2007). Priming of centromere for CENP-A recruitment by human hMis18alpha, hMis18beta, and M18BP1. Dev Cell *12*, 17-30.

Fukagawa, T., and Earnshaw, W.C. (2014). The centromere: chromatin foundation for the kinetochore machinery. Dev Cell *30*, 496-508.

Furuya, S., Kumamoto, Y., and Sugiyama, S. (1978). Fine structure and development of Sertoli junctions in human testis. Arch Androl *1*, 211-219.

Gamba, R., and Fachinetti, D. (2020). From evolution to function: Two sides of the same CENP-B coin? Exp Cell Res *390*, 111959.

Gely-Pernot, A., Raverdeau, M., Teletin, M., Vernet, N., Feret, B.*, et al.* (2015). Retinoic Acid Receptors Control Spermatogonia Cell-Fate and Induce Expression of the SALL4A Transcription Factor. PLoS Genet *11*, e1005501.

Georges, A., Coyaud, E., Marcon, E., Greenblatt, J., Raught, B.*, et al.* (2019). USP7 Regulates Cytokinesis through FBXO38 and KIF20B. Sci Rep *9*, 2724.

Gewiss, R., Topping, T., and Griswold, M.D. (2020). Cycles, waves, and pulses: Retinoic acid and the organization of spermatogenesis. Andrology *8*, 892-897.

Goldstein, G., Scheid, M., Hammerling, U., Schlesinger, D.H., Niall, H.D.*, et al.* (1975). Isolation of a polypeptide that has lymphocyte-differentiating properties and is probably represented universally in living cells. Proc Natl Acad Sci U S A *72*, 11-15.

Golomb, L., Volarevic, S., and Oren, M. (2014). p53 and ribosome biogenesis stress: the essentials. FEBS Lett *588*, 2571-2579.

Greig, G.M., Sharp, C.B., Carrel, L., and Willard, H.F. (1993). Duplicated zinc finger protein genes on the proximal short arm of the human X chromosome: isolation, characterization and X-inactivation studies. Hum Mol Genet *2*, 1611-1618.

Griswold, M. (2015). The initiation of spermatogenesis and the cycle of the seminiferous epithelium. In, pp. 233-245.

Griswold, M.D. (2018). 50 years of spermatogenesis: Sertoli cells and their interactions with germ cells. Biol Reprod *99*, 87-100.

Grunseich, C., Sarkar, N., Lu, J., Owen, M., Schindler, A.*, et al.* (2021). Improving the efficacy of exome sequencing at a quaternary care referral centre: novel mutations, clinical presentations and diagnostic challenges in rare neurogenetic diseases. J Neurol Neurosurg Psychiatry *92*, 1186-1196.

Guardavaccaro, D., Kudo, Y., Boulaire, J., Barchi, M., Busino, L.*, et al.* (2003). Control of meiotic and mitotic progression by the F box protein beta-Trcp1 in vivo. Dev Cell *4*, 799-812.

Haaf, T., Steinlein, C., and Schmid, M. (1990). Nucleolar transcriptional activity in mouse Sertoli cells is dependent on centromere arrangement. Exp Cell Res *191*, 157-160.

Hara, M., and Fukagawa, T. (2017). Critical Foundation of the Kinetochore: The Constitutive Centromere-Associated Network (CCAN). Prog Mol Subcell Biol *56*, 29-57.

Harrington, J.J., Van Bokkelen, G., Mays, R.W., Gustashaw, K., and Willard, H.F. (1997). Formation of de novo centromeres and construction of first-generation human artificial microchromosomes. Nat Genet *15*, 345-355.

Hatakeyama, S., and Nakayama, K.I. (2003). U-box proteins as a new family of ubiquitin ligases. Biochem Biophys Res Commun *302*, 635-645.

Hemmerich, P., Stoyan, T., Wieland, G., Koch, M., Lechner, J.*, et al.* (2000). Interaction of yeast kinetochore proteins with centromere-protein/transcription factor Cbf1. Proc Natl Acad Sci U S A *97*, 12583-12588.

Hershko, A., and Ciechanover, A. (1998). The ubiquitin system. Annu Rev Biochem *67*, 425-479.

Hirvonen, E.A.M., Pitkanen, E., Hemminki, K., Aaltonen, L.A., and Kilpivaara, O. (2017). Whole-exome sequencing identifies novel candidate predisposition genes for familial polycythemia vera. Hum Genomics *11*, 6.

Hoffmann, S., Dumont, M., Barra, V., Ly, P., Nechemia-Arbely, Y.*, et al.* (2016). CENP-A Is Dispensable for Mitotic Centromere Function after Initial Centromere/Kinetochore Assembly. Cell Rep *17*, 2394-2404.

Howman, E.V., Fowler, K.J., Newson, A.J., Redward, S., MacDonald, A.C.*, et al.* (2000). Early disruption of centromeric chromatin organization in centromere protein A (Cenpa) null mice. Proc Natl Acad Sci U S A *97*, 1148-1153.

Huang, A., Kremser, L., Schuler, F., Wilflingseder, D., Lindner, H., *et al.* (2019). Phosphorylation of Drosophila CENP-A on serine 20 regulates protein turn-over and centromere-specific loading. Nucleic Acids Res *47*, 10754-10770.

Hudson, D.F., Fowler, K.J., Earle, E., Saffery, R., Kalitsis, P., *et al.* (1998). Centromere protein B null mice are mitotically and meiotically normal but have lower body and testis weights. J Cell Biol *141*, 309-319.

Huttlin, E.L., Bruckner, R.J., Navarrete-Perea, J., Cannon, J.R., Baltier, K., *et al.* (2021). Dual proteome-scale networks reveal cell-specific remodeling of the human interactome. Cell *184*, 3022-3040 e3028.

Ishikura, S., Yoshida, K., Hashimoto, S., Nakabayashi, K., Tsunoda, T., *et al.* (2021). CENP-B promotes the centromeric localization of ZFAT to control transcription of noncoding RNA. J Biol Chem *297*, 101213.

Janca, F.C., Jost, L.K., and Evenson, D.P. (1986). Mouse testicular and sperm cell development characterized from birth to adulthood by dual parameter flow cytometry. Biol Reprod *34*, 613-623.

Jansen, L.E., Black, B.E., Foltz, D.R., and Cleveland, D.W. (2007). Propagation of centromeric chromatin requires exit from mitosis. J Cell Biol *176*, 795-805.

Jantz, D., and Berg, J.M. (2004). Reduction in DNA-binding affinity of Cys2His2 zinc finger proteins by linker phosphorylation. Proc Natl Acad Sci U S A *101*, 7589-7593.

Jean, P., Hartung, M., Mirre, C., and Stahl, A. (1983). Association of centromeric heterochromatin with the nucleolus in mouse Sertoli cells. Anat Rec *205*, 375-380.

Jeffery, D., Gatto, A., Podsypanina, K., Renaud-Pageot, C., Ponce Landete, R., *et al.* (2021). CENP-A overexpression promotes distinct fates in human cells, depending on p53 status. Commun Biol *4*, 417.

Jiang, X.H., Bukhari, I., Zheng, W., Yin, S., Wang, Z., *et al.* (2014). Blood-testis barrier and spermatogenesis: lessons from genetically-modified mice. Asian J Androl *16*, 572-580.

Jin, J., Cardozo, T., Lovering, R.C., Elledge, S.J., Pagano, M., *et al.* (2004). Systematic analysis and nomenclature of mammalian F-box proteins. Genes Dev *18*, 2573-2580.

Kanarek, N., Horwitz, E., Mayan, I., Leshets, M., Cojocaru, G., *et al.* (2010). Spermatogenesis rescue in a mouse deficient for the ubiquitin ligase SCF{beta}-TrCP by single substrate depletion. Genes Dev *24*, 470-477.

Kapoor, M., Montes de Oca Luna, R., Liu, G., Lozano, G., Cummings, C., *et al.* (1998). The cenpB gene is not essential in mice. Chromosoma *107*, 570-576.

Kato, Y., Katsuki, T., Kokubo, H., Masuda, A., and Saga, Y. (2016). Dazl is a target RNA suppressed by mammalian NANOS2 in sexually differentiating male germ cells. Nat Commun *7*, 11272.

Kawaguchi, R., Yu, J., Honda, J., Hu, J., Whitelegge, J., *et al.* (2007). A membrane receptor for retinol binding protein mediates cellular uptake of vitamin A. Science *315*, 820-825.

Kerr, J.B., and de Kretser, D.M. (1974). Proceedings: The role of the Sertoli cell in phagocytosis of the residual bodies of spermatids. J Reprod Fertil *36*, 439-440.

Kipling, D., and Warburton, P.E. (1997). Centromeres, CENP-B and Tigger too. Trends Genet *13*, 141-145.

Kit, S. (1961). Equilibrium sedimentation in density gradients of DNA preparations from animal tissues. J Mol Biol *3*, 711-716.

Klare, K., Weir, J.R., Basilico, F., Zimniak, T., Massimiliano, L., *et al.* (2015). CENP-C is a blueprint for constitutive centromere-associated network assembly within human kinetochores. J Cell Biol *210*, 11-22.

Komander, D., Clague, M.J., and Urbe, S. (2009). Breaking the chains: structure and function of the deubiquitinases. Nat Rev Mol Cell Biol *10*, 550-563.

Komander, D., and Rape, M. (2012). The ubiquitin code. Annu Rev Biochem *81*, 203-229.

Koopman, P., Gubbay, J., Vivian, N., Goodfellow, P., and Lovell-Badge, R. (1991). Male development of chromosomally female mice transgenic for Sry. Nature *351*, 117-121.

Koubova, J., Menke, D.B., Zhou, Q., Capel, B., Griswold, M.D., *et al.* (2006). Retinoic acid regulates sex-specific timing of meiotic initiation in mice. Proc Natl Acad Sci U S A *103*, 2474-2479.

Kubota, H., and Brinster, R.L. (2018). Spermatogonial stem cells†. Biology of Reproduction *99*, 52-74.

Lachner, M., O'Carroll, D., Rea, S., Mechtler, K., and Jenuwein, T. (2001). Methylation of histone H3 lysine 9 creates a binding site for HP1 proteins. Nature *410*, 116-120.

Laity, J.H., Dyson, H.J., and Wright, P.E. (2000). DNA-induced alpha-helix capping in conserved linker sequences is a determinant of binding affinity in Cys(2)-His(2) zinc fingers. J Mol Biol *295*, 719-727.

Low, T.Y., Peng, M., Magliozzi, R., Mohammed, S., Guardavaccaro, D., *et al.* (2014). A systems-wide screen identifies substrates of the SCFbetaTrCP ubiquitin ligase. Sci Signal *7*, rs8.

Lyapina, S., Cope, G., Shevchenko, A., Serino, G., Tsuge, T., *et al.* (2001). Promotion of NEDD-CUL1 conjugate cleavage by COP9 signalosome. Science *292*, 1382-1385.

MacLean, G., Li, H., Metzger, D., Chambon, P., and Petkovich, M. (2007). Apoptotic extinction of germ cells in testes of Cyp26b1 knockout mice. Endocrinology *148*, 4560-4567.

Maggi, L.B., Jr., Kuchenruether, M., Dadey, D.Y., Schwope, R.M., Grisendi, S., *et al.* (2008). Nucleophosmin serves as a rate-limiting nuclear export chaperone for the Mammalian ribosome. Mol Cell Biol *28*, 7050-7065.

Marshall, O.J., Chueh, A.C., Wong, L.H., and Choo, K.H. (2008). Neocentromeres: new insights into centromere structure, disease development, and karyotype evolution. Am J Hum Genet *82*, 261-282.

Martins, N.M.C., Cisneros-Soberanis, F., Pesenti, E., Kochanova, N.Y., Shang, W.H., *et al.* (2020). H3K9me3 maintenance on a human artificial chromosome is required for segregation but not centromere epigenetic memory. J Cell Sci *133*.

Masumoto, H., Masukata, H., Muro, Y., Nozaki, N., and Okazaki, T. (1989). A human centromere antigen (CENP-B) interacts with a short specific sequence in alphoid DNA, a human centromeric satellite. J Cell Biol *109*, 1963-1973.

Mateo, L., and Gonzalez, J. (2014). Pogo-like transposases have been repeatedly domesticated into CENP-B-related proteins. Genome Biol Evol *6*, 2008-2016.

McKinley, K.L., and Cheeseman, I.M. (2014). Polo-like kinase 1 licenses CENP-A deposition at centromeres. Cell *158*, 397-411.

McKinley, K.L., and Cheeseman, I.M. (2016). The molecular basis for centromere identity and function. Nat Rev Mol Cell Biol *17*, 16-29.

McLachlan, R.I., O'Donnell, L., Meachem, S.J., Stanton, P.G., de Kretser, D.M., *et al.* (2002). Identification of specific sites of hormonal regulation in spermatogenesis in rats, monkeys, and man. Recent Prog Horm Res *57*, 149-179.

Meng, X., Liu, X., Guo, X., Jiang, S., Chen, T.*, et al.* (2018). FBXO38 mediates PD-1 ubiquitination and regulates anti-tumour immunity of T cells. Nature *564*, 130-135.

Meroni, S.B., Galardo, M.N., Rindone, G., Gorga, A., Riera, M.F.*, et al.* (2019). Molecular Mechanisms and Signaling Pathways Involved in Sertoli Cell Proliferation. Front Endocrinol (Lausanne) *10*, 224.

Metzger, M.B., Pruneda, J.N., Klevit, R.E., and Weissman, A.M. (2014). RING-type E3 ligases: master manipulators of E2 ubiquitin-conjugating enzymes and ubiquitination. Biochim Biophys Acta *1843*, 47-60.

Moree, B., Meyer, C.B., Fuller, C.J., and Straight, A.F. (2011). CENP-C recruits M18BP1 to centromeres to promote CENP-A chromatin assembly. J Cell Biol *194*, 855-871.

Morimoto, Y., Ono, S., Imamura, A., Okazaki, Y., Kinoshita, A.*, et al.* (2017). Deep sequencing reveals variations in somatic cell mosaic mutations between monozygotic twins with discordant psychiatric disease. Hum Genome Var *4*, 17032.

Murata, S., Sasaki, K., Kishimoto, T., Niwa, S., Hayashi, H.*, et al.* (2007). Regulation of CD8+ T cell development by thymus-specific proteasomes. Science *316*, 1349-1353.

Murata, S., Takahama, Y., Kasahara, M., and Tanaka, K. (2018). The immunoproteasome and thymoproteasome: functions, evolution and human disease. Nat Immunol *19*, 923-931.

Muro, Y., Masumoto, H., Yoda, K., Nozaki, N., Ohashi, M.*, et al.* (1992). Centromere protein B assembles human centromeric alpha-satellite DNA at the 17-bp sequence, CENP-B box. J Cell Biol *116*, 585-596.

Musacchio, A., and Salmon, E.D. (2007). The spindle-assembly checkpoint in space and time. Nat Rev Mol Cell Biol *8*, 379-393.

Nakanishi, Y., and Shiratsuchi, A. (2004). Phagocytic removal of apoptotic spermatogenic cells by Sertoli cells: mechanisms and consequences. Biol Pharm Bull *27*, 13-16.

Nakayama, K., Nagahama, H., Minamishima, Y.A., Matsumoto, M., Nakamichi, I.*, et al.* (2000). Targeted disruption of Skp2 results in accumulation of cyclin E and p27(Kip1), polyploidy and centrosome overduplication. EMBO J *19*, 2069-2081.

Nicholls, P.K., Harrison, C.A., Rainczuk, K.E., Wayne Vogl, A., and Stanton, P.G. (2013). Retinoic acid promotes Sertoli cell differentiation and antagonises activin-induced proliferation. Mol Cell Endocrinol *377*, 33-43.

O'Connor, A.E., and De Kretser, D.M. (2004). Inhibins in normal male physiology. Semin Reprod Med *22*, 177-185.

O'Donnell, L., Nicholls, P.K., O'Bryan, M.K., McLachlan, R.I., and Stanton, P.G. (2011). Spermiation: The process of sperm release. Spermatogenesis *1*, 14-35.

O'Donnell, L., Smith, L.B., and Rebourcet, D. (2021). Sertoli cells as key drivers of testis function. Semin Cell Dev Biol.

Oatley, J.M., and Brinster, R.L. (2012). The germline stem cell niche unit in mammalian testes. Physiol Rev *92*, 577-595.

Ohzeki, J., Bergmann, J.H., Kouprina, N., Noskov, V.N., Nakano, M.*, et al.* (2012). Breaking the HAC Barrier: histone H3K9 acetyl/methyl balance regulates CENP-A assembly. EMBO J *31*, 2391-2402.

Ohzeki, J., Nakano, M., Okada, T., and Masumoto, H. (2002). CENP-B box is required for de novo centromere chromatin assembly on human alphoid DNA. J Cell Biol *159*, 765-775.

Okada, T., Ohzeki, J., Nakano, M., Yoda, K., Brinkley, W.R., *et al.* (2007). CENP-B controls centromere formation depending on the chromatin context. Cell *131*, 1287-1300.

Olma, M.H., and Dikic, I. (2013). Cullins getting undressed by the protein exchange factor Cand1. Cell *153*, 14-16.

Orth, J.M., Gunsalus, G.L., and Lamperti, A.A. (1988). Evidence from Sertoli cell-depleted rats indicates that spermatid number in adults depends on numbers of Sertoli cells produced during perinatal development. Endocrinology *122*, 787-794.

Otake, K., Ohzeki, J.I., Shono, N., Kugou, K., Okazaki, K., *et al.* (2020). CENP-B creates alternative epigenetic chromatin states permissive for CENP-A or heterochromatin assembly. J Cell Sci *133*.

Oulad-Abdelghani, M., Bouillet, P., Decimo, D., Gansmuller, A., Heyberger, S., *et al.* (1996). Characterization of a premeiotic germ cell-specific cytoplasmic protein encoded by Stra8, a novel retinoic acid-responsive gene. J Cell Biol *135*, 469-477.

Palmer, D.K., O'Day, K., Wener, M.H., Andrews, B.S., and Margolis, R.L. (1987). A 17-kD centromere protein (CENP-A) copurifies with nucleosome core particles and with histones. J Cell Biol *104*, 805-815.

Pan, D., Walstein, K., Take, A., Bier, D., Kaiser, N., *et al.* (2019). Mechanism of centromere recruitment of the CENP-A chaperone HJURP and its implications for centromere licensing. Nat Commun *10*, 4046.

Pao, K.C., Wood, N.T., Knebel, A., Rafie, K., Stanley, M., *et al.* (2018). Activity-based E3 ligase profiling uncovers an E3 ligase with esterification activity. Nature *556*, 381-385.

Peng, Y., Wong, C.C., Nakajima, Y., Tyers, R.G., Sarkeshik, A.S., *et al.* (2011). Overlapping kinetochore targets of CK2 and Aurora B kinases in mitotic regulation. Mol Biol Cell *22*, 2680-2689.

Perez-Castro, A.V., Shamanski, F.L., Meneses, J.J., Lovato, T.L., Vogel, K.G., *et al.* (1998). Centromeric protein B null mice are viable with no apparent abnormalities. Dev Biol *201*, 135-143.

Pesin, J.A., and Orr-Weaver, T.L. (2008). Regulation of APC/C activators in mitosis and meiosis. Annu Rev Cell Dev Biol *24*, 475-499.

Peters, A.H., Kubicek, S., Mechtler, K., O'Sullivan, R.J., Derijck, A.A., *et al.* (2003). Partitioning and plasticity of repressive histone methylation states in mammalian chromatin. Mol Cell *12*, 1577-1589.

Petersen, C., and Soder, O. (2006). The sertoli cell--a hormonal target and 'super' nurse for germ cells that determines testicular size. Horm Res *66*, 153-161.

Przewloka, M.R., Venkei, Z., Bolanos-Garcia, V.M., Debski, J., Dadlez, M., *et al.* (2011). CENP-C is a structural platform for kinetochore assembly. Curr Biol *21*, 399-405.

Ramsey, J.E., and Fontes, J.D. (2013). The zinc finger transcription factor ZXDC activates CCL2 gene expression by opposing BCL6-mediated repression. Mol Immunol *56*, 768-780.

Rizkallah, R., Alexander, K.E., and Hurt, M.M. (2011). Global mitotic phosphorylation of C2H2 zinc finger protein linker peptides. Cell Cycle *10*, 3327-3336.

Rotgers, E., Jorgensen, A., and Yao, H.H. (2018). At the Crossroads of Fate-Somatic Cell Lineage Specification in the Fetal Gonad. Endocr Rev *39*, 739-759.

Rotin, D., and Kumar, S. (2009). Physiological functions of the HECT family of ubiquitin ligases. Nat Rev Mol Cell Biol *10*, 398-409.

Schmahl, J., Eicher, E.M., Washburn, L.L., and Capel, B. (2000). Sry induces cell proliferation in the mouse gonad. Development *127*, 65-73.

Scott, K.C., and Sullivan, B.A. (2014). Neocentromeres: a place for everything and everything in its place. Trends Genet *30*, 66-74.

Sharpe, R.M., McKinnell, C., Kivlin, C., and Fisher, J.S. (2003). Proliferation and functional maturation of Sertoli cells, and their relevance to disorders of testis function in adulthood. Reproduction *125*, 769-784.

Sinclair, A.H., Berta, P., Palmer, M.S., Hawkins, J.R., Griffiths, B.L.*, et al.* (1990). A gene from the human sex-determining region encodes a protein with homology to a conserved DNA-binding motif. Nature *346*, 240-244.

Skaar, J.R., Pagan, J.K., and Pagano, M. (2013). Mechanisms and function of substrate recruitment by F-box proteins. Nat Rev Mol Cell Biol *14*, 369-381.

Smaldone, S., Laub, F., Else, C., Dragomir, C., and Ramirez, F. (2004). Identification of MoKA, a novel F-box protein that modulates Kruppel-like transcription factor 7 activity. Mol Cell Biol *24*, 1058-1069.

Smaldone, S., and Ramirez, F. (2006). Multiple pathways regulate intracellular shuttling of MoKA, a co-activator of transcription factor KLF7. Nucleic Acids Res *34*, 5060-5068.

Smith, L.B., and Walker, W.H. (2014). The regulation of spermatogenesis by androgens. Semin Cell Dev Biol *30*, 2-13.

Soucy, T.A., Smith, P.G., Milhollen, M.A., Berger, A.J., Gavin, J.M.*, et al.* (2009). An inhibitor of NEDD8-activating enzyme as a new approach to treat cancer. Nature *458*, 732-736.

Spratt, D.E., Walden, H., and Shaw, G.S. (2014). RBR E3 ubiquitin ligases: new structures, new insights, new questions. Biochem J *458*, 421-437.

Stankovic, A., Guo, L.Y., Mata, J.F., Bodor, D.L., Cao, X.J.*, et al.* (2017). A Dual Inhibitory Mechanism Sufficient to Maintain Cell-Cycle-Restricted CENP-A Assembly. Mol Cell *65*, 231-246.

Stanton, P.G. (2016). Regulation of the blood-testis barrier. Semin Cell Dev Biol *59*, 166-173.

Sugimoto, K., and Himeno, M. (1992). Casein kinase II site of human centromere protein B (CENP-B) is phosphorylated in vitro. Biosci Biotechnol Biochem *56*, 1174-1175.

Sullivan, B.A., and Karpen, G.H. (2004). Centromeric chromatin exhibits a histone modification pattern that is distinct from both euchromatin and heterochromatin. Nat Struct Mol Biol *11*, 1076-1083.

Sumner, C.J., d'Ydewalle, C., Wooley, J., Fawcett, K.A., Hernandez, D.*, et al.* (2013). A dominant mutation in FBXO38 causes distal spinal muscular atrophy with calf predominance. Am J Hum Genet *93*, 976-983.

Suzuki, A., and Saga, Y. (2008). Nanos2 suppresses meiosis and promotes male germ cell differentiation. Genes Dev *22*, 430-435.

Swatek, K.N., and Komander, D. (2016). Ubiquitin modifications. Cell Res *26*, 399-422.

Tanwar, P.S., Kaneko-Tarui, T., Zhang, L., Rani, P., Taketo, M.M.*, et al.* (2010). Constitutive WNT/beta-catenin signaling in murine Sertoli cells disrupts their differentiation and ability to support spermatogenesis. Biol Reprod *82*, 422-432.

Tokheim, C., Wang, X., Timms, R.T., Zhang, B., Mena, E.L.*, et al.* (2021). Systematic characterization of mutations altering protein degradation in human cancers. Mol Cell *81*, 1292-1308 e1211.

Tsutsumi, T., Kuwabara, H., Arai, T., Xiao, Y., and Decaprio, J.A. (2008). Disruption of the Fbxw8 gene results in pre- and postnatal growth retardation in mice. Mol Cell Biol *28*, 743-751.

Vafa, O., and Sullivan, K.F. (1997). Chromatin containing CENP-A and alpha-satellite DNA is a major component of the inner kinetochore plate. Curr Biol *7*, 897-900.

Vergouwen, R.P., Jacobs, S.G., Huiskamp, R., Davids, J.A., and de Rooij, D.G. (1991). Proliferative activity of gonocytes, Sertoli cells and interstitial cells during testicular development in mice. J Reprod Fertil *93*, 233-243.

Vernet, N., Dennefeld, C., Rochette-Egly, C., Oulad-Abdelghani, M., Chambon, P.*, et al.* (2006). Retinoic acid metabolism and signaling pathways in the adult and developing mouse testis. Endocrinology *147*, 96-110.

Voullaire, L.E., Slater, H.R., Petrovic, V., and Choo, K.H. (1993). A functional marker centromere with no detectable alpha-satellite, satellite III, or CENP-B protein: activation of a latent centromere? Am J Hum Genet *52*, 1153-1163.

Wang, G.Z., and Goff, S.P. (2015). Regulation of Yin Yang 1 by Tyrosine Phosphorylation. J Biol Chem *290*, 21890-21900.

Wang, J., Fang, Y., Fan, R.A., and Kirk, C.J. (2021). Proteasome Inhibitors and Their Pharmacokinetics, Pharmacodynamics, and Metabolism. Int J Mol Sci *22*.

Westhorpe, F.G., and Straight, A.F. (2014). The centromere: epigenetic control of chromosome segregation during mitosis. Cold Spring Harb Perspect Biol *7*, a015818.

White, J.A., Beckett-Jones, B., Guo, Y.D., Dilworth, F.J., Bonasoro, J.*, et al.* (1997). cDNA cloning of human retinoic acid-metabolizing enzyme (hP450RAI) identifies a novel family of cytochromes P450. J Biol Chem *272*, 18538-18541.

Wilkinson, K.D., Urban, M.K., and Haas, A.L. (1980). Ubiquitin is the ATP-dependent proteolysis factor I of rabbit reticulocytes. J Biol Chem *255*, 7529-7532.

Wu, G., Xu, G., Schulman, B.A., Jeffrey, P.D., Harper, J.W.*, et al.* (2003). Structure of a beta-TrCP1-Skp1-beta-catenin complex: destruction motif binding and lysine specificity of the SCF(beta-TrCP1) ubiquitin ligase. Mol Cell *11*, 1445-1456.

Wu, J.C., and Manuelidis, L. (1980). Sequence definition and organization of a human repeated DNA. J Mol Biol *142*, 363-386.

Yamaguchi, Y.L., Tanaka, S.S., Kumagai, M., Fujimoto, Y., Terabayashi, T.*, et al.* (2015). Sall4 is essential for mouse primordial germ cell specification by suppressing somatic cell program genes. Stem Cells *33*, 289-300.

Yan, K., Zhang, Z., Yang, J., McLaughlin, S.H., and Barford, D. (2018). Architecture of the CBF3-centromere complex of the budding yeast kinetochore. Nat Struct Mol Biol *25*, 1103-1110.

Yanagida, M. (2014). The role of model organisms in the history of mitosis research. Cold Spring Harb Perspect Biol *6*, a015768.

Yaron, A., Hatzubai, A., Davis, M., Lavon, I., Amit, S.*, et al.* (1998). Identification of the receptor component of the IkappaBalpha-ubiquitin ligase. Nature *396*, 590-594.

Yi, Q., Chen, Q., Liang, C., Yan, H., Zhang, Z.*, et al.* (2018). HP1 links centromeric heterochromatin to centromere cohesion in mammals. EMBO Rep *19*.

Yung, B.Y., Busch, R.K., Busch, H., Mauger, A.B., and Chan, P.K. (1985). Effects of actinomycin D analogs on nucleolar phosphoprotein B23 (37,000 daltons/pI 5.1). Biochem Pharmacol *34*, 4059-4063.

Zeitlin, S.G., Baker, N.M., Chapados, B.R., Soutoglou, E., Wang, J.Y.*, et al.* (2009). Double-strand DNA breaks recruit the centromeric histone CENP-A. Proc Natl Acad Sci U S A *106*, 15762-15767.

Zhang, W., Mao, J.H., Zhu, W., Jain, A.K., Liu, K.*, et al.* (2016). Centromere and kinetochore gene misexpression predicts cancer patient survival and response to radiotherapy and chemotherapy. Nat Commun *7*, 12619.

Zheng, N., and Shabek, N. (2017). Ubiquitin Ligases: Structure, Function, and Regulation. Annu Rev Biochem *86*, 129-157.

Zhou, L., Jiang, Y., Luo, Q., Li, L., and Jia, L. (2019a). Neddylation: a novel modulator of the tumor microenvironment. Mol Cancer *18*, 77.

Zhou, R., Wu, J., Liu, B., Jiang, Y., Chen, W.*, et al.* (2019b). The roles and mechanisms of Leydig cells and myoid cells in regulating spermatogenesis. Cell Mol Life Sci *76*, 2681-2695.

Zirkin, B.R., and Papadopoulos, V. (2018). Leydig cells: formation, function, and regulation. Biol Reprod *99*, 101-111.

genes

MDPI

Review

Ubiquitin Ligases Involved in the Regulation of Wnt, TGF-β, and Notch Signaling Pathways and Their Roles in Mouse Development and Homeostasis

Nikol Baloghova, Tomas Lidak and Lukas Cermak *

Laboratory of Cancer Biology, Division BIOCEV, Institute of Molecular Genetics of the Czech Academy of Sciences, 252 42 Vestec, Czech Republic; nikol.baloghova@img.cas.cz (N.B.); tomas.lidak@img.cas.cz (T.L.)
* Correspondence: lukas.cermak@img.cas.cz

Received: 8 September 2019; Accepted: 13 October 2019; Published: 16 October 2019



Abstract: The Wnt, TGF-β, and Notch signaling pathways are essential for the regulation of cellular polarity, differentiation, proliferation, and migration. Differential activation and mutual crosstalk of these pathways during animal development are crucial instructive forces in the initiation of the body axis and the development of organs and tissues. Due to the ability to initiate cell proliferation, these pathways are vulnerable to somatic mutations selectively producing cells, which ultimately slip through cellular and organismal checkpoints and develop into cancer. The architecture of the Wnt, TGF-β, and Notch signaling pathways is simple. The transmembrane receptor, activated by the extracellular stimulus, induces nuclear translocation of the transcription factor, which subsequently changes the expression of target genes. Nevertheless, these pathways are regulated by a myriad of factors involved in various feedback mechanisms or crosstalk. The most prominent group of regulators is the ubiquitin–proteasome system (UPS). To open the door to UPS-based therapeutic manipulations, a thorough understanding of these regulations at a molecular level and rigorous confirmation in vivo are required. In this quest, mouse models are exceptional and, thanks to the progress in genetic engineering, also an accessible tool. Here, we reviewed the current understanding of how the UPS regulates the Wnt, TGF-β, and Notch pathways and we summarized the knowledge gained from related mouse models.

Keywords: ubiquitin–proteasome system; cancer; mouse model; gene inactivation

1. Introduction

As revealed by the analysis of The Cancer Genome Atlas (TCGA), the Wnt, transforming growth factor-β (TGF-β), and Notch signaling pathways belong among the ten evaluated and curated canonical signaling pathways that are altered in most cancers [1]. It is the central role in governing and controlling cell proliferation which makes these pathways as well as their regulators vulnerable to cancer-associated somatic mutations [2–4]. The ubiquitin–proteasome system (UPS)-dependent regulation of Wnt, TGF-β, and Notch signaling is well known and established. Importantly, it represents a gateway for therapeutic modification and micromanagement of these signaling pathways, especially in the context of cancer [5,6]. To understand and exploit these possibilities it is necessary to evaluate the knowledge in vivo. Thus, the ambition of this review was to summarize the current understanding of how the UPS regulates Wnt, TGF-β, and Notch signaling. Additionally, we wanted to highlight the physiological roles of the ubiquitin ligases responsible for these regulations as they have been reported from currently available mouse models. Of note, the role of deubiquitinases (DUBs) was out of the scope of this text and is reviewed elsewhere [7].

2. The Ubiquitin–Proteasome System

The ubiquitin–proteasome system regulates many cellular processes, including cell cycle, differentiation, DNA repair, and the immune response (for a review, see Reference [8]). Its main function is to achieve the precise temporal and spatial expression of a diverse repertoire of proteins. Essentially, the UPS delivers unneeded or damaged proteins to the proteasome where they are unfolded and ultimately chopped into small peptides. At a molecular level, the proteasome is a multisubunit protein complex with a central hollow part involved in the proteolysis and two proximal parts involved in the recognition of the substrate and its ATP-dependent unfolding. The selectivity of the UPS is accomplished by specific recognition of the target protein (i.e., substrate) which has to be covalently modified by a chain of small protein ubiquitin—polyubiquitinated (Figure 1a).

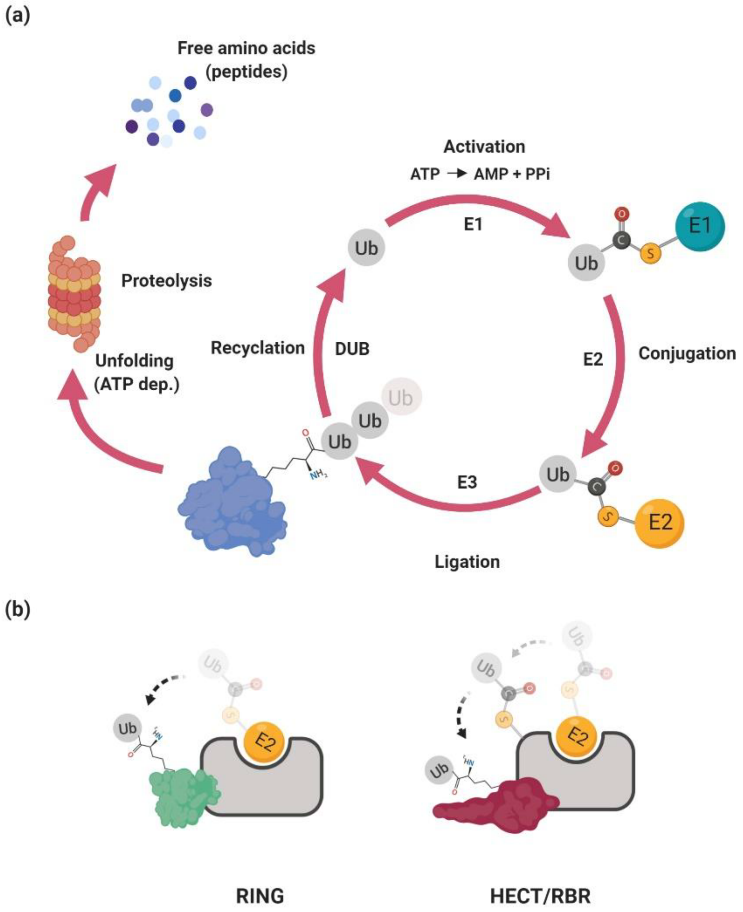


Figure 1. The ubiquitin–proteasome system. (**a**) The mature free ubiquitin monomer protein is either recycled from the ubiquitinated substrate or cleaved from the polyubiquitin precursor. Both of these reactions are catalyzed by deubiquitinases (DUBs). Ubiquitin is then activated (E1), conjugated (E2), and finally ligated to the cognate substrate via ubiquitin ligases (E3). The polyubiquitinated substrate is later transferred to the proteasome, unfolded, and proteolytically degraded to small peptides or free amino acids. For more details see the text. (**b**) RING E3s catalyze the direct transfer of ubiquitin from E2~ubiquitin to the substrate. HECT (homologous to E6AP C-terminus), and RBR (RING-between-RING) E3s accept ubiquitin from E2 to form an E3~ubiquitin thioester intermediate via transthiolation reaction. For more details see the text.

2.1. Ubiquitination

The ubiquitination is achieved via an enzymatic cascade in which ubiquitin is activated by covalent linkage to the E1 ubiquitin-activating enzyme. This activation is dependent on ATP-driven adenylation of ubiquitin followed by the covalent association of ubiquitin with the E1 enzyme via a thioester bond

and subsequent transfer of the activated ubiquitin to the E2 ubiquitin-conjugating enzyme through trans-thioesterification [9]. In the final step, the E3 ubiquitin ligase mediates the transfer of ubiquitin to the lysine residue in the substrate [10]. The covalently linked ubiquitin then serves as an acceptor for another ubiquitin molecule, ultimately producing long polyubiquitin chains. The polyubiquitin chains can be linked via different lysine residues in the ubiquitin. At least for certain E3 ubiquitin ligases the type of polyubiquitin chain seems to be dependent on the different usage of the specific E2 enzyme [11]. Currently, there are more than thirty genes in human genome encoding proteins harboring E2 activity [12]. Some of them specifically modify proteins with linear ubiquitin chains (e.g., lysine 63–K63) that are not recognized by the proteasome but are involved in cellular signaling [13]. Others (e.g., K48, K11) are involved in proteasome-dependent degradation or their role is currently not clear (e.g., K27) [14]. Notably, a key regulatory step of the ubiquitination reaction is dictated by the E3 ubiquitin ligase, which determines substrate selection and a choice of polyubiquitin chain.

2.2. Ubiquitin Ligases

The human genome encodes between 600–1000 E3 ubiquitin ligases. They are responsible for substrate selection and coordination towards the E2 enzyme (for a review, see References [15,16]). Currently, there are four main classes of ubiquitin ligases classified on the basis of the functional and structural features: RING (really interesting new gene), U-box, HECT (homologous to E6AP C-terminus), and RBR (RING-between-RING) [9]. The RING E3s catalyze the direct transfer of ubiquitin from E2~ubiquitin to the substrate. The HECT and RBR E3s harbor a catalytic cysteine residue in their structure that accepts ubiquitin from E2 to form an E3~ubiquitin thioester intermediate via transthiolation reaction (Figures 1b and 2). This step is followed by the transfer of ubiquitin to the substrate lysine via aminolysis reaction.

The E3 ligases recognize the cognate substrates using different mechanisms. The specificity of ubiquitination is achieved via protein–protein interaction between a ubiquitin ligase and a substrate. This interaction can be direct or indirectly mediated by a protein or a small molecule adapter. The direct interaction is usually regulated by post-translational modification of the substrate or the ubiquitin ligase. In certain cellular processes, ubiquitin ligases have to be locally enriched to effectively bind and mediate substrate ubiquitination. A typical example is the RING finger 8 (RNF8) ubiquitin ligase, which is sequestrated at DNA damage sites where it targets a diverse spectrum of proteins (including histones) [17,18].

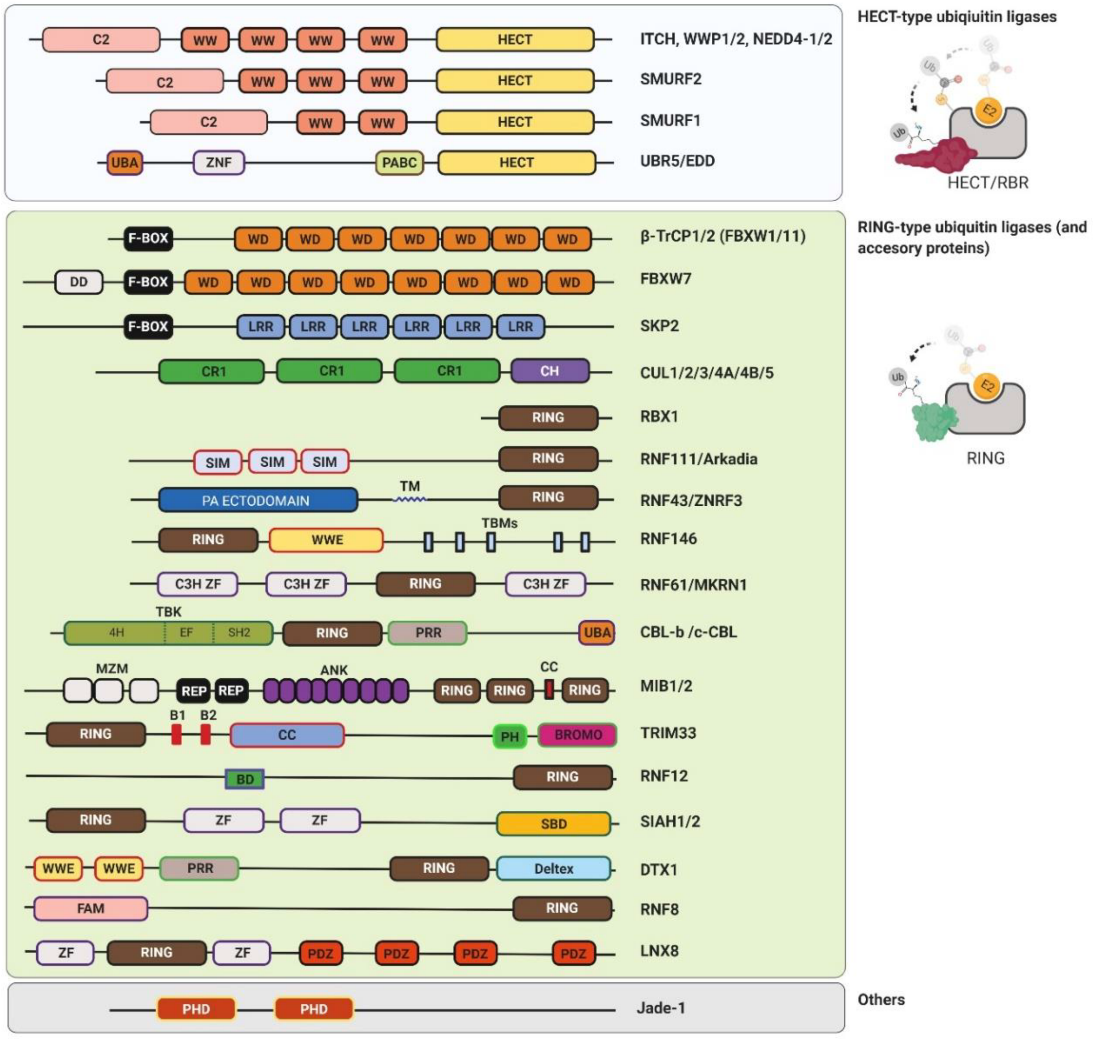


Figure 2. The modular structure of ubiquitin ligases involved in the Wnt, TGF-β, and Notch pathways.

2.2.1. RING-Type Ubiquitin Ligases

The RING ubiquitin ligases constitute two main classes based on the number of subunits (for a review, see References [6,19]). Monosubunit RING ligases form homo- and heterodimers or act as monomers. A typical example of these ubiquitin ligases is the mouse double minute 2 homolog (MDM2) protein. In the absence of DNA damage, MDM2 binds the p53 tumor suppressor and mediates its ubiquitination, with consequent proteasomal degradation [20]. The DNA damage-activated Ataxia-telangiectasia mutated (ATM) kinase inhibits MDM2–p53 interaction leading to p53 stabilization and activation of p53-dependent DNA damage response [21,22].

Multisubunit E3 ubiquitin ligase complexes, such as Cullin-RING ligases (CRLs), mediate ubiquitination of numerous substrates via variable substrate recognition modules [19]. They represent a dominant group of ubiquitin ligases. In mammals, there are eight different cullins which associate with large numbers of adaptor proteins, forming more than 200 CRLs. Many of these ubiquitin ligases are deregulated in a wide range of disorders including cancer and autoimmune syndromes [6,23,24].

2.2.2. U-box-Type Ubiquitin Ligases

A specific group of RING-type ubiquitin ligases is U-box, containing ubiquitin ligases (for a review, see Reference [25]). A U-box is a 70 amino acid long domain with a similar fold as the RING domain. In contrast to RING, the U-box domain lacks conserved cysteine residues and it is not coordinated

with zinc atoms. Nevertheless, the molecular mechanism underlying ubiquitination is similar for both U-box and RING-type ubiquitin ligases.

A typical example of U-box-type ubiquitin ligase is the C terminus of the Hsc70-interacting protein (CHIP) [26]. Upon heat stress, CHIP recognizes its substrates in the context of activated heat shock proteins, controlling the stability and fate of misfolded proteins.

2.2.3. HECT-Type Ubiquitin Ligases

The human genome encodes 28 HECT ubiquitin ligases (for a review, see Reference [27]). They are characterized by a modular structure which comprises the N-terminal substrate-binding domain and the C-terminal HECT domain [27]. The HECT domain contains two lobes connected by a flexible hinge loop. The N-terminal lobe binds E2~ubiquitin and the C-terminal lobe harbors the catalytic cysteine involved in the transfer of ubiquitin to substrates lysines. There are three different HECT-type ligase families: the NEDD (neural precursor cell expressed, developmentally downregulated) family, characterized by the tryptophan-rich WW domain involved in recognition of the PY motif; the HERC (HECT and RCC domain) family, which contains the regulator of chromosome condensation (RCC) 1-like domains; and the HECT family, with a spectrum of different protein–protein interaction domains.

A typical example of the HECT-type ubiquitin ligase is Smad ubiquitination regulatory factor 2 (SMURF2) protein [28]. The SMURF2 protein is a HECT-type E3 ubiquitin ligase from the NEDD4 subfamily. The WW domain, located in the N-terminal part of SMURF2 ubiquitin ligase, recognizes PPxY (PY) motifs in SMURF–targeted substrates [29]. One of the SMURF2 substrates is a TGF-β receptor I (TGF-βRI) [30]. The SMURF2 protein binds this receptor indirectly via Small mothers against decapentaplegic 7 (Smad7), an inhibitor of TGF-β signaling. The SMURF2 interacts with Smad7 in the nucleus. The complex of SMURF2 and Smad7 is then translocated to the cytosol where it recognizes and ubiquitinates TGF-βRI. This represents the strong negative feedback necessary to control TGF-β signaling and its dynamics.

2.2.4. RBR-Type Ubiquitin Ligases

There are 14 RBR E3s identified in the human genome (for a review, see Reference [31]). They all contain a RING1–IBR–RING2 motif. The RING1 domain interacts with E2~ubiquitin and mediates the transfer of ubiquitin to the catalytic cysteine of the RING2 domain. It was shown that RING2 forms a thioester intermediate with the C terminus of ubiquitin in a HECT E3-like manner and, consequently, transfers ubiquitin on the lysines of the selected substrates. An example of an RBR ubiquitin ligase is Parkin [32]. Parkin is involved in the recognition of proteins on the outer mitochondrial membrane [33]. Upon stress exposure, Parkin mediates mitochondria ubiquitination and its clearance via mitophagy [34].

3. Wnt Signaling Pathway and Its Regulation by Ubiquitin Ligases

Wnt ligands are extracellular soluble proteins. They are secreted by a diverse spectrum of cells and they are instrumental in the regulation of cell identity, migration, and proliferation [35,36]. Genes encoding the components of the Wnt signaling pathway are often misregulated or mutated in human cancers, especially in tissues with fast cellular renewal (e.g., breast, intestine, skin, prostate or lung). This is due to the central role of the Wnt signaling pathway in stem cell recovery and progenitor cell pool formation.

The Wnt signaling pathway is initiated upon Wnt binding to its cognate receptor. This is followed by the sequence of activation steps which lead to translocation of the β-catenin transcription co-activator to the nucleus (Figure 3). Nuclear β-catenin associates with DNA-binding transcriptional factors from the T-cell factor/lymphoid enhancer-binding factor (TCF/LEF) family and activates the Wnt-dependent transcriptional program.

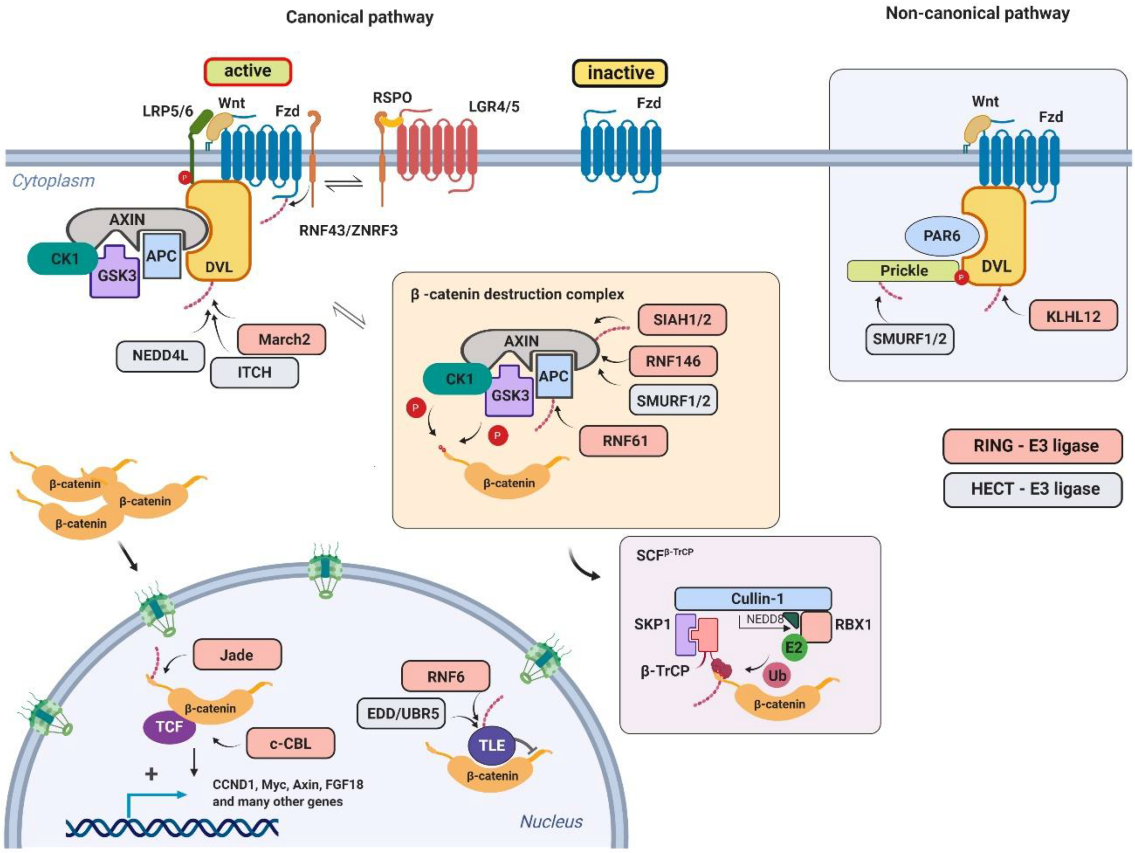


Figure 3. The Wnt signaling pathway and its regulation by ubiquitination The canonical Wnt signaling pathway is triggered by Wnt ligand binding to the complex of its receptor, Frizzled, and co-receptors LRP5/6. The activated receptor associates with the Dishevelled (DVL) protein and inhibits the β-catenin destruction complex. The stabilized β-catenin translocates and accumulates in the nucleus, where it activates the Wnt-dependent transcriptional program. For details see the text.

In more detail, the intracellular signaling is triggered by Wnt binding to the complex of its receptor Frizzled (Fzd) and co-receptor from the lipoprotein receptor-related protein family (LRP5/6) [37]. When inactive, the Fzd protein level and its membrane localization are regulated negatively by two closely related ubiquitin ligases, RNF43 and Zinc–RING finger 3 (ZNRF3) [38,39]. These transmembrane ligases from the RING family interact with Fzd in the extracellular part and mediate ubiquitination of its cytosolic loops via the intracellular RING domain. This interaction is dependent on the intracellular protein Dishevelled, which (in the absence of Wnt stimulation) promotes Fzd degradation [40]. Upon the Wnt ligand engagement to Fzd, RNF43/ZNRF3 is inhibited by sequestration to the complex of leucine-rich repeat-containing G-protein coupled receptor (LGR4/5) transmembrane proteins. This interaction is mediated by a Wnt agonist from the R-spondin family [38].

The essential part of signal transduction initiated from the Fzd receptor relies on β-catenin destruction complex inhibition. This multisubunit complex consists of several regulatory and accessory proteins. Its major role is to mediate β-catenin phosphorylation by coordination of priming casein kinase 1 (CK1) and functionally redundant processing kinases glycogen synthase kinase 3α and 3β (GSK3α and GSK3β, respectivelly) [41–43]. Adapter proteins adenomatous polyposis coli (APC) and AXIN are responsible for this dynamic and precise phosphorylation machinery [44,45]. In detail, AXIN allows β-catenin Ser45 to be phosphorylated by CK1. This phosphorylation creates a docking site for GSK-3α/β, which subsequently phosphorylates β-catenin at Thr41, Ser37, and Ser33. The phosphorylated N-terminal part of β-catenin serves as a binding site (degron) for a β-transducin repeat-containing protein (β-TrCP) [46,47]. The β-TrCP is a canonical Cullin 1 (CUL1)-dependent F-box-containing substrate adapter. It associates via the S-phase kinase-associated protein 1 (SKP1) adapter and CUL1

scaffold proteins with the RING protein Ring-box 1 (RBX1). The RBX1 mediates β-catenin ubiquitination and degradation.

The Fzd activation by Wnt ligands results in Dishevelled-dependent oligomerization of LRP6 co-receptor and its CK1γ/GSK3-mediated phosphorylation [48,49]. In the AXIN-dependent manner, the cytosolic destruction complex is sequestrated to the membrane. This process inhibits the interaction of the destruction complex with β-catenin. Importantly, it was suggested that upon the activation of the Wnt signaling, the destruction complex is not inhibited per se. Rather, it leads to the inhibition of β-TrCP-dependent ubiquitination. Phosphorylated non-ubiquitinated β-catenin stays in the complex and blocks the association of newly translated molecules [50]. Stabilized (non-phosphorylated) β-catenin then translocates and accumulates in the nucleus, where it interacts with DNA-binding transcriptional factors from the TCF/LEF family [45]. The sustained Wnt signaling leads to the strong association of the β-catenin/TCF complex with target gene promoters, engagement of transcriptional co-activators, and, ultimately, to the activation of the Wnt-dependent transcriptional program.

The β-catenin destruction complex itself is a target for several ubiquitin ligases. The main substrate of the UPS-dependent regulation is the AXIN protein. The seven in absentia homolog 1 (SIAH1) ubiquitin ligase mediates ubiquitination of the AXIN protein [51]. The SIAH1 recognizes the AXIN VxP (Val-x-Pro) motif involved in AXIN–GSK3 interaction. The GSK3 counteracts SIAH-dependent AXIN ubiquitination, and, correspondingly, SIAH inactivation leads to the Wnt signaling attenuation. This regulatory process is important for sustained Wnt/β-catenin signaling. In a similar manner, poly ADP-ribosylated (PARylated) AXIN is a target of the ubiquitin ligase RNF146. PARylation of AXIN is dependent on the Tankyrase enzyme [52]. It was shown that RNF146 interacts directly with poly-ADP-ribose through its WWE domain and promotes degradation of many PARylated proteins [53,54]. The AXIN RNF146-dependent degradation seems to be dependent on a physiological context [55]. Both *Xenopus* and *Drosophila* models have shown the role of Tankyrase in AXIN degradation, but based on the findings from *Drosophila* studies, there seems to be redundancy on the RNF146 side [56,57]. HECT-type ubiquitin ligase, SMURF1, was shown to ubiquitinate the AXIN protein in a cell-cycle-dependent manner. Its interaction with AXIN is inhibited during G2/M which correlates with increased Wnt signaling [58]. The SMURF1-mediated AXIN ubiquitination does not lead to its degradation. Instead, Lys29-linked polyubiquitination of AXIN disrupts its interaction with the Wnt coreceptors LRP5/6, consequentially inhibiting Wnt signaling activation [59]. Close homolog of SMURF1, SMURF2, interacts with AXIN in a canonical WW-dependent manner. Ectopic expression of SMURF2 leads to AXIN protein level downregulation, and SMURF2 mediates AXIN ubiquitination in vitro [60]. The other subunit of the β-catenin destruction complex, APC, is also a target for the UPS. The RNF61 ubiquitin ligase, otherwise known as Makorin 1 (Mkrn1), binds to the armadillo repeats region of APC and targets it for proteasomal degradation. Inactivation of RNF61 leads to Wnt signaling inhibition, and this inhibition is rescued by concurrent APC knockdown [61].

The Dishevelled (Dishevelled 1–3) protein level is regulated by three other HECT-like ubiquitin ligases NEDD4L, NEDD4, and ITCH [62–64]. They were all shown to promote Dishevelled ubiquitination. Ubiquitin ligase NEDD4 positively regulates the maturation of cell–cell junctions in cooperation with the small GTPase Ras-related C3 botulinum toxin substrate 1 (Rac1). Activated Rac1 promotes Nedd4-mediated ubiquitination and degradation of Dishevelled 1 [64]. A close homolog of NEDD4, NEDD4L, attenuates Wnt/β-catenin signaling by regulation of Dishevelled 2 stability. The Wnt5a-induced c-Jun N-terminal kinase (JNK)-dependent phosphorylation of NEDD4L is critical for its activity towards Dishevelled 2 [62]. The inhibition of Wnt signaling via the ubiquitin ligase NEDD4L was observed in both *Xenopus* and human models [62,65]. The mammalian ortholog of *Drosophila* Suppressor of Deltex (Su(Dx)), ITCH, inhibits Wnt signaling upstream of β-catenin, by targeting activated Dishevelled 2 to proteasomal degradation [63]. The role of Dishevelled protein is not limited to the β-catenin destruction complex inhibition and its sequestration to the activated receptor. It is also involved in activation of the non-canonical pathway controlling planar polarity and proper tissue architecture. This pathway is β-catenin-independent and it is actively inhibited by ubiquitin ligase

RNF43 and its interaction with Dishevelled protein. Transmembrane RING-type ubiquitin ligase RNF43 inhibits the non-canonical pathway in a ubiquitination-independent manner, and cancer-associated mutations of RNF43 do not have any effect on this activity [66]. Another E3 ubiquitin ligase promoting Dishevelled ubiquitination and degradation in the non-canonical pathway is the Cullin3-dependent substrate-binding adapter Kelch-like protein 12 (KLHL12). The KLHL12 binds Dishevelled in a Wnt-dependent manner, and KLHL12-dependent degradation of Dishevelled antagonizes the convergent extension movements of cells during gastrulation in zebrafish [67]. The study in the *Xenopus* model shows that another RING-type ubiquitin ligase membrane-associated ring-CH-type finger (MARCH2) is targeting Dishevelled during head development. The MARCH2 interaction with Dishevelled is dependent on the Dishevelled interaction partner Dapper1, and ubiquitinated Dishevelled is degraded in the lysosomal compartment [68].

Nuclear bound β-catenin is a target of several ubiquitin ligases. They mostly serve as crosstalk hubs from different pathways and signaling checkpoints involved in the control of the proper shutdown of the activated pathway. In hypoxic conditions, the Von Hippel–Lindau (VHL) tumor suppressor inhibits the Wnt pathway via promoting degradation of activated β-catenin. It is dependent on VHL-induced stabilization of the ubiquitin ligase Jade1 [69]. This is relevant for clear cell renal cell carcinomas (CCRCCs) with mutated VHL. The active VHL stabilizes Jade1 by interaction with its α- and β-domain. The stabilized Jade1 interacts with the β-catenin N-terminus and mediates its ubiquitination and degradation [70,71]. Of note, Jade1 does not belong to either HECT- or RING-type ligases. It contains two pleckstrin homology domain (PHD) fingers, and its intrinsic ubiquitin ligase activity has not yet been supported by independent observations. Casitas B-lineage lymphoma (c-CBL) is another ligase that binds preferentially to active β-catenin [72,73]. Wnt-dependent nuclear c-CBL seems to selectively inhibit pro-angiogenic Wnt effects [72].

One of the paradigms in Wnt signaling is that in the absence of Wnt stimulation, TCF/LEF factors are acting as transcription repressors and that this repression is abrogated by β-catenin binding. Mechanistically, TCF factors associate with repressors from the TLE (transducin-like enhancer) family in the absence of Wnt signaling, and this interaction is blocked by competitive binding between TLE repressors and activated β-catenin. The TLE factors are subsequently targeted by the E3 isolated by differential display/ubiquitin protein ligase E3 component n-recognin 5 (EDD/UBR5) ubiquitin ligase from the HECT family for ubiquitination and degradation [74]. Besides TLE factors, EDD ubiquitinates phosphorylated β-catenin, as well. Instead of degradation, it was observed that in the context of β-catenin, EDD promotes the growth of Lys29- and Lys11-linked ubiquitin chains, supposedly to potentiate β-catenin stability and signaling [75]. This pathway is probably redundant or cell context-dependent, as it was shown that in colorectal cancer it is rather the ubiquitin ligase RNF6 which promotes Wnt signaling via controlling the stability of the TLE3 factor [76].

The UPS-based quality control is another regulatory mechanism in the Wnt signaling pathway. This is important for endoplasmatic reticulum (ER)-associated protein production and restricted to secreted and transmembrane proteins. It was shown that in the absence of Wnt ligands, the cargo protein EVI is degraded via ER-associated degradation (ERAD) [77]. Additionally, the Wnt co-receptor LRP6 is targeted to the ERAD pathway as well [78,79]. Upon ubiquitination of its intracellular part, LRP6 presumably interacts with a ubiquitin-binding protein which acts as a chaperone for its correct folding. The successfully folded LRP6 is palmitoylated and transported to the cell surface [80]. If folding is impaired, another round of polyubiquitination targets LRP6 to the ERAD pathway.

The Wnt signaling pathway is also sensitive to common stress-inducers such as heat stress. Activation of heat shock proteins leads to activation of the U-box ubiquitin ligase CHIP, which is involved in ubiquitin-dependent clearance of misfolded proteins [81]. One of the substrates of CHIP ubiquitin ligase is β-catenin [82]. The recognition of β-catenin via CHIP rather represents a general mechanism involved in unfolded protein and heat shock response than specific regulation of the Wnt signaling pathway.

3.1. Mouse Models of Ubiquitin Ligases Involved in the Wnt Signaling Pathway

As mentioned above, Wnt signaling plays a crucial role in an array of developmental and homeostatic processes. Mouse models defective in the Wnt signaling pathway reflect this fact and display various defects. The phenotypes span from higher cancer incidence, stem cell depletion to defects in tissue polarity and anteroposterior patterning [45,83–85]. The role of several ubiquitin ligases that have been shown to regulate the Wnt signaling pathway in vitro was confirmed in the cognate mouse models. This was true for ZNRF3/RNF43, RNF146, RNF61, SMURF1/2, and partially for β-TrCP1/2 and Nedd4 ubiquitin ligases [39,55,86–89]. However, the mouse models of other ubiquitin ligases did not confirm the function in Wnt signaling and show either different or more general physiological functions. These observations probably arise from the fact that these ubiquitin ligases have other physiological substrates and control different processes. The other possible explanation is that the involvement of these ligases in physiological Wnt signaling is subtle. Therefore, these mouse models require more detailed analysis or challenges such as aging or stress response to show and confirm in vitro observations.

3.1.1. β-Transducin Repeat-Containing Protein (β-TrCP)

Both β-TrCP1 and β-TrCP2 (also known as F-box and WD repeat domain, containing 1/11) are highly evolutionarily conserved F-box proteins [23]. They serve as substrate adapters for the CRL ubiquitin ligase. They both recognize a phosphodegron through seven WD-repeats assembled to a typical propeller structure. They are currently assigned to many different substrates including NFκB Inhibitor α (IκBα), β-catenin, and a canonical regulator of circadian rhythm Period2 [23,90]. Both β-TrCP1 and β-TrCP2 are biochemically indistinguishable in vitro and it is not clear if they recognize a unique set of substrates in vivo.

Mice deficient in β-TrCP1-are viable, with normal circadian rhythm and only minor defects in fertility. Animals do not exhibit any apparent defects up to 16 months of age [86,91–93]. Isolated mouse embryonic fibroblasts (MEFs) have a reduced growth rate, increased size, and abnormal ploidy. Upon Wnt3a stimulation, they show more stable nuclear β-catenin accumulation.

The β-TrCP-deficient male germ cells do not enter meiosis but instead undergo apoptosis. The early mitotic inhibitor 1 (Emi1) accumulation appears to contribute to the slight impairment in spermatogenesis and male fertility [23,92]. Another study shows that simultaneous inactivation of β-TrCP2 expression via inducible shRNA (which reduced β-TrCP2 to ~10% of the original level) leads to more severe testicular defects in otherwise viable and healthy animals. Authors of the study were able to rescue the defect by β-TrCP2 restoration and attributed the observed defect to ineffective degradation of the Snail1 transcription factor [94]. This transcription factor is important for epithelial–mesenchymal transition and its degradation is necessary for the proper development of cell adhesion within the seminiferous tubules. Depletion of Snail1 completely rescues spermatogenesis in β-TrCP1-deficient mice. Another research group used testis-specific inactivation of β-TrCP2 in the context of β-TrCP1-deficient mice. The authors also observed spermatogenesis impairment but attributed this defect to inappropriate degradation of the Doublesex- and mab-3-related transcription factor 1 (Dmrt1) involved in the mitosis–meiosis transition in mouse male germ cells [91].

Ubiquitin ligase β-TrCP1 is also an important factor in other tissues' homeostasis. Contrary to the epidermal or intestinal epithelium, mammary glands of β-TrCP1-deficient female mice display a hypoplastic phenotype [95]. A β-TrCP1-deficient retina shows a complete absence of cholinergic amacrine cells (CACs), decrease in tyrosine hydroxylase-expressing amacrine cells, and reduction in the number of retinal ganglion cells. The population of precursors of CACs is reduced, whereas the population of precursors of retinal ganglion cells increases [96]. The intestine-specific tamoxifen-inducible ablation of both β-TrCP1 and β-TrCP2 results in β-catenin and IκBα stabilization and leads to mucositis, a deleterious gut mucosal inflammation resulting in mucosal barrier defects. The increased NF-κB-independent production of interleukin 1β (IL-1β) is responsible for mucosal barrier defects, and inhibition of IL-1β partially rescues the inflammatory phenotype [97].

Contrary to the mild phenotype of β-TrCP1 deficiency, inactivation of β-TrCP2 results in the developmental arrest and the embryonic death before E10.5 [98]. Embryos lacking β-TrCP2 manifest accumulation of the cyclin-dependent kinase (CDK) inhibitor p19Arf in the yolk sac, but the concomitant inactivation of p19Arf does not rescue the lethal phenotype.

3.1.2. Zinc and RING Finger 3/ RING Finger 43 (ZNRF3/RNF43)

Both ZNRF3/RNF43 are RING-type transmembrane ubiquitin ligases containing the protease-associated ectodomain in the extracellular part. As mentioned, they target the Fzd receptor and mediate its ubiquitination and degradation which leads to attenuation of Wnt signaling. Both RNF43 and ZNRF3 are mutated in pancreatic carcinomas and colorectal and endometrial cancer [99,100].

Mice deficient in Znrf3 die shortly after birth. They have impaired lens development and about 20% of embryos show neural tube closure defects [38]. Simultaneous deletion of both genes (*Znrf3* and *RNF43*) in the intestine leads to the epithelial hyperproliferation phenotype similar to one observed in Apc^{min} mice with constitutively active β-catenin [39]. This phenotype is dependent on paracrine delivery of Wnt3, and the simultaneous inactivation of the Wnt-secretion co-factor Porcupine abrogates the enhanced epithelial proliferation [101]. Expectedly, the adrenocortical deletion of *ZNRF3*, but not *RNF43* (which is not expressed at a significant level in the adrenal cortex), leads to a hyperproliferative phenotype as well. The ZNFR3-dependent expansion is restricted only to the inner zone of the adrenal cortex and does not phenocopy β-catenin hyperactivation [102]. A ZNRF3 deficiency also leads to a disrupted testis determination. This is in agreement with the observation that testis development depends on Wnt signaling inhibition [103]. Mice without Znrf3 have a gonadal reversal in E12.5 and it depends on ectopic Wnt signaling during sex determination [104].

3.1.3. RING Finger 146 (RNF146)

Ubiquitin ligase RNF146 contains the N-terminal RING domain and the WWE domain. It mediates the ubiquitination of proteins PARylated by Tankyrase and its expression level was significantly elevated in a subset of non-small cell lung cancer and colorectal cancer [105].

Mice deficient in RNF146 die during embryogenesis. They are smaller with a delayed bone formation in the calvarium [55]. Mice with the osteoblast-specific RNF146 deletion die perinatally due to the fact of respiratory failure. Embryos have a short stature, fail to close fontanelles, exhibit hypomineralization of the calvarium, have small clavicles, and are osteopenic, with low serum levels of osteocalcin. The phenotype mimics some features observed in patients with cleidocranial dysplasia. Loss of RNF146 results in AXIN stabilization in osteoblasts and inhibition of the Wnt signaling pathway. Defective expression of the Wnt target fibroblasts growth factor 18 (FGF18) leads to inhibition of mitogen-activated protein kinase (MAPK) activity and, subsequently, to decreased osteoblast proliferation. As a consequence of reduced osteocalcin production, the osteoblasts-specific Rnf146-deficient mice exhibit an increase in bone marrow fat stores and glucose intolerance [55].

Contrary to its role in osteoblasts, Wnt signaling inhibits osteoclastogenesis [106]. A major osteoclast factor Rankl restricts Wnt activation via suppression of Rnf146 expression and Axin stabilization. Accordingly, macrophage-specific deletion of *Rnf146* triggers accelerated osteoclastogenesis [107]. Besides Axin, RNF146 is responsible for the degradation of the SH3 domain-binding protein 2 (SH3BP2). Stabilized SH3BP2 potentiates RANKL signaling and osteoclastogenesis, mimicking its "gain-of-function" mutations found in patients with hereditary cherubism [108,109].

3.1.4. RING Finger 61 (RNF61)

Ubiquitin ligase RNF61 is a member of the putative RNA-binding protein family characterized by unusual C3H-Zinc finger domains and the RING domain. Telomerase reverse transcriptase (TERT), phosphatase and tensin homolog (PTEN), adenomatous polyposis coli (APC) or AMP-activated protein kinase (AMPK) are among its potential substrates.

Mice deficient in Rnf61 show chronic AMPK activation in both liver and adipose tissue, resulting in significant suppression of the diet-induced metabolic syndrome [88]. Although no clear connection exists between this phenotype and deregulated Wnt signaling, there is well-described crosstalk between AMPK and β-catenin activity [110–112]. Moreover, AMPK activation by metformin was recently shown to inhibit β-catenin stabilization [113]. Thus, Rnf61-dependent ubiquitination and degradation of AMPK and APC could represent an interesting feedback mechanism between Wnt signaling and metabolism activity.

3.1.5. Seven in Absentia Homolog (SIAH)

Seven in Absentia Homolog 1/2 ubiquitin ligases are homologous proteins consisting of the N-terminal RING domain, two zinc-finger domains, and the substrate-binding domain. There is a number of substrates subjected to degradation mediated by SIAH1/2 ubiquitin ligases. Under hypoxic conditions, SIAH1/2 mediate ubiquitination and degradation of prolyl hydroxylase 1 (PHD1) and PHD3. As a consequence, the hypoxia-inducible factor 1-α (HIF1α) is stabilized and the hypoxia response transcription program is initiated [114].

Seven in Absentia Homolog 1a-deficient mice exhibit growth retardation or early lethality (about 70% of SIAH1a-deficient pups die during the nursing period). They are sterile with defective spermatogenesis due to the impairment of meiotic progression [115]. Mice deficient in Siah1a suffer from osteopenia [116]. Interestingly, Siah2-deficient mice are normal, healthy, and fertile. They have a significant expansion of myeloid progenitor cells and osteoclasts in the bone marrow [117]. Embryos lacking both *SIAH* genes die within several hours of birth. They do not have any obvious defects, and the cause of death remains to be determined. Notably, both Siah1 and Siah2 have been shown to play a role in hypoxia and unfolded protein response (UPR) and their absence can result in a complex phenotype caused by oxidative and proteotoxic cellular stress [117–120].

3.1.6. E3 Isolated by Differential Display (EDD)

The EDD/UBR5 ubiquitin ligase belongs to the HECT ligase family. It has the UBA (ubiquitin-associated) domain in its N-terminus, a centrally located UBR-type zinc finger involved in the recognition of N-terminal degrons and the C-terminal HECT domain. E3 isolated by differential display is predominantly localized in the nucleus. The EDD was shown to target RNF168 ubiquitin ligase and TLE/Groucho repressors for proteasomal degradation [121]. It is deregulated in many types of cancer, e.g., breast and ovarian cancer or mantle cell carcinoma [122].

E3 isolated by differential display-deficient mice have significant developmental arrest characterized by defective vascular development in the yolk sac and allantois, along with defective chorioallantoic fusion [123]. The authors discussed that these extraembryonic defects presumably compromise fetal–maternal circulation, leading to a general failure of embryonic cell proliferation and widespread apoptosis. It is of note that mice deficient in Wnt receptor Fzd5 have similar defects in the yolk sac and placental vasculogenesis [124]. Nevertheless, there is no study of Wnt signaling deregulation in Edd-deficient mice. To investigate the EDD physiologic role in this pathway and generally in mouse development, it is necessary to prepare conditional mouse models. So far only limb bud-specific *Edd* deletion has been reported with no obvious morphological or developmental defects [125].

3.1.7. Neural Precursor Cell Expressed, Developmentally Downregulated 4 (Nedd4)

The Nedd4 ubiquitin ligase belongs to the NEDD-type HECT ligase family. It has a characteristic structure common for all NEDD4 family members: the N-terminal C2 domain, four WW domains, and the C-terminal HECT domain. The NEDD4 was proposed to interact with the tumor suppressor PTEN and to mediate its ubiquitination. It has been also shown to play a role in the regulation of Epithelial Na^+ channel (ENaC) and RNA polymerase 2. The NEDD4 is often overexpressed in many types of human malignancies, e.g., prostate, bladder, colorectal, gastric or breast carcinoma [126].

Mice heterozygous for Nedd4 are moderately insulin-resistant but protected against high-fat diet (HFD)-induced obesity. They show less body weight gain, less fat mass, and smaller adipocytes [127]. Knockout mice die perinatally [128–130]. They are growth-retarded around E11.5 with signs of subcutaneous bleeding in more than half of embryos. At E18.5, embryos do not display any spontaneous movement. The neural circuits are still active as the embryos react to mild pinches. Diaphragm muscles are significantly thinner and fragile with wavy and disorganized muscle fibers. Mice have an impaired innervation pattern in diaphragm muscles, leaving a gap at its ventral region. The Schwann cells differentiation is intact but they have a lower number of axons and motoneurons, impaired formation of neuromuscular synapses, and abnormal neuromuscular synaptic activity [128]. In another study, Nedd4-deficient neurons had more immature dendrites and showed significantly reduced apical dendrite branching, synaptic transmission, and synapse numbers. The authors revealed that the major substrate of Nedd4 involved in neuronal branching regulation is the Ras-related protein 2a (Rap2a) and that the expression of dominant-negative Rap2A rescues correct dendritogenesis [129]. Another research group presents that Nedd4-deficient mice show prominent heart defects (double-outlet right ventricle and atrioventricular cushion defects) and vasculature abnormalities [131]. Follow-up research pinpointed that the inhibitor of insulin signaling the growth factor receptor-bound protein 10 (Grb10) is a major substrate of the Nedd4 ubiquitin ligase. Its stabilization is responsible for delayed embryonic development, reduced growth, body weight, and neonatal lethality. Mechanistically, the stabilized Grb10 inhibits the insulin-like growth factor 1 receptor (Igf1R) cell surface localization. The Grb10 heterozygosity rescues the Nedd4 deficiency lethal phenotype [130]. Vascular-specific deletion of *Nedd4* displays deformed aortas with disarranged elastin fibers. It also results in increased vascular calcification and bone-related marker expression in aortas [132]. The bone-specific Nedd4-mutant mice show enhanced bone mass accrual and upregulated gene expression of osteogenic markers in the bone. Bone formation is decreased, and the proliferation of primary osteoblasts isolated from calvaria is higher. The number and surface area of tibial osteoblasts are higher as well [133]. The neural crest cell-specific Nedd4 deficiency results in significant craniofacial defects with reduction of a cranial bone and decrease in osteoblasts numbers. The Nedd4 seems to be essential for neural crest stem cell self-renewal and survival [134,135]. T cells from Nedd4-deficient fetal liver chimeras display a naïve T cell phenotype. T cells develop normally but proliferate less and their ability to activate B cells is diminished. Biochemically, upon CD28 co-stimulation, Nedd4 controls the stability of another ubiquitin ligase Cbl-b. Inappropriately stabilized Cbl-b ligase targets the T cell receptor (TCR) and its components and ultimately blocks T cell activation and function [136]. Interestingly, Nedd4 deficiency abrogates T cell hyperactivity in Cbl-b-deficient mice [137]. Animals with intestine-specific deletion of *Nedd4* when crossed with $APC^{+/min}$ mice have enhanced tumor growth and Wnt signaling [89].

3.1.8. Neural Precursor Cell Expressed, Developmentally Downregulated 4-Like (NEDD4L)

The NEDD4L ubiquitin ligase is a close homolog to NEDD4 and they share a common structure. The NEDD4L regulates numerous ion channels, especially ENaC [29]. As mentioned in Section 4.1., NEDD4L also mediates degradation of phosphorylated Smad2 and Smad3, and associates with TGF-βRI via the Smad7 adaptor leading to destabilization of the receptor. The polymorphism causing premature truncation of the NEDD4L protein is associated with essential hypertension [138].

Neural precursor cell expressed, developmentally downregulated 4-like heterozygous mice are viable but hyperactive [139]. The mouse model of NEDD4L with complete deficiency suggests that the Nedd4L major ubiquitination target is ENaC [140,141]. This sodium channel is involved in the reabsorption of sodium ions in the kidney, colon, and lungs [142]. It is also necessary for the saltiness perception associated with taste buds [143]. Neural precursor cell expressed, developmentally downregulated 4-like binds to the PY motifs of ENaC subunits via its WW domains. This interaction is responsible for ENaC ubiquitination and subsequent downregulation on the apical membrane. There are two independent mouse models of Nedd4L deficiency. The possibly hypomorphic Nedd4L knockout model has a relatively mild phenotype with higher blood pressure in both normal and

high-salt diets. Concurrent administration of the ENaC inhibitor amiloride rescues the hypertension phenotype. Moreover, a chronic high-salt diet leads to cardiac hypertrophy [144]. In the second model of Nedd4L deficiency, the embryos have collapsed alveolar spaces and die perinatally [145]. The kidney-specific knockout mice suffer from a progressive kidney injury phenotype associated with increased sodium ion reabsorption, hypertension, and reduced levels of aldosterone. The phenotype is manifested by fibrosis, higher apoptosis, and cystic tubules [146]. In the mast cell-specific knockout, NEDD4L limits the intensity and duration of immunoglobulin E (IgE)-Fc$_\varepsilon$RI-induced positive signal transduction. It appears that in mast cells, the tyrosine kinase Syk is the main substrate for the NEDD4L ligase [147].

3.1.9. ITCH

The ITCH ubiquitin ligase belongs to the NEDD-type HECT ligase family. It contains the N-terminal C2 domain, four WW domains, and the HECT domain. Ubiquitin ligase ITCH regulates the stability of transmembrane receptors through monoubiquitination and intracellular proteins through polyubiquitination. It drives the monoubiquitinated and polyubiquitinated substrates to lysosomal and proteasomal degradation, respectively [148]. Reportedly, for proliferation- and survival-associated proteins c-Jun, JunB, p63, Notch, and glioma-associated oncogene homolog 1 (GLI1), TGF-β activated kinase 1 binding protein 1 (TAB1) belong to their substrates [149,150]. Mutations in ITCH cause inflammation, including inflammatory bowel disease or nephritis, and the ITCH deficiency is associated with multisystem autoimmune disease [151].

The non-agouti-lethal *Itchy* mice suffer from severe immune and inflammatory defects which result in persistent scratching of the skin [152,153]. On the C57BL/10 background, Itch deficiency is associated with the spontaneous development of a late-onset and progressively lethal systemic autoimmune-like disease, characterized by lymphoproliferation in the spleen, lymph nodes, and medulla of the thymus and by chronic pulmonary interstitial inflammation. The usual cause of death of these animals is hypoxia. On the JU/Ct background, *Itchy* mice develop an inflammatory disease of the large intestine [153].

For *Itchy* mice, T cells proliferate and adopt an activated phenotype. Production of the Th2 (T helper cell type 2) cytokines IL-4 and IL-5 is augmented upon stimulation, and the Th2-dependent serum concentrations of IgG1 and IgE are increased [154]. The phenotype is partially caused by the dysregulation of regulatory T (Treg) cells in the absence of the ITCH ligase. Treg cell-specific ablation of the Itch E3 ubiquitin ligase causes massive multiorgan lymphocyte infiltration and skin lesions, chronic Th2 cell activation, and the development of severe antigen-induced airway inflammation. The Itch-deficient Treg cells express a higher amount of Th2 cytokines and they are able to instruct naïve T cells to differentiate into Th2 effector cells [155]. The follow-up research has shown that Itch is essential for the differentiation of follicular B helper T cells (T_{FH}), germinal center response, and IgG production following acute viral infection. The development of T_{FH} cells is halted in early stages, and Itch acts intrinsically in CD4+ T cells. At the molecular level, during T_{FH} cell development, the Itch ubiquitin ligase controls the stability of the transcription factor Foxo1 [156]. Mice deficient in the E3 ubiquitin ligases CBL-b and Itch show an increase in T cell activation and display spontaneous autoimmunity. The double-mutant T cells show increased phosphorylation of the TCR-ζ chain, but TCR complex stability and membrane location are intact [157].

Keratinocyte-specific knockout of ITCH revealed its contribution to skin development and wound healing which is independent of the immunological phenotype observed in *Itchy* mice [158]. Moreover, *Itchy* females have reduced implantation sites, decreased corpora lutea, and increased estrous cycle length [159]. Mice deficient in Itch fed a HFD do not gain weight and do not show insulin resistance. It seems that Itch deficiency protects mice from obesity-related non-alcoholic fatty liver disease. Deficient animals have an accelerated metabolism and higher expression of genes involved in fatty acid oxidation. As a result of aberrant T helper cells activation, mutant mice exhibit a lower amount of

M2 (obese adipose tissue)-type macrophages [160]. Moreover, Itch deficiency renders mice resistant to tumor necrosis factor-α (TNF-α)-induced acute liver failure in three distinct models [161].

The E3 ubiquitin ligase Itch negatively regulates the development and function of hematopoietic stem cells (HSCs). Specifically, HSCs deficient in Itch are more competent, have longer repopulating activity, accelerated proliferation rates, and sustained progenitor properties. They also display an accumulation of the activated Notch1 receptor. Consistently, knockdown of Notch1 in Itch-deficient HSCs results in reversion of the phenotype [162].

3.1.10. Casitas B-Lineage Lymphoma (CBL)

Both c-CBL and CBL-b are close homologs from the CBL family and share the N-terminal tyrosine-kinase-binding domain, a linker, and the RING domain [163,164]. Expression of c-CBL is broad with the highest level in the thymus and testes. In activated T cells, it is a prominent target of tyrosine kinases [165].

Mice deficient for either c-CBL or CBL-b show T cell hyperactivation, which is driven by lowering the TCR affinity/avidity threshold and loss of the co-receptor signal requirement [166–169]. While c-Cbl-deficient mice have hyperactive thymocytes, CBL-b-deficient mice have activated mature T cells. Double-positive (CD4+CD8+) thymocytes lacking c-CBL display a higher amount of the membrane-bound TCR/CD3 complex—CD4 and CD8 receptors and tyrosine kinases Lck and Fyn [166]. An elevated level of the TCR complex can be a result of TCR ζ-chain stabilization [170,171]. Mice deficient in Cbl-b have a normal thymus and thymocyte development, but they display hyperproliferation of peripheral T cells. Similarly to CBL-b deficiency, there is no requirement for the second signal, and sole CD3 stimulation leads to T cell activation and proliferation. As a result of inadequate control of T cell activation, the CBL-b mouse model is susceptible to experimentally induced or spontaneous autoimmune diseases such as arthritis and diabetes [172]. Effector T cells in these animals are also insensitive to Treg on the cellular level mediated suppression of its mediator TGF-β [173].

As mentioned above, the c-CBL-deficient mice phenotype is mainly associated with thymocytes hyperactivation and proliferation. On the biochemical level, they display increased protein activation of the tyrosine kinase Lck and Zap-70 and the downstream effectors linker for activation of T cells (Lat) and SH2 domain containing leukocyte protein of 76 kDa (Slp-76). Protein kinase Zap-70 is able to mediate c-CBL interaction with TCRζ but it is probably not the direct target of its ubiquitin ligase activity [170]. Based on the results from c-CBL-deficient thymocytes, it seems that c-CBL can regulate different stages of T cell development, maturation, and selection processes.

The mammary fat pads of c-CBL–mutant female mice show increased ductal density and branching [167]. The decrease in motility of c-CBL-deficient osteoclasts results in a decreased ability of osteoclasts to invade and resorb bone and mineralized cartilage in vivo [174]. Mice deficient in c-Cbl exhibit an increase in whole-body energy expenditure, decrease in adiposity, and an increase in food intake, reduced circulating insulin, leptin, and triglyceride levels and improved glucose tolerance [175]. These changes are accompanied by a significant increase in mouse activity (2 to 3 fold).

Both c-CBL and CBL-b double knockout (DKO) mice are embryonically lethal before E10.5, which suggests that these ligases have important overlapping functions in embryonic development. T cell-specific DKO leads to an exaggeration of the immune phenotype as T cells become hyperresponsive upon CD3 stimulation [168]. The DKO T cells do not downregulate surface TCR after antibody engagement, which results in continuous TCR signaling [168]. The germinal center B cells deficient in both ligases display an early exit of high-affinity antigen-specific B cells from the germinal center reaction and, therefore, impaired clonal expansion [176]. The mouse model of mast cell-specific deficiency of both ligases shows that CBL-b, but not c-CBL, functions as a negative regulator of FcεRI-induced degranulation [177]. The mouse DKO model in HSCs develops a myeloproliferative disorder. The HSCs of c-CBL-deficient mice exhibit only an augmented pool size, hyperproliferation, greater competence, and enhanced long-term repopulating capacity [178]. The mammary gland-specific DKO shows CBL-b and c-CBL redundant function in mammary stem cell renewal [179].

4. TGF-β Signaling Pathway

Transforming growth factor-β belongs to a distinct family of extracellular soluble protein ligands involved in diverse developmental and homeostatic processes of higher eukaryotes [180]. During maturation, TGF-β homodimer forms a complex with a LAP (latency-associated peptide) originally derived from the region of the TGF-β protein between the signaling peptide and the C-terminally located active TGF-β ligand. This small latent complex (SLC) associates with latent TGF-β-binding protein 1 (LTBP1) and it is sequestrated to the fibronectin-based extracellular matrix [181]. Following proteolytic activation, the released TGF-β binds to the TGF-β receptor II (TGF-βRII) and initiates transphosphorylation of the associated TGF-β receptor I (TGF-βRI) (Figure 4) [182]. These events lead to full activation of the serine/threonine kinase located in the intracellular part of TGF-βRI. The activated receptor transduces the signal to downstream factors belonging to the family of regulatory-Smad (r-Smad) transcription factors—Smad2 and Smad3. Phosphorylation of these factors depends on the FYVE (Fab1p, YOTB, Vac1p and EEA1) domain containing protein Smad anchor for receptor activation (SARA) or hepatocyte growth-factor-regulated tyrosine kinase substrate (HGS) [183,184]. These membrane-associated proteins are responsible for delivering Smad factors to the vicinity of the activated receptor complex. Once phosphorylated, Smad2/3 form a trimer complex with Smad4 (co-Smad4) and translocate to the nucleus. The Smads mad homology 1 (MH1) domain is responsible for the specific association with target gene promoters, whereas the mad homology 2 (MH2) domain is responsible for interactions with transcriptional co-factors, transactivators, and other regulators [185,186]. The fully assembled complex initiates expression of TGF-β target genes and, ultimately, activates transcriptional programs which govern and execute tasks like cell cycle inhibition or transdifferentiation [187,188].

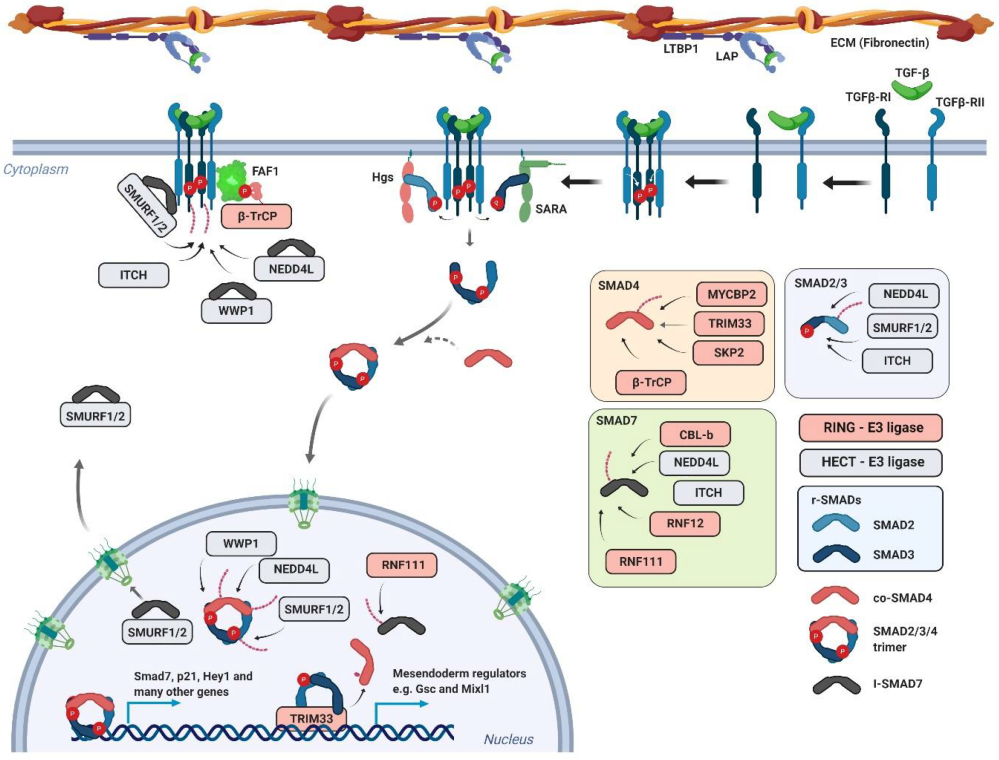


Figure 4. The TGF-β signaling pathway and its regulation by ubiqutination TGF-β released from the LTBP1 complex binds to TGF-β receptor II (TGF-βRII) and initiates transphosphorylation and activation of the associated TGF-β receptor I (TGF-βRI). The fully activated receptor transduces the signal to downstream factors belonging to the family of r-Smad (regulatory-Small mothers against decapentaplegic) transcription factors—Smad2 and Smad3. Smad2/3 form a trimer complex with Smad4 (co-Smad), translocate to the nucleus, and initiate transcription of TGF-β target genes. For details see the text.

4.1. TGF-β Signaling Pathway and its Regulation by Ubiquitin Ligases

The Smad homolog *Smad7* is one of the early target genes of TGF-β signaling [189]. It lacks the N-terminally located MH1 domain but still contains the receptor-binding MH2 domain. In the linker region between N- and C-terminal parts, Smad7 contains the PPxY motif which is responsible for E3 ubiquitin ligase SMURF2 (Smad ubiquitination regulatory factor 2) association [190,191].

Ubiquitin ligase SMURF2 associates with Smad7 in the nucleus and their complex subsequently translocates to the cytosol. The complex then interacts with the activated receptor and causes its proteasome-dependent degradation, which ultimately leads to the inhibition or attenuation of TGF-β signaling. During the TGF-β stimulated epithelial–mesenchymal transition (EMT), SMURF-dependent ubiquitination and degradation of TGF-βRI is blocked by concurrent action of another ubiquitin ligase TNF receptor-associated factor 4 (TRAF4), a member of the RING domain containing E3 ubiquitin ligase family [192–194]. Transforming growth factor β receptor-associated TRAF4 potentiates TGF-β signaling by mediating ubiquitination and proteasome degradation of SMURF. At the same time, it was shown that TRAF4 is also responsible for signaling-type Lys63-linked ubiquitination of TGF-βR, leading to its association with TGF-β activated kinase 1 (TAK1). Ubiquitin ligase SMURF2 also interacts with Smad2/3. It mediates Smad2 ubiquitination and targets it for degradation [195]. Its activity towards Smad3 is much weaker and leads to multiple monoubiquitinations of Smad3. This seems to have no effect on Smad3 stability, but rather on its ability to form a complex with Smad4 [196]. Interestingly, SMURF2 also targets Smad inhibitors Sloan–Kettering Institute (SKI) proteins. It binds them indirectly using Smad2 as an adapter [197].

Another E3 ubiquitin ligase that has been shown to effectively regulate the canonical TGF-β pathway is NEDD4L (NEDD4-like). The activated Smad complex is phosphorylated in the nucleus in a series of events initiated by CDK8/9 [198]. These transcription-associated kinases prime the Smad complex to another round of phosphorylation via GSK3β. The GSK3β-phosphorylated motif is recognized by the WW domain of the HECT-type ubiquitin ligase NEDD4L [199]. NEDD4L-dependent ubiquitination leads to the proteasome-dependent degradation of Smad2/3 and attenuation of TGF-β signaling. Interestingly, the WW domain is flanked by two serines targeted by serum/glucocorticoid regulated kinase 1 (SGK1). This phosphorylation inhibits NEDD4L interaction with Smads and promotes their stability. The ubiquitin ligase NEDD4L and another HECT-type ligase WW domain containing E3 ubiquitin protein ligase 1 (WWP1) were also shown to recognize TGF-βRI in a similar manner as SMURF (Smad7–dependent). The receptor ubiquitination decreases its stability on the membrane and leads to its internalization and subsequent degradation.

Additionally, the HECT-type ITCH ligase positively regulates TGF-β signaling as well. It binds Smad2 but does not have any effect on its stability. It rather promotes, in a HECT-dependent manner, its association with TGF-βR [200]. A possible explanation can be drawn from other studies which have shown that ITCH promotes TGF-β signaling by mediating TGF-βR-dependent degradation of Smad-signaling inhibitors, Smad7 and Ras association domain family 1 isoform A (RASSF1A) [201,202].

The Smad7 protein is also a substrate for ubiquitin ligases RNF111 (Arkadia) and RNF12 (RLIM), which both localize to the nucleus and most probably target Smad7 in this compartment [203–206]. Importantly, RNF111 has a chain of Small ubiquitin-like modifier (SUMO)-interacting motifs in its N-terminal part, and it is possible that it recognizes its substrates once they are sumoylated. Moreover, it has displayed activity towards Smad transcriptional co-repressors SKIL and SKI [207–209]. The protein involved in β-catenin degradation, AXIN, was shown to be a scaffold protein linking the RNF111 ubiquitin ligase and Smad7 [205]. It seems that Rnf12 can recognize Smad7 in the context of its interaction with SMURF [210]. In T cells, CBL-b is another RING ligase targeting Smad7. CBL-b and Smad7 interact physically and genetically, as it was shown that Smad7 inactivation restores the TGF-β signaling defect in CBL-b-deficient T cells [211].

Cullin1-dependent ubiquitin ligase β-TrCP was shown to mediate degradation of TGF-βR. The β-TrCP protein does not bind to the receptor directly but via the linker protein FAS-associated factor 1 (FAF1) [212]. Upon phosphorylation by the AKT kinase, FAF1 relocates to the plasma

membrane where it interacts with TGF-βR and mediates its ubiquitination via the β-TrCP-ubiquitin ligase. This represents interesting crosstalk between PI3-K and TGF-β signaling.

Additionally, the E3 ubiquitin ligase TRIM33 (TIF-1γ or ectodermin) was also shown to interact with the Smad2/3 complex [213,214]. There are conflicting studies regarding its role in TGF-β signaling. It was proposed that TRIM33 and Smad4 associate with the r-Smads in a mutually exclusive manner [215]. Another study suggests that TRIM33 is a bona fide ubiquitin ligase for Smad4 which mediates chromatin-associated Smad4 monoubiquitination [216].

Last two ubiquitin ligases involved in TGF-β signaling are MYC binding protein 2 (MYCBP2) and S-phase kinase associated protein 2 (SKP2) [217–219]. Putative RING finger E3 ubiquitin ligase MYCBP2 could regulate Smad stability in neurons. *Drosophila* MYCBP2 homolog Highwire (Hiw) interacts with the *Drosophila* Smad homolog Medea. Highwire-mutant flies have also unrestrained synaptic growth [218]. Biochemically, Hiw controls the level of *Drosophila* TGF-βR (Tkv) and this could be involved in restricting Medea signalization in *Drosophila* neurons and intestinal stem cells [217]. The cullin1 ubiquitin ligase-dependent substrate adapter SKP2 mediates degradation of Smad4. It preferentially binds cancer-associated forms of Smad4 [219].

4.2. Mouse Models of Ubiquitin Ligases Involved in the TGF-β Signaling Pathway

Since the TGF-β signalling pathway has a crucial role in diverse developmental processes, mouse models deficient in its core components exhibit a wide range of developmental defects [220,221]. As mentioned above, several ubiquitin ligases have been suggested to regulate the TGF-β signalling pathway. However, mouse models of their deficiency show that these ubiquitin ligases often have different functions. While phenotypes of RNF111 (Arkadia) and TRIM33-deficient mice supported a crucial role in the TGF-β signaling pathway, the mouse models examining the deficiencies of other ubiquitin ligases failed to bring evidence of involvement in TGF-β signaling [214,222]. They seem to have other physiological substrates instead and, thus, control different processes as discussed in more detail below.

4.2.1. Smad Ubiquitination Regulatory Factor (SMURF)

Ubiquitin ligases SMURF1/2 share a high protein sequence homology (>70%) and their domain architecture is similar. Structurally they belong to NEDD-type HECT ligases. The N-terminal protein kinase C (PKC)-related C2 domain is followed by two or three WW PPxY/substrate interacting domains, respectively, and the catalytical C-terminal HECT domain. As mentioned above, SMURF1–2 were implicated in activated Smad2/3 and TGF-βRI degradation. Intracellular localization of SMURF1/2 is ambiguous as they were found in both the cytosol and the nucleus. Overexpression of SMURF1/2 was found in many cancer tissues and is associated with worse patient survival.

Individual SMURF1- and SMURF2-deficient mice are viable and fertile without any noticeable defects in embryogenesis [223,224]. The SMURF1 absence leads to an age-dependent bone mass increase due to the enhanced osteoblast activity [223]. One line of evidence shows that SMURF1 inhibits mesenchymal stem cell (MSC) differentiation and their osteoblastic potential via controlling the stability of the transcriptional factor JunB. Simultaneous inactivation of JunB in vitro rescued the osteogenic potential of MSCs to the normal level [225]. Another group revealed that the osteoblast Smurf1 ubiquitin ligase activity was directed towards another factor, Map kinase kinase 2 (Mekk2), an upstream kinase in the Jnk signaling cascade. Hyperactive Jnk signalization was then responsible for the higher activity of osteoblasts [223]. It was also reported that bone loss observed in mice with artificially increased TNF-α signaling was dependent on SMURF1 activation [226]. Another age-dependent phenotype of SMURF1-deficient mice was the spontaneous development of hepatic steatosis. In hepatocytes, the SMURF1 deficiency leads to upregulation of the expression of peroxisome proliferator-activated receptor γ (PPARγ) and its target genes involved in lipid synthesis and fatty acid uptake. In this context, however, SMURF1 does not mediate protein degradation of PPARγ but rather inhibited its activity via the non-proteolytic K63-linked ubiquitin modification. Treatment of

SMURF1-deficient mice with a PPARγ antagonist, GW9662, reversed the lipid accumulation in the mutant mice liver [227].

The SMURF2-deficient mice display an expanded HSC compartment in the bone marrow with a higher repopulating capacity especially in aged animals [224]. The Smurf2 deficiency renders mice susceptible to spontaneous tumorigenesis, most notably the B-cell lymphoma, which resembles human diffuse large B-cell (DLBC) lymphoma with molecular features of germinal or post-germinal center B cells [228]. Mechanistically, Smurf2 is responsible for the degradation of Yin Yang 1 (YY1), a key germinal center transcription factor. Stabilized YY1 is responsible for transactivation of the c-Myc oncogene and activation of B cell proliferation [229].

Transgenic mice deficient for both SMURF1 and SMURF2 display complex developmental defects. Approximately one-third of mutant embryos display gastrulation defects characterized by abnormal posterior structures. The rest of the embryos gastrulate normally but show gross developmental abnormalities including an open neural tube and lateral expansion of the neuroectoderm [87]. This is a feature characteristic for mice with defects in planar cell polarity (PCP) and convergent extension movements (CE). Indeed, mice with only one of the four *SMURFS* alleles (e.g., *SMURF1*$^{-/+}$; *SMURF2*$^{-/-}$) show stereocilia misalignment on the cochlear organ of Corti. Mechanistically, SMURF deficiency is responsible for inappropriate activation of the non-canonical Wnt signaling pathway. Wnt engagement to FZD receptor leads to Dishevelled 2 protein phosphorylation and its translocation to the membrane. The phosphorylated Dishevelled 2 binds the Prickle protein, a major regulator of PCP. This interaction is mediated by the Dishevelled 2 constitutive partner PAR6. The whole complex is later recognized by SMURF which is responsible for the ubiquitination and degradation of Prickle. Inappropriate Prickle degradation leads to PCP and CE defects in SMURF1/2 DKO mice [87].

4.2.2. RING Finger 111/Arkadia

As mentioned above, RNF111 contains several SUMO-binding motifs and it can possibly recognize sumoylated substrates [230]. Mutations affecting RNF111 function were documented in patients with ovarian and colorectal cancer [231].

In mice, the *Arkadia* recessive mutation was generated using gene-trap mutagenesis. Heterozygous *Arkadia* mice are normal and healthy, yet they have reduced expression of several TGF-β target genes [231]. Developmental abnormalities of homozygous animals appear early in mouse embryogenesis. An antero-visceral endoderm (AVE) is formed but the embryo lacks a node, has a reduced head, fails to undergo turning, and dies very early at midgestation [232]. Similarly to Trim33-deficient mice, *Arkadia* mice exhibit defects associated with deregulated Nodal signaling. Embryonic cells show an accumulation of phosphorylated Smad2/3 proteins, yet surprisingly most of Nodal/Smad target genes are downregulated. As a result, *Arkadia* mice have a very similar phenotype-like Smad2-deficient embryos [222].

4.2.3. S-Phase Kinase-Associated Protein 2 (SKP2)

S-phase kinase-associated protein 2 (SKP2) is the F-box protein which is characterized by five leucine-rich repeats in its N-terminus. S-phase kinase-associated protein 2 controls the stability of the CDK inhibitor p27 during the G1/S-phase transition [233]. The p27 protein is specifically recognized upon threonine phosphorylation and in the context of its complex with adapter proteins CDK regulatory subunit 1 (CKS1), CDK2, and cyclin E [234,235].

S-phase kinase-associated protein 2 knockout mice are small but viable [236]. Their cells have enlarged nuclei with polyploidy, aberrant centrosomes, and accumulated p27 protein. Simultaneous inactivation of the *CDKN1B/p27* gene reverts the phenotype [237]. When subjected to partial hepatectomy, SKP2-deficient mice exhibit proliferation-independent liver regeneration (via cellular enlargement) [238]. Similarly, scraping of the corneal epithelium in SKP2-deficient mice leads to defected wound healing [239]. Again, the phenotype was reversed by concurrent deletion of the *CDKN1B/p27* gene.

4.2.4. MYC Binding Protein 2 (MYCBP2)

The MYCBP2 is a putative atypical RING ligase. It is a large protein containing the RCC1-like GEF domain, two PHR-family-specific domains, the RAE1-binding domain, the F-box binding domain 1, the Myc binding domain, and the C-terminal RING domain. Expression of MYCBP2 was found to be reduced in patients with acute lymphoblastic leukemia [240].

In mice, the genetic screen and targeted inactivation revealed MYCBP2 function in motor neuron pathfinding. In *Magellan*-mutant embryos, with the mutation causing MYCBP2 protein truncation, motor axons display navigation defects [241]. Surprisingly, they respond to guidance cues with normal sensitivity in vitro. Motor and sensory neurons from *Magellan* mutants show abnormal axon and growth cone morphologies. The phenotype is probably caused due to the disruption of the polarized distribution of the dual leucine zipper kinase (DLK), which acts upstream from p38Mapk and regulates microtubule stability. In accordance, the *Magellan* phenotype could be reversed by stabilizing microtubules with taxol or inhibiting p38Mapk activity. In a parallel study, the targeted conditional mutant shows that, as in invertebrates, MYCBP2 function is essential for shaping motor neurons terminals and the formation of major CNS axon tracts including those of the internal capsule. Major CNS axon tract phenotypes are partially caused by cell-non-autonomous mechanisms in a Dlk-independent manner [242]. The discrepancies among these models could be a result of different genomic deletions in the *MYCBP2* gene locus. In comparison to the *Magellan* mutant with the C-terminally truncated protein, the motor neuron-specific knockout mice have only 70 amino acid region proximal to the RCC1 domain deleted [241,242]. A follow-up study took advantage of these two models and prepared their cross [243]. The study focused on the previous observation that the MYCBP2 regulates mTOR signaling [244]. In agreement with this observation, mTOR signaling is attenuated in both models but, surprisingly, there are no mTOR signaling alterations in the prepared cross. This suggests that Mycbp2 regulates mTOR signaling via two independent pathways. Moreover, defective mTOR signaling is responsible only for certain neurodevelopmental defects (corpus callosum) associated with MYCBP2 deficiency but does not rescue the whole phenotype (defects in axon fiber tracts of the internal capsule and anterior commissure). Additionally, another study revealed that loss of MYCBP2 results in prolonged survival of severed axons in both the peripheral and central nervous systems. Survival of these axons depends on stabilization of mononucleotide adenyltransferase 2 [245].

4.2.5. Tripartite Motif Containing 33 (TRIM33)

Tripartite motif containing 33 ubiquitin ligase is a member of the tripartite motif (TRIM) protein family. In its N-terminus, it has the RING finger, two B-box domains, and the coiled-coil domain. The C-terminal part of this protein is composed of the plant homeodomain (PHD) followed by the bromodomain. Tripartite motif containing 33 was found to be mutated or downregulated in several human cancers, like chronic myelomonocytic leukemia [246].

Mouse embryos deficient in Trim33 die at E9 [214,247]. They display a dramatic developmental delay. At E8.0–8.5 (3–6 somite pairs in controls), the TRIM33 mutant embryos are aligned at the base of the yolk sac, and, although they have formed the anterior-posterior body axis and recognizable head folds, it is difficult to identify any other embryonal structures. They are smaller and lack a clear distinction between epiblast and extra-embryonic ectoderm. Morphological and histological analyses demonstrated that TRIM33 mutants display remarkable defects in embryonic polarity and tissue patterning. The phenotype of mutant embryos was opposite to those observed in Nodal, Smad2, and Smad4 knockouts. Nodal induces and patterns the anterior visceral endoderm, and sustains trophoblast development. In TRIM33-deficient embryos, Nodal signaling becomes unrestricted leading to dramatic changes in the embryo body plan. In the epiblast, TRIM33 deficiency shifts mesoderm fates towards node/organizer fates. As a result of impaired primitive streak development embryos have defective mesoderm formation.

Mice with TRIM33 inactivation in monocytes, bone-marrow-derived macrophages, peritoneal macrophages, and neutrophils are normal and healthy. They show sustained expression of interferon-β1

at late stages of toll-like receptor-mediated activation in macrophages [248]. Hematopoietic stem cells' specific loss of TRIM33 resulted in significant changes in erythroid, B-lymphoid, and myeloid compartments and decreased HSC capacity in transplantation assays [249]. The following study shows that a block in erythroid maturation in bone marrow was compensated with enhanced spleen erythropoiesis [250]. Another study on TRIM33 deficiency in HSCs showed that four-month-old mutant mice develop an accelerated aging phenotype in HSCs. The authors suggested that TRIM33 inhibition of TGF-β signaling was important for the balance between lymphoid and myeloid lineage differentiation and that myeloid- and lymphoid-biased HSC populations respond differently to TGF-β signaling. As the TGF-β signaling pathway was involved in the inhibition of HSC reentry into the cell cycle, disturbance in this signaling in TRIM33-mutant HSCs could result in the aging phenotype [251]. Tripartite motif containing 33-null mammary gland development appeared to be normal with no obvious developmental defects during the lifespan of virgin mice. However, after giving birth, the mice developed a significant lactation defect. Therefore, TRIM33 is probably essential for the terminal differentiation of alveolar epithelial cells in the mammary gland at the end of pregnancy.

4.2.6. RING Finger 12 (RNF12)

Ubuquitin ligase RNF12 has the C-terminally located RING domain and the central basic domain (BD). It is involved in X-chromosome inactivation (XCI) and in mediating ubiquitination and degradation of pluripotency marker reduced expression protein 1 (REX1) [252,253]. Mutations in RNF12 were reported in X-linked intellectual disability.

Mice deficient in RNF12 mice display early embryonic lethality specific for female embryos due to the defectively imprinted XCI, precluding the development of embryonic trophoblast tissues. Males carrying a germline knockout of *RNF12* (Δ/Y) appear healthy and are fertile [254]. There is a study showing that only 50 percent of male neonates survive and those that die are significantly smaller, with altered lung branching and maturation [255]. Importantly, RNF12 is essential for triggering imprinted XCI but dispensable for random XCI [256]. Its crucial role is to maintain high Xist RNA levels, Xist clouds, and X-silencing in female embryos at blastocyst stages [257]. Mammary gland-specific knockout of RNF12 shows its requirement for alveolar morphogenesis and milk production. It acts as a survival factor for milk-producing alveolar cells. While mammary glands of virgin females contain many living RNF12-negative epithelial cells, lactating glands are only RNF12-positive. Moreover, decreased expression of RNF12 correlates with mammary gland involution [258].

4.2.7. WW Domain Containing E3 Ubiquitin Protein Ligase (WWP)

Ubiquitin ligases WWP1/2 belong to the NEDD-type HECT ligase family [259]. They contain the N-terminal C2 domain, four WW domains, and the C-terminal HECT domain. They are both cytosolic and nuclear. Potential WWP1 substrates include TGF-βRI, Smad2 or Erb-B2 receptor tyrosine kinase 4 (ERBB4). Moreover, WWP2 was shown to mediate degradation of PTEN or the transcription factor OCT4. Interestingly, WWP1 is overexpressed in many types of cancer, especially prostate, breast, and liver, whereas WWP2 is frequently overexpressed in oral cancer.

Mice deficient in Wwp1 are viable and fertile without any obvious abnormalities. Embryos are born at the normal Mendelian ratio and grow relatively healthily. They develop increased bone mass as they age. This phenotype is associated with increased bone formation rates and normal bone resorption parameters [260,261]. They develop malformations of the craniofacial region. At the molecular level, Wwp2 is associated with Goosecoid, a transcriptional activator of the key cartilage regulatory protein Sox6. Importantly, WWP2 facilitates Goosecoid monoubiquitination, a post-translational modification required for its optimal transcriptional activity [260]. Mice defiecent in WWP2 also have reduced body and organ size and they resemble PTEN transgenic mice (Super-PTEN). In support of this, they have elevated and stabilized PTEN protein levels and reduced phosphorylation of the AKT kinase [262]. The bone marrow-derived macrophages have a stronger response to poly(I:C) challenge (regarding secreted TNF-α and IL-6 cytokines) and are more susceptible to poly(I:C)-induced death. These findings

suggest that WWP2 negatively regulates TLR3-mediated innate immune and inflammatory responses. Indeed, WWP2 was shown to target adapter protein in TLR3-mediated NF-κB and IRF3 activation pathways (TRIF) for ubiquitination and degradation [261].

Mice deficient in both WWP1 and WWP2 display defects in axon–dendrite polarity in pyramidal neurons and abnormal laminar cortical distribution [263]. Interestingly, knockout of *miR-140*, encoded in *WWP2* intron, displayed similar phenotypic changes as those upon *WWP1* and *WWP2* deletion. The authors of the study delineated a novel regulatory pathway that involves the Sox9 transcription factor as a major regulator of WWP1/WWP2/miR-140 locus expression, and consequentially, axon specification, acquisition of pyramidal morphology, and accurate laminar distribution of cortical neurons.

5. Notch Signaling Pathway

The highly conserved Notch signaling pathway is critical for cell fate determination during development and tissue homeostasis [264,265]. It translates extracellular stimuli to transcriptional programs involved in cell cycle regulation and cellular differentiation [266,267]. The core architecture of this pathway is simple with only a few important canonical proteins (Figure 5) [268]. The human genome encodes five Notch ligands (Jagged 1/2 and Delta-like 1/3/4) and four Notch receptors (Notch 1–4). Notch ligands are transmembrane proteins expressed by various types of cells and tissues. Notch receptors are single-pass type I transmembrane proteins. They have a different amount of EGF-like repeats in the extracellular part. During maturation, these repeats are fucosylated by *O*-fucosyltransferase, and fucosyl moieties are further modified by the Fringe family of 1,3 *N*-acetylglucosaminyltransferases [269]. Such glycosylations represent "the code" which is responsible for specific recognition of ligands by different receptors. After glycosylation, the extracellular part of the Notch receptor is cleaved by the furin-like convertase (S1 cleavage) [270]. The non-covalently linked heterodimer is subsequently transported from Golgi to the cell surface. There are two additional domains between the membrane and EGF-like repeats—Lin20-Notch repeats (LNR) and heterodimerization domain (HD). Both are involved in ligand-dependent receptor activation.

Upon the receptor binding, the endocytic system is activated in the ligand-bearing cell. This forcefully drags the ligand-receptor complex towards the interior of this cell and, consequently, relaxes the structure of the LNR/HD domains. Once relaxed, the membrane-proximal region of the Notch extracellular domain (NECD) becomes a substrate for a disintegrin and metalloprotease 10/17 (ADAM10/17) metalloproteinases (S2 cleavage) [271,272]. They subsequently cleave NECD, which is then engulfed by a ligand-presenting cell via a transendocytosis [273]. The residual extracellular part is cleaved in the last proteolytic step (S3 cleavage). This is accomplished by γ-secretase, a membrane-bound protein complex involved in intramembrane proteolytic cleavage [274]. After this step, the Notch intracellular domain (NICD) is released to the cytosol and transported to the nucleus. The NICD has several domains. The N-terminally located proline–glutamate–serine–threonine-rich (PEST) domain is followed by a nuclear localization signal, seven ankyrin repeats, transactivation domain (TAD), and C-terminal RBP-Jκ–associated molecule (RAM). Inside the nucleus, NICD interacts via the RAM domain and ankyrin repeats with the CSL/RBP-Jκ transcription factor and its co-factor Mastermind (MAML1) [275,276]. In the absence of Notch receptor activation, CSL interacts with the co-repressor complex (CoR) [277,278]. This complex is tethered to promoters of Notch target genes, actively repressing them. The interaction with NICD and MAML1 leads to the displacement of the CoR complex and the recruitment of transcription co-activators (e.g., p300). This is followed by activation of target genes' expression, including the Hairy enhancer of split 1 (HES1) family of transcriptional repressors, the CDK inhibitor p21, and others [266].

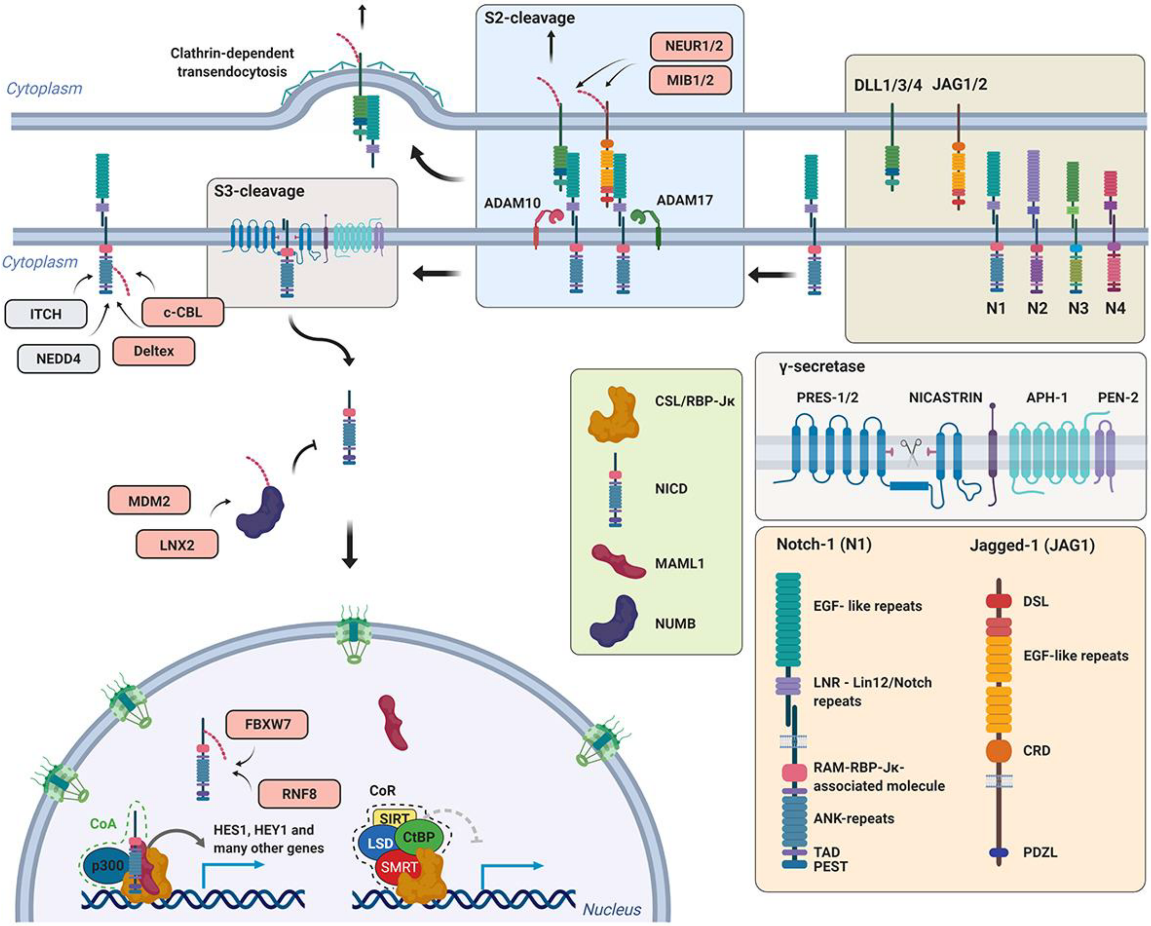


Figure 5. Notch signaling pathway by ubiqutination upon binding of Jagged/Delta (JAG/DLL) ligands to the Notch receptor (N1); the endocytic system is activated in the ligand-bearing cell. This leads to two sequential proteolytic events. The first is metalloproteinase-dependent (ADAM10/17) and it releases the extracellular domain of the Notch receptor which is afterward engulfed via transendocytosis. The second proteolytic cleavage is membrane bound and dependent on γ-secretase activity. After this step, NICD (the Notch intracellular part) is released to the cytosol and transported to the nucleus where it interacts with the CSL/RBP-Jκ transcription factor and its co-factor Mastermind (MAML1). The complex is tethered to promoters of Notch target genes. For details see the text.

5.1. Notch Signaling Pathway and its Regulation by Ubiquitin Ligases

The Notch receptor is a short-lived protein which is targeted by multiple ubiquitin ligases. Several HECT-type ubiquitin ligases regulate its membrane localization and endocytic recycling, promoting "non-activated Notch receptor degradation". Knockdown of the ITCH ubiquitin ligase leads to impaired Notch1 ubiquitination and lysosomal degradation [279]. Ubiquitin ligase ITCH interacts with the Notch receptor indirectly via the α-arrestin 1 (ARRDC1) and β-arrestins complex [280]. Interestingly, ITCH is also the main ubiquitin ligase involved in the NUMB-dependent Notch1 receptor inhibition [281]. Adapter protein NUMB, a major inhibitor of Notch signaling, is also a target of the RING-type ubiquitin ligase LNX2. This ubiquitin ligase, by mediating NUMB degradation, thus potentiates Notch signaling [282]. The WWP2 ubiquitin ligase was shown to mediate Notch1 polyubiquitination in a manner dependent on activated Dishevelled 2. Dishevelled 2 binds to the ubiquitin ligase WWP2 and unlocks its ligase activity from autoinhibition [283]. Of note, Dishevelled 2 involvement could point to possible signaling crosstalk between the Wnt and Notch1 pathways. Moreover, WWP2 also appeared in the screen for Notch3 interacting partners. It mediated ubiquitination of its active form and blocked Notch3 signaling in the context of ovarian cancer [284]. In general, ubiquitination

of transmembrane receptors often regulates the receptor endocytosis and inappropriate activation. This was confirmed for Notch receptor. Its endocytosis is clathrin-dependent and requires epsin1 and the adaptor protein complex 2 (AP2) ubiquitin ligase Nedd4. Inactivation of Nedd4 leads to stabilization of membrane-bound Notch and signaling enhancement [285]. Another ubiquitin ligase involved in the regulation of the Notch cell surface stability is Deltex-1 (DTX1), which colocalizes with Notch1 on tubulovesicular recycling endosomes. Inactivation of DTX1 leads to Notch1 stabilization and cell surface relocation via the RAB4A-mediated transport route. Nevertheless, DTX1 does not mediate direct ubiquitination of the Notch receptor. The main DTX1 substrate in the endosomal compartment is PI5P4Kγ, a lipid kinase involved in PI(4,5)P2 production. It is PI5P4Kγ activity which is necessary for cell surface localization and stability of the Notch1 receptor [286]. The activated form of Notch (NICD) is also targeted by several other ubiquitin ligases, the most important being FBXW7. Phosphodegron-interacting protein FBXW7 belongs to the CRL family of RING-type ubiquitin ligases and recognizes the PEST region of NICD. This recognition is preceded by the sequence of priming and processing phosphorylations. The canonical priming kinase of the FBXW7 degron is CDK8, but integrin-linked kinase (ILK) is also able to phosphorylate it [287,288]. Like in other FBXW7 substrates, the processing kinase is GSK3β [289,290]. Moreover, the NUMB/ITCH complex and RNF8, a ubiquitin ligase involved in DNA damage response, are able to mediate NICD ubiquitination and degradation as well [281]. In support of RNF8 function as the Notch ubiquitin ligase, data from The Cancer Genome Atlas (TCGA) show an inverse correlation between RNF8 expression and Notch activity [291]. The ubiquitin ligase MDM2 targeting the p53 tumor suppressor plays an important role in potentiating the Notch signaling pathway via its interaction with Notch inhibitor NUMB. The mechanism remains to be elucidated [292,293].

Not only the receptors but also Notch ligands are regulated by ubiquitination. The ubiquitination is required for proper trafficking and presentation of the active ligands on the cell membrane and is provided by the E3 ubiquitin ligases Neuralized (NEUR) and Mindbomb (MIB) [273,294,295].

5.2. Mouse Models of Ubiquitin Ligases Involved in the Notch Signaling Pathway

Activation of the Notch receptor signaling pathway is important for embryonic development since it plays a critical role in cell fate determination. Expectedly, mice defective in this pathway often exhibit embryonic lethality and developmental abnormalities [296–298]. Several mouse models of ubiquitin ligases mentioned above confirm the role of these ligases in Notch signaling pathway in vivo. Mice deficient in Mib1 ubiquitin ligase clearly exhibit the Notch-defective phenotype, and mutant mice die early during embryogenesis with many developmental defects. On the other hand, mouse models of ubiquitin ligases which mediate degradation of many different proteins, for example FBW7, reflect this fact in their phenotypic complexity. Importantly, several mouse models do not support the importance of cognate ubiquitin ligases in the Notch signaling pathway, as discussed here [299–301].

5.2.1. F-box and WD Repeat Domain Containing 7 (Fbxw7)

Human FBXW7 is a well-characterized F-box protein that binds to its substrates in a similar manner like β-TrCP. It is also a haploinsufficient tumor suppressor with mutations found in many human cancers [302,303]. It regulates the stability of many substrates involved in the cell cycle and survival, including p100, c-Myc, c-Jun, cyclin E, NF1, and Notch [304,305].

F-box and WD repeat domain containing 7-deficient mouse embryos die around E10.5–11.5. The phenotype clearly reflects that endothelial tissues represent a major site of embryonic Fbxw7 expression. The embryos have significant abnormalities in brain and yolk sac vascular development [306,307]. They also exhibit defects in major trunk veins formation and heart chamber maturation. The animals have the upregulated endothelial cell-specific isoform of the Notch receptors family, Notch4, as well as Notch target genes *HEY1* and *HES1*. Although the phenotype suggests a potential involvement of the Notch signaling pathway hyperactivation, no genetic rescue experiment has been done yet [307]. The T cell-specific deletion of *FBXW7* leads to thymic hyperplasia and

subsequent development of the thymic lymphoma. T cells from knockout mice are immature, accumulate the Myc protein—another canonical FBXW7 substrate—and fail to exit from the cell cycle [308]. The targeted deletion of *FBXW7* in HSCs revealed the essential role of Fbxw7 in maintaining the HSCs pool. In Fbxw7-deficient animals, HSCs are prematurely depleted due to the fact of active cell cycling and p53-dependent apoptosis. The HSC reconstitution capacity and quiescence are impaired [309]. Mice with conditionally inactivated intestinal *FBXW7* develop a hyperproliferative phenotype. They show impairment in goblet cell differentiation and the accumulation of highly proliferating progenitor cells [310]. The brain-specific deletion results in perinatal death of embryos. Animals lack suckling behavior and have morphological abnormalities in the brain structure. On the cellular level, they have a clear impairment of neural stem cells differentiation, resulting in a decrease of mature neurons. They also have disequilibrium in neural cell differentiation towards astrogenesis [311]. The hepatic inactivation results in hepatomegaly and steatohepatitis. Mutant hepatocytes accumulate SREBP and NOTCH1 proteins. The long-term Fbxw7 deficiency leads to the proliferation of the biliary system and appearance of hamartomas as well as the imbalanced ratio between cholangiocyte and hepatocyte lineages [312].

5.2.2. Mindbomb and Neuralized (Mib and Neur)

Mindbomb 1/2 proteins contain two substrate-recognizing domains—the ankyrin repeats domain and several RING domains. Neuralized 1/2 proteins consist of the neuralized homology repeats responsible for protein–protein interactions and the C-terminal RING domain. As described previously, Mib and Neur ubiquitin ligases target Notch ligands and influence Notch signaling.

Mindbomb 2-, NEUR1-, and NEUR2-deficient mice are viable with entirely normal appearance [299]. Mindbomb 1-deficient embryos are severely growth retarded at E9.5 and die at E10.5 from a lack of placental connection and defects in somitogenesis, vasculogenesis, and cardiogenesis [299–301]. The phenotype of these embryos clearly shows defective Notch signaling [296,313]. The yolk sacs have a blistered appearance with only small capillaries and complete lack of large vitelline-collecting vessels. Embryos lack heart looping and have an enlarged balloon-like pericardial sac and a smaller dorsal aorta. Other typical signs of Notch-related defects include irregular somitogenesis, absence of mesenchymal cells, and lack of second branchial arches. Knockout embryos show a strong neurogenic phenotype. The head of embryos appear normal but the neurons prematurely differentiate and undergo apoptosis. The reduction of progenitors leads to a loss of both astrocytes and oligodendrocytes. The embryos also lack intraembryonic hematopoietic progenitors [314]. Inducible inactivation of MIB1 (from E10 to E12), shows MIB1 continuous requirement in neuronal system development as it exhibits the suppression of glial differentiation [315].

The tissue-specific deletion of the *Mib1* gene shows its central role in Notch signaling and mouse development. Endoderm-specific inactivation causes a loss of endocrine progenitors and β-cells [316]. Its inactivation in the mouse myocardium mimics the phenotype of myocardial-specific deletion of *Jagged1*. Embryos have left ventricular non-compaction. They show reduced ventricular Notch1 activity, a dilated heart with a thin compact myocardium, and a large, non-compacted trabeculae protruding toward the ventricular lumen [317]. Mice with Mib1 inactivated in the bone marrow develop the myeloproliferative disease (MPD). They exhibit hepatosplenomegaly, accumulation of immature granulocytes, and anemia. Interestingly, the transplantation of wild-type bone marrow cells into the Mib1-null microenvironment results in a de novo MPD [318]. The absence of Mib1 during the development of the lymphatic system results in the developmental arrest of T cells and marginal zone B cells [319].

5.2.3. Deltex-1 (Dtx1)

Deltex-1 is a RING-finger ubiquitin ligase containing the proline-rich motif and the N-terminal Notch-binding WWE domains. Deltex-1 regulates Notch signaling by controlling PI5P4Kγ stability [286]. It is downregulated in a subset of gastric adenocarcinomas [320].

Deltex-1-deficient mice have diminished Treg-dependent T cell anergy resulting in autoantibody production, augmented T cell activation, and increased inflammatory response [321]. The mice are otherwise healthy and fertile and T and B cell development seems intact [322]. Biochemically, Treg-initiated T cell anergy is dependent on the Foxp3 transcriptional factor. Deltex-1, which is transcriptionally activated by the nuclear factor of activated T cells (Nfat), controls Foxp3 activity via degradation of the FOXP3 inhibitor Hif1α. In Deltex-1-deficient Treg cells, the stabilized Hif1α suppresses FOXP3 and, subsequently, Treg's ability to impose T cell anergy. Simultaneous knockout of Hif1α restores FOXP3 and rescues the defective suppressive activity in Deltex-1-deficient Treg cells in vivo [321,323]. It is not clear if Deltex-1 regulation of the Notch signaling pathway could be part of T cell anergy activation. As mentioned above, Deltex-1 is a positive regulator of Notch signaling [286]. Moreover, Notch was shown to act as the Foxp3 positive regulator [324,325]. Whether Deltex-1 activates Foxp3 also via potentiated Notch signaling or if Notch activation serves as positive feedback to sustain strong T cell anergy remains to be investigated.

5.2.4. RING finger 8 (RNF8)

Ubiquitin ligase RNF8 has the C-terminal RING domain and the N-terminal forkhead-associated (FHA)-domain [326]. The FHA-domain is necessary for DNA-damage association. It binds to the ATM-phosphorylated N-terminus of the mediator of DNA damage checkpoint protein 1 (MDC1) [327]. Specifically, RNF8 targets histones by K63-linked ubiquitination, which is recognized by another ubiquitin-ligase RNF168 and leads to the recruitment of DNA repair proteins.

Transgenic embryos lacking Rnf8 are growth retarded with reduced hematopoietic populations. They have impaired class switch recombination and accumulation of unresolved immunoglobulin heavy chain-associated DNA double-stranded breaks. They are more susceptible to ionizing radiation, exhibit increased genomic instability, and have elevated risk for tumorigenesis [328]. Mouse males deficient in Rnf8 are sterile with defective ubiquitination of the XY chromatin. They are proficient in meiotic sex chromosome inactivation but deficient in global nucleosome removal [329]. Mutant mice also exhibit neuronal degeneration and reactive astrocytosis. Importantly, Rnf8-deficient neurons appear more susceptible to X-ray-induced DNA damage and Rnf8-deficient mice display memory impairment and reduced exploratory behavior in the open-field test. This defect could correlate with higher neuronal loss in these animals [330]. Cerebellar granule cell-specific RNF8 knockout displays a higher number of parallel fiber presynaptic boutons and functional parallel fiber/Purkinje cell synapses. It also revealed that RNF8 is involved in suppression of granule neuron/Purkinje cell transmission [331].

5.2.5. Mouse double minute 2 (MDM2)

Mouse double minute 2 is a ubiquitin ligase with the C-terminal RING domain, the central acidic domain and the adjacent zinc finger region, and the N-terminal p53-binding domain that indicates its main function—to facilitate p53 ubiquitination and subsequent degradation. Despite some conflicting data, MDM2 was reported to be overexpressed in many different types of malignancies and it is usually related to a worse prognosis [332].

Mice with a hypomorphic allele of *MDM2* have defects in hematopoietic lineages. They develop mild anemia and the size of their lymphoid organs is significantly reduced due to the lower number of lymphocytes [333]. Mice with full inactivation of both *MDM2* alleles die early in development, and this phenotype is almost completely reversed with concurrent inactivation of murine *p53* [334]. Interestingly, mice with lowered levels of MDM2 were resistant to tumor formation, but otherwise were healthy and did not age prematurely [335].

6. Concluding Remarks

The importance of the ubiquitin–proteasome system has been emerging over the last three decades. Its discovery helped us to understand the biochemical nature of processes underlying major

developmental and homeostatic events in the life domain. Each and every signaling pathway or cellular process depends on the UPS. The architecture of this system has both pleiotropic and specific facets. The pleiotropy is represented via proteasome while the specificity is ensured by a wide group of enzymes called ubiquitin ligases. Apparently, the UPS is essential for cellular and organismal homeostasis. This holds true especially for cancer cells which have to overcome the instability of the genetic information, and the control of the proteome is one way to do it. Therefore, they are fully dependent on proteasome function and this can be therapeutically exploited. The success of proteasome inhibitor bortezomib in multiple myeloma treatment fulfilled some of these expectations. Moreover, the re-discovery of thalidomide, a specific modulator of the ubiquitin ligase cereblon, for successful treatment of multiple myeloma initiated change of the focus towards the more specific approaches. It also proves that the right therapeutic options arise from fusion of the chemistry, the molecular biology, and the animal models. As presented in this review, there are numerous ubiquitin ligases which were found to be involved in the cancer-associated signaling pathways, but only few were confirmed to play the same role in vivo (Figure 6). Moreover, some of these ubiquitin ligases were shown to have a completely different function than expected. It is of the utmost importance to consider these observations and findings.

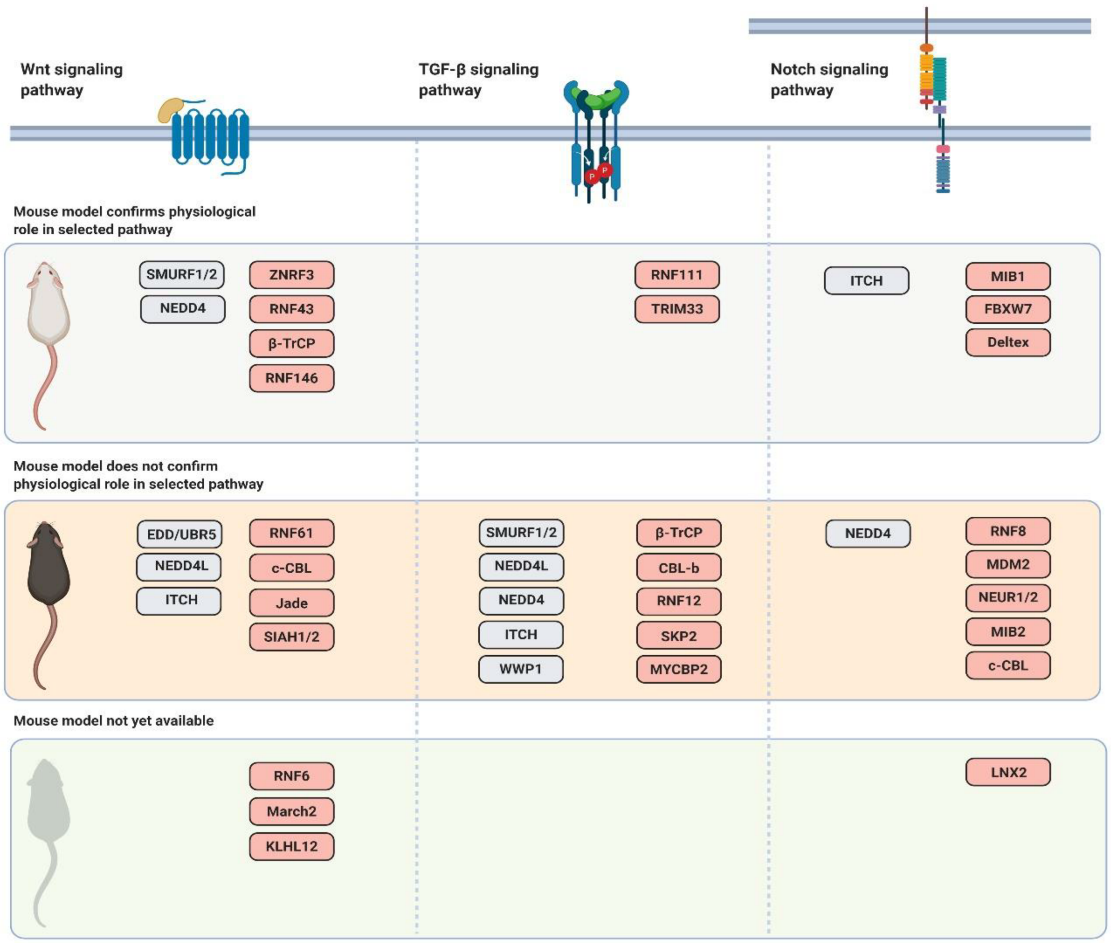


Figure 6. Schematic representation of mouse models of the selected ubiquitin ligases summarizing their physiological role in the Wnt, TGF-β, and Notch signaling pathways.

With the emerging technologies in genetic engineering, it should not be an option but a must to prove our results in mouse models. Because these models will not only confirm what we think we achieved in Petri dishes, they will be an important part of the next step—how to translate these results into better cancer therapy.

Author Contributions: L.C. prepared the manuscript and figures. N.B. and T.L. reviewed and edited the manuscript.

Funding: This work was supported by Grant Agency of Czech Republic (project: 18-27408S) and by the Ministry of Education, Youth and Sports (project LO1419); L.C. was supported by Marie Skłodowska-Curie Fellowship (LIGER).

Acknowledgments: We thank Marketa Vancurova, Emily Langore, Tadeas Cermak, and David Cermak for proofreading the manuscript. L.C. thanks Zuzana Stivinova for the support. L.C. acknowledges the databases OMIM (Online Mendelian Inheritance in Man) and MGI/MGD (Mouse Genome Database) [336,337]. The figures were created with BioRender.com.

Conflicts of Interest: The authors declare no conflict of interest.

References

1. Sanchez-Vega, F.; Mina, M.; Armenia, J.; Chatila, W.K.; Luna, A.; La, K.C.; Dimitriadoy, S.; Liu, D.L.; Kantheti, H.S.; Saghafinia, S.; et al. Oncogenic Signaling Pathways in The Cancer Genome Atlas. *Cell* **2018**, *173*, 321–337. [CrossRef]
2. Kinzler, K.W.; Nilbert, M.C.; Su, L.K.; Vogelstein, B.; Bryan, T.M.; Levy, D.B.; Smith, K.J.; Preisinger, A.C.; Hedge, P.; McKechnie, D.; et al. Identification of FAP locus genes from chromosome 5q21. *Science* **1991**, *253*, 661–665. [CrossRef]
3. Ellisen, L.W.; Bird, J.; West, D.C.; Soreng, A.L.; Reynolds, T.C.; Smith, S.D.; Sklar, J. TAN-1, the human homolog of the Drosophila notch gene, is broken by chromosomal translocations in T lymphoblastic neoplasms. *Cell* **1991**, *66*, 649–661. [CrossRef]
4. Yakicier, M.C.; Irmak, M.B.; Romano, A.; Kew, M.; Ozturk, M. Smad2 and Smad4 gene mutations in hepatocellular carcinoma. *Oncogene* **1999**, *18*, 4879–4883. [CrossRef]
5. Manasanch, E.E.; Orlowski, R.Z. Proteasome inhibitors in cancer therapy. *Nat. Rev. Clin. Oncol.* **2017**, *14*, 417–433. [CrossRef]
6. Skaar, J.R.; Pagan, J.K.; Pagano, M. SCF ubiquitin ligase-targeted therapies. *Nat. Rev. Drug Discov.* **2014**, *13*, 889–903. [CrossRef]
7. Kumari, N.; Jaynes, P.W.; Saei, A.; Iyengar, P.V.; Richard, J.L.C.; Eichhorn, P.J.A. The roles of ubiquitin modifying enzymes in neoplastic disease. *Biochim. Biophys. Acta Rev. Cancer* **2017**, *1868*, 456–483. [CrossRef]
8. Nalepa, G.; Rolfe, M.; Harper, J.W. Drug discovery in the ubiquitin-proteasome system. *Nat. Rev. Drug Discov.* **2006**, *5*, 596–613. [CrossRef]
9. Buetow, L.; Huang, D.T. Structural insights into the catalysis and regulation of E3 ubiquitin ligases. *Nat. Rev. Mol. Cell Biol.* **2016**, *17*, 626–642. [CrossRef]
10. Hershko, A.; Heller, H.; Elias, S.; Ciechanover, A. Components of ubiquitin-protein ligase system. Resolution, affinity purification, and role in protein breakdown. *J. Biol. Chem.* **1983**, *258*, 8206–8214.
11. Deol, K.K.; Lorenz, S.; Strieter, E.R. Enzymatic Logic of Ubiquitin Chain Assembly. *Front. Physiol.* **2019**, *10*, 835. [CrossRef]
12. Stewart, M.D.; Ritterhoff, T.; Klevit, R.E.; Brzovic, P.S. E2 enzymes: More than just middle men. *Cell Res.* **2016**, *26*, 423–440. [CrossRef]
13. Rittinger, K.; Ikeda, F. Linear ubiquitin chains: Enzymes, mechanisms and biology. *Open Biol.* **2017**, *7*. [CrossRef]
14. Akutsu, M.; Dikic, I.; Bremm, A. Ubiquitin chain diversity at a glance. *J. Cell Sci.* **2016**, *129*, 875–880. [CrossRef]
15. Nakayama, K.I.; Nakayama, K. Ubiquitin ligases: Cell-cycle control and cancer. *Nat. Rev. Cancer* **2006**, *6*, 369–381. [CrossRef]
16. Zheng, N.; Shabek, N. Ubiquitin Ligases: Structure, Function, and Regulation. *Annu. Rev. Biochem.* **2017**, *86*, 129–157. [CrossRef]
17. Lilley, C.E.; Chaurushiya, M.S.; Boutell, C.; Landry, S.; Suh, J.; Panier, S.; Everett, R.D.; Stewart, G.S.; Durocher, D.; Weitzman, M.D. A viral E3 ligase targets RNF8 and RNF168 to control histone ubiquitination and DNA damage responses. *EMBO J.* **2010**, *29*, 943–955. [CrossRef]
18. Huen, M.S.; Grant, R.; Manke, I.; Minn, K.; Yu, X.; Yaffe, M.B.; Chen, J. RNF8 transduces the DNA-damage signal via histone ubiquitylation and checkpoint protein assembly. *Cell* **2007**, *131*, 901–914. [CrossRef]

19. Skaar, J.R.; Pagan, J.K.; Pagano, M. Mechanisms and function of substrate recruitment by F-box proteins. *Nat. Rev. Mol. Cell Biol.* **2013**, *14*, 369–381. [CrossRef]
20. Honda, R.; Tanaka, H.; Yasuda, H. Oncoprotein MDM2 is a ubiquitin ligase E3 for tumor suppressor p53. *FEBS Lett.* **1997**, *420*, 25–27. [CrossRef]
21. de Toledo, S.M.; Azzam, E.I.; Dahlberg, W.K.; Gooding, T.B.; Little, J.B. ATM complexes with HDM2 and promotes its rapid phosphorylation in a p53-independent manner in normal and tumor human cells exposed to ionizing radiation. *Oncogene* **2000**, *19*, 6185–6193. [CrossRef] [PubMed]
22. Khosravi, R.; Maya, R.; Gottlieb, T.; Oren, M.; Shiloh, Y.; Shkedy, D. Rapid ATM-dependent phosphorylation of MDM2 precedes p53 accumulation in response to DNA damage. *Proc. Natl. Acad. Sci. USA* **1999**, *96*, 14973–14977. [CrossRef] [PubMed]
23. Frescas, D.; Pagano, M. Deregulated proteolysis by the F-box proteins SKP2 and beta-TrCP: Tipping the scales of cancer. *Nat. Rev. Cancer* **2008**, *8*, 438–449. [CrossRef] [PubMed]
24. Bulatov, E.; Ciulli, A. Targeting Cullin-RING E3 ubiquitin ligases for drug discovery: Structure, assembly and small-molecule modulation. *Biochem. J.* **2015**, *467*, 365–386. [CrossRef]
25. Aravind, L.; Koonin, E.V. The U box is a modified RING finger—A common domain in ubiquitination. *Curr. Biol.* **2000**, *10*, R132–R134. [CrossRef]
26. Wang, T.; Wang, W.; Wang, Q.; Xie, R.; Landay, A.; Chen, D. The E3 ubiquitin ligase CHIP in normal cell function and in disease conditions. *Ann. N. Y. Acad. Sci.* **2019**. [CrossRef]
27. Rotin, D.; Kumar, S. Physiological functions of the HECT family of ubiquitin ligases. *Nat. Rev. Mol. Cell Biol.* **2009**, *10*, 398–409. [CrossRef]
28. Podos, S.D.; Hanson, K.K.; Wang, Y.C.; Ferguson, E.L. The DSmurf ubiquitin-protein ligase restricts BMP signaling spatially and temporally during Drosophila embryogenesis. *Dev. Cell* **2001**, *1*, 567–578. [CrossRef]
29. Staub, O.; Dho, S.; Henry, P.; Correa, J.; Ishikawa, T.; McGlade, J.; Rotin, D. WW domains of Nedd4 bind to the proline-rich PY motifs in the epithelial Na+ channel deleted in Liddle's syndrome. *EMBO J.* **1996**, *15*, 2371–2380. [CrossRef]
30. Ebisawa, T.; Fukuchi, M.; Murakami, G.; Chiba, T.; Tanaka, K.; Imamura, T.; Miyazono, K. Smurf1 interacts with transforming growth factor-beta type I receptor through Smad7 and induces receptor degradation. *J. Biol. Chem.* **2001**, *276*, 12477–12480. [CrossRef]
31. Spratt, D.E.; Walden, H.; Shaw, G.S. RBR E3 ubiquitin ligases: New structures, new insights, new questions. *Biochem. J.* **2014**, *458*, 421–437. [CrossRef] [PubMed]
32. Marin, I.; Ferrus, A. Comparative genomics of the RBR family, including the Parkinson's disease-related gene parkin and the genes of the ariadne subfamily. *Mol. Biol. Evol.* **2002**, *19*, 2039–2050. [CrossRef] [PubMed]
33. Yoshii, S.R.; Kishi, C.; Ishihara, N.; Mizushima, N. Parkin mediates proteasome-dependent protein degradation and rupture of the outer mitochondrial membrane. *J. Biol. Chem.* **2011**, *286*, 19630–19640. [CrossRef] [PubMed]
34. Lee, J.Y.; Nagano, Y.; Taylor, J.P.; Lim, K.L.; Yao, T.P. Disease-causing mutations in parkin impair mitochondrial ubiquitination, aggregation, and HDAC6-dependent mitophagy. *J. Cell Biol.* **2010**, *189*, 671–679. [CrossRef]
35. Zhan, T.; Rindtorff, N.; Boutros, M. Wnt signaling in cancer. *Oncogene* **2017**, *36*, 1461–1473. [CrossRef]
36. Nusse, R.; Clevers, H. Wnt/beta-Catenin Signaling, Disease, and Emerging Therapeutic Modalities. *Cell* **2017**, *169*, 985–999. [CrossRef]
37. Tolwinski, N.S.; Wehrli, M.; Rives, A.; Erdeniz, N.; DiNardo, S.; Wieschaus, E. Wg/Wnt signal can be transmitted through arrow/LRP5,6 and Axin independently of Zw3/Gsk3beta activity. *Dev. Cell* **2003**, *4*, 407–418. [CrossRef]
38. Hao, H.X.; Xie, Y.; Zhang, Y.; Charlat, O.; Oster, E.; Avello, M.; Lei, H.; Mickanin, C.; Liu, D.; Ruffner, H.; et al. ZNRF3 promotes Wnt receptor turnover in an R-spondin-sensitive manner. *Nature* **2012**, *485*, 195–200. [CrossRef]
39. Koo, B.K.; Spit, M.; Jordens, I.; Low, T.Y.; Stange, D.E.; van de Wetering, M.; van Es, J.H.; Mohammed, S.; Heck, A.J.; Maurice, M.M.; et al. Tumour suppressor RNF43 is a stem-cell E3 ligase that induces endocytosis of Wnt receptors. *Nature* **2012**, *488*, 665–669. [CrossRef]
40. Jiang, X.; Charlat, O.; Zamponi, R.; Yang, Y.; Cong, F. Dishevelled promotes Wnt receptor degradation through recruitment of ZNRF3/RNF43 E3 ubiquitin ligases. *Mol. Cell* **2015**, *58*, 522–533. [CrossRef]
41. Peters, J.M.; McKay, R.M.; McKay, J.P.; Graff, J.M. Casein kinase I transduces Wnt signals. *Nature* **1999**, *401*, 345–350. [CrossRef] [PubMed]

42. Ikeda, S.; Kishida, S.; Yamamoto, H.; Murai, H.; Koyama, S.; Kikuchi, A. Axin, a negative regulator of the Wnt signaling pathway, forms a complex with GSK-3beta and beta-catenin and promotes GSK-3beta-dependent phosphorylation of beta-catenin. *EMBO J.* **1998**, *17*, 1371–1384. [CrossRef] [PubMed]
43. Doble, B.W.; Patel, S.; Wood, G.A.; Kockeritz, L.K.; Woodgett, J.R. Functional redundancy of GSK-3alpha and GSK-3beta in Wnt/beta-catenin signaling shown by using an allelic series of embryonic stem cell lines. *Dev. Cell* **2007**, *12*, 957–971. [CrossRef] [PubMed]
44. Morin, P.J.; Sparks, A.B.; Korinek, V.; Barker, N.; Clevers, H.; Vogelstein, B.; Kinzler, K.W. Activation of beta-catenin-Tcf signaling in colon cancer by mutations in beta-catenin or APC. *Science* **1997**, *275*, 1787–1790. [CrossRef]
45. Korinek, V.; Barker, N.; Morin, P.J.; van Wichen, D.; de Weger, R.; Kinzler, K.W.; Vogelstein, B.; Clevers, H. Constitutive transcriptional activation by a beta-catenin-Tcf complex in APC-/- colon carcinoma. *Science* **1997**, *275*, 1784–1787. [CrossRef]
46. Marikawa, Y.; Elinson, R.P. beta-TrCP is a negative regulator of Wnt/beta-catenin signaling pathway and dorsal axis formation in Xenopus embryos. *Mech. Dev.* **1998**, *77*, 75–80. [CrossRef]
47. Hart, M.; Concordet, J.P.; Lassot, I.; Albert, I.; del los Santos, R.; Durand, H.; Perret, C.; Rubinfeld, B.; Margottin, F.; Benarous, R.; et al. The F-box protein beta-TrCP associates with phosphorylated beta-catenin and regulates its activity in the cell. *Curr. Biol.* **1999**, *9*, 207–210. [CrossRef]
48. Zeng, X.; Huang, H.; Tamai, K.; Zhang, X.; Harada, Y.; Yokota, C.; Almeida, K.; Wang, J.; Doble, B.; Woodgett, J.; et al. Initiation of Wnt signaling: Control of Wnt coreceptor Lrp6 phosphorylation/activation via frizzled, dishevelled and axin functions. *Development* **2008**, *135*, 367–375. [CrossRef]
49. Pan, W.; Choi, S.C.; Wang, H.; Qin, Y.; Volpicelli-Daley, L.; Swan, L.; Lucast, L.; Khoo, C.; Zhang, X.; Li, L.; et al. Wnt3a-mediated formation of phosphatidylinositol 4,5-bisphosphate regulates LRP6 phosphorylation. *Science* **2008**, *321*, 1350–1353. [CrossRef]
50. Li, V.S.; Ng, S.S.; Boersema, P.J.; Low, T.Y.; Karthaus, W.R.; Gerlach, J.P.; Mohammed, S.; Heck, A.J.; Maurice, M.M.; Mahmoudi, T.; et al. Wnt signaling through inhibition of beta-catenin degradation in an intact Axin1 complex. *Cell* **2012**, *149*, 1245–1256. [CrossRef]
51. Ji, L.; Jiang, B.; Jiang, X.; Charlat, O.; Chen, A.; Mickanin, C.; Bauer, A.; Xu, W.; Yan, X.; Cong, F. The SIAH E3 ubiquitin ligases promote Wnt/beta-catenin signaling through mediating Wnt-induced Axin degradation. *Genes Dev.* **2017**, *31*, 904–915. [CrossRef] [PubMed]
52. Callow, M.G.; Tran, H.; Phu, L.; Lau, T.; Lee, J.; Sandoval, W.N.; Liu, P.S.; Bheddah, S.; Tao, J.; Lill, J.R.; et al. Ubiquitin ligase RNF146 regulates tankyrase and Axin to promote Wnt signaling. *PLoS ONE* **2011**, *6*, e22595. [CrossRef] [PubMed]
53. Zhang, Y.; Liu, S.; Mickanin, C.; Feng, Y.; Charlat, O.; Michaud, G.A.; Schirle, M.; Shi, X.; Hild, M.; Bauer, A.; et al. RNF146 is a poly(ADP-ribose)-directed E3 ligase that regulates axin degradation and Wnt signalling. *Nat. Cell Biol.* **2011**, *13*, 623–629. [CrossRef] [PubMed]
54. DaRosa, P.A.; Klevit, R.E.; Xu, W. Structural basis for tankyrase-RNF146 interaction reveals noncanonical tankyrase-binding motifs. *Protein Sci. A Publ. Protein Soc.* **2018**, *27*, 1057–1067. [CrossRef]
55. Matsumoto, Y.; La Rose, J.; Lim, M.; Adissu, H.A.; Law, N.; Mao, X.; Cong, F.; Mera, P.; Karsenty, G.; Goltzman, D.; et al. Ubiquitin ligase RNF146 coordinates bone dynamics and energy metabolism. *J. Clin. Investig.* **2017**, *127*, 2612–2625. [CrossRef]
56. Zhu, X.; Xing, R.; Tan, R.; Dai, R.; Tao, Q. The RNF146 E3 ubiquitin ligase is required for the control of Wnt signaling and body pattern formation in Xenopus. *Mech. Dev.* **2017**, *147*, 28–36. [CrossRef]
57. Wang, Z.; Tacchelly-Benites, O.; Noble, G.P.; Johnson, M.K.; Gagne, J.P.; Poirier, G.G.; Ahmed, Y. A Context-Dependent Role for the RNF146 Ubiquitin Ligase in Wingless/Wnt Signaling in Drosophila. *Genetics* **2019**, *211*, 913–923. [CrossRef]
58. Fei, C.; He, X.; Xie, S.; Miao, H.; Zhou, Z.; Li, L. Smurf1-mediated axin ubiquitination requires Smurf1 C2 domain and is cell cycle-dependent. *J. Biol. Chem.* **2014**, *289*, 14170–14177. [CrossRef]
59. Fei, C.; Li, Z.; Li, C.; Chen, Y.; Chen, Z.; He, X.; Mao, L.; Wang, X.; Zeng, R.; Li, L. Smurf1-mediated Lys29-linked nonproteolytic polyubiquitination of axin negatively regulates Wnt/beta-catenin signaling. *Mol. Cell. Biol.* **2013**, *33*, 4095–4105. [CrossRef]
60. Kim, S.; Jho, E.H. The protein stability of Axin, a negative regulator of Wnt signaling, is regulated by Smad ubiquitination regulatory factor 2 (Smurf2). *J. Biol. Chem.* **2010**, *285*, 36420–36426. [CrossRef]

61. Lee, H.K.; Lee, E.W.; Seo, J.; Jeong, M.; Lee, S.H.; Kim, S.Y.; Jho, E.H.; Choi, C.H.; Chung, J.Y.; Song, J. Ubiquitylation and degradation of adenomatous polyposis coli by MKRN1 enhances Wnt/beta-catenin signaling. *Oncogene* **2018**, *37*, 4273–4286. [CrossRef] [PubMed]
62. Ding, Y.; Zhang, Y.; Xu, C.; Tao, Q.H.; Chen, Y.G. HECT domain-containing E3 ubiquitin ligase NEDD4L negatively regulates Wnt signaling by targeting dishevelled for proteasomal degradation. *J. Biol. Chem.* **2013**, *288*, 8289–8298. [CrossRef] [PubMed]
63. Wei, W.; Li, M.; Wang, J.; Nie, F.; Li, L. The E3 ubiquitin ligase ITCH negatively regulates canonical Wnt signaling by targeting dishevelled protein. *Mol. Cell. Biol.* **2012**, *32*, 3903–3912. [CrossRef] [PubMed]
64. Nethe, M.; de Kreuk, B.J.; Tauriello, D.V.; Anthony, E.C.; Snoek, B.; Stumpel, T.; Salinas, P.C.; Maurice, M.M.; Geerts, D.; Deelder, A.M.; et al. Rac1 acts in conjunction with Nedd4 and dishevelled-1 to promote maturation of cell-cell contacts. *J. Cell Sci.* **2012**, *125*, 3430–3442. [CrossRef]
65. Zhang, Y.; Ding, Y.; Chen, Y.G.; Tao, Q. NEDD4L regulates convergent extension movements in Xenopus embryos via Disheveled-mediated non-canonical Wnt signaling. *Dev. Biol.* **2014**, *392*, 15–25. [CrossRef]
66. Tsukiyama, T.; Fukui, A.; Terai, S.; Fujioka, Y.; Shinada, K.; Takahashi, H.; Yamaguchi, T.P.; Ohba, Y.; Hatakeyama, S. Molecular Role of RNF43 in Canonical and Noncanonical Wnt Signaling. *Mol. Cell. Biol.* **2015**, *35*, 2007–2023. [CrossRef]
67. Angers, S.; Thorpe, C.J.; Biechele, T.L.; Goldenberg, S.J.; Zheng, N.; MacCoss, M.J.; Moon, R.T. The KLHL12-Cullin-3 ubiquitin ligase negatively regulates the Wnt-beta-catenin pathway by targeting Dishevelled for degradation. *Nat. Cell Biol.* **2006**, *8*, 348–357. [CrossRef]
68. Lee, H.; Cheong, S.M.; Han, W.; Koo, Y.; Jo, S.B.; Cho, G.S.; Yang, J.S.; Kim, S.; Han, J.K. Head formation requires Dishevelled degradation that is mediated by March2 in concert with Dapper1. *Development* **2018**, *145*. [CrossRef]
69. Zhou, M.I.; Wang, H.; Foy, R.L.; Ross, J.J.; Cohen, H.T. Tumor suppressor von Hippel-Lindau (VHL) stabilization of Jade-1 protein occurs through plant homeodomains and is VHL mutation dependent. *Cancer Res.* **2004**, *64*, 1278–1286. [CrossRef]
70. Shafique, S.; Rashid, S. Structural basis for renal cancer by the dynamics of pVHL-dependent JADE1 stabilization and beta-catenin regulation. *Prog. Biophys. Mol. Biol.* **2019**, *145*, 65–77. [CrossRef]
71. Chitalia, V.C.; Foy, R.L.; Bachschmid, M.M.; Zeng, L.; Panchenko, M.V.; Zhou, M.I.; Bharti, A.; Seldin, D.C.; Lecker, S.H.; Dominguez, I.; et al. Jade-1 inhibits Wnt signalling by ubiquitylating beta-catenin and mediates Wnt pathway inhibition by pVHL. *Nat. Cell Biol.* **2008**, *10*, 1208–1216. [CrossRef] [PubMed]
72. Shivanna, S.; Harrold, I.; Shashar, M.; Meyer, R.; Kiang, C.; Francis, J.; Zhao, Q.; Feng, H.; Edelman, E.R.; Rahimi, N.; et al. The c-Cbl ubiquitin ligase regulates nuclear beta-catenin and angiogenesis by its tyrosine phosphorylation mediated through the Wnt signaling pathway. *J. Biol. Chem.* **2015**, *290*, 12537–12546. [CrossRef] [PubMed]
73. Chitalia, V.; Shivanna, S.; Martorell, J.; Meyer, R.; Edelman, E.; Rahimi, N. c-Cbl, a ubiquitin E3 ligase that targets active beta-catenin: A novel layer of Wnt signaling regulation. *J. Biol. Chem.* **2013**, *288*, 23505–23517. [CrossRef] [PubMed]
74. Flack, J.E.; Mieszczanek, J.; Novcic, N.; Bienz, M. Wnt-Dependent Inactivation of the Groucho/TLE Co-repressor by the HECT E3 Ubiquitin Ligase Hyd/UBR5. *Mol. Cell* **2017**, *67*, 181–193. [CrossRef] [PubMed]
75. Hay-Koren, A.; Caspi, M.; Zilberberg, A.; Rosin-Arbesfeld, R. The EDD E3 ubiquitin ligase ubiquitinates and up-regulates beta-catenin. *Mol. Biol. Cell* **2011**, *22*, 399–411. [CrossRef] [PubMed]
76. Liu, L.; Zhang, Y.; Wong, C.C.; Zhang, J.; Dong, Y.; Li, X.; Kang, W.; Chan, F.K.L.; Sung, J.J.Y.; Yu, J. RNF6 Promotes Colorectal Cancer by Activating the Wnt/beta-Catenin Pathway via Ubiquitination of TLE3. *Cancer Res.* **2018**, *78*, 1958–1971. [CrossRef] [PubMed]
77. Glaeser, K.; Urban, M.; Fenech, E.; Voloshanenko, O.; Kranz, D.; Lari, F.; Christianson, J.C.; Boutros, M. ERAD-dependent control of the Wnt secretory factor Evi. *EMBO J.* **2018**, *37*. [CrossRef]
78. Perrody, E.; Abrami, L.; Feldman, M.; Kunz, B.; Urbe, S.; van der Goot, F.G. Ubiquitin-dependent folding of the Wnt signaling coreceptor LRP6. *Elife* **2016**, *5*. [CrossRef]
79. Feldman, M.; van der Goot, F.G. Novel ubiquitin-dependent quality control in the endoplasmic reticulum. *Trends Cell Biol.* **2009**, *19*, 357–363. [CrossRef]

80. Abrami, L.; Kunz, B.; Iacovache, I.; van der Goot, F.G. Palmitoylation and ubiquitination regulate exit of the Wnt signaling protein LRP6 from the endoplasmic reticulum. *Proc. Natl. Acad. Sci. USA* **2008**, *105*, 5384–5389. [CrossRef]
81. Joshi, V.; Amanullah, A.; Upadhyay, A.; Mishra, R.; Kumar, A.; Mishra, A. A Decade of Boon or Burden: What Has the CHIP Ever Done for Cellular Protein Quality Control Mechanism Implicated in Neurodegeneration and Aging? *Front. Mol. Neurosci.* **2016**, *9*, 93. [CrossRef] [PubMed]
82. Bhuripanyo, K.; Wang, Y.; Liu, X.; Zhou, L.; Liu, R.; Duong, D.; Zhao, B.; Bi, Y.; Zhou, H.; Chen, G.; et al. Identifying the substrate proteins of U-box E3s E4B and CHIP by orthogonal ubiquitin transfer. *Sci. Adv.* **2018**, *4*, e1701393. [CrossRef] [PubMed]
83. Rudloff, S.; Kemler, R. Differential requirements for beta-catenin during mouse development. *Development* **2012**, *139*, 3711–3721. [CrossRef] [PubMed]
84. Wang, Y.; Guo, N.; Nathans, J. The role of Frizzled3 and Frizzled6 in neural tube closure and in the planar polarity of inner-ear sensory hair cells. *J. Neurosci.* **2006**, *26*, 2147–2156. [CrossRef] [PubMed]
85. Korinek, V.; Barker, N.; Moerer, P.; van Donselaar, E.; Huls, G.; Peters, P.J.; Clevers, H. Depletion of epithelial stem-cell compartments in the small intestine of mice lacking Tcf-4. *Nat. Genet.* **1998**, *19*, 379–383. [CrossRef] [PubMed]
86. Nakayama, K.; Hatakeyama, S.; Maruyama, S.; Kikuchi, A.; Onoe, K.; Good, R.A.; Nakayama, K.I. Impaired degradation of inhibitory subunit of NF-kappa B (I kappa B) and beta-catenin as a result of targeted disruption of the beta-TrCP1 gene. *Proc. Natl. Acad. Sci. USA* **2003**, *100*, 8752–8757. [CrossRef] [PubMed]
87. Narimatsu, M.; Bose, R.; Pye, M.; Zhang, L.; Miller, B.; Ching, P.; Sakuma, R.; Luga, V.; Roncari, L.; Attisano, L.; et al. Regulation of planar cell polarity by Smurf ubiquitin ligases. *Cell* **2009**, *137*, 295–307. [CrossRef]
88. Lee, M.S.; Han, H.J.; Han, S.Y.; Kim, I.Y.; Chae, S.; Lee, C.S.; Kim, S.E.; Yoon, S.G.; Park, J.W.; Kim, J.H.; et al. Loss of the E3 ubiquitin ligase MKRN1 represses diet-induced metabolic syndrome through AMPK activation. *Nat. Commun.* **2018**, *9*, 3404. [CrossRef]
89. Lu, C.; Thoeni, C.; Connor, A.; Kawabe, H.; Gallinger, S.; Rotin, D. Intestinal knockout of Nedd4 enhances growth of Apc(min) tumors. *Oncogene* **2016**, *35*, 5839–5849. [CrossRef]
90. Grima, B.; Lamouroux, A.; Chelot, E.; Papin, C.; Limbourg-Bouchon, B.; Rouyer, F. The F-box protein slimb controls the levels of clock proteins period and timeless. *Nature* **2002**, *420*, 178–182. [CrossRef]
91. Nakagawa, T.; Zhang, T.; Kushi, R.; Nakano, S.; Endo, T.; Nakagawa, M.; Yanagihara, N.; Zarkower, D.; Nakayama, K. Regulation of mitosis-meiosis transition by the ubiquitin ligase beta-TrCP in male germ cells. *Development* **2017**, *144*, 4137–4147. [CrossRef] [PubMed]
92. Guardavaccaro, D.; Kudo, Y.; Boulaire, J.; Barchi, M.; Busino, L.; Donzelli, M.; Margottin-Goguet, F.; Jackson, P.K.; Yamasaki, L.; Pagano, M. Control of meiotic and mitotic progression by the F box protein beta-Trcp1 in vivo. *Dev. Cell* **2003**, *4*, 799–812. [CrossRef]
93. Ohsaki, K.; Oishi, K.; Kozono, Y.; Nakayama, K.; Nakayama, K.I.; Ishida, N. The role of {beta}-TrCP1 and {beta}-TrCP2 in circadian rhythm generation by mediating degradation of clock protein PER2. *J. Biochem.* **2008**, *144*, 609–618. [CrossRef] [PubMed]
94. Kanarek, N.; Horwitz, E.; Mayan, I.; Leshets, M.; Cojocaru, G.; Davis, M.; Tsuberi, B.Z.; Pikarsky, E.; Pagano, M.; Ben-Neriah, Y. Spermatogenesis rescue in a mouse deficient for the ubiquitin ligase SCF{beta}-TrCP by single substrate depletion. *Genes Dev.* **2010**, *24*, 470–477. [CrossRef] [PubMed]
95. Kudo, Y.; Guardavaccaro, D.; Santamaria, P.G.; Koyama-Nasu, R.; Latres, E.; Bronson, R.; Yamasaki, L.; Pagano, M. Role of F-box protein betaTrcp1 in mammary gland development and tumorigenesis. *Mol. Cell. Biol.* **2004**, *24*, 8184–8194. [CrossRef] [PubMed]
96. Baguma-Nibasheka, M.; Kablar, B. Abnormal retinal development in the Btrc null mouse. *Dev. Dyn.* **2009**, *238*, 2680–2687. [CrossRef]
97. Kanarek, N.; Grivennikov, S.I.; Leshets, M.; Lasry, A.; Alkalay, I.; Horwitz, E.; Shaul, Y.D.; Stachler, M.; Voronov, E.; Apte, R.N.; et al. Critical role for IL-1beta in DNA damage-induced mucositis. *Proc. Natl. Acad. Sci. USA* **2014**, *111*, E702–E711. [CrossRef]
98. Nakagawa, T.; Araki, T.; Nakagawa, M.; Hirao, A.; Unno, M.; Nakayama, K. S6 Kinase- and beta-TrCP2-Dependent Degradation of p19Arf Is Required for Cell Proliferation. *Mol. Cell. Biol.* **2015**, *35*, 3517–3527. [CrossRef]

99. Bond, C.E.; McKeone, D.M.; Kalimutho, M.; Bettington, M.L.; Pearson, S.A.; Dumenil, T.D.; Wockner, L.F.; Burge, M.; Leggett, B.A.; Whitehall, V.L. RNF43 and ZNRF3 are commonly altered in serrated pathway colorectal tumorigenesis. *Oncotarget* **2016**, *7*, 70589–70600. [CrossRef]
100. Giannakis, M.; Hodis, E.; Jasmine Mu, X.; Yamauchi, M.; Rosenbluh, J.; Cibulskis, K.; Saksena, G.; Lawrence, M.S.; Qian, Z.R.; Nishihara, R.; et al. RNF43 is frequently mutated in colorectal and endometrial cancers. *Nat. Genet.* **2014**, *46*, 1264–1266. [CrossRef]
101. Koo, B.K.; van Es, J.H.; van den Born, M.; Clevers, H. Porcupine inhibitor suppresses paracrine Wnt-driven growth of Rnf43;Znrf3-mutant neoplasia. *Proc. Natl. Acad. Sci. USA* **2015**, *112*, 7548–7550. [CrossRef] [PubMed]
102. Basham, K.J.; Rodriguez, S.; Turcu, A.F.; Lerario, A.M.; Logan, C.Y.; Rysztak, M.R.; Gomez-Sanchez, C.E.; Breault, D.T.; Koo, B.K.; Clevers, H.; et al. A ZNRF3-dependent Wnt/beta-catenin signaling gradient is required for adrenal homeostasis. *Genes Dev.* **2019**, *33*, 209–220. [CrossRef] [PubMed]
103. Jameson, S.A.; Lin, Y.T.; Capel, B. Testis development requires the repression of Wnt4 by Fgf signaling. *Dev. Biol.* **2012**, *370*, 24–32. [CrossRef] [PubMed]
104. Harris, A.; Siggers, P.; Corrochano, S.; Warr, N.; Sagar, D.; Grimes, D.T.; Suzuki, M.; Burdine, R.D.; Cong, F.; Koo, B.K.; et al. ZNRF3 functions in mammalian sex determination by inhibiting canonical WNT signaling. *Proc. Natl. Acad. Sci. USA* **2018**, *115*, 5474–5479. [CrossRef] [PubMed]
105. Shen, J.; Yu, Z.; Li, N. The E3 ubiquitin ligase RNF146 promotes colorectal cancer by activating the Wnt/beta-catenin pathway via ubiquitination of Axin1. *Biochem. Biophys. Res. Commun.* **2018**, *503*, 991–997. [CrossRef]
106. Wei, W.; Zeve, D.; Suh, J.M.; Wang, X.; Du, Y.; Zerwekh, J.E.; Dechow, P.C.; Graff, J.M.; Wan, Y. Biphasic and dosage-dependent regulation of osteoclastogenesis by beta-catenin. *Mol. Cell. Biol.* **2011**, *31*, 4706–4719. [CrossRef]
107. Matsumoto, Y.; Larose, J.; Kent, O.A.; Lim, M.; Changoor, A.; Zhang, L.; Storozhuk, Y.; Mao, X.; Grynpas, M.D.; Cong, F.; et al. RANKL coordinates multiple osteoclastogenic pathways by regulating expression of ubiquitin ligase RNF146. *J. Clin. Investig.* **2017**, *127*, 1303–1315. [CrossRef]
108. Ueki, Y.; Tiziani, V.; Santanna, C.; Fukai, N.; Maulik, C.; Garfinkle, J.; Ninomiya, C.; doAmaral, C.; Peters, H.; Habal, M.; et al. Mutations in the gene encoding c-Abl-binding protein SH3BP2 cause cherubism. *Nat. Genet.* **2001**, *28*, 125–126. [CrossRef]
109. Levaot, N.; Voytyuk, O.; Dimitriou, I.; Sircoulomb, F.; Chandrakumar, A.; Deckert, M.; Krzyzanowski, P.M.; Scotter, A.; Gu, S.; Janmohamed, S.; et al. Loss of Tankyrase-mediated destruction of 3BP2 is the underlying pathogenic mechanism of cherubism. *Cell* **2011**, *147*, 1324–1339. [CrossRef]
110. Zou, Y.F.; Xie, C.W.; Yang, S.X.; Xiong, J.P. AMPK activators suppress breast cancer cell growth by inhibiting DVL3-facilitated Wnt/beta-catenin signaling pathway activity. *Mol. Med. Rep.* **2017**, *15*, 899–907. [CrossRef]
111. Lee, H.; Kang, R.; Bae, S.; Yoon, Y. AICAR, an activator of AMPK, inhibits adipogenesis via the WNT/beta-catenin pathway in 3T3-L1 adipocytes. *Int. J. Mol. Med.* **2011**, *28*, 65–71. [CrossRef] [PubMed]
112. Inoki, K.; Ouyang, H.; Zhu, T.; Lindvall, C.; Wang, Y.; Zhang, X.; Yang, Q.; Bennett, C.; Harada, Y.; Stankunas, K.; et al. TSC2 integrates Wnt and energy signals via a coordinated phosphorylation by AMPK and GSK3 to regulate cell growth. *Cell* **2006**, *126*, 955–968. [CrossRef] [PubMed]
113. Park, S.Y.; Kim, D.; Kee, S.H. Metformin-activated AMPK regulates beta-catenin to reduce cell proliferation in colon carcinoma RKO cells. *Oncol. Lett.* **2019**, *17*, 2695–2702. [CrossRef] [PubMed]
114. Kondo, S.; Seo, S.Y.; Yoshizaki, T.; Wakisaka, N.; Furukawa, M.; Joab, I.; Jang, K.L.; Pagano, J.S. EBV latent membrane protein 1 up-regulates hypoxia-inducible factor 1alpha through Siah1-mediated down-regulation of prolyl hydroxylases 1 and 3 in nasopharyngeal epithelial cells. *Cancer Res.* **2006**, *66*, 9870–9877. [CrossRef]
115. Dickins, R.A.; Frew, I.J.; House, C.M.; O'Bryan, M.K.; Holloway, A.J.; Haviv, I.; Traficante, N.; de Kretser, D.M.; Bowtell, D.D. The ubiquitin ligase component Siah1a is required for completion of meiosis I in male mice. *Mol. Cell. Biol.* **2002**, *22*, 2294–2303. [CrossRef]
116. Frew, I.J.; Sims, N.A.; Quinn, J.M.; Walkley, C.R.; Purton, L.E.; Bowtell, D.D.; Gillespie, M.T. Osteopenia in Siah1a mutant mice. *J. Biol. Chem.* **2004**, *279*, 29583–29588. [CrossRef]
117. Frew, I.J.; Hammond, V.E.; Dickins, R.A.; Quinn, J.M.; Walkley, C.R.; Sims, N.A.; Schnall, R.; Della, N.G.; Holloway, A.J.; Digby, M.R.; et al. Generation and analysis of Siah2 mutant mice. *Mol. Cell. Biol.* **2003**, *23*, 9150–9161. [CrossRef]

118. Scortegagna, M.; Kim, H.; Li, J.L.; Yao, H.; Brill, L.M.; Han, J.; Lau, E.; Bowtell, D.; Haddad, G.; Kaufman, R.J.; et al. Fine tuning of the UPR by the ubiquitin ligases Siah1/2. *PLoS Genet.* **2014**, *10*, e1004348. [CrossRef]
119. Wang, D.; Wang, Y.; Kong, T.; Fan, F.; Jiang, Y. Hypoxia-induced beta-catenin downregulation involves p53-dependent activation of Siah-1. *Cancer Sci.* **2011**, *102*, 1322–1328. [CrossRef]
120. Simon, M.C. Siah proteins, HIF prolyl hydroxylases, and the physiological response to hypoxia. *Cell* **2004**, *117*, 851–853. [CrossRef]
121. Gudjonsson, T.; Altmeyer, M.; Savic, V.; Toledo, L.; Dinant, C.; Grofte, M.; Bartkova, J.; Poulsen, M.; Oka, Y.; Bekker-Jensen, S.; et al. TRIP12 and UBR5 suppress spreading of chromatin ubiquitylation at damaged chromosomes. *Cell* **2012**, *150*, 697–709. [CrossRef] [PubMed]
122. Shearer, R.F.; Iconomou, M.; Watts, C.K.; Saunders, D.N. Functional Roles of the E3 Ubiquitin Ligase UBR5 in Cancer. *Mol. Cancer Res.* **2015**, *13*, 1523–1532. [CrossRef] [PubMed]
123. Saunders, D.N.; Hird, S.L.; Withington, S.L.; Dunwoodie, S.L.; Henderson, M.J.; Biben, C.; Sutherland, R.L.; Ormandy, C.J.; Watts, C.K. Edd, the murine hyperplastic disc gene, is essential for yolk sac vascularization and chorioallantoic fusion. *Mol. Cell. Biol.* **2004**, *24*, 7225–7234. [CrossRef] [PubMed]
124. Ishikawa, T.; Tamai, Y.; Zorn, A.M.; Yoshida, H.; Seldin, M.F.; Nishikawa, S.; Taketo, M.M. Mouse Wnt receptor gene Fzd5 is essential for yolk sac and placental angiogenesis. *Development* **2001**, *128*, 25–33.
125. Kinsella, E.; Dora, N.; Mellis, D.; Lettice, L.; Deveney, P.; Hill, R.; Ditzel, M. Use of a Conditional Ubr5 Mutant Allele to Investigate the Role of an N-End Rule Ubiquitin-Protein Ligase in Hedgehog Signalling and Embryonic Limb Development. *PLoS ONE* **2016**, *11*, e0157079. [CrossRef]
126. Ye, X.; Wang, L.; Shang, B.; Wang, Z.; Wei, W. NEDD4: A promising target for cancer therapy. *Curr. Cancer Drug Targets* **2014**, *14*, 549–556. [CrossRef]
127. Li, J.J.; Ferry, R.J., Jr.; Diao, S.; Xue, B.; Bahouth, S.W.; Liao, F.F. Nedd4 haploinsufficient mice display moderate insulin resistance, enhanced lipolysis, and protection against high-fat diet-induced obesity. *Endocrinology* **2015**, *156*, 1283–1291. [CrossRef]
128. Liu, Y.; Oppenheim, R.W.; Sugiura, Y.; Lin, W. Abnormal development of the neuromuscular junction in Nedd4-deficient mice. *Dev. Biol.* **2009**, *330*, 153–166. [CrossRef]
129. Kawabe, H.; Neeb, A.; Dimova, K.; Young, S.M., Jr.; Takeda, M.; Katsurabayashi, S.; Mitkovski, M.; Malakhova, O.A.; Zhang, D.E.; Umikawa, M.; et al. Regulation of Rap2A by the ubiquitin ligase Nedd4-1 controls neurite development. *Neuron* **2010**, *65*, 358–372. [CrossRef]
130. Cao, X.R.; Lill, N.L.; Boase, N.; Shi, P.P.; Croucher, D.R.; Shan, H.; Qu, J.; Sweezer, E.M.; Place, T.; Kirby, P.A.; et al. Nedd4 controls animal growth by regulating IGF-1 signaling. *Sci. Signal.* **2008**, *1*. [CrossRef]
131. Fouladkou, F.; Lu, C.; Jiang, C.; Zhou, L.; She, Y.; Walls, J.R.; Kawabe, H.; Brose, N.; Henkelman, R.M.; Huang, A.; et al. The ubiquitin ligase Nedd4-1 is required for heart development and is a suppressor of thrombospondin-1. *J. Biol. Chem.* **2010**, *285*, 6770–6780. [CrossRef] [PubMed]
132. Lee, J.H.; Jeon, S.A.; Kim, B.G.; Takeda, M.; Cho, J.J.; Kim, D.I.; Kawabe, H.; Cho, J.Y. Nedd4 Deficiency in Vascular Smooth Muscle Promotes Vascular Calcification by Stabilizing pSmad1. *J. Bone Min. Res.* **2017**, *32*, 927–938. [CrossRef] [PubMed]
133. Jeon, S.A.; Lee, J.H.; Kim, D.W.; Cho, J.Y. E3-ubiquitin ligase NEDD4 enhances bone formation by removing TGFbeta1-induced pSMAD1 in immature osteoblast. *Bone* **2018**, *116*, 248–258. [CrossRef] [PubMed]
134. Wiszniak, S.; Harvey, N.; Schwarz, Q. Cell autonomous roles of Nedd4 in craniofacial bone formation. *Dev. Biol.* **2016**, *410*, 98–107. [CrossRef] [PubMed]
135. Wiszniak, S.; Kabbara, S.; Lumb, R.; Scherer, M.; Secker, G.; Harvey, N.; Kumar, S.; Schwarz, Q. The ubiquitin ligase Nedd4 regulates craniofacial development by promoting cranial neural crest cell survival and stem-cell like properties. *Dev. Biol.* **2013**, *383*, 186–200. [CrossRef] [PubMed]
136. Yang, B.; Gay, D.L.; MacLeod, M.K.; Cao, X.; Hala, T.; Sweezer, E.M.; Kappler, J.; Marrack, P.; Oliver, P.M. Nedd4 augments the adaptive immune response by promoting ubiquitin-mediated degradation of Cbl-b in activated T cells. *Nat. Immunol.* **2008**, *9*, 1356–1363. [CrossRef] [PubMed]
137. Guo, H.; Qiao, G.; Ying, H.; Li, Z.; Zhao, Y.; Liang, Y.; Yang, L.; Lipkowitz, S.; Penninger, J.M.; Langdon, W.Y.; et al. E3 ubiquitin ligase Cbl-b regulates Pten via Nedd4 in T cells independently of its ubiquitin ligase activity. *Cell Rep.* **2012**, *1*, 472–482. [CrossRef]
138. Russo, C.J.; Melista, E.; Cui, J.; DeStefano, A.L.; Bakris, G.L.; Manolis, A.J.; Gavras, H.; Baldwin, C.T. Association of NEDD4L ubiquitin ligase with essential hypertension. *Hypertension* **2005**, *46*, 488–491. [CrossRef]

139. Yanpallewar, S.; Wang, T.; Koh, D.C.; Quarta, E.; Fulgenzi, G.; Tessarollo, L. Nedd4-2 haploinsufficiency causes hyperactivity and increased sensitivity to inflammatory stimuli. *Sci. Rep.* **2016**, *6*, 32957. [CrossRef]
140. Harvey, K.F.; Dinudom, A.; Cook, D.I.; Kumar, S. The Nedd4-like protein KIAA0439 is a potential regulator of the epithelial sodium channel. *J. Biol. Chem.* **2001**, *276*, 8597–8601. [CrossRef]
141. Zhou, R.; Patel, S.V.; Snyder, P.M. Nedd4-2 catalyzes ubiquitination and degradation of cell surface ENaC. *J. Biol. Chem.* **2007**, *282*, 20207–20212. [CrossRef] [PubMed]
142. Hanukoglu, I.; Hanukoglu, A. Epithelial sodium channel (ENaC) family: Phylogeny, structure-function, tissue distribution, and associated inherited diseases. *Gene* **2016**, *579*, 95–132. [CrossRef] [PubMed]
143. Sun, C.; Hummler, E.; Hill, D.L. Selective Deletion of Sodium Salt Taste during Development Leads to Expanded Terminal Fields of Gustatory Nerves in the Adult Mouse Nucleus of the Solitary Tract. *J. Neurosci. Off. J. Soc. Neurosci.* **2017**, *37*, 660–672. [CrossRef] [PubMed]
144. Shi, P.P.; Cao, X.R.; Sweezer, E.M.; Kinney, T.S.; Williams, N.R.; Husted, R.F.; Nair, R.; Weiss, R.M.; Williamson, R.A.; Sigmund, C.D.; et al. Salt-sensitive hypertension and cardiac hypertrophy in mice deficient in the ubiquitin ligase Nedd4-2. *Am. J. Physiol. Ren. Physiol.* **2008**, *295*, F462–F470. [CrossRef] [PubMed]
145. Boase, N.A.; Rychkov, G.Y.; Townley, S.L.; Dinudom, A.; Candi, E.; Voss, A.K.; Tsoutsman, T.; Semsarian, C.; Melino, G.; Koentgen, F.; et al. Respiratory distress and perinatal lethality in Nedd4-2-deficient mice. *Nat. Commun.* **2011**, *2*, 287. [CrossRef] [PubMed]
146. Henshall, T.L.; Manning, J.A.; Alfassy, O.S.; Goel, P.; Boase, N.A.; Kawabe, H.; Kumar, S. Deletion of Nedd4-2 results in progressive kidney disease in mice. *Cell Death Differ.* **2017**, *24*, 2150–2160. [CrossRef] [PubMed]
147. Yip, K.H.; Kolesnikoff, N.; Hauschild, N.; Biggs, L.; Lopez, A.F.; Galli, S.J.; Kumar, S.; Grimbaldeston, M.A. The Nedd4-2/Ndfip1 axis is a negative regulator of IgE-mediated mast cell activation. *Nat. Commun.* **2016**, *7*, 13198. [CrossRef]
148. Infante, P.; Lospinoso Severini, L.; Bernardi, F.; Bufalieri, F.; Di Marcotullio, L. Targeting Hedgehog Signalling through the Ubiquitylation Process: The Multiple Roles of the HECT-E3 Ligase Itch. *Cells* **2019**, *8*. [CrossRef]
149. Liu, Y.C. The E3 ubiquitin ligase Itch in T cell activation, differentiation, and tolerance. *Semin. Immunol.* **2007**, *19*, 197–205. [CrossRef]
150. Gao, M.; Labuda, T.; Xia, Y.; Gallagher, E.; Fang, D.; Liu, Y.C.; Karin, M. Jun turnover is controlled through JNK-dependent phosphorylation of the E3 ligase Itch. *Science* **2004**, *306*, 271–275. [CrossRef]
151. Lohr, N.J.; Molleston, J.P.; Strauss, K.A.; Torres-Martinez, W.; Sherman, E.A.; Squires, R.H.; Rider, N.L.; Chikwava, K.R.; Cummings, O.W.; Morton, D.H.; et al. Human ITCH E3 ubiquitin ligase deficiency causes syndromic multisystem autoimmune disease. *Am. J. Hum. Genet.* **2010**, *86*, 447–453. [CrossRef]
152. Perry, W.L.; Hustad, C.M.; Swing, D.A.; O'Sullivan, T.N.; Jenkins, N.A.; Copeland, N.G. The itchy locus encodes a novel ubiquitin protein ligase that is disrupted in a18H mice. *Nat. Genet.* **1998**, *18*, 143–146. [CrossRef] [PubMed]
153. Hustad, C.M.; Perry, W.L.; Siracusa, L.D.; Rasberry, C.; Cobb, L.; Cattanach, B.M.; Kovatch, R.; Copeland, N.G.; Jenkins, N.A. Molecular genetic characterization of six recessive viable alleles of the mouse agouti locus. *Genetics* **1995**, *140*, 255–265. [PubMed]
154. Fang, D.; Elly, C.; Gao, B.; Fang, N.; Altman, Y.; Joazeiro, C.; Hunter, T.; Copeland, N.; Jenkins, N.; Liu, Y.C. Dysregulation of T lymphocyte function in itchy mice: A role for Itch in TH2 differentiation. *Nat. Immunol.* **2002**, *3*, 281–287. [CrossRef] [PubMed]
155. Jin, H.S.; Park, Y.; Elly, C.; Liu, Y.C. Itch expression by Treg cells controls Th2 inflammatory responses. *J. Clin. Investig.* **2013**, *123*, 4923–4934. [CrossRef] [PubMed]
156. Xiao, N.; Eto, D.; Elly, C.; Peng, G.; Crotty, S.; Liu, Y.C. The E3 ubiquitin ligase Itch is required for the differentiation of follicular helper T cells. *Nat. Immunol.* **2014**, *15*, 657–666. [CrossRef]
157. Huang, H.; Jeon, M.S.; Liao, L.; Yang, C.; Elly, C.; Yates, J.R., 3rd; Liu, Y.C. K33-linked polyubiquitination of T cell receptor-zeta regulates proteolysis-independent T cell signaling. *Immunity* **2010**, *33*, 60–70. [CrossRef]
158. Giamboi-Miraglia, A.; Cianfarani, F.; Cattani, C.; Lena, A.M.; Serra, V.; Campione, E.; Terrinoni, A.; Zambruno, G.; Odorisio, T.; Di Daniele, N.; et al. The E3 ligase Itch knockout mice show hyperproliferation and wound healing alteration. *FEBS J* **2015**, *282*, 4435–4449. [CrossRef]
159. Stermer, A.R.; Myers, J.L.; Murphy, C.J.; Di Bona, K.R.; Matesic, L.; Richburg, J.H. Female mice with loss-of-function ITCH display an altered reproductive phenotype. *Exp. Biol. Med. (Maywood)* **2016**, *241*, 367–374. [CrossRef]

160. Marino, A.; Menghini, R.; Fabrizi, M.; Casagrande, V.; Mavilio, M.; Stoehr, R.; Candi, E.; Mauriello, A.; Moreno-Navarrete, J.M.; Gomez-Serrano, M.; et al. ITCH deficiency protects from diet-induced obesity. *Diabetes* **2014**, *63*, 550–561. [CrossRef]
161. Chang, L.; Kamata, H.; Solinas, G.; Luo, J.L.; Maeda, S.; Venuprasad, K.; Liu, Y.C.; Karin, M. The E3 ubiquitin ligase itch couples JNK activation to TNFalpha-induced cell death by inducing c-FLIP(L) turnover. *Cell* **2006**, *124*, 601–613. [CrossRef] [PubMed]
162. Rathinam, C.; Matesic, L.E.; Flavell, R.A. The E3 ligase Itch is a negative regulator of the homeostasis and function of hematopoietic stem cells. *Nat. Immunol.* **2011**, *12*, 399–407. [CrossRef] [PubMed]
163. Thien, C.B.; Langdon, W.Y. c-Cbl and Cbl-b ubiquitin ligases: Substrate diversity and the negative regulation of signalling responses. *Biochem. J.* **2005**, *391*, 153–166. [CrossRef] [PubMed]
164. Mohapatra, B.; Ahmad, G.; Nadeau, S.; Zutshi, N.; An, W.; Scheffe, S.; Dong, L.; Feng, D.; Goetz, B.; Arya, P.; et al. Protein tyrosine kinase regulation by ubiquitination: Critical roles of Cbl-family ubiquitin ligases. *Biochim. Biophys. Acta* **2013**, *1833*, 122–139. [CrossRef] [PubMed]
165. Tanaka, S.; Neff, L.; Baron, R.; Levy, J.B. Tyrosine phosphorylation and translocation of the c-cbl protein after activation of tyrosine kinase signaling pathways. *J. Biol. Chem.* **1995**, *270*, 14347–14351. [CrossRef] [PubMed]
166. Naramura, M.; Kole, H.K.; Hu, R.J.; Gu, H. Altered thymic positive selection and intracellular signals in Cbl-deficient mice. *Proc. Natl. Acad. Sci. USA* **1998**, *95*, 15547–15552. [CrossRef] [PubMed]
167. Murphy, M.A.; Schnall, R.G.; Venter, D.J.; Barnett, L.; Bertoncello, I.; Thien, C.B.; Langdon, W.Y.; Bowtell, D.D. Tissue hyperplasia and enhanced T-cell signalling via ZAP-70 in c-Cbl-deficient mice. *Mol. Cell. Biol.* **1998**, *18*, 4872–4882. [CrossRef]
168. Naramura, M.; Jang, I.K.; Kole, H.; Huang, F.; Haines, D.; Gu, H. c-Cbl and Cbl-b regulate T cell responsiveness by promoting ligand-induced TCR down-modulation. *Nat. Immunol.* **2002**, *3*, 1192–1199. [CrossRef]
169. Bachmaier, K.; Krawczyk, C.; Kozieradzki, I.; Kong, Y.Y.; Sasaki, T.; Oliveira-dos-Santos, A.; Mariathasan, S.; Bouchard, D.; Wakeham, A.; Itie, A.; et al. Negative regulation of lymphocyte activation and autoimmunity by the molecular adaptor Cbl-b. *Nature* **2000**, *403*, 211–216. [CrossRef]
170. Wang, H.Y.; Altman, Y.; Fang, D.; Elly, C.; Dai, Y.; Shao, Y.; Liu, Y.C. Cbl promotes ubiquitination of the T cell receptor zeta through an adaptor function of Zap-70. *J. Biol. Chem.* **2001**, *276*, 26004–26011. [CrossRef]
171. D'Oro, U.; Munitic, I.; Chacko, G.; Karpova, T.; McNally, J.; Ashwell, J.D. Regulation of constitutive TCR internalization by the zeta-chain. *J. Immunol.* **2002**, *169*, 6269–6278. [CrossRef] [PubMed]
172. Lutz-Nicoladoni, C.; Wolf, D.; Sopper, S. Modulation of Immune Cell Functions by the E3 Ligase Cbl-b. *Front. Oncol.* **2015**, *5*, 58. [CrossRef] [PubMed]
173. Adams, C.O.; Housley, W.J.; Bhowmick, S.; Cone, R.E.; Rajan, T.V.; Forouhar, F.; Clark, R.B. Cbl-b(-/-) T cells demonstrate in vivo resistance to regulatory T cells but a context-dependent resistance to TGF-beta. *J. Immunol.* **2010**, *185*, 2051–2058. [CrossRef] [PubMed]
174. Chiusaroli, R.; Sanjay, A.; Henriksen, K.; Engsig, M.T.; Horne, W.C.; Gu, H.; Baron, R. Deletion of the gene encoding c-Cbl alters the ability of osteoclasts to migrate, delaying resorption and ossification of cartilage during the development of long bones. *Dev. Biol.* **2003**, *261*, 537–547. [CrossRef]
175. Molero, J.C.; Jensen, T.E.; Withers, P.C.; Couzens, M.; Herzog, H.; Thien, C.B.; Langdon, W.Y.; Walder, K.; Murphy, M.A.; Bowtell, D.D.; et al. c-Cbl-deficient mice have reduced adiposity, higher energy expenditure, and improved peripheral insulin action. *J. Clin. Investig.* **2004**, *114*, 1326–1333. [CrossRef]
176. Li, X.; Gadzinsky, A.; Gong, L.; Tong, H.; Calderon, V.; Li, Y.; Kitamura, D.; Klein, U.; Langdon, W.Y.; Hou, F.; et al. Cbl Ubiquitin Ligases Control B Cell Exit from the Germinal-Center Reaction. *Immunity* **2018**, *48*, 530–541.e536. [CrossRef]
177. Gustin, S.E.; Thien, C.B.; Langdon, W.Y. Cbl-b is a negative regulator of inflammatory cytokines produced by IgE-activated mast cells. *J. Immunol.* **2006**, *177*, 5980–5989. [CrossRef]
178. Naramura, M.; Nandwani, N.; Gu, H.; Band, V.; Band, H. Rapidly fatal myeloproliferative disorders in mice with deletion of Casitas B-cell lymphoma (Cbl) and Cbl-b in hematopoietic stem cells. *Proc. Natl. Acad. Sci. USA* **2010**, *107*, 16274–16279. [CrossRef]
179. Mohapatra, B.; Zutshi, N.; An, W.; Goetz, B.; Arya, P.; Bielecki, T.A.; Mushtaq, I.; Storck, M.D.; Meza, J.L.; Band, V.; et al. An essential role of CBL and CBL-B ubiquitin ligases in mammary stem cell maintenance. *Development* **2017**, *144*, 1072–1086. [CrossRef]
180. Meng, X.M.; Nikolic-Paterson, D.J.; Lan, H.Y. TGF-beta: The master regulator of fibrosis. *Nat. Rev. Nephrol.* **2016**, *12*, 325–338. [CrossRef]

181. Taipale, J.; Miyazono, K.; Heldin, C.H.; Keski-Oja, J. Latent transforming growth factor-beta 1 associates to fibroblast extracellular matrix via latent TGF-beta binding protein. *J. Cell Biol.* **1994**, *124*, 171–181. [CrossRef] [PubMed]
182. Massague, J. TGFbeta signalling in context. *Nat. Rev. Mol. Cell Biol.* **2012**, *13*, 616–630. [CrossRef] [PubMed]
183. Itoh, F.; Divecha, N.; Brocks, L.; Oomen, L.; Janssen, H.; Calafat, J.; Itoh, S.; Dijke Pt, P. The FYVE domain in Smad anchor for receptor activation (SARA) is sufficient for localization of SARA in early endosomes and regulates TGF-beta/Smad signalling. *Genes Cells Devoted Mol. Cell. Mech.* **2002**, *7*, 321–331. [CrossRef]
184. Miura, S.; Takeshita, T.; Asao, H.; Kimura, Y.; Murata, K.; Sasaki, Y.; Hanai, J.I.; Beppu, H.; Tsukazaki, T.; Wrana, J.L.; et al. Hgs (Hrs), a FYVE domain protein, is involved in Smad signaling through cooperation with SARA. *Mol. Cell. Biol.* **2000**, *20*, 9346–9355. [CrossRef]
185. Massague, J.; Seoane, J.; Wotton, D. Smad transcription factors. *Genes Dev.* **2005**, *19*, 2783–2810. [CrossRef]
186. Janknecht, R.; Wells, N.J.; Hunter, T. TGF-beta-stimulated cooperation of smad proteins with the coactivators CBP/p300. *Genes Dev.* **1998**, *12*, 2114–2119. [CrossRef]
187. Pei, D.; Shu, X.; Gassama-Diagne, A.; Thiery, J.P. Mesenchymal-epithelial transition in development and reprogramming. *Nat. Cell Biol.* **2019**, *21*, 44–53. [CrossRef]
188. Moustakas, A.; Kardassis, D. Regulation of the human p21/WAF1/Cip1 promoter in hepatic cells by functional interactions between Sp1 and Smad family members. *Proc. Natl. Acad. Sci. USA* **1998**, *95*, 6733–6738. [CrossRef]
189. Nakao, A.; Afrakhte, M.; Moren, A.; Nakayama, T.; Christian, J.L.; Heuchel, R.; Itoh, S.; Kawabata, M.; Heldin, N.E.; Heldin, C.H.; et al. Identification of Smad7, a TGFbeta-inducible antagonist of TGF-beta signalling. *Nature* **1997**, *389*, 631–635. [CrossRef]
190. Chong, P.A.; Lin, H.; Wrana, J.L.; Forman-Kay, J.D. An expanded WW domain recognition motif revealed by the interaction between Smad7 and the E3 ubiquitin ligase Smurf2. *J. Biol. Chem.* **2006**, *281*, 17069–17075. [CrossRef]
191. Kavsak, P.; Rasmussen, R.K.; Causing, C.G.; Bonni, S.; Zhu, H.; Thomsen, G.H.; Wrana, J.L. Smad7 binds to Smurf2 to form an E3 ubiquitin ligase that targets the TGF beta receptor for degradation. *Mol. Cell* **2000**, *6*, 1365–1375. [CrossRef]
192. Zhou, F.; Li, F.; Xie, F.; Zhang, Z.; Huang, H.; Zhang, L. TRAF4 mediates activation of TGF-beta signaling and is a biomarker for oncogenesis in breast cancer. *Sci. China Life Sci.* **2014**, *57*, 1172–1176. [CrossRef] [PubMed]
193. Wang, X.; Jin, C.; Tang, Y.; Tang, L.Y.; Zhang, Y.E. Ubiquitination of tumor necrosis factor receptor-associated factor 4 (TRAF4) by Smad ubiquitination regulatory factor 1 (Smurf1) regulates motility of breast epithelial and cancer cells. *J. Biol. Chem.* **2013**, *288*, 21784–21792. [CrossRef] [PubMed]
194. Zhang, L.; Zhou, F.; Garcia de Vinuesa, A.; de Kruijf, E.M.; Mesker, W.E.; Hui, L.; Drabsch, Y.; Li, Y.; Bauer, A.; Rousseau, A.; et al. TRAF4 promotes TGF-beta receptor signaling and drives breast cancer metastasis. *Mol. Cell* **2013**, *51*, 559–572. [CrossRef] [PubMed]
195. Zhang, Y.; Chang, C.; Gehling, D.J.; Hemmati-Brivanlou, A.; Derynck, R. Regulation of Smad degradation and activity by Smurf2, an E3 ubiquitin ligase. *Proc. Natl. Acad. Sci. USA* **2001**, *98*, 974–979. [CrossRef] [PubMed]
196. Tang, L.Y.; Yamashita, M.; Coussens, N.P.; Tang, Y.; Wang, X.; Li, C.; Deng, C.X.; Cheng, S.Y.; Zhang, Y.E. Ablation of Smurf2 reveals an inhibition in TGF-beta signalling through multiple mono-ubiquitination of Smad3. *EMBO J.* **2011**, *30*, 4777–4789. [CrossRef]
197. Bonni, S.; Wang, H.R.; Causing, C.G.; Kavsak, P.; Stroschein, S.L.; Luo, K.; Wrana, J.L. TGF-beta induces assembly of a Smad2-Smurf2 ubiquitin ligase complex that targets SnoN for degradation. *Nat. Cell Biol.* **2001**, *3*, 587–595. [CrossRef]
198. Alarcon, C.; Zaromytidou, A.I.; Xi, Q.; Gao, S.; Yu, J.; Fujisawa, S.; Barlas, A.; Miller, A.N.; Manova-Todorova, K.; Macias, M.J.; et al. Nuclear CDKs drive Smad transcriptional activation and turnover in BMP and TGF-beta pathways. *Cell* **2009**, *139*, 757–769. [CrossRef]
199. Aragon, E.; Goerner, N.; Zaromytidou, A.I.; Xi, Q.; Escobedo, A.; Massague, J.; Macias, M.J. A Smad action turnover switch operated by WW domain readers of a phosphoserine code. *Genes Dev.* **2011**, *25*, 1275–1288. [CrossRef]
200. Bai, Y.; Yang, C.; Hu, K.; Elly, C.; Liu, Y.C. Itch E3 ligase-mediated regulation of TGF-beta signaling by modulating smad2 phosphorylation. *Mol. Cell* **2004**, *15*, 825–831. [CrossRef]

201. Park, S.H.; Jung, E.H.; Kim, G.Y.; Kim, B.C.; Lim, J.H.; Woo, C.H. Itch E3 ubiquitin ligase positively regulates TGF-beta signaling to EMT via Smad7 ubiquitination. *Mol. Cells* **2015**, *38*, 20–25. [CrossRef] [PubMed]
202. Pefani, D.E.; Pankova, D.; Abraham, A.G.; Grawenda, A.M.; Vlahov, N.; Scrace, S.; O'Neill, E. TGF-beta Targets the Hippo Pathway Scaffold RASSF1A to Facilitate YAP/SMAD2 Nuclear Translocation. *Mol. Cell* **2016**, *63*, 156–166. [CrossRef] [PubMed]
203. Koinuma, D.; Shinozaki, M.; Komuro, A.; Goto, K.; Saitoh, M.; Hanyu, A.; Ebina, M.; Nukiwa, T.; Miyazawa, K.; Imamura, T.; et al. Arkadia amplifies TGF-beta superfamily signalling through degradation of Smad7. *EMBO J.* **2003**, *22*, 6458–6470. [CrossRef] [PubMed]
204. Liu, F.Y.; Li, X.Z.; Peng, Y.M.; Liu, H.; Liu, Y.H. Arkadia-Smad7-mediated positive regulation of TGF-beta signaling in a rat model of tubulointerstitial fibrosis. *Am. J. Nephrol.* **2007**, *27*, 176–183. [CrossRef]
205. Liu, W.; Rui, H.; Wang, J.; Lin, S.; He, Y.; Chen, M.; Li, Q.; Ye, Z.; Zhang, S.; Chan, S.C.; et al. Axin is a scaffold protein in TGF-beta signaling that promotes degradation of Smad7 by Arkadia. *EMBO J.* **2006**, *25*, 1646–1658. [CrossRef]
206. Zhang, L.; Huang, H.; Zhou, F.; Schimmel, J.; Pardo, C.G.; Zhang, T.; Barakat, T.S.; Sheppard, K.A.; Mickanin, C.; Porter, J.A.; et al. RNF12 controls embryonic stem cell fate and morphogenesis in zebrafish embryos by targeting Smad7 for degradation. *Mol. Cell* **2012**, *46*, 650–661. [CrossRef]
207. Nagano, Y.; Mavrakis, K.J.; Lee, K.L.; Fujii, T.; Koinuma, D.; Sase, H.; Yuki, K.; Isogaya, K.; Saitoh, M.; Imamura, T.; et al. Arkadia induces degradation of SnoN and c-Ski to enhance transforming growth factor-beta signaling. *J. Biol. Chem.* **2007**, *282*, 20492–20501. [CrossRef]
208. Inoue, Y.; Imamura, T. Regulation of TGF-beta family signaling by E3 ubiquitin ligases. *Cancer Sci.* **2008**, *99*, 2107–2112. [CrossRef]
209. Le Scolan, E.; Zhu, Q.; Wang, L.; Bandyopadhyay, A.; Javelaud, D.; Mauviel, A.; Sun, L.; Luo, K. Transforming growth factor-beta suppresses the ability of Ski to inhibit tumor metastasis by inducing its degradation. *Cancer Res.* **2008**, *68*, 3277–3285. [CrossRef]
210. Huang, Y.; Yang, Y.; Gao, R.; Yang, X.; Yan, X.; Wang, C.; Jiang, S.; Yu, L. RLIM interacts with Smurf2 and promotes TGF-beta induced U2OS cell migration. *Biochem. Biophys. Res. Commun.* **2011**, *414*, 181–185. [CrossRef]
211. Gruber, T.; Hinterleitner, R.; Hermann-Kleiter, N.; Meisel, M.; Kleiter, I.; Wang, C.M.; Viola, A.; Pfeifhofer-Obermair, C.; Baier, G. Cbl-b mediates TGFbeta sensitivity by downregulating inhibitory SMAD7 in primary T cells. *J. Mol. Cell Biol.* **2013**, *5*, 358–368. [CrossRef] [PubMed]
212. Xie, F.; Jin, K.; Shao, L.; Fan, Y.; Tu, Y.; Li, Y.; Yang, B.; van Dam, H.; Ten Dijke, P.; Weng, H.; et al. FAF1 phosphorylation by AKT accumulates TGF-beta type II receptor and drives breast cancer metastasis. *Nat. Commun.* **2017**, *8*, 15021. [CrossRef] [PubMed]
213. He, W.; Dorn, D.C.; Erdjument-Bromage, H.; Tempst, P.; Moore, M.A.; Massague, J. Hematopoiesis controlled by distinct TIF1gamma and Smad4 branches of the TGFbeta pathway. *Cell* **2006**, *125*, 929–941. [CrossRef] [PubMed]
214. Morsut, L.; Yan, K.P.; Enzo, E.; Aragona, M.; Soligo, S.M.; Wendling, O.; Mark, M.; Khetchoumian, K.; Bressan, G.; Chambon, P.; et al. Negative control of Smad activity by ectodermin/Tif1gamma patterns the mammalian embryo. *Development* **2010**, *137*, 2571–2578. [CrossRef] [PubMed]
215. Xi, Q.; Wang, Z.; Zaromytidou, A.I.; Zhang, X.H.; Chow-Tsang, L.F.; Liu, J.X.; Kim, H.; Barlas, A.; Manova-Todorova, K.; Kaartinen, V.; et al. A poised chromatin platform for TGF-beta access to master regulators. *Cell* **2011**, *147*, 1511–1524. [CrossRef] [PubMed]
216. Agricola, E.; Randall, R.A.; Gaarenstroom, T.; Dupont, S.; Hill, C.S. Recruitment of TIF1gamma to chromatin via its PHD finger-bromodomain activates its ubiquitin ligase and transcriptional repressor activities. *Mol. Cell* **2011**, *43*, 85–96. [CrossRef] [PubMed]
217. Tracy Cai, X.; Li, H.; Safyan, A.; Gawlik, J.; Pyrowolakis, G.; Jasper, H. AWD regulates timed activation of BMP signaling in intestinal stem cells to maintain tissue homeostasis. *Nat. Commun.* **2019**, *10*, 2988. [CrossRef]
218. McCabe, B.D.; Hom, S.; Aberle, H.; Fetter, R.D.; Marques, G.; Haerry, T.E.; Wan, H.; O'Connor, M.B.; Goodman, C.S.; Haghighi, A.P. Highwire regulates presynaptic BMP signaling essential for synaptic growth. *Neuron* **2004**, *41*, 891–905. [CrossRef]

219. Liang, M.; Liang, Y.Y.; Wrighton, K.; Ungermannova, D.; Wang, X.P.; Brunicardi, F.C.; Liu, X.; Feng, X.H.; Lin, X. Ubiquitination and proteolysis of cancer-derived Smad4 mutants by SCFSkp2. *Mol. Cell. Biol.* **2004**, *24*, 7524–7537. [CrossRef]
220. Yang, X.; Li, C.; Xu, X.; Deng, C. The tumor suppressor SMAD4/DPC4 is essential for epiblast proliferation and mesoderm induction in mice. *Proc. Natl. Acad. Sci. USA* **1998**, *95*, 3667–3672. [CrossRef]
221. Shull, M.M.; Ormsby, I.; Kier, A.B.; Pawlowski, S.; Diebold, R.J.; Yin, M.; Allen, R.; Sidman, C.; Proetzel, G.; Calvin, D.; et al. Targeted disruption of the mouse transforming growth factor-beta 1 gene results in multifocal inflammatory disease. *Nature* **1992**, *359*, 693–699. [CrossRef] [PubMed]
222. Mavrakis, K.J.; Andrew, R.L.; Lee, K.L.; Petropoulou, C.; Dixon, J.E.; Navaratnam, N.; Norris, D.P.; Episkopou, V. Arkadia enhances Nodal/TGF-beta signaling by coupling phospho-Smad2/3 activity and turnover. *PLoS Biol.* **2007**, *5*, e67. [CrossRef] [PubMed]
223. Yamashita, M.; Ying, S.X.; Zhang, G.M.; Li, C.; Cheng, S.Y.; Deng, C.X.; Zhang, Y.E. Ubiquitin ligase Smurf1 controls osteoblast activity and bone homeostasis by targeting MEKK2 for degradation. *Cell* **2005**, *121*, 101–113. [CrossRef] [PubMed]
224. Ramkumar, C.; Kong, Y.; Trabucco, S.E.; Gerstein, R.M.; Zhang, H. Smurf2 regulates hematopoietic stem cell self-renewal and aging. *Aging Cell* **2014**, *13*, 478–486. [CrossRef]
225. Zhao, L.; Huang, J.; Guo, R.; Wang, Y.; Chen, D.; Xing, L. Smurf1 inhibits mesenchymal stem cell proliferation and differentiation into osteoblasts through JunB degradation. *J. Bone Min. Res.* **2010**, *25*, 1246–1256. [CrossRef]
226. Guo, R.; Yamashita, M.; Zhang, Q.; Zhou, Q.; Chen, D.; Reynolds, D.G.; Awad, H.A.; Yanoso, L.; Zhao, L.; Schwarz, E.M.; et al. Ubiquitin ligase Smurf1 mediates tumor necrosis factor-induced systemic bone loss by promoting proteasomal degradation of bone morphogenetic signaling proteins. *J. Biol. Chem.* **2008**, *283*, 23084–23092. [CrossRef]
227. Zhu, K.; Tang, Y.; Xu, X.; Dang, H.; Tang, L.Y.; Wang, X.; Wang, X.W.; Zhang, Y.E. Non-proteolytic ubiquitin modification of PPARgamma by Smurf1 protects the liver from steatosis. *PLoS Biol.* **2018**, *16*, e3000091. [CrossRef]
228. Ramkumar, C.; Kong, Y.; Cui, H.; Hao, S.; Jones, S.N.; Gerstein, R.M.; Zhang, H. Smurf2 regulates the senescence response and suppresses tumorigenesis in mice. *Cancer Res.* **2012**, *72*, 2714–2719. [CrossRef]
229. Ramkumar, C.; Cui, H.; Kong, Y.; Jones, S.N.; Gerstein, R.M.; Zhang, H. Smurf2 suppresses B-cell proliferation and lymphomagenesis by mediating ubiquitination and degradation of YY1. *Nat. Commun.* **2013**, *4*, 2598. [CrossRef]
230. Sriramachandran, A.M.; Meyer-Teschendorf, K.; Pabst, S.; Ulrich, H.D.; Gehring, N.H.; Hofmann, K.; Praefcke, G.J.K.; Dohmen, R.J. Arkadia/RNF111 is a SUMO-targeted ubiquitin ligase with preference for substrates marked with SUMO1-capped SUMO2/3 chain. *Nat. Commun.* **2019**, *10*, 3678. [CrossRef]
231. Sharma, V.; Antonacopoulou, A.G.; Tanaka, S.; Panoutsopoulos, A.A.; Bravou, V.; Kalofonos, H.P.; Episkopou, V. Enhancement of TGF-beta signaling responses by the E3 ubiquitin ligase Arkadia provides tumor suppression in colorectal cancer. *Cancer Res.* **2011**, *71*, 6438–6449. [CrossRef] [PubMed]
232. Episkopou, V.; Arkell, R.; Timmons, P.M.; Walsh, J.J.; Andrew, R.L.; Swan, D. Induction of the mammalian node requires Arkadia function in the extraembryonic lineages. *Nature* **2001**, *410*, 825–830. [CrossRef] [PubMed]
233. Carrano, A.C.; Eytan, E.; Hershko, A.; Pagano, M. SKP2 is required for ubiquitin-mediated degradation of the CDK inhibitor p27. *Nat. Cell. Biol.* **1999**, *1*, 193–199. [CrossRef] [PubMed]
234. Tsvetkov, L.M.; Yeh, K.H.; Lee, S.J.; Sun, H.; Zhang, H. p27(Kip1) ubiquitination and degradation is regulated by the SCF(Skp2) complex through phosphorylated Thr187 in p27. *Curr. Biol.* **1999**, *9*, 661–664. [CrossRef]
235. Ganoth, D.; Bornstein, G.; Ko, T.K.; Larsen, B.; Tyers, M.; Pagano, M.; Hershko, A. The cell-cycle regulatory protein Cks1 is required for SCF(Skp2)-mediated ubiquitinylation of p27. *Nat. Cell. Biol.* **2001**, *3*, 321–324. [CrossRef] [PubMed]
236. Nakayama, K.; Nagahama, H.; Minamishima, Y.A.; Matsumoto, M.; Nakamichi, I.; Kitagawa, K.; Shirane, M.; Tsunematsu, R.; Tsukiyama, T.; Ishida, N.; et al. Targeted disruption of Skp2 results in accumulation of cyclin E and p27(Kip1), polyploidy and centrosome overduplication. *EMBO J.* **2000**, *19*, 2069–2081. [CrossRef] [PubMed]
237. Kossatz, U.; Dietrich, N.; Zender, L.; Buer, J.; Manns, M.P.; Malek, N.P. Skp2-dependent degradation of p27kip1 is essential for cell cycle progression. *Genes Dev.* **2004**, *18*, 2602–2607. [CrossRef]

238. Minamishima, Y.A.; Nakayama, K.; Nakayama, K. Recovery of liver mass without proliferation of hepatocytes after partial hepatectomy in Skp2-deficient mice. *Cancer Res.* **2002**, *62*, 995–999.
239. Yoshida, K.; Nakayama, K.; Nagahama, H.; Harada, T.; Harada, C.; Imaki, J.; Matsuda, A.; Yamamoto, K.; Ito, M.; Ohno, S.; et al. Involvement of p27(KIP1) degradation by Skp2 in the regulation of proliferation in response to wounding of corneal epithelium. *Investig. Ophthalmol. Vis. Sci.* **2002**, *43*, 364–370.
240. Ge, Z.; Guo, X.; Li, J.; Hartman, M.; Kawasawa, Y.I.; Dovat, S.; Song, C. Clinical significance of high c-MYC and low MYCBP2 expression and their association with Ikaros dysfunction in adult acute lymphoblastic leukemia. *Oncotarget* **2015**, *6*, 42300–42311. [CrossRef]
241. Lewcock, J.W.; Genoud, N.; Lettieri, K.; Pfaff, S.L. The ubiquitin ligase Phr1 regulates axon outgrowth through modulation of microtubule dynamics. *Neuron* **2007**, *56*, 604–620. [CrossRef] [PubMed]
242. Bloom, A.J.; Miller, B.R.; Sanes, J.R.; DiAntonio, A. The requirement for Phr1 in CNS axon tract formation reveals the corticostriatal boundary as a choice point for cortical axons. *Genes Dev.* **2007**, *21*, 2593–2606. [CrossRef] [PubMed]
243. Han, S.; Kim, S.; Bahl, S.; Li, L.; Burande, C.F.; Smith, N.; James, M.; Beauchamp, R.L.; Bhide, P.; DiAntonio, A.; et al. The E3 ubiquitin ligase protein associated with Myc (Pam) regulates mammalian/mechanistic target of rapamycin complex 1 (mTORC1) signaling in vivo through N- and C-terminal domains. *J. Biol. Chem.* **2012**, *287*, 30063–30072. [CrossRef] [PubMed]
244. Han, S.; Witt, R.M.; Santos, T.M.; Polizzano, C.; Sabatini, B.L.; Ramesh, V. Pam (Protein associated with Myc) functions as an E3 ubiquitin ligase and regulates TSC/mTOR signaling. *Cell Signal* **2008**, *20*, 1084–1091. [CrossRef] [PubMed]
245. Babetto, E.; Beirowski, B.; Russler, E.V.; Milbrandt, J.; DiAntonio, A. The Phr1 ubiquitin ligase promotes injury-induced axon self-destruction. *Cell Rep.* **2013**, *3*, 1422–1429. [CrossRef] [PubMed]
246. Chretien, M.L.; Legouge, C.; Martin, R.Z.; Hammann, A.; Trad, M.; Aucagne, R.; Largeot, A.; Bastie, J.N.; Delva, L.; Quere, R. Trim33/Tif1gamma is involved in late stages of granulomonopoiesis in mice. *Exp. Hematol.* **2016**, *44*, 727–739.e726. [CrossRef]
247. Kim, J.; Kaartinen, V. Generation of mice with a conditional allele for Trim33. *Genesis* **2008**, *46*, 329–333. [CrossRef]
248. Ferri, F.; Parcelier, A.; Petit, V.; Gallouet, A.S.; Lewandowski, D.; Dalloz, M.; van den Heuvel, A.; Kolovos, P.; Soler, E.; Squadrito, M.L.; et al. TRIM33 switches off Ifnb1 gene transcription during the late phase of macrophage activation. *Nat. Commun.* **2015**, *6*, 8900. [CrossRef]
249. Kusy, S.; Gault, N.; Ferri, F.; Lewandowski, D.; Barroca, V.; Jaracz-Ros, A.; Losson, R.; Romeo, P.H. Adult hematopoiesis is regulated by TIF1gamma, a repressor of TAL1 and PU.1 transcriptional activity. *Cell Stem Cell* **2011**, *8*, 412–425. [CrossRef]
250. Bai, X.; Trowbridge, J.J.; Riley, E.; Lee, J.A.; DiBiase, A.; Kaartinen, V.M.; Orkin, S.H.; Zon, L.I. TiF1-gamma plays an essential role in murine hematopoiesis and regulates transcriptional elongation of erythroid genes. *Dev. Biol.* **2013**, *373*, 422–430. [CrossRef]
251. Quere, R.; Saint-Paul, L.; Carmignac, V.; Martin, R.Z.; Chretien, M.L.; Largeot, A.; Hammann, A.; Pais de Barros, J.P.; Bastie, J.N.; Delva, L. Tif1gamma regulates the TGF-beta1 receptor and promotes physiological aging of hematopoietic stem cells. *Proc. Natl. Acad. Sci. USA* **2014**, *111*, 10592–10597. [CrossRef] [PubMed]
252. Gontan, C.; Achame, E.M.; Demmers, J.; Barakat, T.S.; Rentmeester, E.; van, I.W.; Grootegoed, J.A.; Gribnau, J. RNF12 initiates X-chromosome inactivation by targeting REX1 for degradation. *Nature* **2012**, *485*, 386–390. [CrossRef] [PubMed]
253. Goodrich, L.; Panning, B.; Leung, K.N. Activators and repressors: A balancing act for X-inactivation. *Semin. Cell Dev. Biol.* **2016**, *56*, 3–8. [CrossRef] [PubMed]
254. Shin, J.; Bossenz, M.; Chung, Y.; Ma, H.; Byron, M.; Taniguchi-Ishigaki, N.; Zhu, X.; Jiao, B.; Hall, L.L.; Green, M.R.; et al. Maternal Rnf12/RLIM is required for imprinted X-chromosome inactivation in mice. *Nature* **2010**, *467*, 977–981. [CrossRef] [PubMed]
255. Kammoun, M.; Maas, E.; Criem, N.; Gribnau, J.; Zwijsen, A.; Vermeesch, J.R. RLIM enhances BMP signalling mediated fetal lung development in mice. *bioRxiv* **2018**. [CrossRef]
256. Shin, J.; Wallingford, M.C.; Gallant, J.; Marcho, C.; Jiao, B.; Byron, M.; Bossenz, M.; Lawrence, J.B.; Jones, S.N.; Mager, J.; et al. RLIM is dispensable for X-chromosome inactivation in the mouse embryonic epiblast. *Nature* **2014**, *511*, 86–89. [CrossRef]

257. Wang, F.; Shin, J.; Shea, J.M.; Yu, J.; Boskovic, A.; Byron, M.; Zhu, X.; Shalek, A.K.; Regev, A.; Lawrence, J.B.; et al. Regulation of X-linked gene expression during early mouse development by Rlim. *Elife* **2016**, 5. [CrossRef]
258. Jiao, B.; Ma, H.; Shokhirev, M.N.; Drung, A.; Yang, Q.; Shin, J.; Lu, S.; Byron, M.; Kalantry, S.; Mercurio, A.M.; et al. Paternal RLIM/Rnf12 is a survival factor for milk-producing alveolar cells. *Cell* **2012**, *149*, 630–641. [CrossRef]
259. Chen, W.; Jiang, X.; Luo, Z. WWP2: A multifunctional ubiquitin ligase gene. *Pathol. Oncol. Res.* **2014**, *20*, 799–803. [CrossRef]
260. Zou, W.; Chen, X.; Shim, J.H.; Huang, Z.; Brady, N.; Hu, D.; Drapp, R.; Sigrist, K.; Glimcher, L.H.; Jones, D. The E3 ubiquitin ligase Wwp2 regulates craniofacial development through mono-ubiquitylation of Goosecoid. *Nat. Cell Biol.* **2011**, *13*, 59–65. [CrossRef]
261. Yang, Y.; Liao, B.; Wang, S.; Yan, B.; Jin, Y.; Shu, H.B.; Wang, Y.Y. E3 ligase WWP2 negatively regulates TLR3-mediated innate immune response by targeting TRIF for ubiquitination and degradation. *Proc. Natl. Acad. Sci. USA* **2013**, *110*, 5115–5120. [CrossRef]
262. Li, H.; Zhang, P.; Zhang, Q.; Li, C.; Zou, W.; Chang, Z.; Cui, C.P.; Zhang, L. WWP2 is a physiological ubiquitin ligase for phosphatase and tensin homolog (PTEN) in mice. *J. Biol. Chem.* **2018**, *293*, 8886–8899. [CrossRef]
263. Ambrozkiewicz, M.C.; Schwark, M.; Kishimoto-Suga, M.; Borisova, E.; Hori, K.; Salazar-Lazaro, A.; Rusanova, A.; Altas, B.; Piepkorn, L.; Bessa, P.; et al. Polarity Acquisition in Cortical Neurons Is Driven by Synergistic Action of Sox9-Regulated Wwp1 and Wwp2 E3 Ubiquitin Ligases and Intronic miR-140. *Neuron* **2018**, *100*, 1097–1115.e1015. [CrossRef]
264. Guruharsha, K.G.; Kankel, M.W.; Artavanis-Tsakonas, S. The Notch signalling system: Recent insights into the complexity of a conserved pathway. *Nat. Rev. Genet.* **2012**, *13*, 654–666. [CrossRef]
265. Nowell, C.S.; Radtke, F. Notch as a tumour suppressor. *Nat. Rev. Cancer* **2017**, *17*, 145–159. [CrossRef]
266. Zavadil, J.; Cermak, L.; Soto-Nieves, N.; Bottinger, E.P. Integration of TGF-beta/Smad and Jagged1/Notch signalling in epithelial-to-mesenchymal transition. *EMBO J.* **2004**, *23*, 1155–1165. [CrossRef]
267. Niimi, H.; Pardali, K.; Vanlandewijck, M.; Heldin, C.H.; Moustakas, A. Notch signaling is necessary for epithelial growth arrest by TGF-beta. *J. Cell Biol.* **2007**, *176*, 695–707. [CrossRef]
268. Bray, S.J. Notch signalling in context. *Nat. Rev. Mol. Cell Biol.* **2016**, *17*, 722–735. [CrossRef]
269. Haines, N.; Irvine, K.D. Glycosylation regulates Notch signalling. *Nat. Rev. Mol. Cell Biol.* **2003**, *4*, 786–797. [CrossRef]
270. Logeat, F.; Bessia, C.; Brou, C.; LeBail, O.; Jarriault, S.; Seidah, N.G.; Israel, A. The Notch1 receptor is cleaved constitutively by a furin-like convertase. *Proc. Natl. Acad. Sci. USA* **1998**, *95*, 8108–8112. [CrossRef]
271. Blobel, C.P. Metalloprotease-disintegrins: Links to cell adhesion and cleavage of TNF alpha and Notch. *Cell* **1997**, *90*, 589–592. [CrossRef]
272. Pan, D.; Rubin, G.M. Kuzbanian controls proteolytic processing of Notch and mediates lateral inhibition during Drosophila and vertebrate neurogenesis. *Cell* **1997**, *90*, 271–280. [CrossRef]
273. Itoh, M.; Kim, C.H.; Palardy, G.; Oda, T.; Jiang, Y.J.; Maust, D.; Yeo, S.Y.; Lorick, K.; Wright, G.J.; Ariza-McNaughton, L.; et al. Mind bomb is a ubiquitin ligase that is essential for efficient activation of Notch signaling by Delta. *Dev. Cell* **2003**, *4*, 67–82. [CrossRef]
274. De Strooper, B.; Annaert, W.; Cupers, P.; Saftig, P.; Craessaerts, K.; Mumm, J.S.; Schroeter, E.H.; Schrijvers, V.; Wolfe, M.S.; Ray, W.J.; et al. A presenilin-1-dependent gamma-secretase-like protease mediates release of Notch intracellular domain. *Nature* **1999**, *398*, 518–522. [CrossRef]
275. Wu, L.; Aster, J.C.; Blacklow, S.C.; Lake, R.; Artavanis-Tsakonas, S.; Griffin, J.D. MAML1, a human homologue of Drosophila mastermind, is a transcriptional co-activator for NOTCH receptors. *Nat. Genet.* **2000**, *26*, 484–489. [CrossRef]
276. Tamura, K.; Taniguchi, Y.; Minoguchi, S.; Sakai, T.; Tun, T.; Furukawa, T.; Honjo, T. Physical interaction between a novel domain of the receptor Notch and the transcription factor RBP-J kappa/Su(H). *Curr. Biol.* **1995**, *5*, 1416–1423. [CrossRef]
277. Nagel, A.C.; Krejci, A.; Tenin, G.; Bravo-Patino, A.; Bray, S.; Maier, D.; Preiss, A. Hairless-mediated repression of notch target genes requires the combined activity of Groucho and CtBP corepressors. *Mol. Cell. Biol.* **2005**, *25*, 10433–10441. [CrossRef]

278. Oswald, F.; Winkler, M.; Cao, Y.; Astrahantseff, K.; Bourteele, S.; Knochel, W.; Borggrefe, T. RBP-Jkappa/SHARP recruits CtIP/CtBP corepressors to silence Notch target genes. *Mol. Cell. Biol.* **2005**, *25*, 10379–10390. [CrossRef]
279. Qiu, L.; Joazeiro, C.; Fang, N.; Wang, H.Y.; Elly, C.; Altman, Y.; Fang, D.; Hunter, T.; Liu, Y.C. Recognition and ubiquitination of Notch by Itch, a hect-type E3 ubiquitin ligase. *J. Biol. Chem.* **2000**, *275*, 35734–35737. [CrossRef]
280. Puca, L.; Chastagner, P.; Meas-Yedid, V.; Israel, A.; Brou, C. Alpha-arrestin 1 (ARRDC1) and beta-arrestins cooperate to mediate Notch degradation in mammals. *J. Cell Sci.* **2013**, *126*, 4457–4468. [CrossRef]
281. McGill, M.A.; McGlade, C.J. Mammalian numb proteins promote Notch1 receptor ubiquitination and degradation of the Notch1 intracellular domain. *J. Biol. Chem.* **2003**, *278*, 23196–23203. [CrossRef]
282. Nie, J.; McGill, M.A.; Dermer, M.; Dho, S.E.; Wolting, C.D.; McGlade, C.J. LNX functions as a RING type E3 ubiquitin ligase that targets the cell fate determinant Numb for ubiquitin-dependent degradation. *EMBO J.* **2002**, *21*, 93–102. [CrossRef]
283. Mund, T.; Graeb, M.; Mieszczanek, J.; Gammons, M.; Pelham, H.R.; Bienz, M. Disinhibition of the HECT E3 ubiquitin ligase WWP2 by polymerized Dishevelled. *Open Biol.* **2015**, *5*, 150185. [CrossRef]
284. Jung, J.G.; Stoeck, A.; Guan, B.; Wu, R.C.; Zhu, H.; Blackshaw, S.; Shih Ie, M.; Wang, T.L. Notch3 interactome analysis identified WWP2 as a negative regulator of Notch3 signaling in ovarian cancer. *PLoS Genet.* **2014**, *10*, e1004751. [CrossRef]
285. Sorensen, E.B.; Conner, S.D. gamma-secretase-dependent cleavage initiates notch signaling from the plasma membrane. *Traffic* **2010**, *11*, 1234–1245. [CrossRef]
286. Zheng, L.; Conner, S.D. PI5P4Kgamma functions in DTX1-mediated Notch signaling. *Proc. Natl. Acad. Sci. USA* **2018**, *115*, E1983–E1990. [CrossRef]
287. Fryer, C.J.; White, J.B.; Jones, K.A. Mastermind recruits CycC:CDK8 to phosphorylate the Notch ICD and coordinate activation with turnover. *Mol. Cell* **2004**, *16*, 509–520. [CrossRef]
288. Rallis, C.; Pinchin, S.M.; Ish-Horowicz, D. Cell-autonomous integrin control of Wnt and Notch signalling during somitogenesis. *Development* **2010**, *137*, 3591–3601. [CrossRef]
289. Ruel, L.; Bourouis, M.; Heitzler, P.; Pantesco, V.; Simpson, P. Drosophila shaggy kinase and rat glycogen synthase kinase-3 have conserved activities and act downstream of Notch. *Nature* **1993**, *362*, 557–560. [CrossRef]
290. Espinosa, L.; Ingles-Esteve, J.; Aguilera, C.; Bigas, A. Phosphorylation by glycogen synthase kinase-3 beta down-regulates Notch activity, a link for Notch and Wnt pathways. *J. Biol. Chem.* **2003**, *278*, 32227–32235. [CrossRef]
291. Zhou, T.; Yi, F.; Wang, Z.; Guo, Q.; Liu, J.; Bai, N.; Li, X.; Dong, X.; Ren, L.; Cao, L.; et al. The Functions of DNA Damage Factor RNF8 in the Pathogenesis and Progression of Cancer. *Int. J. Biol. Sci.* **2019**, *15*, 909–918. [CrossRef] [PubMed]
292. Pettersson, S.; Sczaniecka, M.; McLaren, L.; Russell, F.; Gladstone, K.; Hupp, T.; Wallace, M. Non-degradative ubiquitination of the Notch1 receptor by the E3 ligase MDM2 activates the Notch signalling pathway. *Biochem. J.* **2013**, *450*, 523–536. [CrossRef] [PubMed]
293. Kim, H.; Ronai, Z.A. Rewired Notch/p53 by Numb'ing Mdm2. *J. Cell Biol.* **2018**, *217*, 445–446. [CrossRef] [PubMed]
294. Deblandre, G.A.; Lai, E.C.; Kintner, C. Xenopus neuralized is a ubiquitin ligase that interacts with XDelta1 and regulates Notch signaling. *Dev. Cell* **2001**, *1*, 795–806. [CrossRef]
295. Kramer, H. Neuralized: Regulating notch by putting away delta. *Dev. Cell* **2001**, *1*, 725–726. [CrossRef]
296. Fischer, A.; Schumacher, N.; Maier, M.; Sendtner, M.; Gessler, M. The Notch target genes Hey1 and Hey2 are required for embryonic vascular development. *Genes Dev.* **2004**, *18*, 901–911. [CrossRef]
297. Zhang, N.; Gridley, T. Defects in somite formation in lunatic fringe-deficient mice. *Nature* **1998**, *394*, 374–377. [CrossRef]
298. Swiatek, P.J.; Lindsell, C.E.; del Amo, F.F.; Weinmaster, G.; Gridley, T. Notch1 is essential for postimplantation development in mice. *Genes Dev.* **1994**, *8*, 707–719. [CrossRef]
299. Koo, B.K.; Yoon, M.J.; Yoon, K.J.; Im, S.K.; Kim, Y.Y.; Kim, C.H.; Suh, P.G.; Jan, Y.N.; Kong, Y.Y. An obligatory role of mind bomb-1 in notch signaling of mammalian development. *PLoS ONE* **2007**, *2*, e1221. [CrossRef]

300. Koo, B.K.; Lim, H.S.; Song, R.; Yoon, M.J.; Yoon, K.J.; Moon, J.S.; Kim, Y.W.; Kwon, M.C.; Yoo, K.W.; Kong, M.P.; et al. Mind bomb 1 is essential for generating functional Notch ligands to activate Notch. *Development* **2005**, *132*, 3459–3470. [CrossRef]
301. Barsi, J.C.; Rajendra, R.; Wu, J.I.; Artzt, K. Mind bomb1 is a ubiquitin ligase essential for mouse embryonic development and Notch signaling. *Mech. Dev.* **2005**, *122*, 1106–1117. [CrossRef] [PubMed]
302. Yeh, C.H.; Bellon, M.; Nicot, C. FBXW7: A critical tumor suppressor of human cancers. *Mol. Cancer* **2018**, *17*, 115. [CrossRef] [PubMed]
303. Mao, J.H.; Perez-Losada, J.; Wu, D.; Delrosario, R.; Tsunematsu, R.; Nakayama, K.I.; Brown, K.; Bryson, S.; Balmain, A. Fbxw7/Cdc4 is a p53-dependent, haploinsufficient tumour suppressor gene. *Nature* **2004**, *432*, 775–779. [CrossRef] [PubMed]
304. Busino, L.; Millman, S.E.; Scotto, L.; Kyratsous, C.A.; Basrur, V.; O'Connor, O.; Hoffmann, A.; Elenitoba-Johnson, K.S.; Pagano, M. Fbxw7alpha- and GSK3-mediated degradation of p100 is a pro-survival mechanism in multiple myeloma. *Nat. Cell Biol.* **2012**, *14*, 375–385. [CrossRef] [PubMed]
305. Sato, M.; Rodriguez-Barrueco, R.; Yu, J.; Do, C.; Silva, J.M.; Gautier, J. MYC is a critical target of FBXW7. *Oncotarget* **2015**, *6*, 3292–3305. [CrossRef] [PubMed]
306. Tetzlaff, M.T.; Yu, W.; Li, M.; Zhang, P.; Finegold, M.; Mahon, K.; Harper, J.W.; Schwartz, R.J.; Elledge, S.J. Defective cardiovascular development and elevated cyclin E and Notch proteins in mice lacking the Fbw7 F-box protein. *Proc. Natl. Acad. Sci. USA* **2004**, *101*, 3338–3345. [CrossRef]
307. Tsunematsu, R.; Nakayama, K.; Oike, Y.; Nishiyama, M.; Ishida, N.; Hatakeyama, S.; Bessho, Y.; Kageyama, R.; Suda, T.; Nakayama, K.I. Mouse Fbw7/Sel-10/Cdc4 is required for notch degradation during vascular development. *J. Biol. Chem.* **2004**, *279*, 9417–9423. [CrossRef]
308. Onoyama, I.; Tsunematsu, R.; Matsumoto, A.; Kimura, T.; de Alboran, I.M.; Nakayama, K.; Nakayama, K.I. Conditional inactivation of Fbxw7 impairs cell-cycle exit during T cell differentiation and results in lymphomatogenesis. *J. Exp. Med.* **2007**, *204*, 2875–2888. [CrossRef]
309. Matsuoka, S.; Oike, Y.; Onoyama, I.; Iwama, A.; Arai, F.; Takubo, K.; Mashimo, Y.; Oguro, H.; Nitta, E.; Ito, K.; et al. Fbxw7 acts as a critical fail-safe against premature loss of hematopoietic stem cells and development of T-ALL. *Genes Dev.* **2008**, *22*, 986–991. [CrossRef]
310. Sancho, R.; Jandke, A.; Davis, H.; Diefenbacher, M.E.; Tomlinson, I.; Behrens, A. F-box and WD repeat domain-containing 7 regulates intestinal cell lineage commitment and is a haploinsufficient tumor suppressor. *Gastroenterology* **2010**, *139*, 929–941. [CrossRef]
311. Matsumoto, A.; Onoyama, I.; Sunabori, T.; Kageyama, R.; Okano, H.; Nakayama, K.I. Fbxw7-dependent degradation of Notch is required for control of "stemness" and neuronal-glial differentiation in neural stem cells. *J. Biol. Chem.* **2011**, *286*, 13754–13764. [CrossRef] [PubMed]
312. Onoyama, I.; Suzuki, A.; Matsumoto, A.; Tomita, K.; Katagiri, H.; Oike, Y.; Nakayama, K.; Nakayama, K.I. Fbxw7 regulates lipid metabolism and cell fate decisions in the mouse liver. *J. Clin. Investig.* **2011**, *121*, 342–354. [CrossRef] [PubMed]
313. Krebs, L.T.; Iwai, N.; Nonaka, S.; Welsh, I.C.; Lan, Y.; Jiang, R.; Saijoh, Y.; O'Brien, T.P.; Hamada, H.; Gridley, T. Notch signaling regulates left-right asymmetry determination by inducing Nodal expression. *Genes Dev.* **2003**, *17*, 1207–1212. [CrossRef] [PubMed]
314. Yoon, M.J.; Koo, B.K.; Song, R.; Jeong, H.W.; Shin, J.; Kim, Y.W.; Kong, Y.Y.; Suh, P.G. Mind bomb-1 is essential for intraembryonic hematopoiesis in the aortic endothelium and the subaortic patches. *Mol. Cell. Biol.* **2008**, *28*, 4794–4804. [CrossRef] [PubMed]
315. Kang, K.; Lee, D.; Hong, S.; Park, S.G.; Song, M.R. The E3 ligase Mind bomb-1 (Mib1) modulates Delta-Notch signaling to control neurogenesis and gliogenesis in the developing spinal cord. *J. Biol. Chem.* **2013**, *288*, 2580–2592. [CrossRef] [PubMed]
316. Horn, S.; Kobberup, S.; Jorgensen, M.C.; Kalisz, M.; Klein, T.; Kageyama, R.; Gegg, M.; Lickert, H.; Lindner, J.; Magnuson, M.A.; et al. Mind bomb 1 is required for pancreatic beta-cell formation. *Proc. Natl. Acad. Sci. USA* **2012**, *109*, 7356–7361. [CrossRef] [PubMed]

317. Luxan, G.; Casanova, J.C.; Martinez-Poveda, B.; Prados, B.; D'Amato, G.; MacGrogan, D.; Gonzalez-Rajal, A.; Dobarro, D.; Torroja, C.; Martinez, F.; et al. Mutations in the NOTCH pathway regulator MIB1 cause left ventricular noncompaction cardiomyopathy. *Nat. Med.* **2013**, *19*, 193–201. [CrossRef]
318. Kim, Y.W.; Koo, B.K.; Jeong, H.W.; Yoon, M.J.; Song, R.; Shin, J.; Jeong, D.C.; Kim, S.H.; Kong, Y.Y. Defective Notch activation in microenvironment leads to myeloproliferative disease. *Blood* **2008**, *112*, 4628–4638. [CrossRef]
319. Song, R.; Kim, Y.W.; Koo, B.K.; Jeong, H.W.; Yoon, M.J.; Yoon, K.J.; Jun, D.J.; Im, S.K.; Shin, J.; Kong, M.P.; et al. Mind bomb 1 in the lymphopoietic niches is essential for T and marginal zone B cell development. *J. Exp. Med.* **2008**, *205*, 2525–2536. [CrossRef]
320. Hsu, T.S.; Mo, S.T.; Hsu, P.N.; Lai, M.Z. c-FLIP is a target of the E3 ligase deltex1 in gastric cancer. *Cell Death Dis.* **2018**, *9*, 135. [CrossRef]
321. Hsiao, H.W.; Liu, W.H.; Wang, C.J.; Lo, Y.H.; Wu, Y.H.; Jiang, S.T.; Lai, M.Z. Deltex1 is a target of the transcription factor NFAT that promotes T cell anergy. *Immunity* **2009**, *31*, 72–83. [CrossRef] [PubMed]
322. Storck, S.; Delbos, F.; Stadler, N.; Thirion-Delalande, C.; Bernex, F.; Verthuy, C.; Ferrier, P.; Weill, J.C.; Reynaud, C.A. Normal immune system development in mice lacking the Deltex-1 RING finger domain. *Mol. Cell. Biol.* **2005**, *25*, 1437–1445. [CrossRef] [PubMed]
323. Hsiao, H.W.; Hsu, T.S.; Liu, W.H.; Hsieh, W.C.; Chou, T.F.; Wu, Y.J.; Jiang, S.T.; Lai, M.Z. Deltex1 antagonizes HIF-1alpha and sustains the stability of regulatory T cells in vivo. *Nat. Commun.* **2015**, *6*, 6353. [CrossRef] [PubMed]
324. Ou-Yang, H.F.; Zhang, H.W.; Wu, C.G.; Zhang, P.; Zhang, J.; Li, J.C.; Hou, L.H.; He, F.; Ti, X.Y.; Song, L.Q.; et al. Notch signaling regulates the FOXP3 promoter through RBP-J- and Hes1-dependent mechanisms. *Mol. Cell Biochem.* **2009**, *320*, 109–114. [CrossRef]
325. Burghardt, S.; Claass, B.; Erhardt, A.; Karimi, K.; Tiegs, G. Hepatocytes induce Foxp3(+) regulatory T cells by Notch signaling. *J. Leukoc. Biol.* **2014**, *96*, 571–577. [CrossRef]
326. Panier, S.; Durocher, D. Regulatory ubiquitylation in response to DNA double-strand breaks. *DNA Repair.* **2009**, *8*, 436–443. [CrossRef]
327. Kolas, N.K.; Chapman, J.R.; Nakada, S.; Ylanko, J.; Chahwan, R.; Sweeney, F.D.; Panier, S.; Mendez, M.; Wildenhain, J.; Thomson, T.M.; et al. Orchestration of the DNA-damage response by the RNF8 ubiquitin ligase. *Science* **2007**, *318*, 1637–1640. [CrossRef]
328. Li, L.; Halaby, M.J.; Hakem, A.; Cardoso, R.; El Ghamrasni, S.; Harding, S.; Chan, N.; Bristow, R.; Sanchez, O.; Durocher, D.; et al. Rnf8 deficiency impairs class switch recombination, spermatogenesis, and genomic integrity and predisposes for cancer. *J. Exp. Med.* **2010**, *207*, 983–997. [CrossRef]
329. Lu, L.Y.; Wu, J.; Ye, L.; Gavrilina, G.B.; Saunders, T.L.; Yu, X. RNF8-dependent histone modifications regulate nucleosome removal during spermatogenesis. *Dev. Cell* **2010**, *18*, 371–384. [CrossRef]
330. Ouyang, S.; Song, Y.; Tian, Y.; Chen, Y.; Yu, X.; Wang, D. RNF8 deficiency results in neurodegeneration in mice. *Neurobiol. Aging* **2015**, *36*, 2850–2860. [CrossRef]
331. Valnegri, P.; Huang, J.; Yamada, T.; Yang, Y.; Mejia, L.A.; Cho, H.Y.; Oldenborg, A.; Bonni, A. RNF8/UBC13 ubiquitin signaling suppresses synapse formation in the mammalian brain. *Nat. Commun.* **2017**, *8*, 1271. [CrossRef] [PubMed]
332. Senturk, E.; Manfredi, J.J. Mdm2 and tumorigenesis: Evolving theories and unsolved mysteries. *Genes Cancer* **2012**, *3*, 192–198. [CrossRef] [PubMed]
333. Mendrysa, S.M.; McElwee, M.K.; Michalowski, J.; O'Leary, K.A.; Young, K.M.; Perry, M.E. mdm2 Is critical for inhibition of p53 during lymphopoiesis and the response to ionizing irradiation. *Mol. Cell. Biol.* **2003**, *23*, 462–472. [CrossRef] [PubMed]
334. Jones, S.N.; Roe, A.E.; Donehower, L.A.; Bradley, A. Rescue of embryonic lethality in Mdm2-deficient mice by absence of p53. *Nature* **1995**, *378*, 206–208. [CrossRef]
335. Mendrysa, S.M.; O'Leary, K.A.; McElwee, M.K.; Michalowski, J.; Eisenman, R.N.; Powell, D.A.; Perry, M.E. Tumor suppression and normal aging in mice with constitutively high p53 activity. *Genes Dev.* **2006**, *20*, 16–21. [CrossRef]

336. Bult, C.J.; Blake, J.A.; Smith, C.L.; Kadin, J.A.; Richardson, J.E.; Mouse Genome Database, G. Mouse Genome Database (MGD) 2019. *Nucleic Acids Res.* **2019**, *47*, D801–D806. [CrossRef]
337. Amberger, J.S.; Bocchini, C.A.; Schiettecatte, F.; Scott, A.F.; Hamosh, A. OMIM.org: Online Mendelian Inheritance in Man (OMIM(R)), an online catalog of human genes and genetic disorders. *Nucleic Acids Res.* **2015**, *43*, D789–D798. [CrossRef]



© 2019 by the authors. Licensee MDPI, Basel, Switzerland. This article is an open access article distributed under the terms and conditions of the Creative Commons Attribution (CC BY) license (http://creativecommons.org/licenses/by/4.0/).